Ecole doctorale : Science de la Matière, du Rayonnement et de l'Environnement

THESE

Pour obtenir le grade de **Docteur de l'Université de Lille**

Spécialité de doctorat : Science des Matériaux

Soutenue le 24/01/2024 par :

Van-Hau VO LE

PLA/carbon nanotubes composites for thermoelectric applications: relationships between elaboration, structure and properties

(Composites PLA/nanotubes de carbone pour applications à la thermoélectricité : relations entre élaboration, structure et propriétés)

Composition de jury :

Pr. Sébastien PRUVOST	Professeur - INSA Lyon	Rapporteur
Pr. Jean-François FELLER	Professeur - Université Bretagne Sud	Rapporteur
Pr. Loïc LE PLUART	Professeur - Université Caen Normandie	Examinateur
Pr. Aurélie CAYLA	Professeure – ENSAIT Roubaix	Examinatrice, **Présidente**
Dr. Corinne BINET	Maîtresse de conférences - UMET - Université de Lille	Co-encadrante
Pr. Valérie GAUCHER	Professeure - UMET - Université de Lille	Directrice de thèse
Invité		
Dr. Jean-François BRUN	Maître de conférences - UMET - Université de Lille	Co-encadrant

Acknowledgement

This thesis brings to me not only scientific experience but also valuable human experiences. I would like to express my gratitude to those who have taught, supported and shared their time with me during these three years.

First of all, I would like to express my sincere gratitude to my thesis supervisors, Valérie Gaucher, Corinne Binet, and Jean-François Brun, who bring this opportunity to me and always help me in the long-life of the thesis and difficulties in my daily life since I came to France. Their support, advice and inspiration give me the confidence to carry out this thesis. Especially, their expertise in scientific, patience and human morality helped me to grow up in professionally and personally.

I also wish to thank to Aurélie Cayla, who helped me to prepare samples, and did experiments on my materials at GEMTEX, ENSAIT.

I would like to express my great thanks to all members of the jury for their availability and evaluation of my thesis.

This thesis has been done at UMET laboratory, University of Lille. It was funded by Région Hauts de France and University of Lille. I am deeply grateful for their financial support.

This work could not have been done without the help of the people who took their time to analyze my samples. I extend my sincere thanks to Frédéric Cazaux for TGA analysis, Alexandre Fadel for SEM analysis, Jean-François Tahon for XRD analysis, and Adeline Marin for uniaxial tensile test.

I never miss this opportunity to express my gratitude to permanent researches, and to all the postdoctoral, graduate students of UMET, as well as all of my Vietnamese friends who have spent their time with me during three years for discussion and explanation, as well as exchange about the different cultures. Thank for being and helping me during a long time. Thanks to all of you, Mouloud, Ahmed, Sylvain, Michèle, Mélanie, Thibaut, Hélène, Chi Kien, Hong Quan, Nhat Thanh, Kien Phuong, Hoang Long, …

This thesis including all my efforts is dedicated to my family. Particularly, a huge thank to my parents, my grandfather and grandmother. Few sentences will not enough to describe everything they've done for me. Thank you very much for sharing and always being there for me.

Last but not least, I will forever be thankful to my girlfriend, Thuy Duyen, who patiently waited for and supported me during these three years.

Table of content

Symbols & Abbreviations

Symbols

$\dot{\varepsilon}$	Initial strain rate
2θ	Bragg's angle
λ	Wavelength
d	Interplanar distance of the considered (hkl) plane
χ_c	Crystallinity
ΔH_m	Melting enthalpy
ΔH_{cc}	Enthalpy of cold crystallization
ΔH_m^0	Enthalpy of melting of 100 % crystalline PLA
T_g	Glass transition temperature
T_{cc}	Cold crystallization temperature
T_m	Melt temperature
C_p	Specific heat capacity
ρ	Density
w	Weight fraction of CNT
Φ	Volume fraction of CNT
ZT	Figure of merit
PF	Power factor
S	Seebeck coefficient
κ	Thermal conductivity
T	Temperature
α	Thermal diffusivity
σ	Electrical conductivity
ε^*	Complex dielectric permittivity
ε'	Real part of the complex permittivity
ε''	Imaginary parts of the complex permittivity
ε_0	Vacuum permittivity
i	Imaginary constant
R	Resistance
t	Sample thickness
F	Geometrical correction factor

V	Voltage
I	Current
ΔV	Voltage difference
ΔT	Temperature gradient

Abbreviations

CNT	Carbon nanotubes
MWCNT	Multi-walled carbon nanotubes
DWCNT	Double-walled carbon nanotubes
SWCNT	Single-walled carbon nanotubes
PLA	Polylactic acid
A-PLA	Amorphous PLA
Sc-PLA	Semi-crystalline PLA
$CHCl_3$	Chloroforme
PP	Polypropylene
PC	Polycarbonate
PS	Polystyrene
PVAc	Polyvinyl acetate
PVDF	Polyvinylidene fluoride
ABS	Acrylonitrile butadiene styrene
PA6	Polyamide 6
PA66	Polyamide 66
PBT	Poly(butylene terephthalate)
PEDOT	Poly(3,4-ethylenedioxythiophene)
PEDOT:PSS	PEDOT:polystyrene sulfonate
PEDOT:Tos	PEDOT:tosylate
DMSO	Dimethylsulfoxide
DMF	N,N-dimethylformamide
PANI	Polyaniline
TCPP	Meso-tetra(4-carboxylphenyl) porphine
PPy	Polypyrrole
TE	Thermoelectric
VDP	Van-der Pauw

General introduction

Challenges related to the environment and energy are one of the major issues in the 21st century. Several studies show that around 66 % of all global primary energy consumed by the human activity is lost as waste heat after conversion [1]. Due to the growing global energy demand and limited access to cost-effective renewable energy, the conversion of waste heat into electricity would make a significant contribution to energy efficiency. Thermoelectric (TE) generators would be the perfect solution to these problems, as they can convert heat directly into electricity without any moving parts and fluid, but some major scientific and technological locks remain.

The fundamental concept of TE technology relies on TE materials, which have the ability, thanks to the Seebeck effect, to generate electrical power from the thermal energy and vice versa, to create a temperature gradient when a voltage is applied, thanks to the Peltier effect. This conversion has numerous advantages, such as producing no chemical waste, resulting in minimal environmental impact. Moreover, TE materials can be used over a wide temperature range, ensuring high reliability in various applications. The performance of a thermoelectric material is assessed in terms of its figure of merit ZT, which is a function of its electrical conductivity, its thermal conductivity, its Seebeck coefficient (also known as thermoelectric power) and the temperature T. Depending on the application, it is generally accepted that a good thermoelectric material should have a ZT greater than 1. With less accuracy, the power factor (PF), which depends only on the electrical conductivity and the Seebeck coefficient, can also be used to describe the thermoelectric properties of a material.

From Fig. 1, it can be seen that the most efficient TE materials are inorganic semiconductors made from metalloids and metal alloys such as skutterudites, telluride-based materials (e.g., BiSbTe), copper ion liquid like materials (e.g., Si-Ge alloys). For applications relatively closed to ambient temperature (around 300 K), only bismuth telluride (Bi_2Te_3) and its derivatives such as $Bi_{2-x}Sb_xTe_3$ are enough competitive with a ZT higher than 1.5. However, due to their potential toxicity and mechanical rigidity, this class of semiconductors are not suitable for large scale applications.

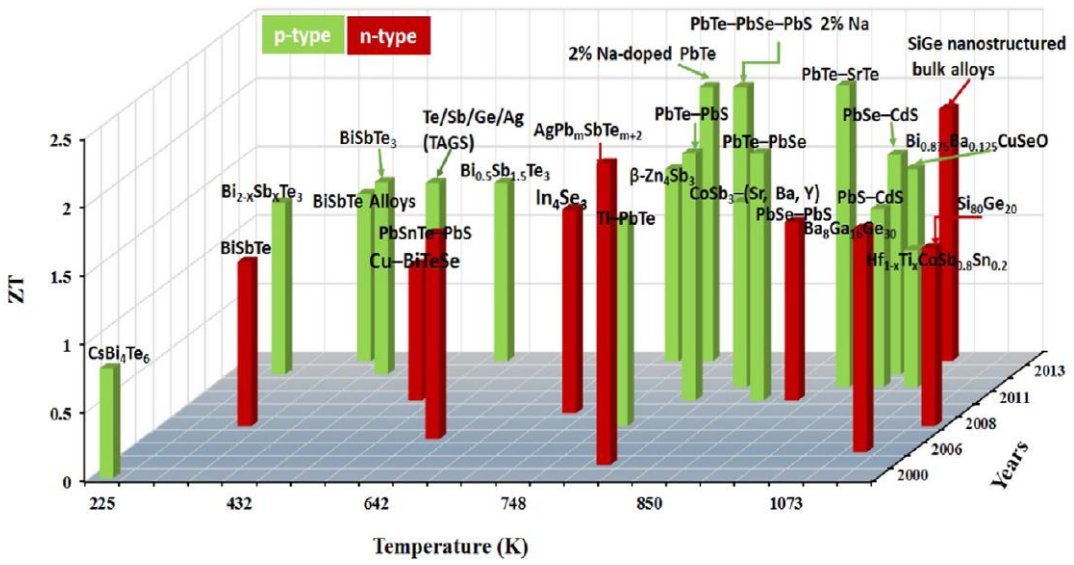

Figure 1. Figure of merit (ZT) of the most efficient TE materials as a function of temperature application [2].

At the same time, over the last decade, a new field named Organic Electronics has emerged with the development of organic semiconductors, especially for photovoltaic applications. It is now possible to use this new class of materials for thermoelectric applications. These organic materials offer an alternative that is both less expensive and easier to process compared to their inorganic equivalents. For example, organic materials based on electronically conducting polymers such as poly(3,4-ethylenedioxythiophene) (PEDOT), or polyaniline (PANI) and their nanocomposites containing conductive nanofillers have been proposed for TE applications. Fig. 2 presents the power factor (PF) and figure of merit (ZT) of polymer-based materials at room temperature which were reported in the last 10 years. As can be seen, hybrid organic-inorganic composites, composed of a polymer matrix and an inorganic nanofiller, are currently the most efficient thermoelectrics: PEDOT filled with Bi_2Te_3 achieves a ZT of 0.6 and polyvinylpyrrolidone (PVP) filled with Ag_2Se nanostructures achieves 1.1. Besides, organic semiconductors, made from insulating polymer matrix filled with carbon nanotubes (CNT) have also attracted considerable interest for low-temperature TE uses ($T < 500$ K) due to their easy processability, flexibility, low cost, and low intrinsic thermal conductivity.

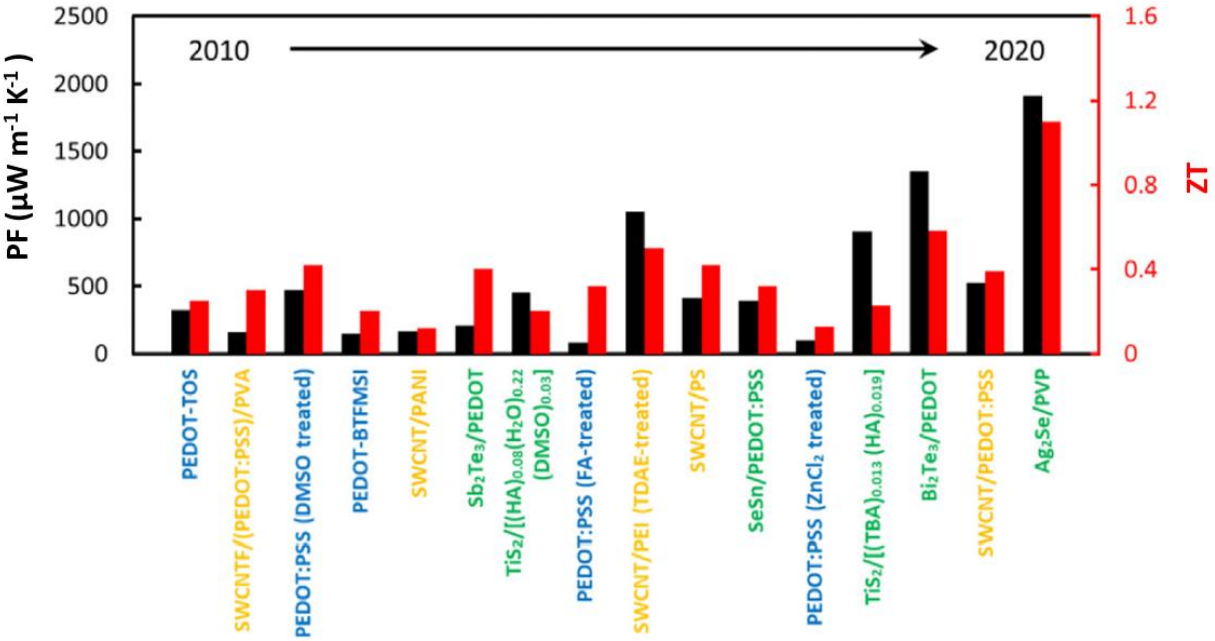

Figure 2. PF and ZT of polymer-based materials for thermoelectric application at room temperature [3].

Up to now, the relationships between the structure and TE properties of polymer/CNT nanocomposites are not well understood. Therefore, in order to optimize the TE performances of these materials, it is necessary to investigate the correlation between the elaboration, morphology and TE properties. For instance, it is essential to investigate the influence of CNT dispersion and orientation, as well as the impact of crystallinity of the polymer matrix on TE properties of nanocomposites. In addition, considering the depletion of petroleum resources and the need for more sustainable products, it seems relevant to replace petro-sourced polymers by bio-based polymers wherever possible. Among natural polymers, polylactic acid (PLA) is readily available commercially and exists in both amorphous and crystallizable forms. Therefore, the aim of this dissertation is to comprehensively study the correlation between elaboration, structure and thermoelectric properties of PLA/carbon nanotubes nanocomposites, for several types of CNT including multi-walled-, single-walled- and functionalized single-walled carbon nanotubes, in order to contribute to the development of new flexible organic thermoelectric materials.

This manuscript is divided into four chapters.

Chapter I is a state of the art review that aims to provide background knowledge on TE principles, a summary of the most popular TE materials, and a presentation of the main materials used in this research, *i.e.* PLA and CNT.

Chapter II provides detailed information on all materials, the different elaboration processes and characterization methods.

Chapter III, partly in the form of an article, is devoted to the study of the TE properties of PLA/CNT nanocomposites containing filler weight fractions from 2 to 40 wt%. The impact of the elaboration processes and the structure (amorphous/semi-crystalline) of the polymer matrix on the TE properties of thick PLA/CNT samples is investigated. The anisotropic TE properties of thick samples are also discussed. In addition, the effect of CNT orientation on the electrical conductivity of PLA/CNT nanocomposites is also analyzed.

Chapter IV focuses on the influence of CNT types (Multi-Walled CNT, Single Walled CNT, and functionalized Single Walled CNT) on the TE properties of thin films of PLA-based nanocomposites. Finally, the evolution of the TE properties of thin films with temperature from room temperature to 400 K is discussed in this last chapter.

References

1. Forman, C., Muritala, I. K., Pardemann, R., & Meyer, B. (2016). Estimating the global waste heat potential. *Renewable and Sustainable Energy Reviews, 57,* 1568–1579. https://doi.org/10.1016/j.rser.2015.12.192
2. Fitriani, Ovik, R., Long, B. D., Barma, M. C., Riaz, M., Sabri, M. F. M., … Saidur, R. (2016). A review on nanostructures of high-temperature thermoelectric materials for waste heat recovery. *Renewable and Sustainable Energy Reviews*, *64,* 635–659. https://doi.org/10.1016/j.rser.2016.06.035
3. Li, J., Huckleby, A. B., & Zhang, M. (2022). Polymer-based thermoelectric materials: A review of power factor improving strategies. *Journal of Materiomics*, *8*(1), 204–220. https://doi.org/10.1016/j.jmat.2021.03.013

Chapter I. State of the art

1. Introduction

This chapter presents a literature review about the most popular thermoelectric (TE) materials and their applications. First of all, a brief introduction to the thermoelectricity and TE effects will be highlighted, followed by a presentation of TE generators and their operating principle. Then, the summarizing of widely-used TE materials including inorganic and organic materials will be presented, along with their dimensionless figure of merit (ZT) or power factor (PF). Finally, this chapter will be devoted to the discussion of thermoplastic polymer/carbon nanotubes (CNT) nanocomposites, with the main focus on the elaboration processes and their impact on TE properties. In particular, a state of the art on PLA/CNT nanocomposites, which is the material used in this study will be reviewed with a focus on their elaboration process, structure, and TE properties for room temperature applications.

2. Generalities on thermoelectricity

2.1. Thermoelectric effects

When two ends of a conducting or semiconducting material are kept at different temperatures, a temperature gradient is created across the material, and the resulting movement of charge carries from the hot end to the cold end, creates a potential difference. Conversely, when an electric current or voltage is applied across a material, the release or absorption of heat occurs at the two ends of the material, depending on the direction of the current. These phenomena are known as thermoelectric effects.

2.1.1. Seebeck effect

In 1821, Thomas Seebeck, an Estonian-German physicist, discovered that when two dissimilar metals A and B are used to make two junctions in an open circuit, one of which is heated and the other is cooled, a resultant electromotive force (Seebeck voltage) is generated between the two metals (Fig 1.1). This phenomenon was entitled the Seebeck effect. The induced voltage difference (ΔV) can be raised by increasing the temperature gradient (ΔT), but the voltages produced by Seebeck effect are small, usually only a few microvolts per kelvin of temperature difference at the junction of two metals.

The voltage is proportional to the temperature difference as the eq. 1.1:

$$S = -\frac{\Delta V}{\Delta T} = -\frac{V_H - V_C}{T_H - T_C} \qquad \text{(eq 1.1)}$$

where S is the Seebeck coefficient (V K^{-1}), ΔV is the difference in voltage (V), and ΔT is the difference in temperature (K), the indices H and C refer to the hot junction and the cold junction, respectively [1–3]. This linear relation is true only for small changes of temperatures. The Seebeck coefficient is also called thermopower or TE power. This coefficient is an inherent property of the circuit. S is of the order of μV K^{-1} for metals and 100 μV K^{-1} for semiconductors. The sign can be both negative and positive, depending on the charge of the majority carriers.

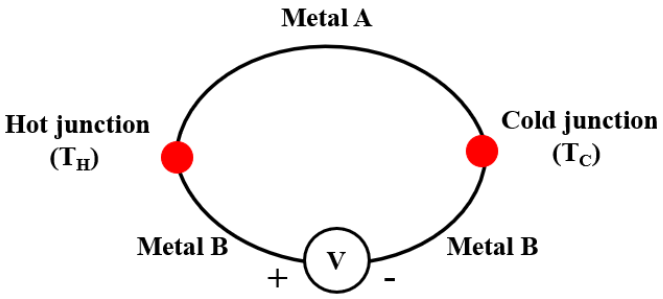

Figure 1.1. Schematic of the Seebeck effect.

2.1.2. Peltier effect

In 1834, Jean-Charles A.Peltier, a French physicist, discovered the inverse of the Seebeck effect. He observed that a current flowing in the circuit of two dissimilar conducting materials resulted in a temperature difference across the two junctions. This effect represents the calorific effect of an electrical current at the junction of two different metals (Fig. 1.2). The direction of the current would determine the heating or cooling of the junction. The rate of heat absorbed or emitted at either of the two junctions in the circuit is given by eq. 1.2:

$$Q_{A-B} = \pi_{AB}.I = (\pi_A - \pi_B).I \qquad \text{(eq 1.2)}$$

where Q_{A-B} is the heat generated at the junction per unit time (W), π_A and π_B are the Peltier coefficient of the conductors A and B (V), and I is the electric current (A) [1].

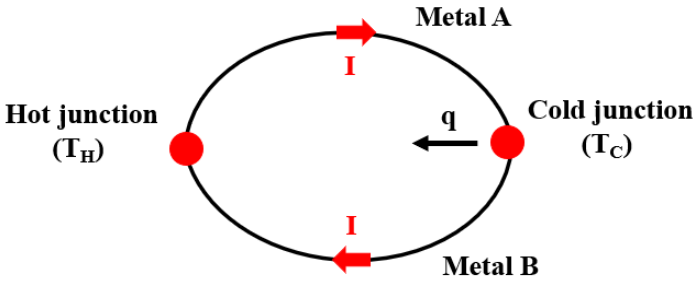

Figure 1.2. Schematic of the Peltier effect.

2.1.3. Thomson effect

In 1851, William Thomson (also known as Lord Kelvin), a British scientist, observed the interdependency between Seebeck and Peltier effects. Unlike previous effects, Thomson effect does not require junctions. Thomson described that a conductor with a current flowing through it and subject to a temperature gradient exchanges heat with its surroundings and that, conversely, a current is generated in a material subject to a temperature difference and through which heat flows [4]. A quantity of linear heat $\boldsymbol{dQ/dx}$ absorbed or emitted by a portion of the

conductor of length $\boldsymbol{dx}$ is proportional to the product of the thermal gradient $\boldsymbol{dT/dx}$ and the current intensity I as expressed in eq. 1.3. The proportionality coefficient is called the Thomson coefficient β given in V K^{-1}.

$$\frac{dQ}{dx} = \beta I \frac{dT}{dx} \qquad \text{(eq 1.3)}$$

By convention, β is positive if the conductor absorbs heat when the current flows from the hot end to the cold end.

Lord Kelvin established that the three coefficients (S, π, β) governing the thermoelectric effects are linked by two relationships, namely the Thomson relations:

$$\pi_{AB} = S_{AB}.T \qquad \text{(eq 1.4)}$$

$$\beta = T \frac{dS}{dT} \qquad \text{(eq 1.5)}$$

2.2. Thermoelectrics and energy conversion

2.2.1. Seebeck coefficient

The Seebeck coefficient is basically the voltage developed per unit temperature difference applied across a material and it is expressed in μV K^{-1}. The Seebeck coefficient is positive for p-type and negative for n-type semiconductors. The typical values of the Seebeck coefficient for metals, semiconductors, and insulators are ~5, ~100 μV K^{-1}, and >1 mV K^{-1}, respectively. Table 1.1 summarizes S values for some materials at room temperature. It can be seen that the semiconductor materials exhibit higher Seebeck values than metals, indicating the potential for using these materials in thermoelectric applications.

Table 1.1. Seebeck values of some materials at room temperature.

Materials		**S (µV K^{-1})**	**Ref.**
Metal	Zn	2.4	[5]
	In	1.68	
	Rb	- 10	
	Pb	- 1.05	
	Cd	2.55	
	Cu	1.83	
	Al	- 1.66	
	Ag	1.5	
Semiconductor	Si	148	[6]
	Ge	280	[6]
	Bi_2Te_3	- 140	[7]
	Mg_2Si	- 250	[8]
	$CaZn_2Sb_2$	120	[9]
	$CoSb_3$	- 120	[10]
Insulator	Thermoplastic polymers	-	

A good way to understand the microscopic origin of the Seebeck coefficient is to use the Mott relation (eq. 1.6) [11], which gives the expression of the Seebeck coefficient for metals, intrinsic semiconductors, and conducting polymers.

$$S = \frac{\pi^2}{3}\frac{{k_\beta}^2}{q}T\left(\frac{dln\sigma}{dE}\right)_{E=E_F} = \frac{\pi^2}{3}\frac{{k_\beta}^2}{q}T\left(\frac{1}{n}\frac{dn(E)}{dE}+\frac{1}{\mu}\frac{d\mu(E)}{dE}\right)_{E=E_F} \quad \text{(eq 1.6)}$$

where k_β is the Boltzmann constant, q is the carrier charge, T is the temperature, σ is the electrical conductivity, $n(E)$ is the charge carrier density at energy E, n is the carrier concentration, $\mu(E)$ is the mobility at energy E, and E_F is the Fermi energy. Using the Constant Scattering Time Approximation, it can be shown that

$$S = \frac{8\pi^2{k_\beta}^2}{3qh^2}m^*T(\frac{\pi}{3n})^{2/3} \quad \text{(eq 1.7)}$$

where h is the Planck's constant, m^* is the effective mass of the charge carriers [1]. As can be seen, the Seebeck coefficient depends on the electronic band structure of the materials and the density of states (DOS) essentially at the Fermi level. Higher DOS and moderate carrier concentration will generate a larger Seebeck coefficient [12, 13].

Measuring the Seebeck coefficient of TE materials involves some criteria (i) both temperature and voltage gradient should be measured simultaneously when the system is in a

steady state, (ii) the voltage response to the temperature gradient should be linear, and (iii) temperature and voltage should be measured within the same points [6].

2.2.2. Electrical conductivity

Electrical conductivity (σ in S m^{-1}) is an important property of material, which measures the ability of a material to conduct electrical current. The electrical conductivity of a semiconductor is given by the following equation:

$$\sigma = e(\mu_e n + \mu_h p) \quad \text{(eq 1.8)}$$

where e, n, p, μ_e and μ_h are the elementary charge (1.6 x 10^{-19} C), electron concentration (m^{-3}), hole concentration, electron mobility (m^2 V^{-1} m^{-1}), the hole mobility, respectively. The charge mobility is expressed as the following relation:

$$\mu = \frac{e\tau}{m^*} \quad \text{(eq 1.9)}$$

where τ is the scattering time (s) *i.e.* the average time between two carrier collisions, and m^* is the effective mass (kg).

The electrical conductivity of materials can be tuned either by varying the carrier concentration or by varying the carrier mobility. The carrier mobility and concentration depend on the temperature. In semiconductors, electrical conductivity rises with temperature. A high carrier concentration is generally required for a high electrical conductivity, which needs to be optimized to have a high thermoelectric efficiency. High carrier mobility is also desired for efficient conduction of electricity, which is determined by the electronic structure of the materials and the various scattering mechanisms, such as lattice scattering, impurity scattering, etc. For example, lattice scattering increases with temperature leading to a decrease in carrier mobility. Contrary to this, impurity scattering is dominant at low temperature. Hence, the type of material, doping, impurities, and temperature determine the electrical conductivity of TE materials [6, 13, 14].

Typical values of the electrical conductivity for a good TE material are on the order of 10^7 S m^{-1}. Table 1.2 summarizes the conductivity values for various metals, semiconductors, and thermoplastic polymers. It is evident that metals consistently have the highest conductivity values, followed by semiconductors, and finally, thermoplastics, which exhibit σ values close to insulators.

Table 1.2. Electrical conductivity of some materials at room temperature.

Materials		**σ (S m^{-1})**	**Ref.**
Metal	Zn	1.7 x 10^{7}	[15]
	In	1.2 x 10^{7}	
	Rb	0.8 x 10^{7}	
	Pb	0.5 x 10^{7}	
	Cd	1.4 x 10^{7}	
	Cu	5.9 x 10^{7}	
	Al	3.8 x 10^{7}	
	Ag	6.3 x 10^{7}	
Semiconductor	Si	2.5 x 10^{-4}	[15]
	Ge	1.5	
	Bi_2Te_3	4 x 10^{4}	[16]
	Mg_2Si	3 x 10^{4}	[8]
	$CaZn_2Sb_2$	4.2 x 10^{4}	[9]
	$CoSb_3$	4 x 10^{4}	[17]
Insulator	Thermoplastic polymers	10^{-12} – 10^{-15}	[18]

2.2.3. Thermal conductivity

The thermal conductivity (κ) of a material determines its ability to conduct heat. It was experimentally introduced by Joseph Fourier through the following law named after him:

$$\vec{\varphi} = -\kappa \overrightarrow{grad} T \qquad \text{(eq 1.10)}$$

where $\vec{\varphi}$ is the heat rate through the material (W m^{-2}), $\overrightarrow{\text{grad}}T$ is the thermal gradient across the material (K m^{-1}) and κ is the thermal conductivity of the material (W m^{-1} K^{-1}).

The thermal conductivity (κ) is the sum of the lattice thermal conductivity (κ_l), due to lattice vibrations called phonon, and the charge carrier thermal conductivity (κ_c), due to electrons and/or holes:

$$\kappa = \kappa_l + \kappa_c \qquad \text{(eq 1.11)}$$

The charge-carrier component is related to the electrical conductivity σ via the Widemann-Franz law

$$\kappa_c = L\sigma T \qquad \text{(eq 1.12)}$$

where σ is the electrical conductivity (S m^{-1}), L is the Lorentz constant, which is equal to 2.45 x 10^{-8} V^2 K^{-2} for metals and 1.5 x 10^{-8} V^2 K^{-2} for nondegenerate semiconductor, and T is the absolute temperature (K). Hence, an increase in electrical conductivity, in turn, leads to an

increase in the thermal conductivity due to charge-carriers. In a metal, the contribution of κ_c is much greater than that of κ_l, whereas in an insulator the opposite is true. Thermal conductivity will not be the same for an amorphous solid as for a crystalline solid. Moreover, the lattice thermal conductivity depends on the crystal structure and lattice parameters of the material [6, 13].

The lattice thermal conductivity can be expressed as:

$$\kappa_l = \frac{1}{3} C_p v_a l_p \qquad \text{(eq 1.13)}$$

where C_p is the specific heat capacity, l_p is the mean free path of the phonons and v_a is the group velocity of the phonons. The smaller the mean path, the more collisions there are between phonons and the lower the thermal conductivity. For example, the use of nanostructured materials makes this possible and therefore reduces the thermal performance of the material compare to bulk material.

Typical values of thermal conductivity for some metals, semiconductors, and thermoplastic polymers are summarized in Table 1.3. Thermoplastic polymers which have low electrical values (Table 1.2) also exhibit low thermal conductivity values, which limits their use in thermoelectric application.

Table 1.3. Thermal conductivity of some materials at room temperature.

Materials		**κ (W m^{-1} K^{-1})**	**Ref.**
Metal	Zn	116	[15]
	In	82	
	Rb	58	
	Pb	35	
	Cd	97	
	Cu	401	
	Al	237	
	Ag	429	
Semiconductor	Si	148	[15]
	Ge	59.9	
	Bi_2Te_3	2.1	[16]
	Mg_2Si	12.14	[8]
	$CaZn_2Sb_2$	2.6	[9]
	$CoSb_3$	10	[17]
Insulator	Thermoplastic polymers	0.1 – 0.5	[19]

2.2.4. Power factor and Figure of merit

The conversion efficiency of a thermoelectric material depends on the performance of the material that is determined by its dimensionless figure of merit (ZT) given by:

$$ZT = \frac{S^2\sigma}{\kappa}T \qquad \text{(eq 1.14)}$$

where, $S^2\sigma$ is the power factor (PF) (μW m^{-1} K^{-2}), S is the Seebeck coefficient (μV K^{-1}), σ is the electrical conductivity (S m^{-1}), κ is the thermal conductivity of the material (W m^{-1} K^{-1}), and T is the absolute temperature (K). A good TE material should then possess a high electrical conductivity (σ), a high Seebeck coefficient (S), and a low thermal conductivity (κ) in order to have a high ZT.

The efficiency of a TE generator is expressed in terms of figure of merit as eq. 1.15:

$$\eta = \frac{T_H - T_C}{T_H}\frac{\sqrt{1+ZT_M}-1}{\sqrt{1+ZT_M}+\frac{T_C}{T_H}} \qquad \text{(eq 1.15)}$$

where, ZT_M is the average ZT of temperature drop (T_M=(T_H+T_c)/2), T_H and T_C are the temperatures of the heat source (hot side) and cold side, respectively [20, 21].

A maximum ZT value leads to maximum conversion efficiency. For TE materials at high temperature (Fig. 1.3), ZT should be equal to or higher than 1 to obtain a conversion efficiency of 10 %. To obtain a conversion efficiency of 20 % to 25 %, ZT of at least 3 would have to be achieved, but such ZT values have not yet been reached. Experimentally, the highest ZT values are around 2.5 obtained for PbTe and SnSe.

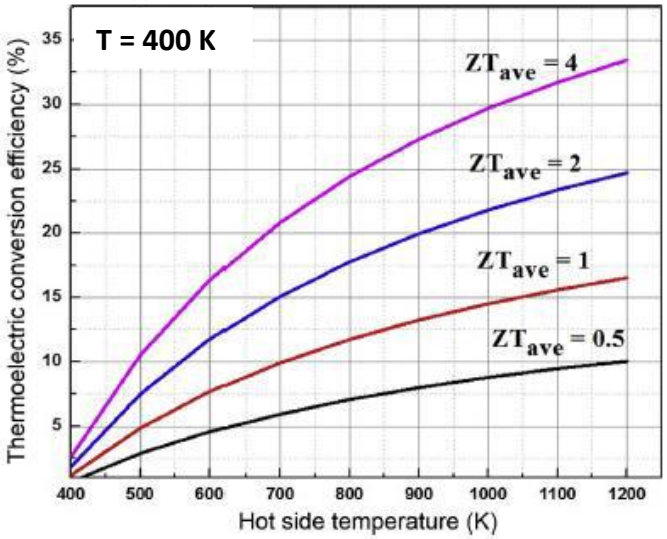

Figure 1.3. The thermoelectric conversion efficiency as a function of differential operating temperature and ZT [6]. T_{cold} = 400 K, and ZT_{ave} = ZT_M of eq. 1.5.

2.2.5. Thermoelectric module

TE element (TE couple) is the basic working unit of TE devices. Fig. 1.3 illustrates the working mechanism of TE devices. TE element consists of a p-type (containing positive charge carriers - holes) and a n-type semiconductor (containing negative charge carriers - electrons). In this, a junction is formed from these two conducting materials. Heat source at the junction causes carriers to flow away from the junction, making an electrical generator which is also called power generation mode. In this case, the Seebeck effect comes into play (Fig 1.4a). Similarly, when electrical current is passed in the appropriate direction through the junction, both types of charge carriers move away from the junction, and convey heat away, thus cooling the junction (cooling mode) [20]. In this case the Peltier effect is involved (Fig 1.4b).

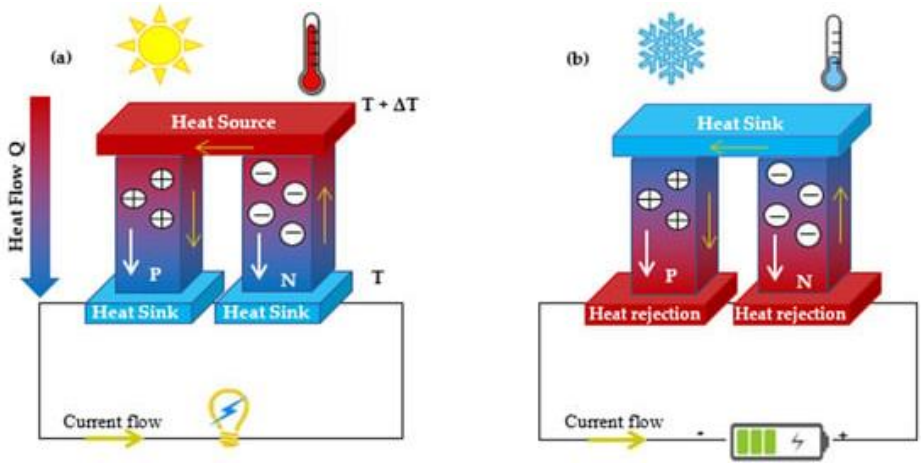

Figure 1.4. Thermoelectric couple operating (a) in power generation mode and (b) in cooling mode [22].

The TE performance of a single couple is not sufficient, so it is necessary to combine several units to increase efficiency. Alternating p-type and n-type semiconductors arranged thermally in parallel and electrically in series compose a thermoelectric module. The TE semiconductors are connected by copper conducting strips fixed at a thermal conducting and electrical insulating spare ceramic plate. Each thermoelectric module consists of several tens to hundreds of pairs of TE couples (Fig. 1.5) [23] .

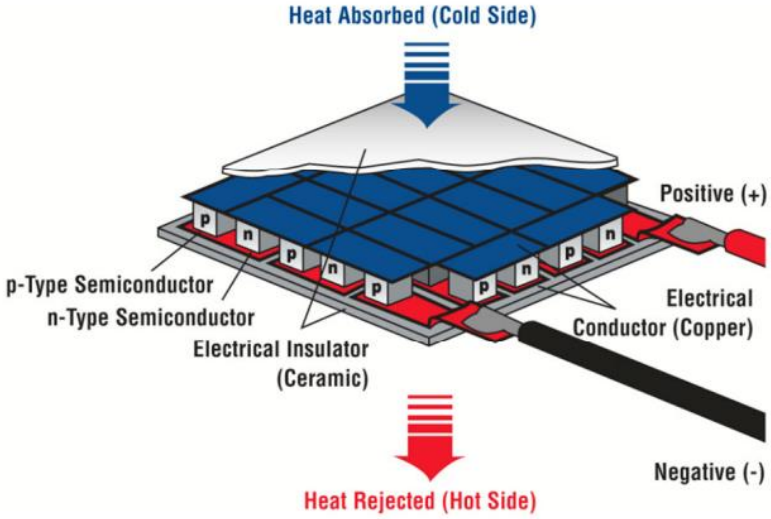

Figure 1.5. A thermoelectric module [23].

2.2.6. Evolution with charge carrier concentration

The relationships between the Seebeck coefficient, the electrical conductivity, the thermal conductivity as well as its lattice component, ZT and charge carrier concentration are presented in Fig. 1.6. It can be seen that the charge carrier concentration has an inverse effect on the electrical conductivity and the Seebeck coefficient since an increase in the charge carrier concentration leads to an increase in the electrical conductivity and a decrease in the Seebeck coefficient. Therefore, an optimal carrier concentration can tune the power factor ($S^2\sigma$), implying that semiconductors are potential candidates for TE applications. The thermal conductivity is almost constant and is mainly determined by lattice scattering phenomena until at high concentration charge carriers which contributes to increase the total thermal conductivity. Indeed, in metals, the increase of electronic thermal conductivity degrades thermoelectric performance. Usually, the highest figures of merit are obtained for charge carrier concentrations between 10^{18} and 10^{22} cm^{-3}, which corresponds to highly doped semiconductors.

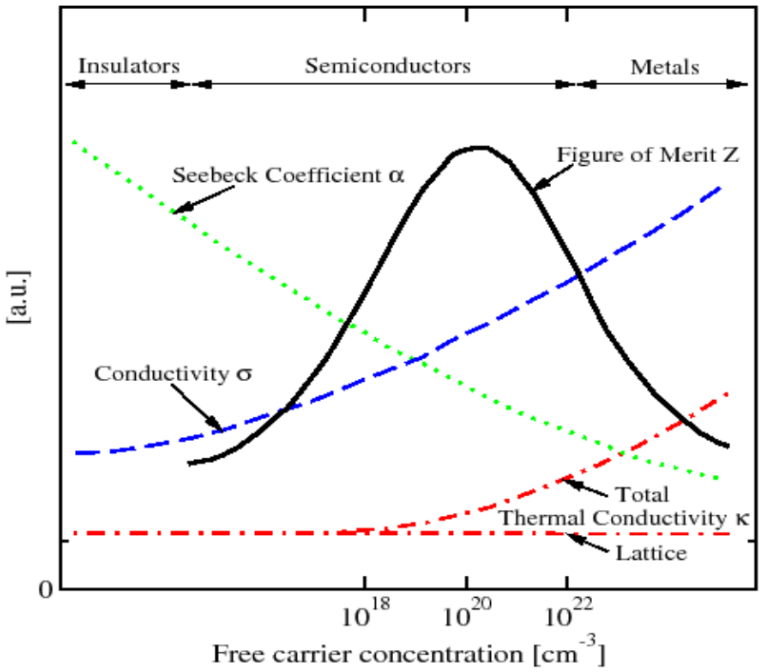

Figure 1.6. Evolution of electrical and thermal conductivities, Seebeck coefficient, and figure of merit as a function of carrier concentration in insulators, semiconductors, and metals [24].

3. Thermoelectric materials

3.1. Inorganic materials

Historically, research into TE materials initially focused on inorganic materials. Fig. 1.7 illustrates the summary of figures of merits of various p-type and n-type inorganic TE materials.

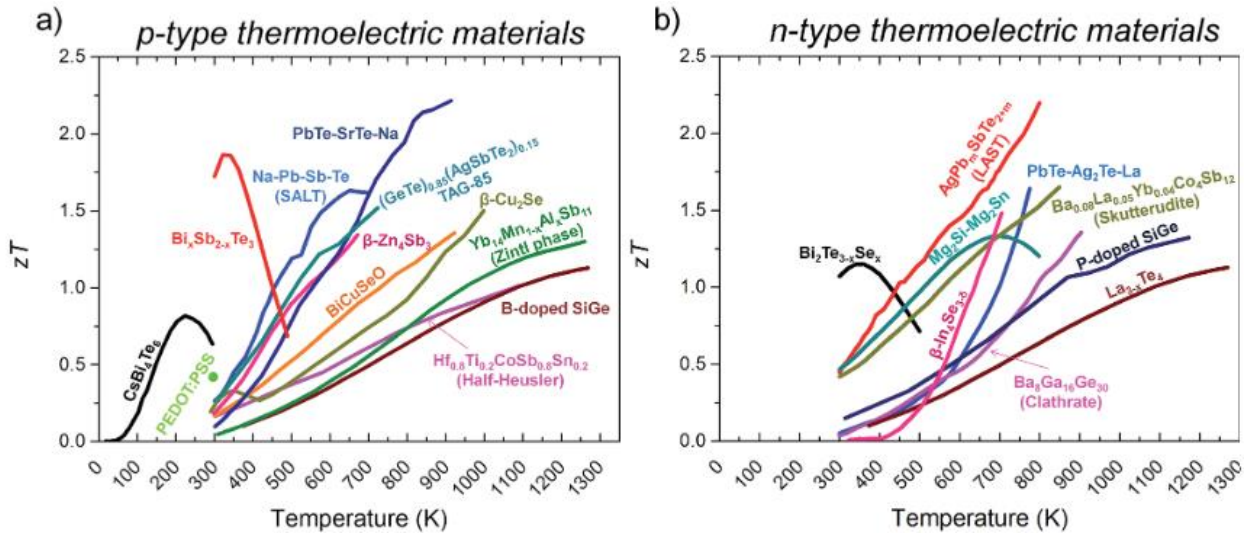

Figure 1.7. Summary of some of the best ZT for bulk inorganic TE materials as a function of applied temperature [25]: a) p-type and b) n-type.

The following paragraphs will describe some of the conventional inorganic TE materials.

- **Bismuth telluride (Bi_2Te_3)** has been known as a very effective semiconductor with a narrow band gap of approximately 0.15 eV, for energy conversion at low temperature (ambient temperature range). This material is often described as having a distorted rock-salt structure with a repeat of five layers Te^1-Bi-Te^2-Bi-Te^1 that are hold together through Van der Waals interactions [26].

Bi_2Te_3 displays unique properties such as a high Seebeck coefficient (~ 200 µV K^{-1}), good electrical conductivity (~ 4 x 10^4 S m^{-1}), and low thermal conductivity (~ 1.5 W m^{-1} K^{-1}) [16]. The high ZT of 1.35 at room temperature has been reported for the bulk p-type Bi_2Te_3 with a layer structure synthesized by the melt-spinning and spark plasma sintering (SPS) process [27].

- **Lead telluride (PbTe)** is a promising TE material than can efficiently operate at medium temperature (600 – 800 K). It forms a crystalline structure similar to NaCl, where the cation sites are occupied by Pb atoms, and Te creates the anionic lattice. A band gap of 0.32 eV allows it to be optimized for power-generation applications and can be doped either n- or p-type with appropriate dopants. The highest ZT values for PbTe have been reported to be 0.8 – 1.0 at around 650 K [28].

- **Skutterudites** normally refer to naturally occurring mineral $CoAs_3$, which are materials that crystallize in a BCC (body-centered cubic) structure made up of XY_6 octahedral molecules (where X = Co, Rh, Ir and Y = P, As, Sb). The spaces between these octahedrons can accommodate a large metal atom, giving rise to a filled skutterudite. This structure was first synthesized by Jeitschko et al. [29], is written $R^{4+}[T_4X_{12}]^{4-}$, where R is an electropositive ion, T is Fe, Ru or Os, and X is As, P, or Sb. The atoms filling the skutterudite modulate the electronic concentration of the material and reduce thermal conductivity by phonon reflection [30]. The most recent results concern nickel-doped skutterudites and show ZT between 0.45 and 1.25 at temperature between 600 and 900 K [28].

- **TAGS (Te-Ag-Ge-Sb)** has been developed for applications around 700 K. Its thermal conductivity is low, but sophisticated mixtures are required to combine mechanical strength with thermal and electrical properties. Recent improvements have been made possible by complex formulation, yielding a ZT value of 2 [31].

- **Half-Heusler (HH)** compounds (HH alloys) are ternary intermetallic compounds with the formula of ABX, where A is a transition metal, a noble metal, or a rare earth element, B is a transition metal or noble metal, and X is the main group element. HH alloys contain MgAgAs-

type cubic structure with the space group *F*43m. It is made up of three filled interpenetrating FCC (face-centered cubic) sublattices and one vacant FCC sublattice. The most attractive properties of HH compounds for thermoelectricity are high S (up to 300 $\mu V\ K^{-1}$), and high σ (~ $10^5 – 10^6\ S\ m^{-1}$) at room temperature. However, they also present high thermal conductivity (~ 10 $W\ m^{-1}K^{-1}$) which is the only drawback of HH compounds. Therefore, to degrade the thermal conductivity, some techniques currently have been studied for this material such as introducing nano-scale composites, doping and increasing the phonon scattering on the boundaries [6, 32]. The ZT values close to 1.5 at 700 K have been reported by Shutoh and Sakurada [33] for the compound $Ti_{0.5}(Zr_{0.5}Hf_{0.5})_{0.5}NiSn_{0.998}Sb_{0.002}$.

3.2. Organic thermoelectrics

Inorganic TE materials demonstrate excellent TE properties (ZT > 1) but their high cost, difficulty in processing, and rigidity restrict their use. Organic TE materials have therefore attracted increasing attention. These materials are commonly based either on intrinsic conducting polymers or polymers filled with conductive nanoparticles, such as carbon nanotubes.

3.2.1. Carbon nanotubes (CNT)

Carbon nanotubes (CNT) were first observed and described in 1952 by Radushkevich and Lukyanovich [34]. But, the discovery of CNT is often attributed to Lijima as the first scientist who described the multi-walled carbon nanotubes (MWCNT) preparation process after a random event during the testing of a new arc evaporation method for C_{60} carbon molecule fabrication in 1991 [35]. CNT are graphene sheets rolled into a seamless cylinder that can be open ended or capped, having very high aspect ratio with diameters as small as 1 nm and a length of several micrometers. Depending on the number of sheets rolled into concentric cylinders, there are two main kinds of CNT, namely multi-walled carbon nanotubes (MWCNT) and single-walled carbon nanotubes (SWCNT). Fig. 1.8 illustrates the transmission electron microscopy (TEM) images of different types of CNT.

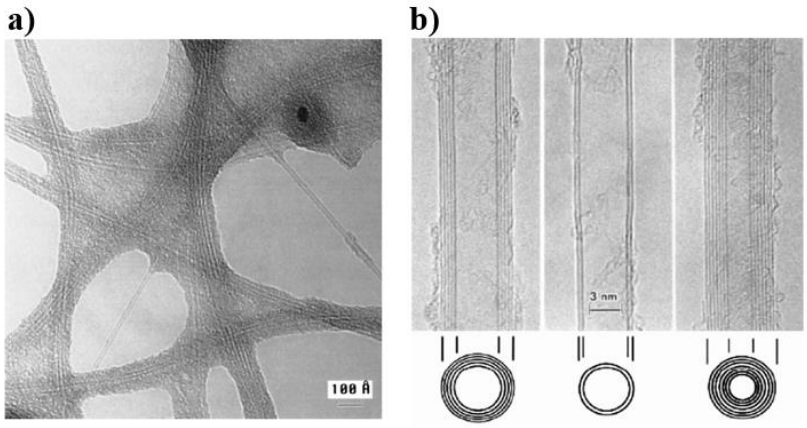

Figure 1.8. TEM images of different types of CNT. a) SWCNT, b) MWCNT with different number of layers (5, 2, and 7) [35, 36].

The atomic structure of nanotubes can be described in terms of chiral vector: $\overrightarrow{C_h} = n\overrightarrow{a_1} + m\overrightarrow{a_2}$, as shown in Fig. 1.9, where n, m are integers, and $\overrightarrow{a_1}$ and $\overrightarrow{a_2}$ are unit vectors. Nanotubes with n = m are called armchair tubes (chiral angle of 30°), and nanotubes with m = 0 are known as zigzag tubes (chiral angles are 0°). For any other values of n and m the tubes are chiral tubes [37].

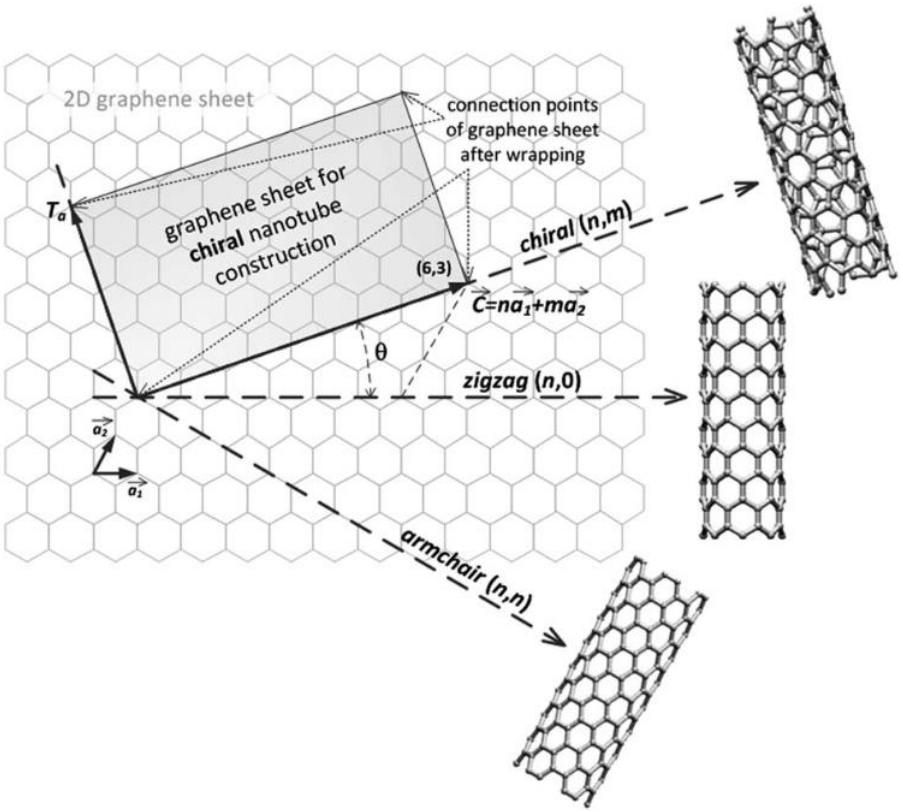

Figure 1.9. The schematic representation of the construction of a nanotube by rolling-up a graphene sheet [38].

- **Single-walled carbon nanotubes (SWCNT)**

SWCNT (Fig. 1.10) are made up of a single graphene layer wrapped into a hexagonal close-packed cylindrical structure whose diameter varies from 0.4 – 3.0 nm and length ranges from 20-1000 nm [39]. Armchair single-walled carbon nanotubes are metallic, while zigzag nanotubes are semiconducting. Statistically, a commercial powder batch of SWCNT contains 1/3 of metallic and 2/3 of semiconducting nanotubes [40]. SWCNT have a high electrical conductivity (up to 10^9 S m^{-1}), excellent current-carrying capacity (up to 10^9 A cm^{-2}), high charge-carrier mobility (up to 10^5 cm^2 V^{-1} s^{-1} at room temperature), and chirality-dependent conductivity and optical properties which promise a wide range of applications, especially in the field of TE applications [41–43].

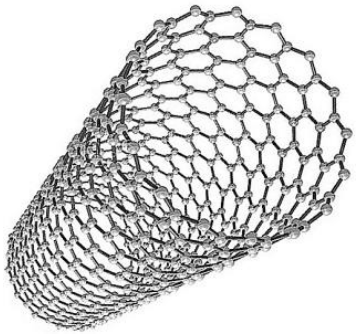

Figure 1.10. Single-walled carbon nanotubes [44].

- **Multi-walled carbon nanotubes (MWCNT)**

MWCNT (Fig. 1.11) consist of several concentric single-walled tubes, which are held together by Van der Waals bonding. The outer diameter of MWCNT can range from 2 to 100 nm, but usually between 10 and 20 nm, while the inner diameter is in the range of 1-3 nm, the interlayer spacing is around 0.34 nm and their length is 0.2 to several μm [45]. To describe the structures of MWCNT two models can be used, namely Russian doll model and parchment model. According to Russian doll model, sheets of graphene are arranged in concentric cylinders. In the parchment model, a single sheet of graphite is rolled in around itself, resembling a scroll of parchment or a rolled newspaper [45].

Owing to the sp^2 hybridization in MWCNT, delocalized electrons are generated along the wall which are responsible for the π-π interactions between adjacent cylindrical layers leading to less flexibility and more structural defects. Therefore, MWCNT always have more defects than SWCNT, which reduces their desired properties.

Figure 1.11. Multi-walled carbon nanotubes [44] with Russian doll model.

Table 1.4 presents the typical properties of MWCNT and SWCNT.

Table 1.4. Typical properties of MWCNT and SWCNT [46–50].

Properties	MWCNT	SWCNT
Tensile strength (GPa)	10 – 60	50 – 500
Elastic modulus (TPa)	0.3 – 1	~ 1
Elongation at break (%)	-	5.8
Density (g cm^{-3})	1.8 – 2.0	1.3 – 1.5
Electrical conductivity (S m^{-1})	10^7 (individual CNT)	10^8 (individual CNT)
Thermal conductivity (W m^{-1} K^{-1})	3000	6000
Thermal stability	> 700 °C	
Typical diameter (nm)	~ 20	~ 1
Specific surface area (m^2 g^{-1})	10 – 20	

- **Carbon nanotube functionalization (f-CNT)**

Functionalization is the generation of functional groups on the surfaces of CNT. Due to the presence of functional groups, the translational symmetry of CNT is disrupted by changing sp^2 carbon atoms to sp^3 carbon atoms, and properties of CNT, such as electronic and electron transport are influenced. Besides, the functionalization of CNT can enhance the solubility and can increase the interaction between CNT and the polymer leading to a homogenous dispersion of CNT in the polymer matrix [51, 52].

In a general context, the functional groups can be divided into three main categories: hydrocarbon groups (which include alkyl and alkenyl), halogen groups (such as fluorine and chlorin), and oxygen groups (which include hydroxyl, carbonyl, carboxyl, and ester). Out of these groups, oxygen groups are most often used in functionalization at the defect sites. In the present work, in order to investigate the effect of functionalization group on the thermoelectric

properties of nanocomposites, commercial SWCNT functionalized with - COOH group (Fig. 1.12) will be used as fillers in the polymer matrix.

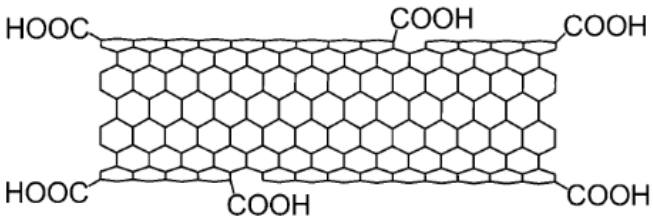

Figure 1.12. SWCNT functionalization (SWCNT-COOH).

3.2.1.1. Synthesis methods

The unique structures and properties of CNT are strongly affected by the synthesis methods of CNT. Fig. 1.13 summarizes several methods that can be used to produce CNT. Among these methods, three primary approaches taken to produce CNT including chemical vapor deposition, arc-discharge, and laser ablation [38, 53, 54].

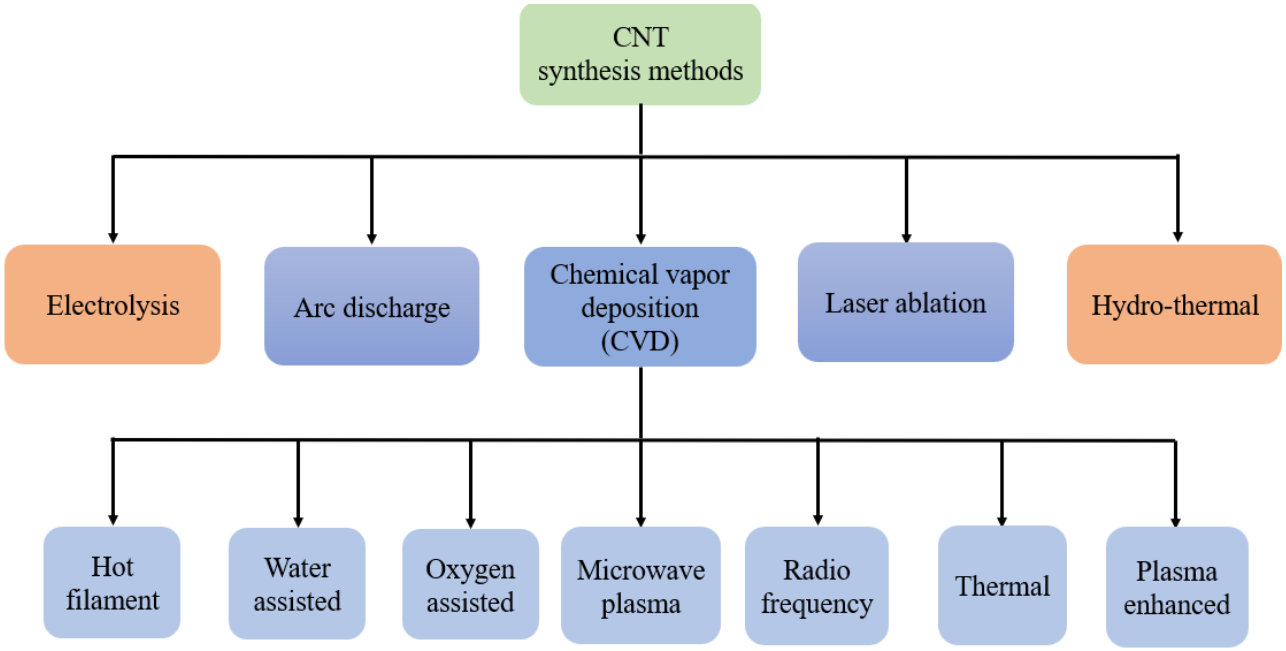

Figure 1.13. Currently used methods for CNT synthesis [53].

- **Chemical vapor deposition (CVD)**

CVD is currently the most widely used technique due to its low cost, high yield, and good controllability [55]. In this process, a combination of hydrocarbon gases such as ethylene, methane, or acetylene is mixed with a process gas consisting of ammonia, nitrogen, or hydrogen. This mixture undergoes a chemical reaction with a heated metal substrate inside a

reaction chamber, typically at a temperature of around 700 to 900 °C, at atmospheric pressure. So, CNT are grown by decomposing an organic gas over a substrate covered with metal catalyst particles. The catalyst particles can either remain at bottom or top of the growing CNT. The catalyst is one of the most important factors in CVD method, because the nature and the type of CNT will be defined by this latter. The typical substrate material is silicon, but glass and alumina are also employed. Metal nanoparticles such as Fe, Co, Ni can be used as catalysts and can be deposited on substrates by means of electron beam evaporation, physical sputtering or solution deposition [55, 56]. Nanotubes synthetized by CVD are generally known to be longer than those obtained by other methods.

- **Arc discharge**

Arc discharge is known as the oldest method for the production of CNT. This technique was first used to synthesize carbon nano-onions in 1980 [57], and then in 1991, Lijima used this method [35] to synthesize MWCNT. In this method, two high-purity graphite rods are used as anode and cathode, and a stable arc is created by applying direct current (or pulse current). Due to the power of the arc, carbon is separated from the anode and condensed on the cathode to form soot. Most CNT synthesized by arc discharge are MWCNT but, by penetrating graphite rods, and filling them with graphite powder and metal catalyst, SWCNT can be achieved [58], [36]. CNT synthesized by arc discharge have very few structural defects and are quite straight. However, the yield of this process is low and the purification procedure is complex.

- **Laser ablation**

Laser ablation is a process of removing materials from a solid surface by irradiating the surface with a laser beam. At low laser flux, the solid material is heated by the absorbed laser energy to evaporate or sublimate. Laser ablation was developed in 1995 to produce CNT [59]. In a typical laser ablation process for CNT growth, a graphite block is placed inside an oven and irradiated by a pulsed laser, and Argon gas is pumped along the direction of the laser point. The oven temperature is set at approximately 1200 °C. As the laser ablates the target, carbon is vaporized and carried by the following gas onto a cool copper collector. CNT grow on the cooler surfaces of the reactor as the vaporized carbon condenses. SWCNT are formed from a composite block of graphite and metal catalyst particles [59], whereas MWCNT are formed from pure graphite as the starting material [60]. CNT produced by this method have high purity, high yield and are mainly SWCNT, but are not suitable for mass production and also require expensive and specialized equipment.

3.2.1.2. Carbon nanotubes in thermoelectricity

There are two main reasons why CNT are a potential material for thermoelectric applications. Firstly, CNT represent a unique one-dimensional (1D) structure which satisfies the conditions of quantum confinement effect to enhance the TE efficiency [61]. Low-dimensional materials can significant increase the ZT value mainly due to the change in the density of state. Therefore, 1D conductors exhibit significantly better TE performance compared to both bulk and two-dimensional (2D) materials [62]. Secondly, due to their mechanical properties, CNT provide a framework for the development of light weight and flexible TE devices. Although carbon nanotubes have been extensively studied since the discovery by Lijima in 1991, enormously different values of physical properties can be found in the literature, especially regarding the electrical and thermal conductivities, meaning that there are still a lot to understand about these very particular objects.

CNT can exhibit both p-type and n-type thermoelectric properties through the introduction of different kinds of dopants. However, CNT are typically regarded as p-type materials, in which holes are the main charge carriers [63]. In general, the TE properties of CNT are considered for SWCNT. SWCNT samples can consist of either only metallic SWCNT (m-SWCNT) or a combination of both metallic and semiconducting SWCNT (s-SWCNT). Tables 1.5 and 1.6 illustrate the TE properties of p-type and n-type SWCNT at room temperature. It can be seen that the TE properties will be different depending on the nature of CNT (metallic or semiconductor), and the form of samples (bundles, individual, or films).

Table 1.5. TE properties of p-type SWCNT at room temperature.

Samples	**S ($\mu V\ K^{-1}$)**	**σ ($S\ m^{-1}$)**	**PF ($\mu W\ m^{-1}\ K^{-2}$)**	**Ref.**
SWCNT bundle (Metallic)	48	-	-	[64]
Individual SWCNT (Metallic)	35	-	-	[65]
Individual SWCNT (Semiconductor)	260	-	-	
SWCNT films (Metallic)	13	3×10^4	5.1	[66]
SWCNT films (Semiconductor)	88	2.7×10^4	510	

Table 1.6. TE properties of n-type SWCNT at room temperature.

Samples	S ($\mu V\ K^{-1}$)	σ ($S\ m^{-1}$)	PF ($\mu W\ m^{-1}\ K^{-2}$)	Ref.
SWCNT bundle (Metallic)	- 30	-	-	[64]
Individual SWCNT (Metallic)	- 40	-	-	[65]
SWCNT films (Semiconductor)	- 78.5	11.9×10^4	730	[67]
SWCNT films (Semiconductor)	-64	36.3×10^4	1500	[68]

- **Electrical conductivity**

As we know, CNT are effectively rolled-up graphene sheets and share the exceptional physical properties of graphene. In terms of carbon atoms bonding in CNT, which are organized in a hexagonal lattice, each carbon atom is covalently connected to three nearest neighbors through sp^2 molecular orbitals. As a result, the fourth valence electron in each unit stays free, and these free electrons are delocalized over all atoms and contribute to the electrical character of CNT [69]. The inherent structure of CNT significantly impacts their characteristics, especially when it comes to electrical conductivity. Armchair nanotubes display a semi-metallic or metallic nature, with a slight overlap between their conduction and valence bands, zigzag and chiral nanotubes, depending on their diameter and in case of chiral nanotubes their exact chirality, may have different widths of bandgaps. Thus, their characteristics can vary from practically semi-metals up to wide bandgap semiconductor properties [70].

The electrical properties of perfect MWCNT are rather similar to perfect SWCNT. However, due to weak coupling between concentric cylinders of MWCNT, only the outer shell contributes to the electron transport and thus to the final electrical conductivity of MWCNT [71]. The electrical resistivity of individual SWCNT and MWCNT has been reported around 10^{-8} Ω m [72, 73] and 3×10^{-7} Ω m [74], respectively. This indicates that, at room temperature, CNT could be better conductor than metal like copper. However, in most cases, the presence of various defects or impurities that form during the growth of CNT leads to significantly lower conductivity in individual CNT compared to those observed under ideal conduction conditions [75].

- **Thermal conductivity**

Thermal conductivity mechanism of CNT is similar to non-metallic materials, based on the phonon conduction mechanism. There are many factors that directly affect the conduction mechanism of phonon such as the number of phonon active modes, the boundary surface scattering, the phonon mean free path [19]. The thermal conductivity of CNT depends on the atomic arrangement (CNT structure: armchair, zigzag, chiral), the length and diameter of CNT, types of CNT (SWCNT or MWCNT), the structural defects, the morphology, and the presence of impurities [76, 77]. According to the report of Kumanek and Janas [78], CNT demonstrate different values of thermal conductivity, from the level of thermal insulation with the thermal conductivity of 0.1 W m^{-1} K^{-1} (bundle CNT) to such high values of 6600 W m^{-1} K^{-1} (individual CNT).

In addition, as mentioned above, SWCNT are formed by the rolling of a single layer of graphene, meanwhile MWCNT are composed of several graphene cylinders leading to more phonons scattering between walls and inducing thermal conductivity values decrease. Numerical simulations shows that the thermal conductivity of isolated SWCNT and MWCNT reached high levels of more than 6000 W m^{-1} K^{-1} [79] and 3000 W m^{-1} K^{-1} [80], respectively .

3.2.2. Conducting polymers

Although inorganic semiconductor materials exhibit high thermoelectric performance, the disadvantages in using inorganics for thermal energy harvesting are their high cost, brittleness, use of rare elements, and unsuitability for large scale applications [81]. In addition, for applications at near-ambient temperatures, only bismuth telluride (Bi_2Te_3) and its derivatives are enough competitive, with a ZT higher than 1 [6]. These challenges have recently led the scientific community to turn its attention to organic semiconductors, especially conducting polymers, also known as electronically or intrinsically conducting polymers. Although they have been studied since the 1960s, they have become the real backbone of a new field called “organic electronics” since the Nobel prize in Chemistry of MacDiarmid, Heeger and Shirakawa in 2000. During the last decade, they have become really appealing for thermoelectric applications, because they are naturally abundant carbon- and hydrogen-based systems, often inexpensive due to the availability of cheap raw materials, light weight, flexible, and thus promising systems for low-cost and large-scale applications.

Conducting polymers constitute a special class of organic materials whose ability to conduct electrical charge is uniquely due to π-conjugation, hence their name: conjugated polymers.

In a regular thermoplastic polymer, all the available electrons are bound in strong covalent bonds and are characterized by sp^3 hybridization, making them insulator materials with very low electrical conductivity values (10^{-12} – 10^{-15} S m^{-1} [18]). In conjugated polymers, sp^2 hybridization enable π-bond electrons to be delocalized over many carbon atoms. However, the band gaps of these conjugated polymers lie in the range 2 – 3 eV, which is characteristic of semiconductors, even insulators. In order to acquire semi-metallic characteristics, a doping process is used, but in contrast to inorganic doping, involving atoms replacement, doping in conducting polymers is due to an oxidation or reduction process. The latter obtained by removing/adding an electron from/to the polymer via an electron transfer reaction with a chemical species (redox reaction) or with an electron (electrochemical reaction). The doping charge is stabilized on the polymer by a counterion (cation/anion) to ensure electroneutrality of the materials.

Another major attraction of conducting polymers for thermoelectric applications is their inherently low thermal conductivity, which varies from 0.2 W m^{-1} K^{-1} for poly(3,4-ethylenedioxythiophene) complexed with polystyrene sulphonic acid (PEDOT:PSS) to 0.7 W $m^{-1}K^{-1}$ for highly doped polyacetylene [82–84].

In this section, we will summary the most popular electronically conducting polymers for thermoelectric applications, especially for room temperature applications.

- **Poly(3,4-ethylenedioxythiophene) (PEDOT)**

PEDOT is simply the most widely used conducting polymers in the last 40 years, especially as transparent conducting electrodes in organic photovoltaics [85]. In addition, PEDOT also exhibits a low thermal conductivity, low density, easy handling, and high thermoelectric performance [86, 87]. Fig. 1.14 presents the chemical structure of PEDOT and its copolymers. PEDOT exhibits a bandgap of 0.9 eV, a Seebeck coefficient of about −140 µV K^{-1} for n-type and about 100 µV K^{-1} for p-type. However, its low electrical conductivity value and its poor solubility are major drawbacks for thermoelectric applications [88]. These disadvantages are usually solved by using polystyrene sulfonate as a counterion to form copolymers such as PEDOT:tosylate (PEDOT:Tos) or PEDOT:polystyrene sulfonate (PEDOT:PSS), giving an aqueous dispersion that is commercially available at different levels of oxidation, hence electrical conductivity. At room temperature, the ZT value of PEDOT:Tos

is about 0.25 [89]. For PEDOT:PSS, the electrical conductivity is increased by 9 % compared to PEDOT:Tos. In the report of Kim *et al.* [90], when PEDOT:PSS mixed with dimethylsulfoxide (DMSO) is treated with ethylene glycol, the electrical conductivity again increases improving the ZT value to 0.42. In addition to DMSO, N,N-dimethyl formamide (DMF) is also known to enhance carrier transport and help to improve thermoelectric properties of PEDOT:PSS [91].

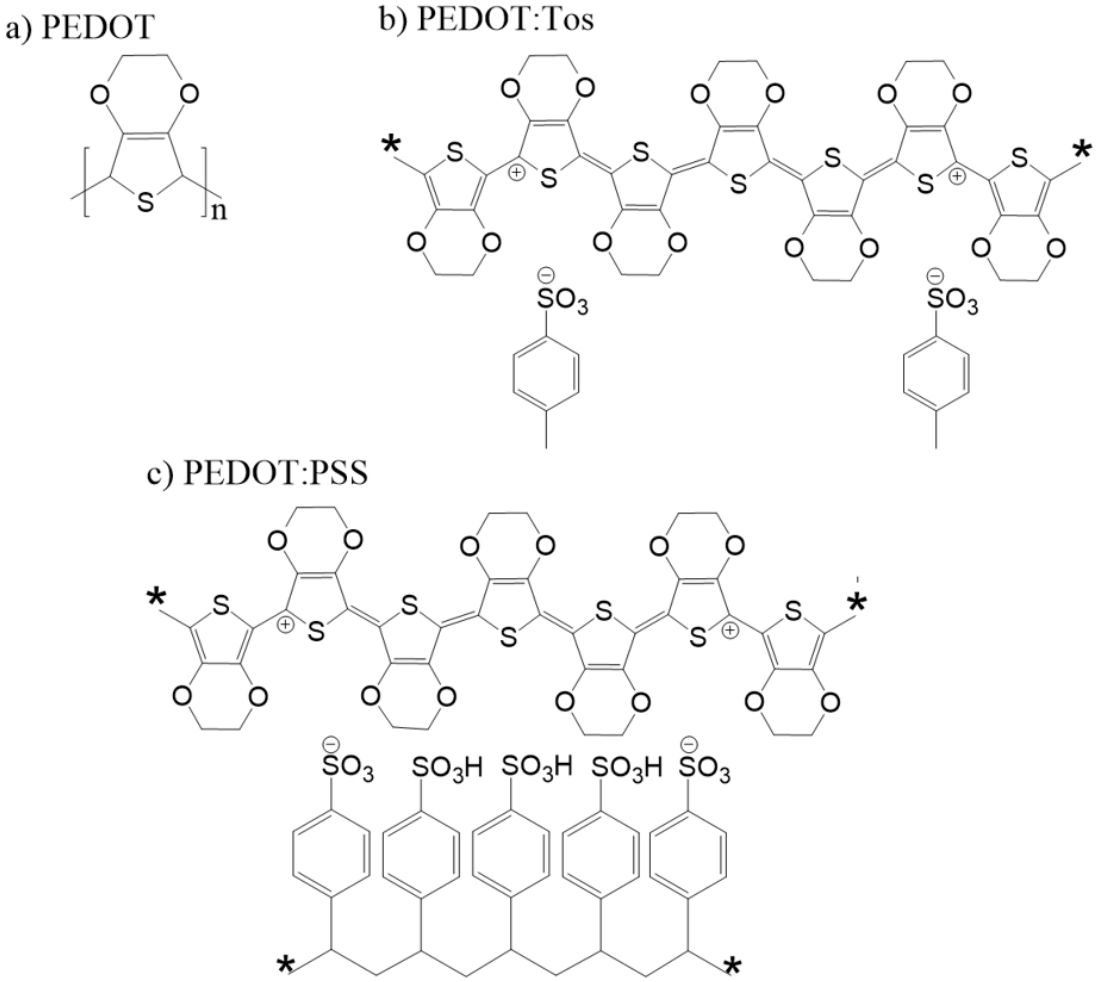

Figure 1.14. Chemical structure of a) PEDOT, b) PEDOT:Tos, and c) PEDOT:PSS [92].

- **Poly(2,7-carbazole)**

Electronic band structure calculations performed on poly(2,7-carbazole) and its derivatives have revealed good potential for these materials in thermoelectric applications [93]. From the chemical structure in Fig. 1.15, it was found for poly(2,7-carbazole) derivatives that the nitrogen atom is oxidized before the backbone, and the charge is then localized [94–96]. This feature could contribute to a large Seebeck coefficient in poly(2,7-carbazole). According to the study of Aïch *et al.* [97], doping poly (2,7-carbazole) revealed high electrical conductivity

(up to 5 x 10^4 S m^{-1}) and a high Seebeck coefficient, up to 70 µV K^{-1}. This polymer presents a maximum power factor value of 19 µW m^{-1} K^{-2}.

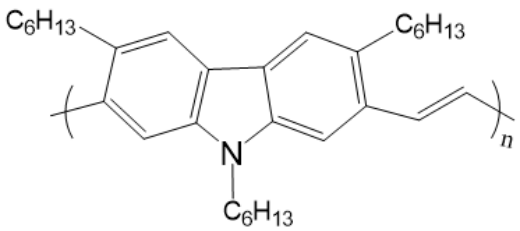

Figure 1.15. Chemical structure of poly(2,7-carbazole) [6].

- **Poly(3-hexylthiophene) (P3HT)**

P3HT (Fig. 1.16) is an alkylated derivative of polythiophene, and widely used in organic electronic applications. It has good solubility in a variety of organic solvents, which enhances its film processing properties, and it is commercial available [98]. In 2010, Xuan *et al.* [99] evaluated thermoelectric properties of P3HT films doped with nitrosonium hexafluorophosphate ($NOPF_6$). The maximum power factor was achieved at approximately 1.4 x 10^{-7} W m^{-1} K^{-1} when the doping was increased between 20 % and 31 %. By doping P3HT with ferric salt of triflimide ($TFSI^-$) anions, Zhang *et al.* also succeed in optimizing its power factor to a value greater than 20 µW m^{-1} K^{-1} [100].

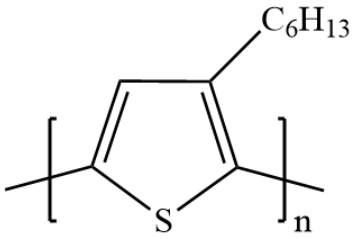

Figure 1.16. Chemical structure of Poly(3-hexylthiophene) [99].

- **Polyaniline (PANI)**

PANI is promising for wide thermoelectric applications because of several attractive properties such as easy preparation, easy processing, and low cost. The chemical structure of PANI is shown in Fig. 1.17. Depending on the y value, three different structures can be obtained. Due to a very poor thermoelectric response of pure PANI, the electronic conductivity and Seebeck coefficient of PANI can be further improve through "doping" [101, 102]. Li *et al.* [101] prepared hydrochloric acid-doped PANI by chemical oxidative polymerization. The results show that when HCl concentration increases, the electrical conductivity and ZT are

found to increase, along with the decrease in the Seebeck coefficient. The maximum ZT can obtain 2.67 x 10^{-4} at 432 K for 1 M HCl-doped PANI.

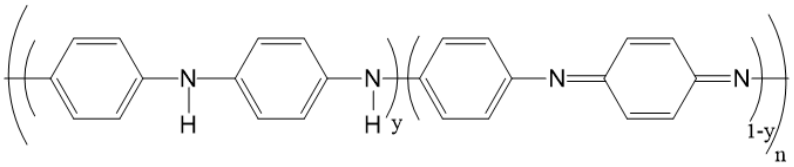

Figure 1.17. Chemical structure of Polyaniline (PANI) [6].
(y=1: Leucoemeraldine, y=0: Pernigraniline, y=0.5: Emeraldine)

Table 1.7 gathers the TE performance of the various conducting polymers presented in this section.

Table 1.7. Thermoelectric performance of conducting polymers at room temperature.

Materials	**σ (S m^{-1})**	**S (μV K^{-1})**	**κ (W m^{-1} K^{-1})**	**PF (μW m^{-1} K^{-2})**	**ZT**	**Ref.**
PEDOT : Tos films	6.7 x 10^3	220	0.37	324	0.25	[89]
PEDOT : PSS + EG (DMSO treatment)	8.8 x 10^4	72	0.24	4.8 x 10^4	0.42	[90]
PEDOT : PSS (Formamide treatment)	2.9 x 10^5	17.4	0.19	8870	0.04	[91]
P3HT (doped $NOPF_6$)	10^{-2} - 10^2	25 - 340	-	10^{-4} – 0.14	-	[99]
P3HT (doped ferric salt of $TFSI^-$)	~ 5 x 10^3	~ 60	-	~ 20	-	[100]
Poly(2,7-carbazole) (doped film)	5 x 10^4	70	-	19 x 10^2	-	[97]
PANI (doped HCl)	4.1 x 10^4	9	0.276	-	0.4 x 10^{-4}	[101]

3.2.3. Conducting polymer/CNT nanocomposites

The preparation of conducting polymer/CNT nanocomposites is a common strategy to enhance the properties of organic thermoelectric materials [103–105]. The conducting polymers possess conjugated π bonds that can create strong π-π interactions between their backbones and the surfaces of CNT [106–108]. The interaction not only strengthens the bonds between the polymer chains and the CNT but also induces a structured chain arrangement on the CNT surface. These improved connections and ordered structure contribute to increase carrier mobility, thereby enhance the electrical transport properties of materials [109–111]. Table 1.8

summarizes the TE properties of various CNT-based nanocomposites with different conducting polymers. It can be seen that both MWCNT and SWCNT can enhance the TE properties of nanocomposites. However, SWCNT demonstrates a comparative advantage over MWCNT in terms of improving the electrical conductivity (σ) and Seebeck coefficient (S), resulting in higher TE efficiency. It should be noticed that in all the reported studies on conducting polymer/CNT nanocomposites, the filler content is high (up to 60 wt%).

Table 1.8. TE properties of CNT- conducting polymer-based composites at room temperature.

Material + % fillers	σ (S m^{-1})	S (μV K^{-1})	κ (W m^{-1} K^{-1})	PF (μW m^{-1} K^{-2})	ZT (T=300K)	Ref.
PANI/PEDOT:PSS + 22.6 wt% graphene + 31.7 wt% DWCNT	1.9×10^5	120	-	2710	-	[112]
PEDOT:PSS + 60 wt% SWCNT	1.7×10^5	55.6	0.5	526	0.4	[113]
PEDOT:PSS/TCPP + 40 wt% SWCNT	9.6×10^4	70	-	470	-	[108]
PEDOT:PSS/PVAc + 60 wt% SWCNT	10^5	40	~ 0.2	160	~ 0.3	[114]
PANI + 65 wt% SWCNT	1.4×10^5	38.9	0.44	217	0.14	[115]
P3HT + 10 wt% MWCNT	5.89×10^4	29	-	53	-	[110]
PEDOT + 26.5 wt% MWCNT	9.5×10^3	56.1	-	25.9	-	[116]
PEDOT:PSS/TCPP + 40 wt% MWCNT	9.5×10^3	40	-	15	-	[108]
PPy + 20 wt% MWCNT	35	25	-	2	-	[117]

PANI: Polyaniline / **PEDOT**: Poly(3,4-ethylenedioxythiophene) / **PEDOT:PSS :** PEDOT:polystyrene sulfonate / **P3HT:** Poly(3-hexylthiophene) / **PPy**: Polypyrrole

3.2.4. Insulating polymer/CNT nanocomposites

Nanocomposites based on insulating thermoplastic polymers and conductive fillers such as CNT are also interesting systems to consider for thermoelectric applications because of the ease of processability and flexibility of thermoplastic polymers compared with conductive polymers.

3.2.4.1. Elaboration processes

CNT form aggregates due to Van der Waals interactions, making it difficult to achieve a homogenous dispersion in polymer matrices, which can have a direct impact on the properties of nanocomposites. Several methods are currently used to disperse the CNT in polymer matrices, of which melt blending, solution mixing, and *in situ* polymerization are the most widely used. Each of these methods has advantages and disadvantages that can have a direct impact on the resulting properties of the nanocomposites.

- **Melt-blending**

Melt-blending has been known as the simplest and most effective method, particularly from an industrial perspective, as it enables the production of high-performance polymer nanocomposites at large scale with low process cost. In this method, CNT are mechanically dispersed into a polymer matrix using a high temperature and high shear force mixer or compounder. The shear force helps to break nanotube aggregates or prevent their formation [118]. To get well dispersed CNT within the polymer phase during melt-blending process, several parameters need to be optimized such as mixing time, screw speed, and mixing temperature. Many studies have investigated these parameters to improve the properties of materials. For example, Kasaliwal *et al.* [119] study the influence of varying mixing speed on the dispersion of CNT on polycarbonate (PC) matrix of different molecular weights. The results show that at high speed of mixing, regardless of temperature or melt viscosity, the degree of dispersion of CNT in the PC matrix was the same. However, when the melt mixing speed was low, a good dispersion was achieved either at a low temperature or at a high melt viscosity of the PC matrix. Min *et al.* [120] have studied the impact of various processing parameters (mixing time, rotor speed, cooling rate) on the surface resistivity of nanocomposites polypropylene (PP)/MWCNT and ethylene-propylene-diene (EPD)/MWCNT. Melt mixing has been successfully applied for the preparation of various polymer-CNT nanocomposites in thermoelectric applications such as polycarbonate (PC)/CNT [121], polypropylene (PP)/CNT [122, 123], poly(lactic acid) PLA/MWCNT/expanded graphite [124].

Generally, the direct melt preparation method does not give a very good dispersion of the nanofillers in the different polymer matrices because the aggregates of nanotubes are highly stabilized and the compatibility between the polymer chains and CNT is low. Moreover, high shear during the melt-blending process may also lead to CNT breakage that can limit the expected increase in mechanical and electrical properties. In addition, the CNT content is limited to low content due to the viscosity increase with the addition of CNT.

- **Solution mixing**

To increase the CNT content and improve the dispersion of CNT in the polymer matrix phase, solution mixing is the process mostly employed in preparing nanocomposites. This process usually involves three main steps: dispersing the CNT in a suitable solvent using mechanical stirring and/or sonication, then dissolving the polymer in the previous dispersion while stirring it appropriately, and finally removing all the remaining solvents from nanocomposites. Note that during the solvent evaporation step, a CNT re-aggregation can occur. The complete removal of the solvent is a critical issue when using solution mixing for the preparation of nanocomposites, as toxicity concerns can arise when organic solvents are used. Besides, the presence of residual solvents results in plasticization of the polymer matrix, which can have a significant effect on its physical properties such as the mechanical properties [125]. Many studies have employed solution mixing to prepare nanocomposites, based on thermoplastic matrix as well as conducting polymer matrix, and investigated the thermoelectric properties as shown in Tables 1.7 and 1.8 for conducting polymer-based composites.

As mentioned earlier, it is extremely difficult to achieve a homogenous dispersion of pristine CNT in the solvent by simple stirring. Therefore, high-power ultrasonication method is more effective for the formation of a CNT dispersion. The aggregation and entanglement of CNT can be effectively broken down by using the multi-effects of ultrasound [51]. However, it should be noticed that high-power sonication for a long period of time can break tubes, reduce the aspect ratio, which is detrimental to the nanocomposite properties and increases the surface defects [126]. The optimum sonication conditions (time and power) need to be determined and depend on the nanotube concentration. Chen *et al.* [127] prepared polycarbonate (PC)/MWCNT composites through solution mixing and precipitation technique, the dispersion of CNT in PC solution was processed by sonication at frequency of 20 kHz for 10 min. The results show that the CNT were unentangled and well dispersed into PC matrix due to both ultrasonic and stirring. Safadi *et al.* [128] dispersed MWCNT in polystyrene (PS) using ultrasound at 300 W for 30 min. Homogenous dispersion of CNT in PS was achieved by sonication. Additionally, the

functional groups of CNT is another effective way to prevent the agglomeration of nanotubes, the covalent functionalization of nanotube can improve nanotube dispersion in solvents and polymer [51, 129], but it can significantly impact the electric and thermal properties. A dispersing agent like dodecylbenzene sulfonate can also be used to favor dispersion of CNT.

3.2.3.2. Thermoelectric properties of insulating thermoplastic polymer/CNT

Most of thermoplastic polymer matrices are intrinsically poor thermal conductors, ideal for thermoelectricity, but also electrical insulators, which prevents them from being potential candidates for TE applications. The use of CNT as fillers has been shown to greatly improve the electrical conductivity of nanocomposites, as soon as the fillers concentration is higher than the percolation threshold, while maintaining the poor thermal conductivity of the polymer matrix, resulting in improved TE properties.

The thermoelectric behavior of polyvinyl acetate (PVAc)/CNT was first demonstrated by Yu *et al.* [81]. In this study, with 20 wt% of SWCNT, a segregated-network was observed between CNT and the PVAc matrix, which yielded to an electrical conductivity of 4800 S m^{-1}, a thermal conductivity of 0.34 W m^{-1} K^{-1}, a Seebeck coefficient of 40 µV K^{-1} and a final ZT of 0.006 at room temperature. The results demonstrated that the electrical conductivity was significantly enhanced by the formation of the CNT network, while the evolution of Seebeck coefficient and the thermal conductivity do not mainly depend on the concentration of CNT, in particular notably to the existence of the junctions that significantly hinder the thermal transport. Liebscher *et al.* [121] showed that different MWCNT surface functionalization groups can have an impact on the Seebeck coefficient of PC/MWCNT nanocomposites. At a loading of 2.5 wt%, the highest Seebeck coefficient was 11 µV K^{-1} obtained for carboxyl functionalized MWCNT meanwhile non-functionalized MWCNT resulted in a S value of 7.5 µV K^{-1}.

Tables 1.9 and 1.10 provide a summary of TE properties of various thermoplastic polymer/CNT (MWCNT and SWCNT) composites at room temperature. Generally, due to the intrinsic properties of SWCNT compared to those of MWCNT, composites using SWCNT as fillers exhibit ZT values 100 times higher than those using MWCNT. Additionally, it can be seen that the thermoelectric performance of nanocomposites is strongly dependent on the CNT concentration. Typically, a higher concentration of CNT contributes to the enhancement of thermoelectric performance. PVDF-based nanocomposites containing 50 wt% of MWCNT, as investigated by Brun *et al.* [130], achieved a ZT value of around 10^{-5}, significantly higher than the ZT value reported for PVDF containing 8 wt% filler by Sun *et al.* [131], which is around

10^{-9}. Another example is ABS/MWCNT nanocomposites with 4 wt% of fillers, exhibiting a ZT value more than 100 times higher than that of 1 wt% of MWCNT [132]. The improvement of the ZT value with the addition of CNT mainly comes from the huge increase of the electrical conductivity while a slight decrease of the Seebeck coefficient and a weak increase of the thermal conductivity are observed. Note that in the case of PS/75 wt% SWCNT nanocomposites, Suemori *et al.* [81] report a ZT value of 0.41 which is much higher than those of other insulated polymer based nanocomposites filled with SWCNT in Table 1.9. Here again, the origin of its high value of ZT seems to mainly come from the high electrical conductivity. Even if this ZT value should be taken with caution (in particular, the thermal conductivity value which is very low considering the high content of SWCNT), this result suggests that it is possible to achieve good thermoelectric materials based on insulating polymer nanocomposites with high filler CNT. However, a high increase in the CNT content will affect the elaboration process due to the increasing viscosity [124].

In addition, it is important to note that the morphology and the structure of nanocomposites can vary depending on the sample elaboration processes, leading to a direct impact on the thermoelectric properties. Porosity generation in polymers and their composites is widely used to enhance the thermoelectric performance [103, 133]. From Table 1.9, it can be observed that PVDF/ MWCNT nanocomposites with a porous structure [134] exhibit a ZT value (3.3×10^{-3}, at 15 wt% MWCNT) much higher than those of bulk PVDF/MWCNT samples (1.6×10^{-9}, 8 wt% MWCNT) [131]. This significant difference is mainly due to the porous structure which could reduce the thermal conductivity and enhance the Seebeck coefficient by inducing the phonon scattering and the energy-filtering effect [134].

Regarding the effect of the polymer matrix on the thermoelectric properties of nanocomposites, Table 1.10 shows that in the case of SWCNT, the Seebeck coefficient can be positive or negative, depending on the polymer matrix. To our knowledge, the origin of this phenomenon is not clear up to now. Some authors suggest that the nitrogen present in the amide and amine groups in polyamides and ABS can bring an electron-donating effect resulting in a negative Seebeck coefficient [132]. Furthermore, some works showed that the crystallinity of the polymer could also impact the electrical and thermal conductivities, as well as the Seebeck coefficient. For example, in the work of Brun *et al.* [130], the thermoelectric properties of bulk poly(vinylidene fluoride)/multi-walled carbon nanotubes (PVDF/CNT) composites have been investigated. The results showed that the nature of the crystalline phase of PVDF has a significant influence: the polar γ−phase of PVDF brought a slight effect on σ and κ, and yielded a 30 % increase in Seebeck value, resulting in the improvement in ZT value. Wang *et al.* [135]

demonstrated the increase in electrical conductivity and the reduction in electrical percolation thresholds of PP/CNT nanocomposites by inducing crystallinity in the PP matrix by controlling the cooling rate. Therefore, understanding the structure-property relationships in polymer/CNT nanocomposites is essential for improving their thermoelectric performances.

Finally, the electrical conductivity of polymer nanocomposites reinforced by CNT has exhibited anisotropic behavior as shown in literature by the measurements of σ values in two directions (in-plane and cross-plane) on the same sample [136, 137]. Especially, the anisotropy of σ values is a critical issue which can bring significant impact on the final ZT [130]. Detailed values illustrating the influence of anisotropy on the thermoelectric properties are presented in Table 1.9 for PVDF/ 50 wt% MWCNT nanocomposites [130], in which $\sigma_{in\text{-}plane}$ is 10-100 times higher than the cross-plane value, resulting in the final $ZT_{in\text{-}plane}$ appearing 1-2 orders of magnitude higher compared to the $ZT_{cross\text{-}plane}$ at the same filler fraction.

Regarding the effect of the elaboration process (melt blending/solution mixing…) on the TE properties, it is difficult to conclude from the results summarized in Table 1.9 and 1.10 because there is no comparison of the processes for a same composite (same polymer matrix, same fillers).

Table 1.9. TE properties of **MWCNT**- thermoplastic polymer-based composites at room temperature.

Polymer + % MWCNT	**Preparation method**	**σ (S m^{-1})**	**S (μV K^{-1})**	**κ (W m^{-1} K^{-1})**	**PF (μW m^{-1} K^{-2})**	**ZT (300)**	**Ref.**
PLA + 18 vol%	Melt-blending	1.15 x 10^{2}	9.0	0.41	-	7.0 x 10^{-5}	[124]
PBT + 2 wt%	Melt-blending	5.1	6.8	0.27	2.0 x 10^{-4}	2.7 x 10^{-7} **(313 K)**	[132]
PVDF + 2 wt%	Melt-blending	3.2	14.3	0.28	7.0 x 10^{-4}	7.4 x 10^{-7} **(313 K)**	
PVDF + 50 wt%	Solution mixing	1.2 x 10^{2} **(cross-plane)**	20	0.87	4.6 x 10^{-2}	1.6 x 10^{-5}	[130]
PVDF + 50 wt%		1.9 x 10^{3} **(in-plane)**	20	0.87	7.6 x 10^{-1}	2.6 x 10^{-4}	
PVDF + 8 wt% **(solid)**	Melt-blending	2.0 x 10^{-2}	12	0.55	-	1.6 x 10^{-9}	[131]
PVDF + 15 wt% **(porous)**	Solution mixing/phase separation	16	325	0.15	1.7	3.3 x 10^{-3}	[134]
PP + 2 wt%	Melt-blending	1.6	9.5	0.28	1.0 x 10^{-4}	1.7 x 10^{-7} **(313 K)**	[132]
PC + 2.5 wt%		8.5	8.5	0.28	6.0 x 10^{-4}	6.8 x 10^{-7}	
ABS + 1 wt%		0.3	3.0	0.28	2.2 x 10^{-6}	2.9 x 10^{-9}	
ABS + 4 wt%		25.7	3.6	0.26	3.0 x 10^{-4}	3.8 x 10^{-7}	
PA6 + 5 wt%		2.0 x 10^{-2}	6.1	0.26	7.7 x 10^{-7}	8.6 x 10^{-10}	
PA66 + 2 wt%		5.0	6.3	0.28	2.0 x 10^{-4}	2.2 x 10^{-7}	
Cellulose film + 5 wt%	Solution mixing	15	10	0.08	1.5 x 10^{-3}	6.0 x 10^{-6}	[138]
Cellulose aerogel + 5 wt%	Solution mixing	3.5 x 10^{-1}	11	0.03	4.2 x 10^{-5}	4.7 x 10^{-7}	

PLA: Polylactic acid / **PBT**: Poly(butylene terephthalate) / **PVDF**: Poly(vinylidene fluoride) / **PP**: Polypropylene / **PC**: Polycarbonate / **ABS:** Acrylonitrile butadiene styrene/ **PA6**: Polyamide 6/ **PA66**: Polyamide 66

Table 1.10. TE properties of **SWCNT**-thermoplastic polymer-based composites at room temperature.

Polymer + % SWCNT	**Preparation method**	**σ (S m^{-1})**	**S (μV K^{-1})**	**κ (W m^{-1} K^{-1})**	**PF (μW m^{-1} K^{-2})**	**ZT (300)**	**Ref.**
PVAc + 20 wt%	Polymer emulsion	4800	40.0	0.34	7.70	6.0 x 10^{-3}	[81]
PS + 75 wt%	Solution mixing/planetary ball milling	1.25 x 10^{5}	61	0.3	413	0.41	[107]
PBT + 2 wt%	Melt-blending	18.6	58.2	0.27	6.3 x 10^{-2}	7.0 x 10^{-5}	[132]
PVDF + 2 wt%		139.3	24.0	0.27	8.0 x 10^{-2}	9.0 x 10^{-5}	
PP + 2 wt%		12.1	47.2	0.27	2.7 x 10^{-2}	3.0 x 10^{-5}	
PC + 2 wt%		1.0	34.8	0.26	1.2 x 10^{-3}	1.4 x 10^{-6}	
ABS + 1 wt%		4.2	- 50.9	0.27	1.0 x 10^{-2}	1.2 x 10^{-5}	
ABS + 4 wt%		66.2	- 32.7	0.27	7.0 x 10^{-2}	7.9 x 10^{-5}	
PA6 + 5 wt%		64.6	- 47.0	0.27	1.4 x 10^{-1}	1.6 x 10^{-4}	
PA66 + 2 wt%		28.2	- 29.5	0.27	2.5 x 10^{-2}	2.7 x 10^{-5}	
Cellulose film + 8 wt%	Solution mixing	125	45.6	0.11	2.6 x 10^{-1}	7.4 x 10^{-4}	[138]
Cellulose aerogel + 10 wt%	Solution mixing	22	29.3	0.09	1.9 x 10^{-2}	6.4 x 10^{-5}	

PVAc: Polyvinyl acetate/ **PS:** Polystyrene

- **Electrical conductivity models**

The electrical conductivity of the polymer-based nanocomposites can vary significantly depending on a lot of parameters such as the intrinsic properties of the components, the volume fraction and the distribution of the fillers, defect concentration, purity of both the polymer and fillers, temperature.... To understand the conduction mechanism and to estimate the evolution of the electrical conductivity of the nanocomposites as a function of filler fraction and temperature, several electrical models have been proposed in literature. This section will describe some of the most important electrical conductivity models for nanocomposites, especially those relating to volume fraction of fillers and temperature.

- *Percolation threshold model*

The electrical conductivity of a nanocomposite is strongly dependent on the volume fraction of the conductive phase. The evolution of electrical conductivity as a function of CNT volume fraction is shown in Fig. 1.17. At low volume fractions (region A), the electrical conductivity remains very close to that of the pure matrix. When a certain volume fraction is reached (region B), the electrical conductivity of the nanocomposites increases dramatically by several orders of magnitude indicating the existence of conduction paths via connecting CNT. This phenomenon is known as percolation threshold and can be explained by the scaling law of percolation theory (eq. 1.16), also known as Kirkpatrick law [139]:

$$\sigma = \sigma_o(\Phi - \Phi_c)^t \qquad \text{(eq 1.16)}$$

where σ is the electrical conductivity of nanocomposites (S m^{-1}), σ_o is the intrinsic electrical conductivity of filler (S m^{-1}), Φ is the volume fraction of filler (vol%), Φ_c is the volume percolation concentration or percolation threshold (vol%), and t is a critical exponent. This equation is valid when $\Phi > \Phi_c$ and $(\Phi - \Phi_c)$ is small. The critical exponent t depends on the dimensionality of the percolation structure with calculated values of t ~ 1.3 and t ~ 2.0 in two and three dimensions, respectively [140, 141].

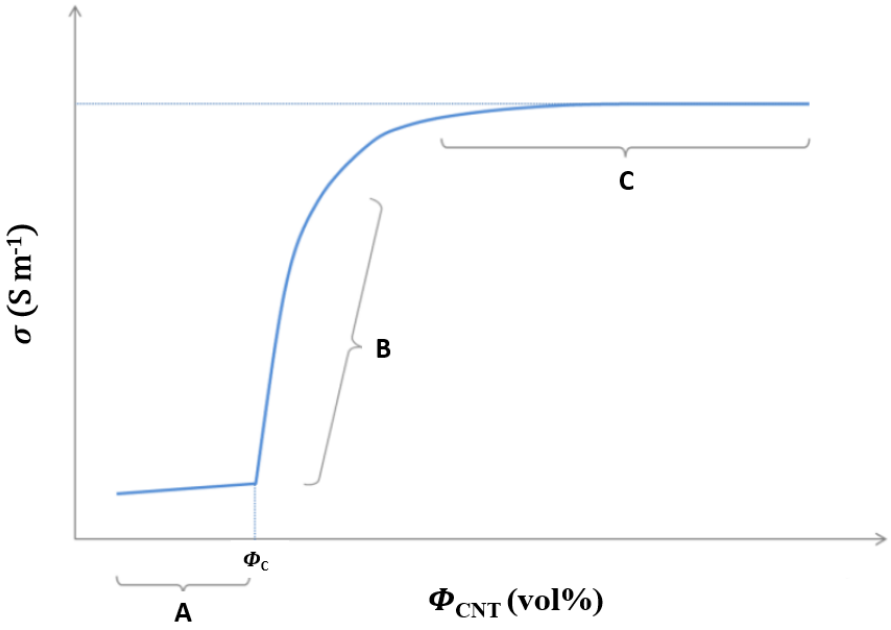

Figure 1.17. Electrical conductivity of composites as a function of filler fraction [142].

- *Influence of temperature on electrical conductivity*

The influence of temperature on electrical conductivity depends on the nature of the material: σ decreases with increasing temperature for metals whereas the opposite behavior is observed for ordered semiconducting materials. In the former case, this is due to the reduced mobility of charge carriers as the temperature rises. In the latter case, it is due to the increase of the charge carriers number with temperature.

In the case of disordered semi-conducting material such as polymer/CNT nanocomposites, it can be considered that the number of charge carriers almost remains constant, while the mobility of the charge carriers increases with temperature. In this case, charge carriers move either by tunneling or by hopping.

Note that if MWCNT are uniformly dispersed in the polymer matrix, the conductivity of nanocomposites at a given temperature can be described by the behavior of a single tunnel junction [143]. In that case, the conductivity should follow the following rule:

$$ln\,\sigma \propto w^{-\frac{1}{3}} \qquad \text{(eq 1.17)}$$

Where, w is the weight fraction of MWCNT in nanocomposites.

- *Temperature dependent models*

Various models are proposed in literature to characterize charge transport mechanisms in disordered solids. The most encountered models are:

- For homogenous systems, the Mott or Variable-range hopping (VRH) and the Efros and Shklovskii models.
- For heterogenous systems, the charging energy limited tunneling (CELT) and the thermal fluctuation induced tunneling (FIT) models.

Mott or Variable-range hopping (VRH) model (eq. 1.18) is developed for homogenous and amorphous system. The charge carriers are assumed to have no interactions and the electrical conductivity is expressed as:

$$\sigma(T) = \sigma_0 exp[-(T_0/T)^{\gamma}] \; ; \; \gamma = \frac{1}{z+1} \qquad \text{(eq 1.18)}$$

where σ is the electrical conductivity (S m^{-1}), σ_0 is a constant (S m^{-1}), T_0 is the Mott temperature (K), and γ is related to the dimensionality of system (z represents the dimension of conduction process) [144].

When the density of charge carriers is high, it is not possible to neglect the interactions between the charges. The Efros and Shklovskii model describes the mechanism of movement of charges by hopping to the empty nearest neighboring site. The formula is similar to eq. 1.18 where γ is equal to ½ and T_0 is the Efros and Shklovskii temperature.

The charging energy limited tunneling (CELT) model was developed for granular media where the charge energy of the gap Ec is higher than the thermal energy k_BT. This is the case when the size of the conductivity fillers is smaller than the thickness of the insulating polymer matrix layer between fillers (heterogenous systems). The equation of the model is similar to eq. 1. 18 but the exponent γ depends on the temperature. At low temperature γ is equal to ¼, at intermediate temperature γ is equal to ½ and γ is higher than ½ for high temperature.

The thermal fluctuation induced tunneling (FIT) model [145] corresponds to the reverse situation, when the thermal energy is higher than the charge energy of the gap, *i.e.* when the layer of the insulating polymer is thin compared to the CNT. In these systems, electrical conductivity is ascribed to tunneling through a potential barrier of varying height due to thermal fluctuations. This behavior is described by:

$$\sigma_{dc}(T) = \sigma_0 exp\left[-\frac{T_1}{T+T_0}\right] \qquad \text{(eq 1.19)}$$

where, σ_0 is a pre-exponential factor, T_1 is the temperature at which thermal fluctuations become large enough to allow charge carriers to cross the insulator gap between particles

aggregates and T_0 is the temperature below which the tunneling effect is independent of thermal fluctuations.

4. Thermoelectrics of Polylactic acid (PLA)/CNT materials

4.1. Polylactic acid (PLA)

4.1.1. Synthesis

Polymers obtained from sustainable sources are now seen as promising alternatives to traditional petroleum-based polymers as they address current environment concerns. Among them, polylactic acid (PLA) stands out as a highly promising bioplastic due to its mechanical properties compare to the ones of polyethylene terephthalate (PET), or polystyrene (PS), low emission of greenhouse gases, low amount of energy used for its production, potential biodegradability and high industrial production capacity [146, 147].

Polylactic acid is a linear aliphatic polyester with a repeat unit $(C_3H_4O_2)_n$. The monomer, the lactic acid is generally made from fermented plant starch such as corn, sugarcane or cassava. Lactic acid has a chiral carbon, leading to the presence of two stereoisomers consisting of enantiomeric D- and L-lactic acid units in different ratios, as presented in Fig. 1.17.

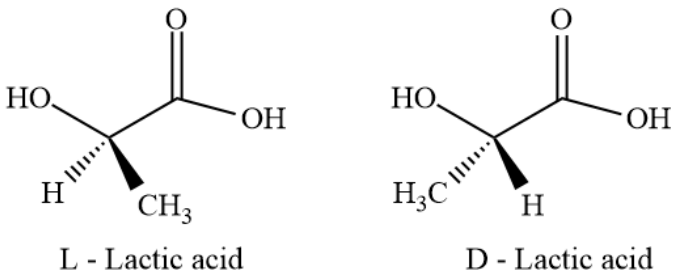

Figure 1.17. Different isomeric forms of lactic acid [148].

Two main routes are used to synthesize PLA polymers from lactic acid as illustrated in Fig. 1.18.

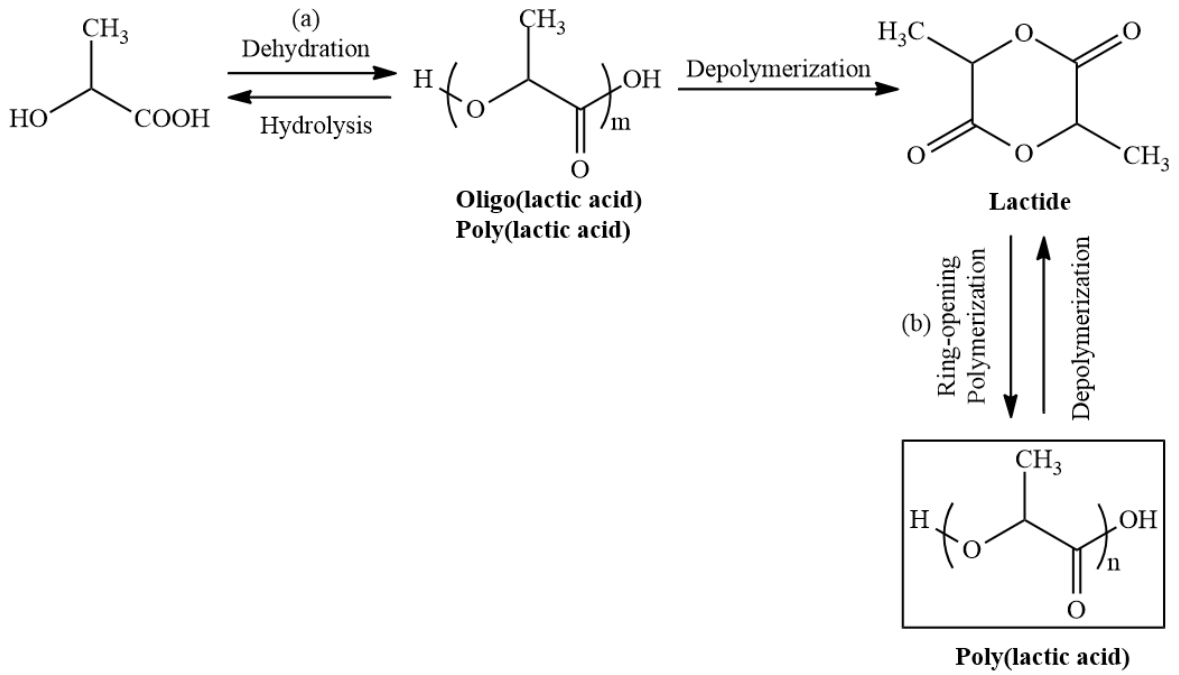

Figure 1.18. Routes for synthesis of PLA polymers: (a) direct polycondensation of lactic acid, (b) ring-opening polymerization of lactide (ROP) [149].

- The direct polycondensation of lactic acid: this process yields a low-molecular-weight leading to a brittle polymer, which is not suitable for many applications.

- The polymerization of lactide by Ring-opening Polymerization (ROP): this method permits the synthesis of high-molecular-weight PLA (M_w > 100 000 g mol^{-1}), which is adopted by major PLA manufactures. In this method, PLA is dehydrated at high temperature and under vacuum condition is poly-condensed into its oligomers. Then, through internal transesterification, it would be catalytically depolymerized into lactide. Finally, L/D/meso-lactide monomer is converted into corresponding polymer by ROP. This step must be carried out using a metal catalyst depending of PLA required [150].

As mentioned before, lactic acid possesses asymmetric carbons which bring lactide to a chiral diester. It is then possible to obtain 3 different stereoisomeric forms of lactides: DD-, LL-, and DL-lactides (meso-lactide), as shown in Fig. 1.19.

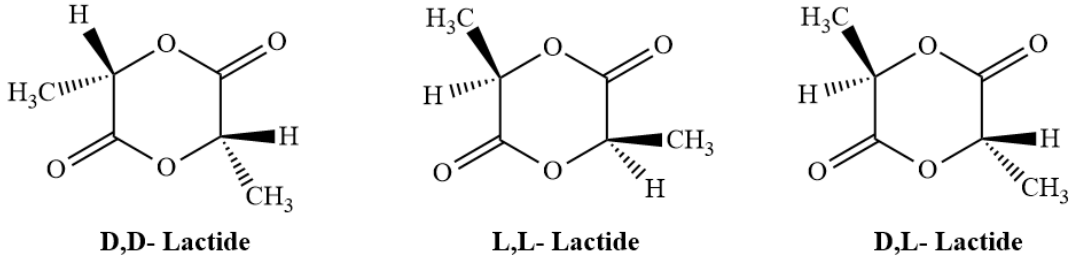

Figure 1.19. Different forms of lactide isomers [148].

Based on these three types of dimers, three types of polylactic acid can be produced:

- Poly-L-Lactic acid (PLLA), resulting from the synthesis of L-Lactide
- Poly-D-lactic acid (PDLA), resulting from the synthesis of D-lactide
- Poly-D,L-lactic acid (PDLLA), a random copolymer issued from synthesis of a mixing of L-lactide and D-lactide or meso-lactide. These materials are classified into different grades according to the different L/D isomer ratios. It has been shown in the literature that this D-isomer content strongly influences the properties of the material. Particularly this parameter has a direct influence on the crystallinity degree of the material. In general, high stereochemical purity (higher L-) favors crystallization of the material, while those rich in D- isomers are fully amorphous [151].

The polylactides of this PhD work are PDLLA copolymers containing different D- isomer as minor units. For sake of simplification these copolymers will be noted only as PLA.

4.1.2. PLA properties

Properties of PLA strongly depend on the D-isomer content, processing temperature, annealing time and molecular weight [152–154]. Besides, the thermal history and stereochemistry directly influence PLA crystallinity and therefore its end-use properties such as hardness, elastic, modulus, tensile strength, stiffness, and melting point [155]. Crystallinity is therefore one of the most important factors in selecting a polymer for a required application. PLA can be amorphous or semi-crystalline according to its stereochemical structure with a crystallinity degree up to 40 % [156]. PLA containing more than 93 % L-Lactic acid is semi-crystalline, whereas those containing between 50 % and 93 % of L-lactic acid are completely amorphous [157].

PLA exhibits three different crystalline structures (α, β, and γ forms) depending on their preparation conditions. The α form, which is the most encountered one, is induced upon thermally crystallization by slow cooling from the melt and upon stretching. On the other hand, the β form can be obtained upon mechanical stretching under specific stretching conditions (e.g. high stretching speed). Finally, the γ form is a specific crystalline structure which has been reported to develop on hexamethylbenzene substrate [158]. Note that another form of crystalline PLA phase is the stereo-complex form obtained from the mixing of enantiomeric PLLA and PDLA [159].

PLA is a slow-crystallizing material similarly to PET. The fastest rates of isothermal crystallization for pure PLA are found in the temperature range between 110 and 130 °C. The

rate and extent of crystallization depends on numerous factor such as temperature-above-T_g, molecular weight and the presence or not of nucleating agents... D-isomer content strongly influences the crystallization kinetics of PLA. Huang *et al.* [160] reported that a copolymer containing 0.4 % of D-isomer crystallize over 40 times faster than the one containing 6.6 % of D-isomer. Recently, Tábi *et al.* [161] also presented that the decrease of the D-isomer content induces a shift of the cold crystallization towards lower temperatures. Saeidlou *et al.* [162] summarized in their review that the increase of D-isomer results in a severely slowing down of isothermal crystallization kinetics, resulting in a limitation of maximum achievable crystallinity. For PLA containing higher than 10 % of D content, crystallization is suppressed, leading to non-crystallizable amorphous materials.

Regarding thermal properties (see Table 1.11), the glass transition temperature (T_g) of PLA is comprised between 50 – 60 °C and its melting temperature (T_m) is around 180 °C for PLLA and steadily decreases up to 140 – 150 °C with the increase of the D-isomer content. The standard melting of 100 % crystalline PLA (ΔH_m^0) has been reported equal to 93 J g^{-1} [163]. The T_m and degree of crystallinity are dependent on the molar mass, thermal history and purity of the polymer, and the crystallization kinetics [155, 160, 164]. The density of amorphous and semi-crystalline PLLA has been reported as 1.248 g cm^{-3} and 1.290 g cm^{-3} [165], respectively.

Regarding thermal stability, thermal degradation occurs when PLA is exposed to elevated temperatures, resulting in the breakdown of polymer chains and the release of volatile degradation products, independently of initial lactic distribution. PLA polymers start to thermally degrade at above 200 °C and completely decompose at 400 °C when tested under dried nitrogen environment [166].

In terms of solubility of PLA, PLA products are soluble in dioxane, acetonitrile, chloroform, methylene chloride, 1,1,2-trichloroethane and dichloroacetic acid. At lower temperature, ethylene, toluene, acetone and tetrahydrofuran exhibit limited ability to dissolve PLA, whereas they readily dissolve in these solvents when they are heated to their boiling points. PLA is not soluble in water, alcohols (methanol, ethanol and poly propylene glycol), and unsubstituted hydrocarbons (hexane and heptane) [167].

Concerning the mechanical properties, PLA can cover a wide range of properties spanning from soft and elastic plastics to rigid, and high-strength materials. Generally, when seeking enhanced mechanical properties, semi-crystalline PLA is the preferred choice over its amorphous counterpart [155]. Semi-crystalline PLA has an approximately tensile modulus of ~1 to ~ 5 GPa, a tensile strength of 50 – 70 MPa, a flexural strength of 100 MPa, and an

elongation at break of few % at room temperature [168, 169]. Table 1.11 summarized the mechanical properties of PLA, as a function of the dimer used.

Table 1.11. Physical properties of PLA [170].

Properties	PLA	PLLA
ρ (g cm^{-3})	1.21 – 1.25	1.24 – 1.30
σ (MPa)	21 – 60	15 – 150
E (GPa)	0.35 – 3.5	2.7 – 4.14
E_{break} (%)	2.5 – 6	3.0 – 10.0
T_g (°C)	45 – 60	55 – 65
T_m (°C)	150 – 162	170 – 200

A review of the literature also reveals that PLA is sensitive to degradation. On the one hand, as PLA belongs to the family of aliphatic polyesters, the hydrolytic degradation of its ester groups can happen in the presence of water leading to the formation of lactic acid monomers, and this process is accelerated at higher temperatures, *i.e.* in its processing temperature range [171]. One the other hand, exposure to ultraviolet (UV) light also induces photochemical degradation, breaking PLA chains and generating free radicals. Mechanical stress combined with environmental and humidity contribute to the mechanical degradation of PLA. Finally, regarding its end of life, PLA demonstrates biodegradability under composting conditions, breaking down into environmentally friendly compounds [155, 171].

4.2. PLA/CNT nanocomposites

4.2.1. Elaboration processes

Concerning the melt-blending process, numerous studies have focused on optimizing the manufacturing process to achieve PLA/CNT nanocomposites with the desired properties. For example, Villmow *et at.* [172] studied the impact of different screw profiles, temperature profiles and rotation speeds on the dispersion of MWCNT within PLA matrix. In general, according to literature about PLA/CNT nanocomposites, the typical processing conditions correspond to temperatures between 160 and 180 °C, mixing times of 5 to 10 min, and rotation speed between 50 and 100 rpm. After mixing, the nanocomposites are often molded into flat sheets obtained by thermo-compression. This one is usually performed between 160 and 200 °C for 2 – 5 min, under 10 to 15 MPa [125].

Regarding the solution mixing, as previously mentioned, PLA is soluble in some organic solvents such as $CHCl_3$, THF, or DMF… Among these solvents, $CHCl_3$ is the most used solvent

to prepare PLA/CNT nanocomposites [173–177]. Despite, some authors obtain good results with THF [178, 179], and dichloromethane [180, 181]. McCullen *et al.* [182] conclude that a combination of $CHCl_3$ and DMF is beneficial.

4.2.2. PLA/CNT nanocomposites and thermoelectricity

Pristine PLA is an electrical insulator with extremely low electrical conductivity ($\sigma \approx 1 \times 10^{-12}$ to 10^{-15} S m^{-1}) [183], [184]. Dispersing CNT in such an insulating polymer can form conductive polymer nanocomposites, indicating potential applications for thermoelectric materials. Besides, CNT reinforcement also affects the crystallization behavior of PLA, and this can directly affect the thermoelectric parameters such as thermal and electrical conductivities.

The incorporation of CNT can act as nucleating agents, accelerating the crystallization rate and improving the crystallinity of PLA. The presence of CNT provides sites for PLA molecules align and organize, facilitating the nucleation and growth of crystalline regions [185–187]. Many studies have focused on the impact of CNT on crystallization behaviors and crystal structure of PLA. For example, the work of Barrau *et al.* [188] analyzed the non-isothermal and isothermal crystallization behaviors of PLA/CNT nanocomposites prepared by solution and melt-mixing processes. The results show that the presence of CNT significantly increased the crystallization kinetics of the PLA matrix, and the incorporation of 1 wt% CNT does not modify the crystalline structure of PLA, α-type was formed for both PLA and PLA/CNT nanocomposites. In addition, from the optical microscopy results, nanofillers increase the number of nucleation sites and thus decrease the average crystalline size. A similar observation was also reported in the study of Wu *et al.* [185], in which MWCNT-COOH act as nucleating agents on both the melt-crystallization and the cold-crystallization of PLA. Furthermore, it was found that the crystallinity of the PLA matrix had a significant influence on electrical conductivity of the nanocomposites [189, 190]. Huang *et al.* [190] have reported that electrical conductivity of PLA/CNT composites was enhanced by increasing the degree of crystallinity of PLA matrix for CNT filler lower than percolation threshold ($w_c \approx 0.73$ wt%).

Until now, most published research has focused on the electrical conductivity [178, 191–193] and thermal conductivity [177, 193, 194] of PLA-based nanocomposites with CNT as fillers. Regarding thermoelectric properties, to the best of our knowledge, only the research of Antar *et al.* [124] has focused on this area. In this research, the authors present the thermoelectric properties of PLA/MWCNT/EG (expanded graphite) composites. The results

show the Seebeck coefficient was 17 µV K^{-1} at 32 vol% of EG and the maximum achieved ZT was 7.0 x 10^{-5} at 18 vol% of MWCNT at room temperature.

5. Conclusion and objectives of the study

This state-of-the-art chapter has presented the basic principle of thermoelectricity, the materials developed for thermoelectric applications, and the PLA. The limitations of conventional inorganic materials for application at near ambient temperature have been highlighted. These limitations justify the need for the development of new, cost-effective and environmentally friendly materials.

Nanocomposites based on insulating polymer matrix filled with conductive nanofillers have been developed for thermoelectric applications in recent year. In particular, the use of CNT as the filler for polymer-based nanocomposite has revealed some interesting properties in terms of electrical and thermal conductivities.

In this context, the main goal of this study is to investigate the relationships between elaboration, structure, and thermoelectric properties of PLA/CNT nanocomposites. Two commercial grades of PLA including amorphous (A-) and crystallizable (Sc-) will be selected as polymer matrix, and three different types of CNT including MWCNT, SWCNT, and SWCNT-COOH will be used as fillers.

The materials and experimental methods used in this work will be described in **Chapter II**.

Chapter III will be dedicated to the influence of different elaboration processes (melt-blending and solution mixing) on the thermoelectric properties of PLA/CNT nanocomposites. The impact of crystallinity of PLA and the effect of CNT orientation in PLA matrix on the thermoelectric properties will also be investigated and discussed.

Then, **Chapter IV** will be focused on the thermoelectric properties of thin film nanocomposites, based on A-PLA matrix filled with three types of CNT including MWCNT, SWCNT, and SWCNT-COOH and the effect of temperature between 300 and 400 K on the thermoelectric properties will be presented.

Finally, a conclusion and perspective of this work will be presented.

References

1. Szczech, J. R., Higgins, J. M., & Jin, S. (2011). Enhancement of the thermoelectric properties in nanoscale and nanostructured materials. *J. Mater. Chem.*, *21*(12), 4037–4055. https://doi.org/10.1039/C0JM02755C

2. Bell, L. E. (2008). Cooling, Heating, Generating Power, and Recovering Waste Heat with Thermoelectric Systems. *Science*, *321*(5895), 1457–1461. https://doi.org/10.1126/science.1158899

3. Hamid Elsheikh, M., Shnawah, D. A., Sabri, M. F. M., Said, S. B. M., Haji Hassan, M., Ali Bashir, M. B., & Mohamad, M. (2014). A review on thermoelectric renewable energy: Principle parameters that affect their performance. *Renewable and Sustainable Energy Reviews*, *30*, 337–355. https://doi.org/10.1016/j.rser.2013.10.027

4. Beretta, D., Neophytou, N., Hodges, J. M., Kanatzidis, M. G., Narducci, D., Martin-Gonzalez, M., … Caironi, M. (2019). Thermoelectrics: From history, a window to the future. *Materials Science and Engineering: R: Reports*, *138*, 100501. https://doi.org/10.1016/j.mser.2018.09.001

5. Mili, I., Latelli, H., Charifi, Z., Baaziz, H., & Ghellab, T. (2022). A simple formula for calculating the carrier relaxation time. *Computational Materials Science*, *213*, 111678. https://doi.org/10.1016/j.commatsci.2022.111678

6. Gayner, C., & Kar, K. K. (2016). Recent advances in thermoelectric materials. *Progress in Materials Science*, *83*, 330–382. https://doi.org/10.1016/j.pmatsci.2016.07.002

7. Hegde, G. S., Prabhu, A. N., Rao, A., & Chattopadhyay, M. K. (2021). Enhancement in thermoelectric figure of merit of bismuth telluride system due to tin and selenium co-doping. *Materials Science in Semiconductor Processing*, *127*, 105645. https://doi.org/10.1016/j.mssp.2020.105645

8. Fan, T., Xie, C., Wang, S., Oganov, A. R., & Cheng, L. (2018). First-principles study of thermoelectric properties of Mg $_2$ Si–Mg $_2$ Pb semiconductor materials. *RSC Advances*, *8*(31), 17168–17175. https://doi.org/10.1039/C8RA02436G

9. Gascoin, F., Ottensmann, S., Stark, D., Haïle, S. M., & Snyder, G. J. (2005). Zintl Phases as Thermoelectric Materials: Tuned Transport Properties of the Compounds $Ca_xYb_{1-x}Zn_2Sb_2$. *Advanced Functional Materials*, *15*(11), 1860–1864. https://doi.org/10.1002/adfm.200500043

10. Sharp, J. W., Jones, E. C., Williams, R. K., Martin, P. M., & Sales, B. C. (1995). Thermoelectric properties of CoSb3 and related alloys. *Journal of Applied Physics*, *78*(2), 1013–1018. https://doi.org/10.1063/1.360402

11. Petsagkourakis, I., Pavlopoulou, E., Cloutet, E., Chen, Y. F., Liu, X., Fahlman, M., … Hadziioannou, G. (2018). Correlating the Seebeck coefficient of thermoelectric polymer thin films to their charge transport mechanism. *Organic Electronics*, *52*, 335–341. https://doi.org/10.1016/j.orgel.2017.11.018

12. Bubnova, O., & Crispin, X. (2012). Towards polymer-based organic thermoelectric generators. *Energy & Environmental Science*, *5*(11), 9345. https://doi.org/10.1039/c2ee22777k

13. Sharma, A., Lee, J. H., Kim, K. H., & Jung, J. P. (2017). Recent Advances in Thermoelectric Power Generation Technology. *Journal of the Microelectronics and Packaging Society*, *24*(1), 9–16. https://doi.org/10.6117/KMEPS.2017.24.1.009

14. Pichanusakorn, P., & Bandaru, P. (2010). Nanostructured thermoelectrics. *Materials Science and Engineering: R: Reports*, *67*(2–4), 19–63. https://doi.org/10.1016/j.mser.2009.10.001

15. CRC handbook <http://environmentalchemistry.com/yogi/periodic/>.

16. Goldsmid, H. J. (2010). *Introduction to Thermoelectricity* (Vol. 121). Berlin, Heidelberg: Springer Berlin Heidelberg. https://doi.org/10.1007/978-3-642-00716-3

17. Nolas, G. S., Kaeser, M., Littleton, R. T., & Tritt, T. M. (2000). High figure of merit in partially filled ytterbium skutterudite materials. *Applied Physics Letters*, *77*(12), 1855–1857. https://doi.org/10.1063/1.1311597

18. Zare, Y., & Rhee, K. Y. (2020). Calculation of the Electrical Conductivity of Polymer Nanocomposites Assuming the Interphase Layer Surrounding Carbon Nanotubes. *Polymers*, *12*(2), 404. https://doi.org/10.3390/polym12020404

19. Han, Z., & Fina, A. (2011). Thermal conductivity of carbon nanotubes and their polymer nanocomposites: A review. *Progress in Polymer Science*, *36*(7), 914–944. https://doi.org/10.1016/j.progpolymsci.2010.11.004

20. Zebarjadi, M., Esfarjani, K., Dresselhaus, M. S., Ren, Z. F., & Chen, G. (2012). Perspectives on thermoelectrics: from fundamentals to device applications. *Energy Environ. Sci.*, *5*(1), 5147–5162. https://doi.org/10.1039/C1EE02497C

21. Liu, W., & Bai, S. (2019). Thermoelectric interface materials: A perspective to the challenge of thermoelectric power generation module. *Journal of Materiomics*, *5*(3), 321–336. https://doi.org/10.1016/j.jmat.2019.04.004

22. Aridi, R., Faraj, J., Ali, S., Lemenand, T., & Khaled, M. (2021). Thermoelectric Power Generators: State-of-the-Art, Heat Recovery Method, and Challenges. *Electricity*, *2*(3), 359–386. https://doi.org/10.3390/electricity2030022

23. Chen, L., Meng, F., & Sun, F. (2016). Thermodynamic analyses and optimization for thermoelectric devices: The state of the arts. *Science China Technological Sciences*, *59*(3), 442–455. https://doi.org/10.1007/s11431-015-5970-5

24. Dughaish, Z. H. (2002). Lead telluride as a thermoelectric material for thermoelectric power generation. *Physica B: Condensed Matter*, *322*(1–2), 205–223. https://doi.org/10.1016/S0921-4526(02)01187-0

25. Rull-Bravo, M., Moure, A., Fernández, J. F., & Martín-González, M. (2015). Skutterudites as thermoelectric materials: revisited. *RSC Advances*, *5*(52), 41653–41667. https://doi.org/10.1039/C5RA03942H

26. Witting, I. T., Chasapis, T. C., Ricci, F., Peters, M., Heinz, N. A., Hautier, G., & Snyder, G. J. (2019). The Thermoelectric Properties of Bismuth Telluride. *Advanced Electronic Materials*, *5*(6), 1800904. https://doi.org/10.1002/aelm.201800904

27. Tang, X., Xie, W., Li, H., Zhao, W., Zhang, Q., & Niino, M. (2007). Preparation and thermoelectric transport properties of high-performance p-type Bi2Te3 with layered nanostructure. *Applied Physics Letters*, *90*(1), 012102. https://doi.org/10.1063/1.2425007

28. Sootsman, J. R., Chung, D. Y., & Kanatzidis, M. G. (2009). New and Old Concepts in Thermoelectric Materials. *Angewandte Chemie International Edition*, *48*(46), 8616–8639. https://doi.org/10.1002/anie.200900598

29. Jeitschko, W., and Braun, D. (1997). $LaFe_4P_{12}$ with Filled $CoAs_3$-Type Structure and Isotypic Lanthanoid-Transition Metal Polyphosphides. *Acta Crystallographica Section B*, *33*, 3401–3406. https://doi.org/10.1107/S056774087701108X

30. Bérardan, D. (2004). Étude de skutterudites de terres-rares (R) et de métaux d (M) du type RM4Sb12: de nouveaux matériaux thermoélectriques pour la génération d'électricité. *Matériaux, Université Paris XII Val de Marne.*

31. Godart, C. (2009). Matériaux à effets thermoélectriques. *Matériaux fonctionnels - Matériaux biosourcés*. https://doi.org/10.51257/a-v1-n1500

32. Zhu, T., Fu, C., Xie, H., Liu, Y., & Zhao, X. (2015). High Efficiency Half-Heusler Thermoelectric Materials for Energy Harvesting. *Advanced Energy Materials*, *5*(19), 1500588. https://doi.org/10.1002/aenm.201500588

33. Shutoh, N., & Sakurada, S. (2005). Thermoelectric properties of the TiX(Zr0.5Hf0.5)1−XNiSn half-Heusler compounds. *Journal of Alloys and Compounds*, *389*(1–2), 204–208. https://doi.org/10.1016/j.jallcom.2004.05.078

34. Radushkevich, L. V., Lukyanovich, V.M. (1952). About the structure of carbon formed by thermal decomposition of carbon monoxide on iron substrate. *Journal of Physical Chemistry (Moscow)*, *26*, 88-95.

35. Lijima, S. (1991). Helical Microtubules of Graphitic Carbon. *Nature*, *354*, 56–58. https://doi.org/10.1038/354056a0

36. Bethune, D. S., Kiang, C. H., De Vries, M. S., Gorman, G., Savoy, R., Vazquez, J., & Beyers, R. (1993). Cobalt-catalysed growth of carbon nanotubes with single-atomic-layer walls. *Nature*, *363*(6430), 605–607. https://doi.org/10.1038/363605a0

37. Thostenson, E. T., Ren, Z., & Chou, T.-W. (2001). Advances in the science and technology of carbon nanotubes and their composites: a review. *Composites Science and Technology*, *61*(13), 1899–1912. https://doi.org/10.1016/S0266-3538(01)00094-X

38. Prasek, J., Drbohlavova, J., Chomoucka, J., Hubalek, J., Jasek, O., Adam, V., & Kizek, R. (2011). Methods for carbon nanotubes synthesis—review. *Journal of Materials Chemistry*, *21*(40), 15872. https://doi.org/10.1039/c1jm12254a

39. Kostarelos, K., Lacerda, L., Partidos, C. D., Prato, M., & Bianco, A. (2005). Carbon nanotube-mediated delivery of peptides and genes to cells: translating nanobiotechnology to therapeutics. *Journal of Drug Delivery Science and Technology*, *15*(1), 41–47. https://doi.org/10.1016/S1773-2247(05)50005-4

40. Xie, P., Sun, Y., Chen, C., Guo, S.-Y., Zhao, Y., Jiao, X., … Cheng, H.-M. (2023). Enrichment of Large-Diameter Semiconducting Single-Walled Carbon Nanotubes by Conjugated Polymer-Assisted Separation. *Nanomaterials*, *13*(13), 2001. https://doi.org/10.3390/nano13132001

41. Zhang, Q., Wei, N., Laiho, P., & Kauppinen, E. I. (2017). Recent Developments in Single-Walled Carbon Nanotube Thin Films Fabricated by Dry Floating Catalyst Chemical Vapor Deposition. *Topics in Current Chemistry*, *375*(6), 90. https://doi.org/10.1007/s41061-017-0178-8

42. Yao, Z., Kane, C. L., & Dekker, C. (2000). High-Field Electrical Transport in Single-Wall Carbon Nanotubes. *Physical Review Letters*, *84*(13), 2941–2944. https://doi.org/10.1103/PhysRevLett.84.2941

43. Zhou, X., Park, J.-Y., Huang, S., Liu, J., & McEuen, P. L. (2005). Band Structure, Phonon Scattering, and the Performance Limit of Single-Walled Carbon Nanotube Transistors. *Physical Review Letters*, *95*(14), 146805. https://doi.org/10.1103/PhysRevLett.95.146805

44. Liew, K. M., Kai, M. F., & Zhang, L. W. (2016). Carbon nanotube reinforced cementitious composites: An overview. *Composites Part A: Applied Science and Manufacturing*, *91*, 301–323. https://doi.org/10.1016/j.compositesa.2016.10.020

45. Gupta, D., Choudhary, B. P., Singh, N. B., & Gajbhiye, N. S. (2013). Carbon nanotubes: an overview. *Emerging Materials Research*, *2*(6), 299–337. https://doi.org/10.1680/emr.12.00043

46. O'Connell, M. (Ed.). (2006). *Carbon nanotubes: properties and applications*. Boca Raton, Fla.: CRC/Taylor & Francis.

47. Ma, C., Zhang, W., Zhu, Y., Ji, L., Zhang, R., Koratkar, N., & Liang, J. (2008). Alignment and dispersion of functionalized carbon nanotubes in polymer composites induced by an electric field. *Carbon*, *46*(4), 706–710. https://doi.org/10.1016/j.carbon.2008.01.019

48. Lu, J. P. (1997). Elastic Properties of Carbon Nanotubes and Nanoropes. *PHYSICAL REVIEW LETTERS*, *79*(7).

49. Yu, M.-F., Lourie, O., Dyer, M. J., Moloni, K., Kelly, T. F., & Ruoff, R. S. (2000). Strength and Breaking Mechanism of Multiwalled Carbon Nanotubes Under Tensile Load. *Science*, *287*(5453), 637–640. https://doi.org/10.1126/science.287.5453.637

50. Li, Y., Wang, K., Wei, J., Gu, Z., Wang, Z., Luo, J., & Wu, D. (2005). Tensile properties of long aligned double-walled carbon nanotube strands. *Carbon*, *43*(1), 31–35. https://doi.org/10.1016/j.carbon.2004.08.017

51. Sahoo, N. G., Rana, S., Cho, J. W., Li, L., & Chan, S. H. (2010). Polymer nanocomposites based on functionalized carbon nanotubes. *Progress in Polymer Science*, *35*(7), 837–867. https://doi.org/10.1016/j.progpolymsci.2010.03.002

52. Park, H., Zhao, J., & Lu, J. P. (2006). Effects of Sidewall Functionalization on Conducting Properties of Single Wall Carbon Nanotubes. *Nano Letters*, *6*(5), 916–919. https://doi.org/10.1021/nl052488d

53. Mamalis, A. G., Vogtländer, L. O. G., & Markopoulos, A. (2004). Nanotechnology and nanostructured materials: trends in carbon nanotubes. *Precision Engineering*, *28*(1), 16–30. https://doi.org/10.1016/j.precisioneng.2002.11.002

54. Mirabootalebi, S. O., & Akbari, G. H. (2017). Methods for synthesis of carbon nanotubes - Review. International journal of Bio-Inorganic Hybrid Nanomaterials, *6*(2), 49–57.

55. Hou, P., Zhang, F., Zhang, L., Liu, C., & Cheng, H. (2022). Synthesis of Carbon Nanotubes by Floating Catalyst Chemical Vapor Deposition and Their Applications. *Advanced Functional Materials*, *32*(11), 2108541. https://doi.org/10.1002/adfm.202108541

56. Rafique, M. M. A., & Iqbal, J. (2011). Production of Carbon Nanotubes by Different Routes-A Review. *Journal of Encapsulation and Adsorption Sciences*, *01*(02), 29–34. https://doi.org/10.4236/jeas.2011.12004

57. Iijima, S. (1980). Direct Observation of the Tetrahedral Bonding in Graphitized Carbon Black by High Resolution Electron Microscopy. *Journal of Crystal growth*, *50*(3), 675–683. https://doi.org/10.1016/0022-0248(80)90013-5

58. Iijima, S., and Ichihashi, T. (1993). Single-shell carbon nanotubes of 1-nm diameter. *Nature*, *363*, 603–605. https://doi.org/10.1038/363603a0

59. Guo, T., Nikolaev, P., Thess, A., Colbert, D.T., Smalley, R.E. (1995). Catalytic growth of single-walled nanotubes by laser vaporization. *Chemical Physics Letters*, *243*, 49-54. https://doi.org/10.1016/0009-2614(95)00825-O

60. Guo, T., Nikolaev, P., Rinzler, A. G., Tománek, D., Colbert, D. T., and Smalley, R. E. (1995). Self-Assembly of Tubular Fullerenes. *The Journal of Physical Chemistry*, *99*, 10694–10697. https://doi.org/10.1021/j100027a002

61. Hung, N. T., Nugraha, A. R. T., & Saito, R. (2019). Thermoelectric Properties of Carbon Nanotubes. *Energies*, *12*(23), 4561. https://doi.org/10.3390/en12234561

62. Hicks, L. D., & Dresselhaus, M. S. (1993). Thermoelectric figure of merit of a one-dimensional conductor. *Physical Review B*, *47*(24), 16631–16634. https://doi.org/10.1103/PhysRevB.47.16631

63. Wang, X., Wang, H., & Liu, B. (2018). Carbon Nanotube-Based Organic Thermoelectric Materials for Energy Harvesting. *Polymers*, *10*(11), 1196. https://doi.org/10.3390/polym10111196

64. Sumanasekera, G. U., Adu, C. K. W., Fang, S., & Eklund, P. C. (2000). Effects of Gas Adsorption and Collisions on Electrical Transport in Single-Walled Carbon Nanotubes. *Physical Review Letters*, *85*(5), 1096–1099. https://doi.org/10.1103/PhysRevLett.85.1096

65. Small, J. P., Perez, K. M., & Kim, P. (2003). Modulation of Thermoelectric Power of Individual Carbon Nanotubes. *Physical Review Letters*, *91*(25), 256801. https://doi.org/10.1103/PhysRevLett.91.256801

66. Piao, M., Joo, M.-K., Na, J., Kim, Y.-J., Mouis, M., Ghibaudo, G., … Kim, G.-T. (2014). Effect of Intertube Junctions on the Thermoelectric Power of Monodispersed Single Walled Carbon Nanotube Networks. *The Journal of Physical Chemistry C*, *118*(46), 26454–26461. https://doi.org/10.1021/jp505682f

67. MacLeod, B. A., Stanton, N. J., Gould, I. E., Wesenberg, D., Ihly, R., Owczarczyk, Z. R., … Ferguson, A. J. (2017). Large n- and p-type thermoelectric power factors from doped semiconducting single-walled carbon nanotube thin films. *Energy & Environmental Science*, *10*(10), 2168–2179. https://doi.org/10.1039/C7EE01130J

68. Zhou, W., Fan, Q., Zhang, Q., Cai, L., Li, K., Gu, X., … Xie, S. (2017). High-performance and compact-designed flexible thermoelectric modules enabled by a reticulate carbon nanotube architecture. *Nature Communications*, *8*(1), 14886. https://doi.org/10.1038/ncomms14886

69. Ibrahim, K. S. (2013). Carbon nanotubes-properties and applications: a review. *Carbon letters*, *14*(3), 131–144. https://doi.org/10.5714/CL.2013.14.3.131

70. Lekawa-Raus A., Patmore J., Kurzepa L., Bulmer, J., and Koziol, K. 2014. Electrical Properties of Carbon Nanotube Based Fibers and Their Future Use in Electrical Wiring. *Advanced Functional Materials*, *24*(24), 3661–3682. https://doi.org/10.1002/adfm.201303716

71. Min, C., Shen, X., Shi, Z., Chen, L., & Xu, Z. (2010). The Electrical Properties and Conducting Mechanisms of Carbon Nanotube/Polymer Nanocomposites: A Review. *Polymer-Plastics Technology and Engineering*, *49*(12), 1172–1181. https://doi.org/10.1080/03602559.2010.496405

72. Boschetto, G., Carapezzi, S., & Todri-Sanial, A. (2021). Graphene and Carbon Nanotubes for Electronics Nanopackaging. *IEEE Open Journal of Nanotechnology*, *2*, 120–128. https://doi.org/10.1109/OJNANO.2021.3127652

73. McEuen, P. L., Fuhrer, M. S., & Hongkun Park. (2002). Single-walled carbon nanotube electronics. *IEEE Transactions on Nanotechnology*, *1*(1), 78–85. https://doi.org/10.1109/TNANO.2002.1005429

74. Bachtold, A., Henny, M., Terrier, C., Strunk, C., Schönenberger, C., Salvetat, J.-P., … Forró, L. (1998). Contacting carbon nanotubes selectively with low-ohmic contacts for four-probe electric measurements. *Applied Physics Letters*, *73*(2), 274–276. https://doi.org/10.1063/1.121778

75. Dai, H., Wong, E. W., & Lieber, C. M. (1996). Probing Electrical Transport in Nanomaterials: Conductivity of Individual Carbon Nanotubes. *Science*, *272*(5261), 523–526. https://doi.org/10.1126/science.272.5261.523

76. Popov, V. N. (2004). Theoretical evidence for T1/2 specific heat behavior in carbon nanotube systems. *Carbon*, *42*(5–6), 991–995. https://doi.org/10.1016/j.carbon.2003.12.014

77. Maeda, T., & Horie, C. (1999). Phonon modes in single-wall nanotubes with a small diameter. *Physica B: Condensed Matter*, *263–264*, 479–481. https://doi.org/10.1016/S0921-4526(98)01415-X

78. Kumanek, B., & Janas, D. (2019). Thermal conductivity of carbon nanotube networks: a review. *Journal of Materials Science*, *54*(10), 7397–7427. https://doi.org/10.1007/s10853-019-03368-0

79. Berber, S., Kwon, Y.-K., & Tománek, D. (2000). Unusually High Thermal Conductivity of Carbon Nanotubes. *Physical Review Letters*, *84*(20), 4613–4616. https://doi.org/10.1103/PhysRevLett.84.4613

80. Kim, P., Shi, L., Majumdar, A., & McEuen, P. L. (2001). Thermal Transport Measurements of Individual Multiwalled Nanotubes. *Physical Review Letters*, *87*(21), 215502. https://doi.org/10.1103/PhysRevLett.87.215502

81. Yu, C., Kim, Y. S., Kim, D., & Grunlan, J. C. (2008). Thermoelectric Behavior of Segregated-Network Polymer Nanocomposites. *Nano Letters*, *8*(12), 4428–4432. https://doi.org/10.1021/nl802345s

82. Yan, H., Sada, N., & Toshima, N. (2002). Thermal transporting properties of electrically conductive polyaniline films as organic thermoelectric materials. *Journal of Thermal Analysis and Calorimetry*, *69*, 881–887. https://doi.org/10.1023/A:1020612123826

83. Feng-Xing, J., Jing-Kun, X., Bao-Yang, L., Yu, X., Rong-Jin, H., & Lai-Feng, L. (2008). Thermoelectric Performance of Poly(3,4-ethylenedioxythiophene): Poly(styrenesulfonate). *Chinese Physics Letters*, *25*(6), 2202–2205. https://doi.org/10.1088/0256-307X/25/6/076

84. Moses, D., & Denenstein, A. (1984). Experimental determination of the thermal conductivity of a conducting polymer: Pure and heavily doped polyacetylene. *Physical Review B*, *30*(4), 2090–2097. https://doi.org/10.1103/PhysRevB.30.2090

85. Zhang, F., Johansson, M., Andersson, M. R., Hummelen, J. C., & Inganäs, O. (2002). Polymer Photovoltaic Cells with Conducting Polymer Anodes. *Advanced Materials*, *14*(9), 662–665. https://doi.org/10.1002/1521-4095(20020503)14:9<662::AID-ADMA662>3.0.CO;2-N

86. Wang, L., Zhang, Z., Liu, Y., Wang, B., Fang, L., Qiu, J., … Wang, S. (2018). Exceptional thermoelectric properties of flexible organic−inorganic hybrids with monodispersed and periodic nanophase. *Nature Communications*, *9*(1), 3817. https://doi.org/10.1038/s41467-018-06251-9

87. Fan, Z., Du, D., Guan, X., & Ouyang, J. (2018). Polymer films with ultrahigh thermoelectric properties arising from significant seebeck coefficient enhancement by ion accumulation on surface. *Nano Energy*, *51*, 481–488. https://doi.org/10.1016/j.nanoen.2018.07.002

88. Du, Y., Shen, S. Z., Cai, K., & Casey, P. S. (2012). Research progress on polymer–inorganic thermoelectric nanocomposite materials. *Progress in Polymer Science*, *37*(6), 820–841. https://doi.org/10.1016/j.progpolymsci.2011.11.003

89. Bubnova, O., Khan, Z. U., Malti, A., Braun, S., Fahlman, M., Berggren, M., & Crispin, X. (2011). Optimization of the thermoelectric figure of merit in the conducting polymer poly(3,4-ethylenedioxythiophene). *Nature Materials*, *10*(6), 429–433. https://doi.org/10.1038/nmat3012

90. Kim, G.-H., Shao, L., Zhang, K., & Pipe, K. P. (2013). Engineered doping of organic semiconductors for enhanced thermoelectric efficiency. *Nature Materials*, *12*(8), 719–723. https://doi.org/10.1038/nmat3635

91. Kyaw, A. K. K., Yemata, T. A., Wang, X., Lim, S. L., Chin, W. S., Hippalgaonkar, K., Xu, J. 2018. Enhanced Thermoelectric Performance of PEDOT:PSS Films by Sequential Post-Treatment with Formamide. *Macromolecular Materials and Engineering*, *303*, 1700429. https://doi.org/10.1002/mame.201700429

92. Goel, M., & Thelakkat, M. (2020). Polymer Thermoelectrics: Opportunities and Challenges. *Macromolecules*, *53*(10), 3632–3642. https://doi.org/10.1021/acs.macromol.9b02453

93. Dubey, N., & Leclerc, M. (2011). Conducting polymers: Efficient thermoelectric materials. *Journal of Polymer Science Part B: Polymer Physics*, *49*(7), 467–475. https://doi.org/10.1002/polb.22206

94. Grazulevicius, J. V., Strohriegl, P., Pielichowski, J., & Pielichowski, K. (2003). Carbazole-containing polymers: synthesis, properties and applications. *Progress in Polymer Science*, *28*(9), 1297–1353. https://doi.org/10.1016/S0079-6700(03)00036-4

95. Zotti, G., Schiavon, G., Zecchin, S., Morin, J.-F., & Leclerc, M. (2002). Electrochemical, Conductive, and Magnetic Properties of 2,7-Carbazole-Based Conjugated Polymers. *Macromolecules*, *35*(6), 2122–2128. https://doi.org/10.1021/ma011311c

96. Morin, J.-F., Leclerc, M., Adès, D., & Siove, A. (2005). Polycarbazoles: 25 Years of Progress. *Macromolecular Rapid Communications*, *26*(10), 761–778. https://doi.org/10.1002/marc.200500096

97. Aïch, R. B., Blouin, N., Bouchard, A., & Leclerc, M. (2009). Electrical and Thermoelectric Properties of Poly(2,7-Carbazole) Derivatives. *Chemistry of Materials*, *21*(4), 751–757. https://doi.org/10.1021/cm8031175

98. Endrődi, B., Mellár, J., Gingl, Z., Visy, C., & Janáky, C. (2015). Molecular and Supramolecular Parameters Dictating the Thermoelectric Performance of Conducting Polymers: A Case Study Using Poly(3-alkylthiophene)s. *The Journal of Physical Chemistry C*, *119*, 8472–8479. https://doi.org/10.1021/acs.jpcc.5b00135

99. Xuan, Y., Liu, X., Desbief, S., Leclère, P., Fahlman, M., Lazzaroni, R., … Crispin, X. (2010). Thermoelectric properties of conducting polymers: The case of poly(3-hexylthiophene). *Physical Review B*, *82*(11), 115454. https://doi.org/10.1103/PhysRevB.82.115454

100. Zhang, Q., Sun, Y., Xu, W., & Zhu, D. (2012). Thermoelectric energy from flexible P3HT films doped with a ferric salt of triflimide anions. *Energy & Environmental Science*, *5*(11), 9639. https://doi.org/10.1039/c2ee23006b

101. Li, J., Tang, X., Li, H., Yan, Y., & Zhang, Q. (2010). Synthesis and thermoelectric properties of hydrochloric acid-doped polyaniline. *Synthetic Metals*, *160*(11–12), 1153–1158. https://doi.org/10.1016/j.synthmet.2010.03.001

102. Bhadra, S., Khastgir, D., Singha, N. K., & Lee, J. H. (2009). Progress in preparation, processing and applications of polyaniline. *Progress in Polymer Science*, *34*(8), 783–810. https://doi.org/10.1016/j.progpolymsci.2009.04.003

103. Chen, J., Gui, X., Wang, Z., Li, Z., Xiang, R., Wang, K., … Chen, L. (2012). Superlow Thermal Conductivity 3D Carbon Nanotube Network for Thermoelectric Applications. *ACS Applied Materials & Interfaces*, *4*(1), 81–86. https://doi.org/10.1021/am201330f

104. Nonoguchi, Y., Ohashi, K., Kanazawa, R., Ashiba, K., Hata, K., Nakagawa, T., … Kawai, T. (2013). Systematic Conversion of Single Walled Carbon Nanotubes into n-type Thermoelectric Materials by Molecular Dopants. *Scientific Reports*, *3*(1), 3344. https://doi.org/10.1038/srep03344

105. He, X., Wang, X., Nanot, S., Cong, K., Jiang, Q., Kane, A. A., … Kono, J. (2013). Photothermoelectric p–n Junction Photodetector with Intrinsic Broadband Polarimetry Based on Macroscopic Carbon Nanotube Films. *ACS Nano*, *7*(8), 7271–7277. https://doi.org/10.1021/nn402679u

106. Wang, Y., Yang, L., Shi, X., Shi, X., Chen, L., Dargusch, M. S., … Chen, Z. (2019). Flexible Thermoelectric Materials and Generators: Challenges and Innovations. *Advanced Materials*, *31*(29), 1807916. https://doi.org/10.1002/adma.201807916

107. Suemori, K., Watanabe, Y., & Hoshino, S. (2015). Carbon nanotube bundles/polystyrene composites as high-performance flexible thermoelectric materials. *Applied Physics Letters*, *106*(11), 113902. https://doi.org/10.1063/1.4915622

108. Moriarty, G. P., Briggs, K., Stevens, B., Yu, C., & Grunlan, J. C. (2013). Fully Organic Nanocomposites with High Thermoelectric Power Factors by using a Dual-Stabilizer Preparation. *Energy Technology*, *1*(4), 265–272. https://doi.org/10.1002/ente.201300018

109. Li, J., Huckleby, A. B., & Zhang, M. (2022). Polymer-based thermoelectric materials: A review of power factor improving strategies. *Journal of Materiomics*, *8*(1), 204–220. https://doi.org/10.1016/j.jmat.2021.03.013

110. Qu, S., Wang, M., Chen, Y., Yao, Q., & Chen, L. (2018). Enhanced thermoelectric performance of CNT/P3HT composites with low CNT content. *RSC Advances*, *8*(59), 33855–33863. https://doi.org/10.1039/C8RA07297C

111. Yao, Q., Chen, L., Zhang, W., Liufu, S., & Chen, X. (2010). Enhanced Thermoelectric Performance of Single-Walled Carbon Nanotubes/Polyaniline Hybrid Nanocomposites. *ACS Nano*, *4*(4), 2445–2451. https://doi.org/10.1021/nn1002562

112. Cho, C., Wallace, K. L., Tzeng, P., Hsu, J., Yu, C., & Grunlan, J. C. (2016). Outstanding Low Temperature Thermoelectric Power Factor from Completely Organic Thin Films Enabled by Multidimensional Conjugated Nanomaterials. *Advanced Energy Materials*, *6*(7), 1502168. https://doi.org/10.1002/aenm.201502168

113. Liu, S., Li, H., & He, C. (2019). Simultaneous enhancement of electrical conductivity and seebeck coefficient in organic thermoelectric SWNT/PEDOT:PSS nanocomposites. *Carbon*, *149*, 25–32. https://doi.org/10.1016/j.carbon.2019.04.007

114. Yu, C., Choi, K., Yin, L., & Grunlan, J. C. (2011). Light-Weight Flexible Carbon Nanotube Based Organic Composites with Large Thermoelectric Power Factors. *ACS Nano*, *5*(10), 7885–7892. https://doi.org/10.1021/nn202868a

115. Wang, L., Yao, Q., Xiao, J., Zeng, K., Qu, S., Shi, W., Wang, Q., Chen, L. 2016. Engineered Molecular Chain Ordering in Single-Walled Carbon Nanotubes/Polyaniline Composite Films for High-Performance Organic Thermoelectric Materials. *Chemistry An Asian Journal*, *11*, 1804–1810. https://doi.org/10.1002/asia.201600212

116. Wang, Y. Y., Cai, K. F., Shen, S., & Yao, X. (2015). In-situ fabrication and enhanced thermoelectric properties of carbon nanotubes filled poly(3,4-ethylenedioxythiophene) composites. *Synthetic Metals*, *209*, 480–483. https://doi.org/10.1016/j.synthmet.2015.08.034

117. Wang, J., Cai, K., Shen, S., & Yin, J. (2014). Preparation and thermoelectric properties of multi-walled carbon nanotubes/polypyrrole composites. *Synthetic Metals*, *195*, 132–136. https://doi.org/10.1016/j.synthmet.2014.06.003

118. Andrews, R., Jacques, D., Minot, M., & Rantell, T. (2002). Fabrication of Carbon Multiwall Nanotube/Polymer Composites by Shear Mixing. *Macromolecular Materials and Engineering*, *287*(6), 395. https://doi.org/10.1002/1439-2054(20020601)287:6<395::AID-MAME395>3.0.CO;2-S

119. Kasaliwal, G. R., Göldel, A., Pötschke, P., & Heinrich, G. (2011). Influences of polymer matrix melt viscosity and molecular weight on MWCNT agglomerate dispersion. *Polymer*, *52*(4), 1027–1036. https://doi.org/10.1016/j.polymer.2011.01.007

120. Min, K.-T., & Kim, G.-H. (2011). Effect of the viscosity and processing parameters on the surface resistivity of polypropylene/multiwalled carbon nanotube and ethylene-propylene-diene/multiwalled carbon nanotube nanocomposites. *Journal of Applied Polymer Science*, *120*(1), 95–100. https://doi.org/10.1002/app.33078

121. Liebscher, M., Gärtner, T., Tzounis, L., Mičušík, M., Pötschke, P., Stamm, M., … Voit, B. (2014). Influence of the MWCNT surface functionalization on the thermoelectric properties of melt-mixed polycarbonate composites. *Composites Science and Technology*, *101*, 133–138. https://doi.org/10.1016/j.compscitech.2014.07.009

122. Luo, J., Cerretti, G., Krause, B., Zhang, L., Otto, T., Jenschke, W., … Pötschke, P. (2017). Polypropylene-based melt mixed composites with singlewalled carbon nanotubes for thermoelectric applications: Switching from p-type to n-type by the addition of polyethylene glycol. *Polymer*, *108*, 513–520. https://doi.org/10.1016/j.polymer.2016.12.019

123. Luo, J., Krause, B., Pötschke, P., & Leibniz-Institut für Polymerforschung Dresden e.V., Hohe Strasse 6, D-01069, Dresden, Germany. (2016). Melt-mixed thermoplastic composites containing carbon nanotubes for thermoelectric applications. *AIMS Materials Science*, *3*(3), 1107–1116. https://doi.org/10.3934/matersci.2016.3.1107

124. Antar, Z., Feller, J. F., Noël, H., Glouannec, P., & Elleuch, K. (2012). Thermoelectric behaviour of melt processed carbon nanotube/graphite/poly(lactic acid) conductive biopolymer nanocomposites (CPC). *Materials Letters*, *67*(1), 210–214. https://doi.org/10.1016/j.matlet.2011.09.060

125. Gonçalves, C., Gonçalves, I., Magalhães, F., & Pinto, A. (2017). Poly(lactic acid) Composites Containing Carbon-Based Nanomaterials: A Review. *Polymers*, *9*(12), 269. https://doi.org/10.3390/polym9070269

126. Badaire, S., Poulin, P., Maugey, M., & Zakri, C. (2004). In Situ Measurements of Nanotube Dimensions in Suspensions by Depolarized Dynamic Light Scattering. *Langmuir*, *20*(24), 10367–10370. https://doi.org/10.1021/la049096r

127. Chen, L., Pang, X.-J., Qu, M.-Z., Zhang, Q., Wang, B., Zhang, B.-L., & Yu, Z.-L. (2006). Fabrication and characterization of polycarbonate/carbon nanotubes composites. *Composites Part A: Applied Science and Manufacturing*, *37*(9), 1485–1489. https://doi.org/10.1016/j.compositesa.2005.08.009

128. Safadi, B., Andrews, R., & Grulke, E. A. (2002). Multiwalled carbon nanotube polymer composites: Synthesis and characterization of thin films. *Journal of Applied Polymer Science*, *84*(14), 2660–2669. https://doi.org/10.1002/app.10436

129. Georgakilas, V., Kordatos, K., Prato, M., Guldi, D. M., Holzinger, M., & Hirsch, A. (2002). Organic Functionalization of Carbon Nanotubes. *Journal of the American Chemical Society*, *124*(5), 760–761. https://doi.org/10.1021/ja016954m

130. Brun, J.-F., Binet, C., Tahon, J.-F., Addad, A., Tranchard, P., & Barrau, S. (2020). Thermoelectric properties of bulk multi-walled carbon nanotube - poly(vinylidene fluoride) nanocomposites: Study of the structure/property relationships. *Synthetic Metals*, *269*, 116525. https://doi.org/10.1016/j.synthmet.2020.116525

131. Sun, Y.-C., Terakita, D., Tseng, A. C., & Naguib, H. E. (2015). Study on the thermoelectric properties of PVDF/MWCNT and PVDF/GNP composite foam. *Smart Materials and Structures*, *24*(8), 085034. https://doi.org/10.1088/0964-1726/24/8/085034

132. Krause, B., Barbier, C., Levente, J., Klaus, M., & Pötschke, P. (2019). Screening of Different Carbon Nanotubes in Melt-Mixed Polymer Composites with Different Polymer Matrices for Their Thermoelectrical Properties. *Journal of Composites Science*, *3*(4), 106. https://doi.org/10.3390/jcs3040106

133. Lee, H., Vashaee, D., Wang, D. Z., Dresselhaus, M. S., Ren, Z. F., & Chen, G. (2010). Effects of nanoscale porosity on thermoelectric properties of SiGe. *Journal of Applied Physics*, *107*(9), 094308. https://doi.org/10.1063/1.3388076

134. Du, F.-P., Qiao, X., Wu, Y.-G., Fu, P., Liu, S.-P., Zhang, Y.-F., & Wang, Q.-Y. (2018). Fabrication of Porous Polyvinylidene Fluoride/Multi-Walled Carbon Nanotube Nanocomposites and Their Enhanced Thermoelectric Performance. *Polymers*, *10*(7), 797. https://doi.org/10.3390/polym10070797

135. Wang, J., Kazemi, Y., Wang, S., Hamidinejad, M., Mahmud, M. B., Pötschke, P., & Park, C. B. (2020). Enhancing the electrical conductivity of PP/CNT nanocomposites through crystal-induced volume exclusion effect with a slow cooling rate. *Composites Part B: Engineering*, *183*, 107663. https://doi.org/10.1016/j.compositesb.2019.107663

136. Audoit, J., Laffont, L., Lonjon, A., Dantras, E., & Lacabanne, C. (2015). Percolative silver nanoplates/PVDF nanocomposites: Bulk and surface electrical conduction. *Polymer*, *78*, 104–110. https://doi.org/10.1016/j.polymer.2015.09.062

137. Kunz, K., Krause, B., Kretzschmar, B., Juhasz, L., Kobsch, O., Jenschke, W., … Pötschke, P. (2019). Direction Dependent Electrical Conductivity of Polymer/Carbon Filler Composites. *Polymers*, *11*(4), 591. https://doi.org/10.3390/polym11040591

138. Gnanaseelan, M., Chen, Y., Luo, J., Krause, B., Pionteck, J., Pötschke, P., & Qi, H. (2018). Cellulose-carbon nanotube composite aerogels as novel thermoelectric materials. *Composites Science and Technology*, *163*, 133–140. https://doi.org/10.1016/j.compscitech.2018.04.026

139. Kirkpatrick, S. (1973). Percolation and Conduction. *Reviews of Modern Physics*, *45*(4), 574–588. https://doi.org/10.1103/RevModPhys.45.574

140. Spinelli, G., Kotsilkova, R., Ivanov, E., Georgiev, V., Ivanova, R., Naddeo, C., & Romano, V. (2020). Dielectric Spectroscopy and Thermal Properties of Poly(lactic) Acid Reinforced with Carbon-Based Particles: Experimental Study and Design Theory. *Polymers*, *12*(10), 2414. https://doi.org/10.3390/polym12102414

141. Nan, C.-W., Shen, Y., & Ma, J. (2010). Physical Properties of Composites Near Percolation. *Annual Review of Materials Research*, *40*(1), 131–151. https://doi.org/10.1146/annurev-matsci-070909-104529

142. Medalia, A. I. (1986). Electrical Conduction in Carbon Black Composites. *Rubber Chemistry and Technology*, *59*(3), 432–454. https://doi.org/10.5254/1.3538209

143. Barrau, S., Demont, P., Peigney, A., Laurent, C., & Lacabanne, C. (2003). DC and AC Conductivity of Carbon Nanotubes−Polyepoxy Composites. *Macromolecules*, *36*(14), 5187–5194. https://doi.org/10.1021/ma021263b

144. Hill, R. M. (1976). Variable-range Hopping. *Physica Status Solidi (a)*, *34*(2), 601–613. https://doi.org/10.1002/pssa.2210340223145. Sheng, P. (1980). Fluctuation-induced tunneling conduction in disordered materials. *Physical Review B*, *21*(6), 2180–2195. https://doi.org/10.1103/PhysRevB.21.2180

146. Auras, R., Harte, B., & Selke, S. (2004). An Overview of Polylactides as Packaging Materials. *Macromolecular Bioscience*, *4*(9), 835–864. https://doi.org/10.1002/mabi.200400043

147. Raquez, J.-M., Habibi, Y., Murariu, M., & Dubois, P. (2013). Polylactide (PLA)-based nanocomposites. *Progress in Polymer Science*, *38*(10–11), 1504–1542. https://doi.org/10.1016/j.progpolymsci.2013.05.014

148. Gupta, A. P., & Kumar, V. (2007). New emerging trends in synthetic biodegradable polymers – Polylactide: A critique. *European Polymer Journal*, *43*(10), 4053–4074. https://doi.org/10.1016/j.eurpolymj.2007.06.045

149. Fukushima, K., Kimura, Y. (2006). Stereocomplexed Polylactides (Neo-PLA) as High-performance Bio-based Polymers: Their Formation, Properties, and Application. *Polymer International*, *55*(6), 626–642. https://doi.org/10.1002/pi.2010

150. Gupta, B., Revagade, N., & Hilborn, J. (2007). Poly(lactic acid) fiber: An overview. *Progress in Polymer Science*, *32*(4), 455–482. https://doi.org/10.1016/j.progpolymsci.2007.01.005

151. Mehta, R., Kumar, V., Bhunia, H., & Upadhyay, S. N. (2005). Synthesis of Poly(Lactic Acid): A Review. *Journal of Macromolecular Science, Part C: Polymer Reviews*, *45*(4), 325–349. https://doi.org/10.1080/15321790500304148

152. Lasprilla, A. J. R., Martinez, G. A. R., Lunelli, B. H., Jardini, A. L., & Filho, R. M. (2012). Poly-lactic acid synthesis for application in biomedical devices — A review. *Biotechnology Advances*, *30*(1), 321–328. https://doi.org/10.1016/j.biotechadv.2011.06.019

153. Malmgren, T., Mays, J., & Pyda, M. (2006). Characterization of poly(lactic acid) by size exclusion chromatography, differential refractometry, light scattering and thermal analysis. *Journal of Thermal Analysis and Calorimetry*, *83*(1), 35–40. https://doi.org/10.1007/s10973-005-7066-0

154. Fraschini, C., Plesu, R., Sarasua, J.-R., & Prud'homme, R. E. (2005). Cracking in polylactide spherulites. *Journal of Polymer Science Part B: Polymer Physics*, *43*(22), 3308–3315. https://doi.org/10.1002/polb.20616

155. Farah, S., Anderson, D. G., & Langer, R. (2016). Physical and mechanical properties of PLA, and their functions in widespread applications — A comprehensive review. *Advanced Drug Delivery Reviews*, *107*, 367–392. https://doi.org/10.1016/j.addr.2016.06.012

156. Stoclet, G., Seguela, R., Vanmansart, C., Rochas, C., & Lefebvre, J.-M. (2012). WAXS study of the structural reorganization of semi-crystalline polylactide under tensile drawing. *Polymer*, *53*(2), 519–528. https://doi.org/10.1016/j.polymer.2011.11.063

157. Sangeetha, V. H., Deka, H., Varghese, T. O., & Nayak, S. K. (2018). State of the art and future prospectives of poly(lactic acid) based blends and composites. *Polymer Composites*, *39*(1), 81–101. https://doi.org/10.1002/pc.23906

158. Di Lorenzo, M. L. (2005). Crystallization behavior of poly(l-lactic acid). *European Polymer Journal*, *41*(3), 569–575. https://doi.org/10.1016/j.eurpolymj.2004.10.020

159. Ikada, Y., Jamshidi, K., Tsuji, H., & Hyon, S. H. (1987). Stereocomplex formation between enantiomeric poly(lactides). *Macromolecules*, *20*(4), 904–906. https://doi.org/10.1021/ma00170a034

160. Huang, J., Lisowski, M. S., Runt, J., Hall, E. S., Kean, R. T., Buehler, N., & Lin, J. S. (1998). Crystallization and Microstructure of Poly(L -lactide- *co* - *meso* -lactide) Copolymers. *Macromolecules*, *31*(8), 2593–2599. https://doi.org/10.1021/ma9714629

161. Tábi, T., Wacha, A. F., & Hajba, S. (2019). Effect of D-lactide content of annealed poly(lactic acid) on its thermal, mechanical, heat deflection temperature, and creep properties. *Journal of Applied Polymer Science*, *136*(8), 47103. https://doi.org/10.1002/app.47103

162. Saeidlou, S., Huneault, M. A., Li, H., & Park, C. B. (2012). Poly(lactic acid) crystallization. *Progress in Polymer Science*, *37*(12), 1657–1677. https://doi.org/10.1016/j.progpolymsci.2012.07.005

163. Wang, L., Qiu, J., Sakai, E., & Wei, X. (2016). The relationship between microstructure and mechanical properties of carbon nanotubes/polylactic acid nanocomposites prepared by twin-screw extrusion. *Composites Part A: Applied Science and Manufacturing*, *89*, 18–25. https://doi.org/10.1016/j.compositesa.2015.12.016

164. Baratian, S., Hall, E. S., Lin, J. S., Xu, R., & Runt, J. (2001). Crystallization and Solid-State Structure of Random Polylactide Copolymers: Poly(L -lactide- *co* - D -lactide)s. *Macromolecules*, *34*(14), 4857–4864. https://doi.org/10.1021/ma001125r

165. Dana, H, R., Ebrahimi, F. (2023). Synthesis, Properties and Applications of Polylactic Acid-based Polymers. Polymer Engineering And Science, *63*(1), pp. 22–43. https://doi.org/10.1002/pen.26193

166. Carrasco, F., Santana Pérez, O., & Maspoch, M. (2021). Kinetics of the Thermal Degradation of Poly(lactic acid) and Polyamide Bioblends. *Polymers*, *13*(22), 3996. https://doi.org/10.3390/polym13223996

167. Lopes, M. S., Jardini, A. L., & Filho, R. M. (2012). Poly (Lactic Acid) Production for Tissue Engineering Applications. *Procedia Engineering*, *42*, 1402–1413. https://doi.org/10.1016/j.proeng.2012.07.534

168. Södergård, A., & Stolt, M. (2002). Properties of lactic acid based polymers and their correlation with composition. *Progress in Polymer Science*, *27*(6), 1123–1163. https://doi.org/10.1016/S0079-6700(02)00012-6

169. Jacobsen, S., & Fritz, H. G. (1999). Plasticizing polylactide?the effect of different plasticizers on the mechanical properties. *Polymer Engineering & Science*, *39*(7), 1303–1310. https://doi.org/10.1002/pen.11517

170. Van De Velde, K., & Kiekens, P. (2002). Biopolymers: overview of several properties and consequences on their applications. *Polymer Testing*, *21*(4), 433–442. https://doi.org/10.1016/S0142-9418(01)00107-6

171. Tsuji, H. (2013). Poly(Lactic Acid). In S. Kabasci (Ed.), *Bio-Based Plastics* (1st ed., pp. 171–239). Wiley. https://doi.org/10.1002/9781118676646.ch8

172. Villmow, T., Pötschke, P., Pegel, S., Häussler, L., & Kretzschmar, B. (2008). Influence of twin-screw extrusion conditions on the dispersion of multi-walled carbon nanotubes in a poly(lactic acid) matrix. *Polymer*, *49*(16), 3500–3509. https://doi.org/10.1016/j.polymer.2008.06.010

173. Moon, S., Jin, F., Lee, C., Tsutsumi, S., & Hyon, S. (2005). Novel Carbon Nanotube/Poly(L-lactic acid) Nanocomposites; Their Modulus, Thermal Stability, and Electrical Conductivity. *Macromolecular Symposia*, *224*(1), 287–296. https://doi.org/10.1002/masy.200550625

174. He, L., Sun, J., Wang, X., Fan, X., Zhao, Q., Cai, L., … Huang, W. (2012). Unzipped multiwalled carbon nanotubes-incorporated poly(l-lactide) nanocomposites with enhanced interface and hydrolytic degradation. *Materials Chemistry and Physics*, *134*(2–3), 1059–1066. https://doi.org/10.1016/j.matchemphys.2012.03.113

175. Seligra, P. G., Nuevo, F., Lamanna, M., & Famá, L. (2013). Covalent grafting of carbon nanotubes to PLA in order to improve compatibility. *Composites Part B: Engineering*, *46*, 61–68. https://doi.org/10.1016/j.compositesb.2012.10.013

176. Yoon, J. T., Jeong, Y. G., Lee, S. C., & Min, B. G. (2009). Influences of poly(lactic acid)-grafted carbon nanotube on thermal, mechanical, and electrical properties of poly(lactic acid). *Polymers for Advanced Technologies*, *20*(7), 631–638. https://doi.org/10.1002/pat.1312

177. Kim, H.-S., Chae, Y. S., Park, B. H., Yoon, J.-S., Kang, M., & Jin, H.-J. (2008). Thermal and electrical conductivity of poly(l-lactide)/multiwalled carbon nanotube nanocomposites. *Current Applied Physics*, *8*(6), 803–806. https://doi.org/10.1016/j.cap.2007.04.032

178. Chiu, W., Chang, Y., Kuo, H., Lin, M., & Wen, H. (2008). A study of carbon nanotubes/biodegradable plastic polylactic acid composites. *Journal of Applied Polymer Science*, *108*(5), 3024–3030. https://doi.org/10.1002/app.27796

179. Chiu, W.-M., Kuo, H.-Y., Tsai, P.-A., & Wu, J.-H. (2013). Preparation and Properties of Poly (Lactic Acid) Nanocomposites Filled with Functionalized Single-Walled Carbon Nanotubes. *Journal of Polymers and the Environment*, *21*(2), 350–358. https://doi.org/10.1007/s10924-012-0514-6

180. Kong, Y., Yuan, J., Wang, Z., & Qiu, J. (2012). Study on the preparation and properties of aligned carbon nanotubes/polylactide composite fibers. *Polymer Composites*, *33*(9), 1613–1619. https://doi.org/10.1002/pc.22298

181. Chrissafis, K., Paraskevopoulos, K. M., Jannakoudakis, A., Beslikas, T., & Bikiaris, D. (2010). Oxidized multiwalled carbon nanotubes as effective reinforcement and thermal stability agents of poly(lactic acid) ligaments. *Journal of Applied Polymer Science*, *118*(5), 2712–2721. https://doi.org/10.1002/app.32626

182. McCullen, S. D., Stano, K. L., Stevens, D. R., Roberts, W. A., Monteiro-Riviere, N. A., Clarke, L. I., & Gorga, R. E. (2007). Development, optimization, and characterization of electrospun poly(lactic acid) nanofibers containing multi-walled carbon nanotubes. *Journal of Applied Polymer Science*, *105*(3), 1668–1678. https://doi.org/10.1002/app.26288

183. Laredo, E., Bello, A., Diaz, J., Grimau, M., Martinez-Tong, D., Wu, D., Wu, L. (2013). Effect of Cold-crystallization on the AC and DC Conductive Properties of Polylactide Biocomposites with Carboxylic or Neat Large Aspect Ratio MWCNT. *Polymer Composites*, *34*(1), 67–76. https://doi.org/10.1002/pc.22378

184. Rizvi, R., Kim, J.-K., & Naguib, H. (2010). The effect of processing and composition on the properties of polylactide–multiwall carbon nanotube composites prepared by solvent casting. *Smart Materials and Structures*, *19*(9), 094003. https://doi.org/10.1088/0964-1726/19/9/094003

185. Wu, D., Wu, L., Zhou, W., Zhang, M., & Yang, T. (2010). Crystallization and biodegradation of polylactide/carbon nanotube composites. *Polymer Engineering & Science*, *50*(9), 1721–1733. https://doi.org/10.1002/pen.21695

186. Zhao, Y., Qiu, Z., Yan, S., & Yang, W. (2011). Crystallization behavior of biodegradable poly(L-lactide)/multiwalled carbon nanotubes nanocomposites from the amorphous state. *Polymer Engineering & Science*, *51*(8), 1564–1573. https://doi.org/10.1002/pen.21933

187. Park, S. H., Lee, S. G., & Kim, S. H. (2013). Isothermal crystallization behavior and mechanical properties of polylactide/carbon nanotube nanocomposites. *Composites Part A: Applied Science and Manufacturing*, *46*, 11–18. https://doi.org/10.1016/j.compositesa.2012.10.011

188. Barrau, S., Vanmansart, C., Moreau, M., Addad, A., Stoclet, G., Lefebvre, J.-M., & Seguela, R. (2011). Crystallization Behavior of Carbon Nanotube−Polylactide Nanocomposites. *Macromolecules*, *44*(16), 6496–6502. https://doi.org/10.1021/ma200842n

189. Quan, H., Zhang, S., Qiao, J., & Zhang, L. (2012). The electrical properties and crystallization of stereocomplex poly(lactic acid) filled with carbon nanotubes. *Polymer*, *53*(20), 4547–4552. https://doi.org/10.1016/j.polymer.2012.07.061

190. Huang, C., Bai, H., Xiu, H., Zhang, Q., & Fu, Q. (2014). Matrix crystallization induced simultaneous enhancement of electrical conductivity and mechanical performance in poly(l-lactide)/multiwalled carbon nanotubes (PLLA/MWCNTs) nanocomposites. *Composites Science and Technology*, *102*, 20–27. https://doi.org/10.1016/j.compscitech.2014.07.016

191. Pötschke, P., Andres, T., Villmow, T., Pegel, S., Brünig, H., Kobashi, K., … Häussler, L. (2010). Liquid sensing properties of fibres prepared by melt spinning from poly(lactic acid) containing multi-walled carbon nanotubes. *Composites Science and Technology*, *70*(2), 343–349. https://doi.org/10.1016/j.compscitech.2009.11.005

192. Shao, S., Zhou, S., Li, L., Li, J., Luo, C., Wang, J., … Weng, J. (2011). Osteoblast function on electrically conductive electrospun PLA/MWCNTs nanofibers. *Biomaterials*, *32*(11), 2821–2833. https://doi.org/10.1016/j.biomaterials.2011.01.051

193. Lebedev, S. M., Gefle, O. S., Amitov, E. T., Berchuk, D. Yu., & Zhuravlev, D. V. (2017). Poly(lactic acid)-based polymer composites with high electric and thermal conductivity and their characterization. *Polymer Testing*, *58*, 241–248. https://doi.org/10.1016/j.polymertesting.2016.12.033

194. Lamberti, P., Spinelli, G., Kuzhir, P. P., Guadagno, L., Naddeo, C., Romano, V., … Georgiev, V. (2018). Evaluation of thermal and electrical conductivity of carbon-based PLA nanocomposites for 3D printing (p. 020158). Presented at the 9TH INTERNATIONAL CONFERENCE ON "TIMES OF POLYMERS AND COMPOSITES": From Aerospace to Nanotechnology, Ischia, Italy. https://doi.org/10.1063/1.5046020

Chapter II. Materials and experimental method

1. Introduction

This chapter will firstly provide detailed information about all materials used in this study for preparing nanocomposites.

This work investigates the impact of elaboration processes and structure on the TE properties of PLA/CNT nanocomposites. Different elaboration processes including melt-blending, solution mixing, and combination between solution mixing and melt-blending will be carefully described. Two kinds of sample prepared from the above elaboration processes, including thick disc (bulk sample) and thin films nanocomposites, will also be detailed.

Then, a detailed description of the techniques and methodologies used in this work to investigate the properties of PLA/CNT nanocomposites such as structure of nanocomposites, the dispersion of CNT in PLA, and in-plane or cross-plane TE properties will be presented.

2. Materials

Both commercial amorphous PLA grade (4060D) and semi-crystalline PLA grade (6202D) were purchased from NatureWorks LLC. The amorphous PLA is a copolymer containing 12 % of D-isomer. Its weight- and number- average molar weights are $\overline{M_w}$ = 240 000 g mol^{-1} and $\overline{M_n}$ 108 000 g mol^{-1} [1]. The semi-crystalline PLA contains less than 2 % of D-lactide and molar weights are $\overline{M_w}$ = 234 000 g mol^{-1} and $\overline{M_n}$ = 112 890 g mol^{-1} [2]. The amorphous and semi-crystalline PLA will be denoted further A-PLA and Sc-PLA, respectively

All carbon nanotubes (CNT) used in this study were commercially available and were used without purification:

- MWCNT are Nanocyl 7000 produced by catalytic chemical vapor deposition; their length and average diameter are 1.5 µm and 9.5 nm, respectively and the purity is around 90 %.
- SWCNT come from IOLITEC (Ionic Liquids Technologies GmbH). Their outside diameter and length are 1-2 nm and 5-20 µm, respectively and the purity is higher than 90%.
- SWCNT-COOH come from Timesnano. They were produced by methane decomposition over Co-based catalyst; the COOH content is 2.73 wt%, the outside diameter and length are 1-2 nm and 5-30 µm, respectively. The purity is higher than 90 %.

Chloroform ($CHCl_3$) was purchased from Sigma-Aldrich, the purity is higher than 99 %, the boiling point temperature is 61.5 °C. This $CHCl_3$ was used as a solvent to dissolve PLA pellets and MWCNT in the solution mixing protocol.

3. Elaboration processes

3.1. Thick discs of PLA/MWCNT nanocomposites (bulk samples)

In this section, the 3 different elaboration processes will be described for preparing thick disc nanocomposites (thickness around 500 µm). Both A- and Sc-PLA grades were chosen as the polymer matrix, MWCNT were used as fillers.

3.1.1. Melt-blending process (Extrusion process)

Fig. 2.1 gives a schematic view of the followed melt-blending process.

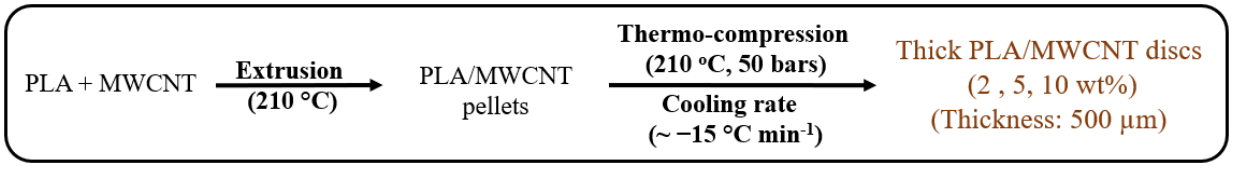

Figure 2.1. Melt-blending process for thick samples made with PLA/MWCNT preparation.

In this process, mixed PLA pellets with MWCNT were extruded by using a twin-screw extruder (Thermo Scientific Process 11 Parallel Twin-Screw Extruder) under atmospheric condition. Before processing, PLA granules were dried in a blast drying oven at 55 °C during 12 h to minimize water content. The adjusted temperature profile along the melting zone was from 190 to 210 °C (from the feed zone to die), and the screw speed was 100 rpm. The weight fractions of MWCNT were 2, 5, and 10 wt%. Note that in this study, we are dealing with electrically conductive materials. In this context, the minimum weight fraction of MWCNT was fixed at 2 wt%. Due to the increase in viscosity with increasing CNT content, the highest concentration of CNT was fixed at 10 wt% in accordance with the limitation of the extrusion equipment. PLA/MWCNT pellets were then thermo-compressed into thick discs of 13 mm in diameter. During the thermo-compression step, pellets were heated at 210 °C, compressed during 5 min, under 50 bar, and cooled down to room temperature under pressure using a cooling rate of about - 15 °C min^{-1}. For comparison, a thick pristine PLA disc was processed under similar conditions to ensure identical thermal history.

The final stage (thermo-compression process) will be performed to all thick samples from the other processes and will not be detailed again.

The melt extruded samples were elaborated at ENSAIT GEMTEX.

3.1.2. Solution mixing process

Solution mixing was used as a second protocol to prepare thick PLA/MWCNT samples. The purpose of using this second protocol is, on one hand to compare the effect of processing conditions (solution/extrusion) on the thermoelectrical properties and on the other hand, to be able to increase the CNT content within the PLA matrix beyond 10 wt%.

As described in Fig. 2.2, MWCNT were first dispersed in $CHCl_3$ by ultrasonic tip at room temperature. Then, PLA was dissolved in the previous solution and the PLA/CNT ratio has been calculated to elaborate nanocomposites with 2, 5, 10, 30, 40 wt% MWCNT contents. The mass ratio of (PLA/CNT)/$CHCl_3$ was 1:20 (weight to weight). Finally, the solution was magnetically stirred at 40 °C, for 12 h to obtain homogenous dispersion.

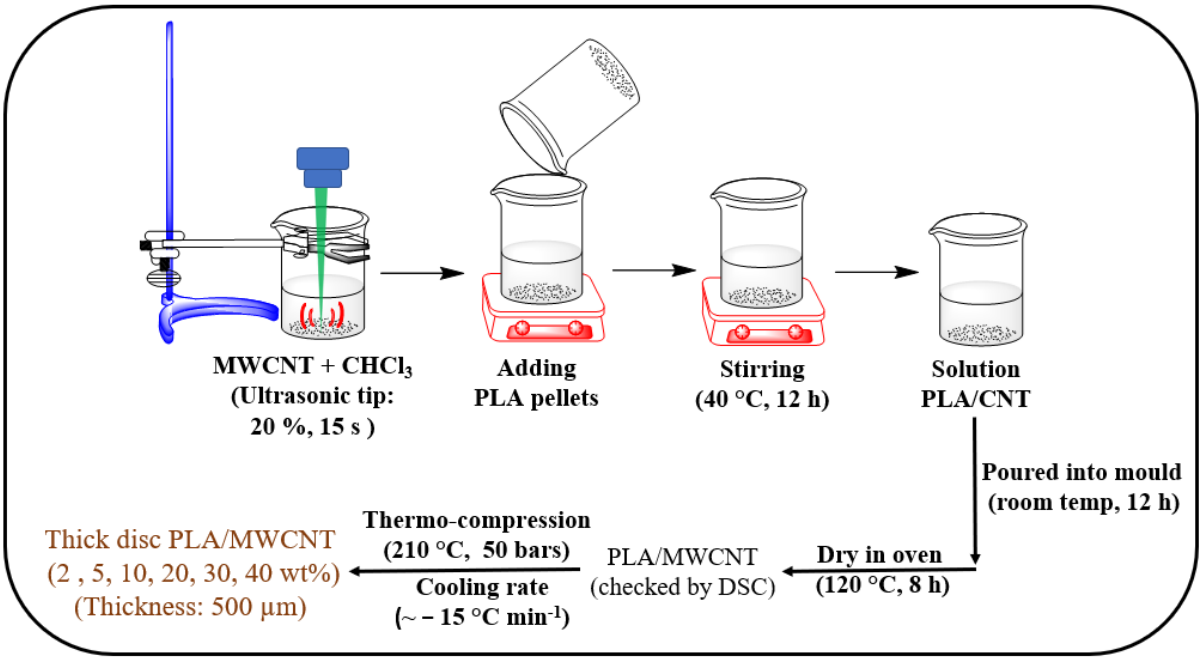

Figure 2.2. Solution mixing process for thick samples made with PLA/MWCNT preparation.

To allow solvent evaporation, the obtained solution was poured into a silicon mold and left at room temperature under atmospheric pressure for 12 h. Then, the residual solvent was removed by placing the nanocomposites in a vacuum oven at 120 °C for 8 h. These conditions have been defined based on complementary experiments presented in the Appendix-1 (A.1.1).

In this solution mixing process, the crucial step is the dispersion of the nanotubes in the solvent. Since MWCNT form stabilized bundles due to Van der Waals interactions, the dispersion of MWCNT in $CHCl_3$ and PLA matrix is a challenge [3]. Therefore, different ultrasonic conditions (step one) were used to investigate the dispersion of MWCNT in $CHCl_3$, the Appendix-1 (A.1.2) summarizes all the conditions tested. Based on these experiments, CNT were dispersed in $CHCl_3$ by ultrasonic tip with the optimum condition at 20 % of maximum amplitude, during 15 seconds (maximum power: 200W) at room temperature.

3.1.3. Combining solution mixing and melt-blending processes

With the purpose of improving the dispersion of MWCNT in the PLA matrix, a combination between solution mixing and melt-blending processes was applied. In this preparation, only the nanocomposite containing A-PLA matrix and 2 wt% of MWCNT was processed due to the viscosity limitation of the micro-extruder used. The nanocomposite was elaborated in two main steps, first by solution mixing using the same protocol described in section 3.1.2, and then by extrusion. In the second step, a twin-screw micro-extruder from DSM

Xplore operated at 210 °C, with a screw speed of 50 rpm, and a residence time of 10 min under nitrogen atmosphere was used.

3.1.4. Inducing crystallinity in semi-crystalline PLA/MWCNT nanocomposites

To study the impact of the crystallinity on the thermoelectric properties of nanocomposites, two thermal treatments were used to induce crystallinity in the Sc-PLA matrix:

- The first treatment is an annealing of the sample in solid state at 120 °C for 60 min, the chosen temperature and duration were selected from literatures [4,5].
- The second treatment corresponds to a slow cooling from melt state (cooling rate: ~ -1 °C min^{-1}).

Nanocomposites from the melt-blending process containing 2 and 5 wt% MWCNT were chosen for this investigation, and for the sake of comparison, pristine Sc-PLA was processed under similar conditions to ensure identical thermal history. The crystal structure was characterized by wide-angle X-ray scattering (WAXS) and the degree of crystallinity was determined by both DSC and WAXS.

3.1.5. Inducing orientation of MWCNT in nanocomposites

To study the potential effect of MWCNT orientation on the thermoelectric properties of nanocomposites, uniaxial tensile tests have been performed on nanocomposites containing 2 and 5 wt% of MWCNT using an Instron 4466 apparatus. For each nanocomposite, specimens with 100 mm, 30 mm and 0.5 mm in length, width and thickness respectively were compression molded using the same procedure as described in section 3.1.1.

Tests were carried out at 70 ± 2 ºC (*i.e.* above the glass transition temperature of A-PLA) using an initial strain rate ($\dot{\varepsilon}$) of 10^{-2} s^{-1}. It is recalled that:

$$\dot{\varepsilon}(t) = \frac{d}{dt}\left(\frac{L-L_0}{L_0}\right) = \frac{1}{L_0}\frac{dL}{dt} = \frac{v}{L_0} \qquad \text{(eq 2.1)}$$

where $\dot{\varepsilon}$, L_0, L, and v are the strain rate, the initial gauge length (6 cm), the length at time t, and the crosshead speed (0.6 mm min^{-1}), respectively. The goal is to achieve strains (ε) of 100 %, 150 % and 250 %.

3.2. Thin films of A-PLA/CNT nanocomposites

A-PLA/MWCNT thin films, with thicknesses of around 15 µm, were obtained by drop casting. The key points in this process are the nature of the substrate and its surface properties. Here the choice of the substrate is governed by the future analyses carried out on the samples.

The substrate is a specific consumable supply, a Van-der Pauw (VDP) electronic chip, purchased from the manufacturer of the thermoelectric Thin Film Analyser (TFA Linseis) described below in section 4.3.

The detailed process for preparing thin films combines three main steps: solution preparation (same protocol as described in solution mixing process Fig. 2.2), plasma cleaning of the chip and solution deposition on the chip. In this elaboration, A-PLA was chosen as the polymer matrix, and three types of nanotubes were used including MWCNT, SWCNT, and SWCNT-COOH.

Plasma treatment was used to clean and to activate the area dedicated to the sample to be deposited. Indeed, with the action of the plasma, traces of contaminants (organic matter) will be removed from the surface of the chip without affecting the membrane. By eliminating the impurities, the adhesion between the sample solution and the VDP chip is improved and the wettability is increased due to decrease of the surface tension [6,7]. In order to target only the useful area of the chip and to protect platinum contacts during the deposition of the sample, a Teflon mask have been adapted as illustrate in Fig. 2.3.

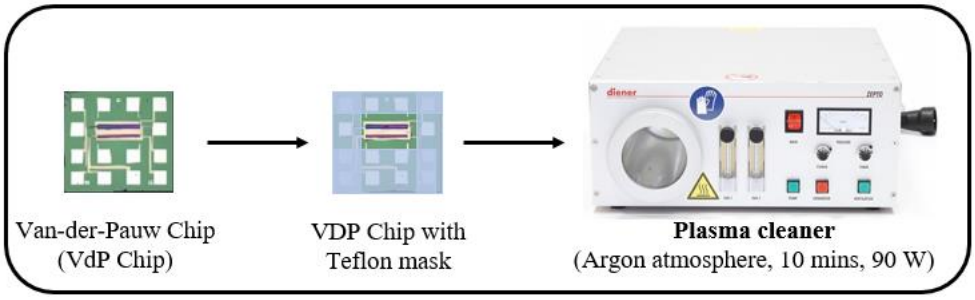

Figure 2.3. Plasma cleaning for VDP chip.

The plasma cleaner used is the Zepto model from Diener Electronic which operates at the frequency of 40 kHz at a maximum power of 100 W into a small vacuum chamber. The plasma cleaning of the chips was performed at 90 W during 10 minutes under argon at low pressure. Although the manufacture of the TFA, LINSEIS, recommends a plasma cleaning under pure O_2 in its application note, argon was found to give better results compared to pure O_2 and even air.

After cleaning, the VDP chips are ready for solvent solution deposition by the drop casting method (Fig. 2.4). The amount of solvent in the solution was adjusted to obtain a solution with the right viscosity (1:20 weight to weight sample solvent). A pipetting of around 10 µL of solution, is carried out and then deposited on the substrate. Chips were dried in the

oven under vacuum at 120 °C, for 60 min to remove all residual solvents before measurements. Finally, the thickness of the films was determined using a stylus profilometer (KLA-Tencor Alpha Step IQ) was typically between 10 and 20 µm.

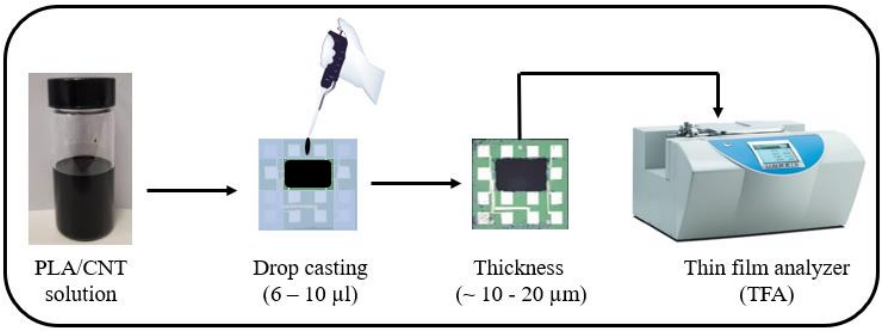

Figure 2.4. Drop casting of PLA/CNT solution on VDP chip for TFA measurement.

4. Characterization

4.1. Characterization techniques

4.1.1. Thermogravimetric analysis (TGA)

Thermogravimetric analysis (TGA) was used in this work to measure the CNT content in the nanocomposites. The measurements were performed on Analyzer TA Discovery – TA instrument under nitrogen flow (50 mL min^{-1}), from 25 to 850 °C with a heating rate of 10 °C min^{-1}. Three replicas were done for each concentration.

From the TGA curve, both pristine PLA grades degrade at around 380 °C (Fig. 2.5 and 2.6). In the case of Sc-PLA, a small residue is still present at temperature above the degradation one (~ 0.5 wt% at 550 °C for Sc-PLA from two elaboration processes). All nanocomposites show similar temperature degradation as pristine PLA which suggests that degradation of both PLA matrix is not influenced by the presence of CNT. Moreover, according to literature, we consider that CNT do not degrade until 600 °C [8].

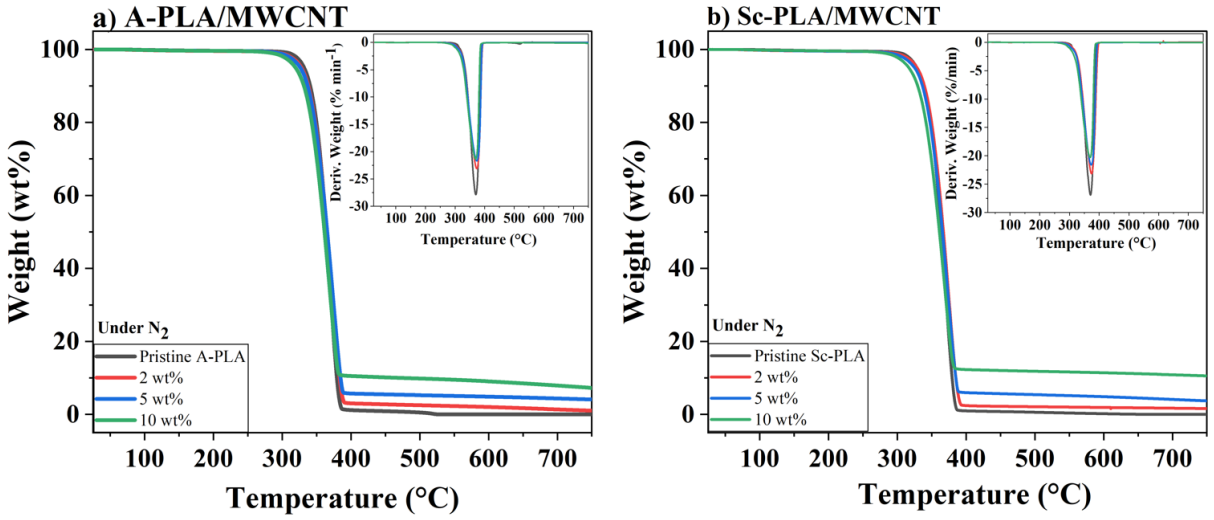

Figure 2.5. TGA and DTG (inset graphs) for thick PLA/MWCNT samples from melt-blending process: a) A-PLA/MWCNT, b) Sc-PLA/MWCNT.

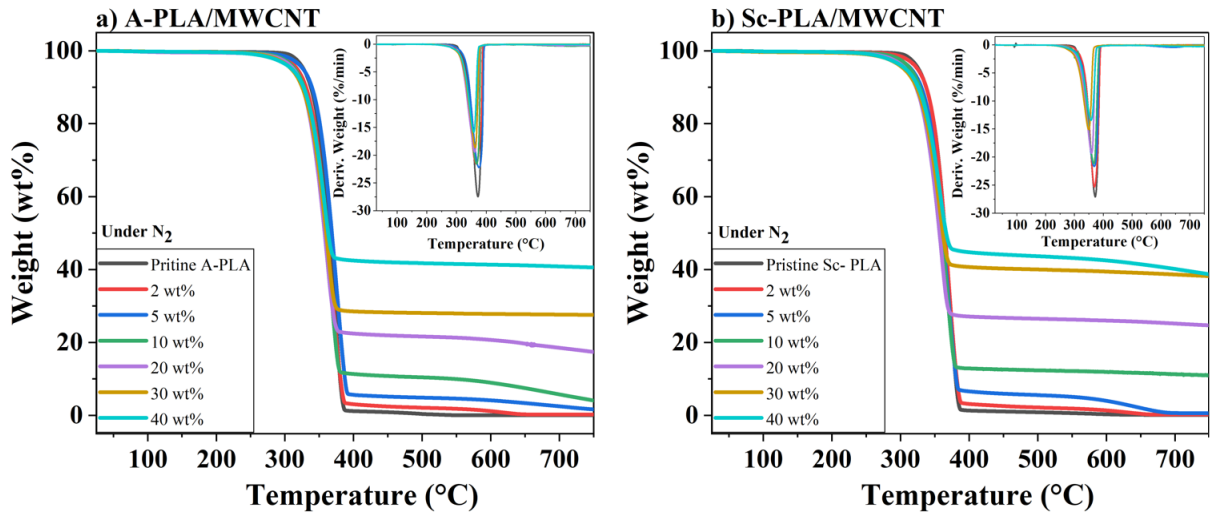

Figure 2.6. TGA and DTG (inset graphs) for thick PLA/MWCNT samples from solution mixing process: a) A-PLA/MWCNT, b) Sc-PLA/MWCNT.

For the determination of the CNT content in the nanocomposites, the Sc-PLA residue in the nanocomposite is considered in order to be as accurate as possible in particular for low CNT concentrations.

Results are summarized in Tables 2.1 and 2.2 for thick samples. It can be seen that the experimental MWCNT content is closed to or in the same order of magnitude as the expected value. Note that in the results section, the physical properties will be presented as a function of experimental values of MWCNT content measured by TGA.

Regarding thin films, the experimental CNT content was also checked. To do that the nanocomposites solution was drop-cast on the glass substrate and then the dry samples were

removed and TGA measurement was performed. The obtained CNT weight fractions are close to the expected one.

Table 2.1. Experimental MWCNT content (wt%) in thick samples from melt-blending.

Samples	2 wt%	5 wt%	10 wt%
A-PLA/MWCNT	2.1 ± 0.4	4.8 ± 0.5	9.6 ± 0.1
Sc-PLA/MWCNT	2.0 ± 0.5	4.6 ± 0.3	11.5 ± 0.4

Table 2.2. Experimental MWCNT content (wt%) in thick samples from solution-mixing.

Samples	2 wt%	5 wt%	10 wt%	20 wt%	30 wt%	40 wt%
A-PLA/MWCNT	2.0 ± 0.3	4.8 ± 0.3	9.8 ± 0.4	22.8 ± 1.7	29.7 ± 2.6	43.3 ± 2.5
Sc-PLA/MWCNT	1.1 ± 0.5	4.5 ± 0.1	11.2 ± 0.7	26.6 ± 3.3	37.9 ± 2.4	43.9 ± 9.0

4.1.2. Hydrostatic density balance

Density is an important parameter because it is involved in the calculation of thermal conductivity as will be shown latter. The density (ρ) of each sample was determined at room temperature with a precision scale thanks to a kit for density measurement. The sample was initially weighed in air, and then immersed into ethanol (Fluka, purity ≥ 99.8 %); the density is calculated by applying the Archimedes' principle (eq. 2.2):

$$\rho_{sample} = \frac{m_{sample\ (air)}}{m_{sample\ (air)} - m_{sample(ethanol)}}\ \rho_{ethanol} \qquad \text{(eq 2.2)}$$

where ρ_{sample} is the density of nanocomposites or pristine PLA (g cm^{-3}), $\rho_{ethanol}$ is the density of ethanol (0.79 g cm^{-3} at 20 °C), $m_{sample\ (air)}$ and $m_{sample\ (ethanol)}$ are the weight of sample in air and immersed into ethanol, respectively (g).

Tables 2.3 and 2.4 show the densities of thick disc PLA/MWCNT nanocomposites from the two elaboration processes.

Table 2.3. Density in g cm^{-3} of thick samples from melt-blending.

Samples	Pristine PLA	2 wt%	5 wt%	10 wt%
A-PLA	1.24 ± 0.01	1.25 ± 0.01	1.26 ± 0.01	1.29 ± 0.01
Sc-PLA	1.24 ± 0.01	1.25 ± 0.01	1.26 ± 0.01	1.29 ± 0.01

Table 2.4. Density in g cm^{-3} of thick samples from solution mixing.

Samples	Pristine PLA	2 wt%	5 wt%	10 wt%	20 wt%	30 wt%	40 wt%
A-PLA	1.23 ± 0.01	1.25 ± 0.01	1.26 ± 0.01	1.28 ± 0.01	1.32 ± 0.02	1.36 ± 0.02	1.41 ± 0.02
Sc-PLA	1.24 ± 0.01	1.25 ± 0.01	1.26 ± 0.01	1.28 ± 0.01	1.33 ± 0.01	1.37 ± 0.01	1.40 ± 0.02

Density also allows the conversion of weight fraction to volume fraction of MWCNT which is often used to model physical behaviors thanks to the following equation:

$$\Phi_{MWCNT} = \frac{\rho_{nanocomposite}}{\rho_{MWCNT}} . w_{MWCNT} \qquad \text{(eq 2.3)}$$

where Φ_{MWCNT} is the volume fraction of MWCNT (vol%), $\rho_{nanocomposite}$ and ρ_{MWCNT} are the density of nanocomposites and MWCNT, respectively (g cm^{-3}), w_{MWCNT} is the weight fraction of MWCNT in nanocomposites (wt%).

ρ_{MWCNT} was determined using eq. 2.4 which relates the density of nanocomposites to the density of PLA, MWCNT and the weight fraction of MWCNT:

$$\frac{1}{\rho_{nanocomposite}} = w_{MWCNT}\left(\frac{1}{\rho_{MWCNT}} - \frac{1}{\rho_{PLA}}\right) + \frac{1}{\rho_{PLA}} \qquad \text{(eq 2.4)}$$

The evolution of $\frac{1}{\rho_{nanocomposite}}$ as a function of the weight fraction of MWCNT should be linear with the slope corresponding to $(\frac{1}{\rho_{MWCNT}} - \frac{1}{\rho_{PLA}})$ and the y-intercept to $\frac{1}{\rho_{PLA}}$. Fig. 2.7 shows an example of curve obtained for A-PLA/MWCNT nanocomposites. The linear evolution is satisfied and gives the outcome values of 1.24 ± 0.01 and 1.74 ± 0.04 g.cm^{-3} for densities of A-PLA and MWCNT, respectively.

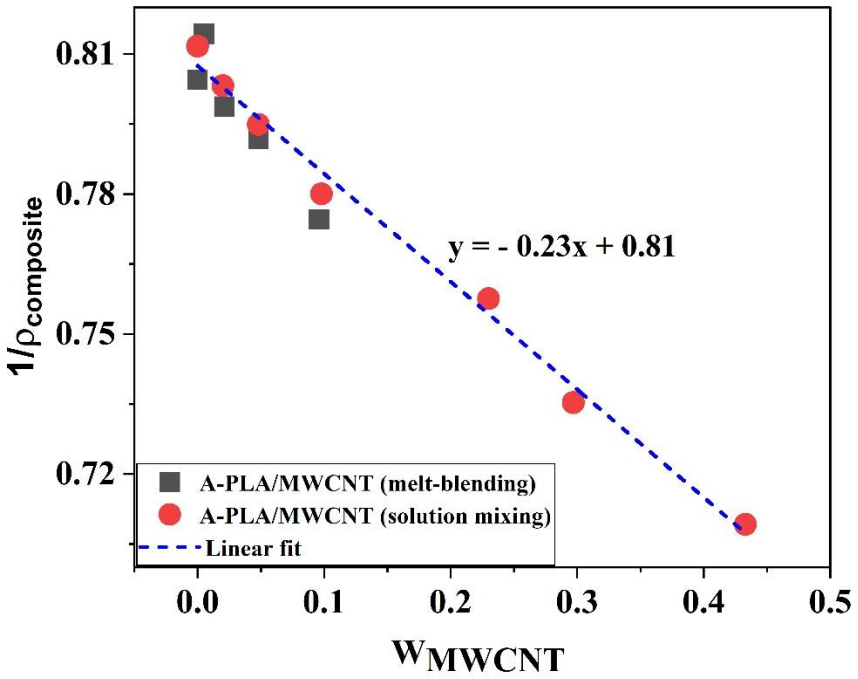

Figure 2.7. Linear fitting for calculating the density of A-PLA and MWCNT.

Compared to values found in literature, the density of A-PLA is in good agreement with the work of Bai *et al.* [9] and the density of MWCNT is closed to the measured value from the study of Kim *et al.* [10]. In addition, according to the work of Laurent *et al.* [11], with the outer diameter and the obtained density of MWCNT, we can estimate the number of walls of MWCNT in this study which varies between 5 and 10 walls (Fig. 2.8).

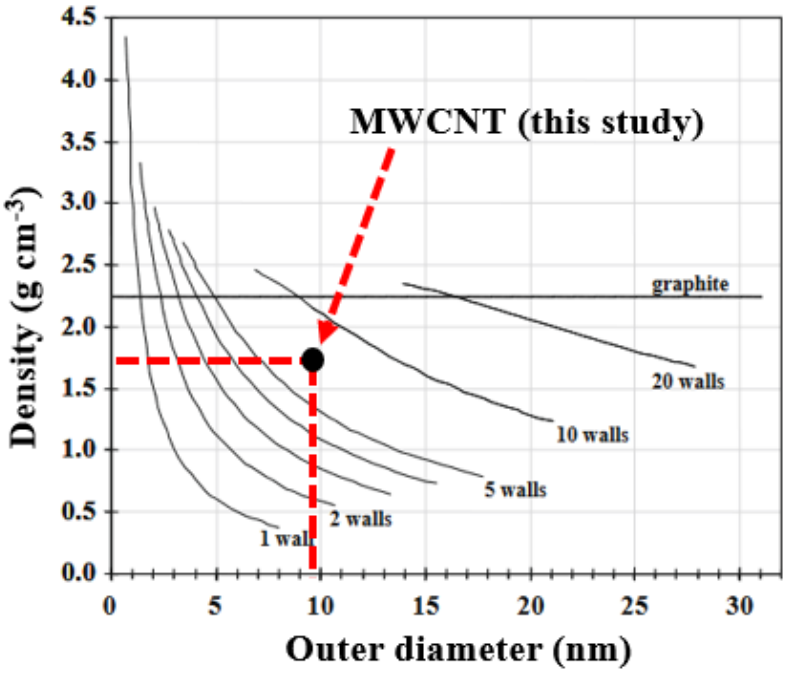

Figure 2.8. The density of CNT versus the outer diameter for different numbers of walls [11].

Finally, based on the density of MWCNT, the volume fraction of MWCNT (vol%) in nanocomposites was calculated and presented in Table 2.5.

Table 2.5. Convert value from weight fraction to volume fraction for PLA/MWCNT nanocomposites.

Samples		**2 wt%**	**5 wt%**	**10 wt%**	**20 wt%**	**30 wt%**	**40 wt%**
Melt-blending (A-PLA/MWCNT)	**wt%**	2.1 ± 0.4	4.8 ± 0.5	9.6 ± 0.1	-	-	-
	vol%	1.5 ± 0.3	3.5 ± 0.4	7.1 ± 0.1	-	-	-
Melt-blending (Sc-PLA/MWCNT)	**wt%**	2.0 ± 0.5	4.6 ± 0.3	11.5 ± 0.4	-	-	-
	vol%	1.5 ± 0.4	3.5 ± 0.3	8.9 ± 0.3	-	-	-
Solution mixing (A-PLA/MWCNT)	**wt%**	2.0 ± 0.3	4.8 ± 0.3	9.8 ± 0.4	22.8 ± 1.7	29.7 ± 2.6	43.3 ± 2.5
	vol%	1.4 ± 0.2	3.5 ± 0.2	7.2 ± 0.3	17.3 ± 1.3	23.3 ± 2.1	35.2 ± 2.1
Solution mixing (Sc-PLA/MWCNT)	**wt%**	1.1 ± 0.5	4.5 ± 0.1	11.2 ± 0.7	26.6 ± 3.3	37.9 ± 2.4	43.9 ± 9.0
	vol%	0.8 ± 0.4	3.4 ± 0.1	8.7 ± 0.5	21.3 ± 2.6	31.3 ± 2.0	37.0 ± 7.6

4.1.3. Scanning electron microscopy (SEM)

The morphology of PLA/CNT nanocomposites was observed by scanning electron microscopy (SEM). Basically, the electrons from the microscope interact with the sample, this generates electron and photons. For imaging, two types of electrons are used: the backscattered and secondary electrons which give information on chemical composition and on topography, respectively. In this study, only the image from secondary electrons are used.

Observations are realized on a field emission scanning electron microscopy (FE-SEM), a JEOL 7800F apparatus operating at an acceleration voltage of 3 kV and smallest aperture to reduce beam damage. All samples were cryo-fractured after immersion in liquid nitrogen and the surface was sputter coated with carbon coating to prevent electrical discharge during observation. All experiments were carried out by Alexandre Fadel, Institut Chevreul.

4.1.4. Differential scanning calorimetry (DSC)

The thermal transitions of nanocomposites (melting, crystallization, glass transition temperature….) have been characterized by conventional DSC experiments in which the difference of the amount of heat required to increase the temperature of a sample and reference is measured as a function of temperature. The basic principle of this technique is to always

maintain the temperature measured in the sample pan equals to that of the reference pan. When the sample undergoes phase transitions, more or less heat will be needed to keep the same temperature as reference. The increase or decrease of heat flow depends on whether the process is exothermic (such as crystallization) or endothermic (such as melting). In addition, the variation of heat capacity during the glass transition will also be recorded. Fig. 2.9 illustrates a typical DSC curve for a semi-crystalline polymer exhibiting a cold crystallization phenomenon.

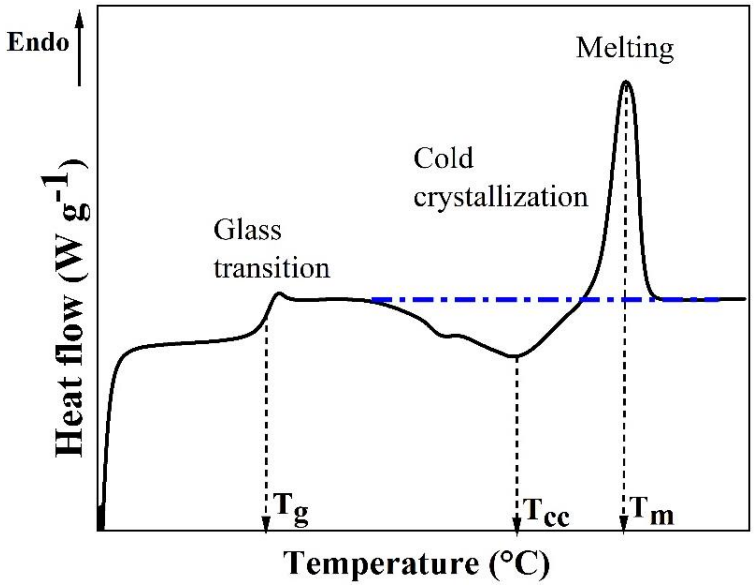

Figure 2.9. Typical DSC thermogram of a semi-crystalline polymer during a heating scan.

Differential scanning calorimetry (DSC) analysis were performed using a Q20 DSC apparatus from TA Instrument under nitrogen (50 mL min^{-1}). Temperature and heat flow were calibrated with a high-purity indium sample using a standard procedure. Aluminum non-hermetic pans and lids were used. The sample (~10 mg) was heated from 10 to 200 °C at 10 °C min^{-1}. The glass transition temperature T_g is defined as the temperature at the half value of step change of heat capacity (Cp). Cold crystallization (T_{cc}) and melting (T_m) temperatures were taken at the maximum of the corresponding peaks.

The degree of crystallinity χ_c of pristine Sc-PLA and Sc-PLA/CNT nanocomposites was determined by DSC by using following equation:

$$\chi_c = \left[\frac{(\Delta H_m - \Delta H_{cc})}{\Delta H_m^0 \cdot (1-w)}\right] . 100\% \qquad \text{(eq 2.5)}$$

where ΔH_m is the melting enthalpy during the heating process (J g^{-1}), ΔH_{cc} is the enthalpy of cold crystallization, ΔH_m^0 is the enthalpy of melting of 100 % crystalline PLA, which is 93.6 J g^{-1} [5], and w is the weight fraction of CNT (wt%).

The heat capacity (Cp) values have been measured by modulated DSC (MDSC) which is known to give quicker and more accurate Cp value than conventional DSC. The operating principle of MDSC uses two simultaneous heating rates - a linear heating rate that provides information similar to standard DSC, and a sinusoidal or modulated heating rate that allows the measurement of reversing heat capacity [12].

Cp measurement was performed using Q2000 DSC apparatus from TA Instrumental under nitrogen (50 mL min^{-1}). The mass of the sample was around 15 mg. The experimental program set-up used for Cp measurement is summarized in Table 2.6 according to the TA application note [12]. A calibration test with sapphire sample is previously performed, knowing that the value of Cp (sapphire) at 26.8 °C is 0.7788 J g^{-1} $°C^{-1}$. Three samples for each concentration were tested to ensure the reproducibility of the results. Fig. 2.10 illustrates the way to determine the Rev Cp of sample.

Table 2.6. Experimental set-up for **Cp** measurement by MDSC.

Number	Description
1	Data storage OFF
2	Zero heat flow at 26.8 °C
3	Equilibrate at 26.8 °C
4	Modulate ± 1.00 °C every 100 seconds
5	Isothermal for 5.00 mins
6	Data storage ON
7	Isothermal for 10.00 mins

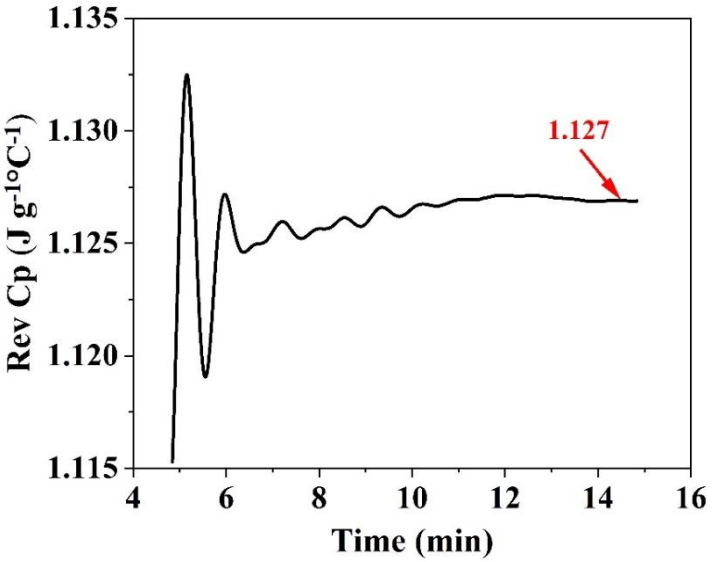

Figure 2.10. Example of determination of Rev. **Cp** value using MDSC with an A-PLA/ 5 wt% MWCNT nanocomposite.

4.1.5. Wide angle X-ray diffraction analysis (WAXS)

Wide-angle X-ray diffraction is a non-destructive technique that provides detailed information about the crystallographic structure of materials. When an X-ray beam is sent on matter, photons interact with the internal structure of the material and the re-emitted waves scattered by the electrons of atoms can result in diffuse scattering as well as constructive or destructive interferences (Fig. 2.11). Particularly, the interferences are constructive when Bragg's condition is satisfied:

$$2d\ sin\ \theta = n.\lambda \qquad \text{(eq 2.6)}$$

with n = 1, 2, 3…the order of interference, d the interplanar distance of the considered (hkl) plane, 2θ the Bragg's angle and λ the used wavelength.

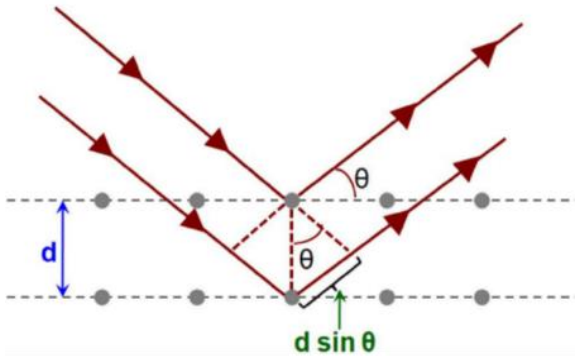

Figure 2.11. X-ray diffraction scheme in a crystal structure.

In this work, WAXS experiments were used to investigate the amorphous and crystalline part of PLA and PLA/CNT nanocomposites. The experiments were performed on a Xeuss 2.0 (Xenocs) in transmission mode at room temperature. The equipment is composed of a microsource using the Cu Kα radiation (λ = 1.54 Å), collimated and monochromatized by a FOX3D optic. 2D WAXS patterns are collected on a Pilatus 200k hybrid pixel detector (Dectris). The sample-to-detector distance is precisely determined using reference sample (AgBe powder). 1D intensity files are computed using the Foxtrot® software by radial integration of the 2D WAXS patterns. Standard corrections, such as dark current and background removal, were applied before analysis.

The determination of the phase(s) content(s) is proceeded by deconvolution of the average intensity profile $I = f(2\theta)$ using the Peakfit® software. Gaussian functions are used in a fitting process as previously used in literature [13]. A Gaussian function can be expressed by:

$$I(x) = I° \times e^{-0.5\times\left[\frac{x-x°}{\Delta x}\right]^2} \qquad \text{(eq 2.7)}$$

where $x°$ is the central peak position, Δx is the full-width at half-maximum (FWHM) value, and $I°$ is the maximum peak intensity.

Deconvolution is performed in the 2θ range: 5 – 46°. The profile for A-PLA was deconvoluted into three components with 2θ ≈ 15.5°, 2θ ≈ 21.7°, and 2θ ≈ 32.5° as proposed in [14]. In case of nanocomposites, the additional reflexion peak observed at 2θ ≈ 25.5° corresponds to the (002) lattice planes related to CNT [15]. An example of deconvoluted profiles from pristine A-PLA and A-PLA/ 5 wt% MWCNT nanocomposites can be seen in Fig. 2.12. For each simulation the four representative components of amorphous phase were fixed in terms of peak position and FWHM values.

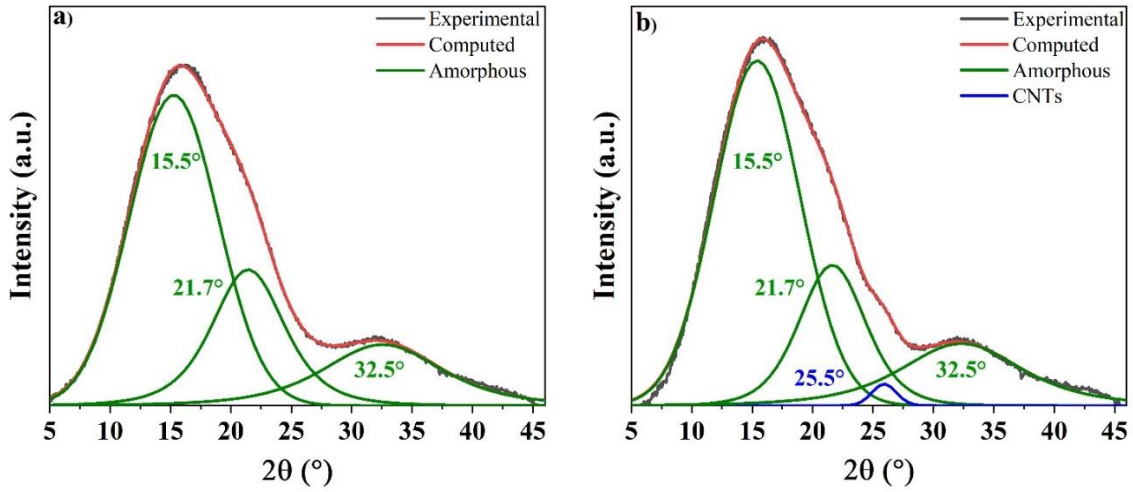

Figure 2.12. Examples of deconvoluted profiles from an extruded pristine A-PLA (a) and a A-PLA/ 5 wt% MWCNT nanocomposite (b).

In the case of Sc-PLA grade, different organized phases can be encountered. Fig. 2.13. shows an example of deconvolution of a pristine Sc-PLA sample (in this case the α crystalline form is involved). It is observed that, by adding Gaussian functions of peaks at 2θ ≈ 14.7°, 2θ ≈ 16.5°, 2θ ≈ 18.9° and 2θ ≈ 22.2° to the formerly defined functions for amorphous phase, the fitting is satisfying. The new peaks are functions with small FWHM values (usually ≈ 0.5°) characteristic of long range order.

Note that the positions of the crystalline phase characteristic peaks were found to be in agreement with what has been reported in literature [14,16].

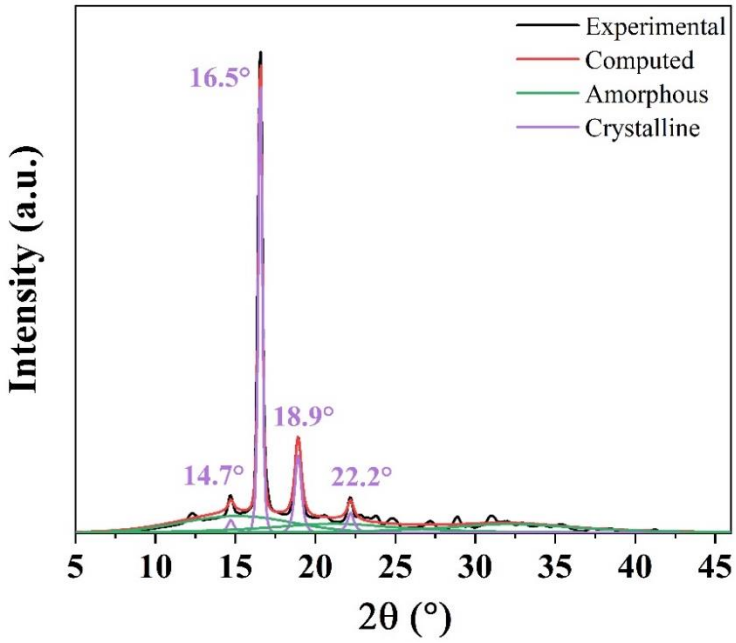

Figure 2.13. A deconvoluted profile example from a pristine Sc-PLA containing **α** phase.

From these deconvolutions, the proportion of the different phases (amorphous/crystalline) can be calculated by dividing the area of the characteristic peaks of the phase by the total scattered area. The obtained crystallinity will be compared with that determined by DSC (degree of crystallinity).

4.2. Thermoelectric properties for thick PLA/MWCNT samples (cross-plane)

First of all, let's remind that three parameters are required to obtain the thermoelectric figure of merit ZT at the temperature T: the thermal conductivity κ, the electrical conductivity σ, and the Seebeck coefficient S. The following paragraphs are dedicated to the various techniques that were used during this work to measure these physical quantities. Regarding thick discs (500 µm thick), thermoelectric parameters were measured cross-plane, *i.e.* through the thickness, and at room temperature. Note that for electrical conductivity, an in-plane measurement has also been performed for thick discs as presented in the following.

4.2.1. Thermal conductivity

The thermal conductivity κ of thick PLA/CNT samples was deduced from thermal diffusivity measurements according to the following equation

$$\kappa = \alpha \rho C_p \qquad \text{(eq 2.8)}$$

where α is the thermal diffusivity ($m^2\ s^{-1}$), ρ is the density ($kg\ m^{-3}$) and C_p is the specific heat capacity ($J\ kg^{-1}\ °K^{-1}$). Thermal conductivity (κ) is expressed in $W\ m^{-1}\ K^{-1}$. Three samples for

each filler fraction were systematically measured to ensure the reproducibility of the results. The ρ and C_p measurement have already been presented in section 4.1.2 and 4.1.4, respectively.

Thermal diffusivity of the samples was measured by a Netzsch light flash analyzer (LFA) 467 HyperFlash (Netzsch-Gerätebau GmbH). In this technique, the lower surface of a plane-parallel sample is heated by a light pulse and the resulting temperature rise of the sample top surface is recorded as a function of time. In our system, a xenon flash lamp is used and the increase in temperature of the upper sample surface is measured by an infrared (IR) detector (Fig. 2.14). The thermal diffusivity value is calculated using eq. 2.9 where L_s is the specimen thickness and $t_{1/2}$ is the time required for the rear face temperature rise to reach half of temperature increase as shown in Fig. 2.15.

$$\alpha = 0.1388.\frac{L_s^2}{t_{\frac{1}{2}}} \qquad \text{(eq 2.9)}$$

Note that the pristine PLA sample required a small dusting of graphene on both sides by contrast to the nanocomposites where CNT have an excellent light absorption.

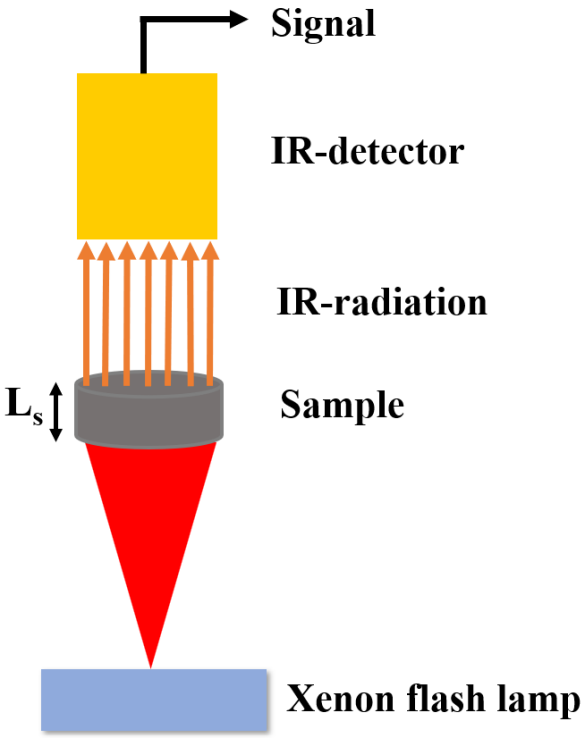

Figure 2.14. Principle of a laser flash analyzer experiment.

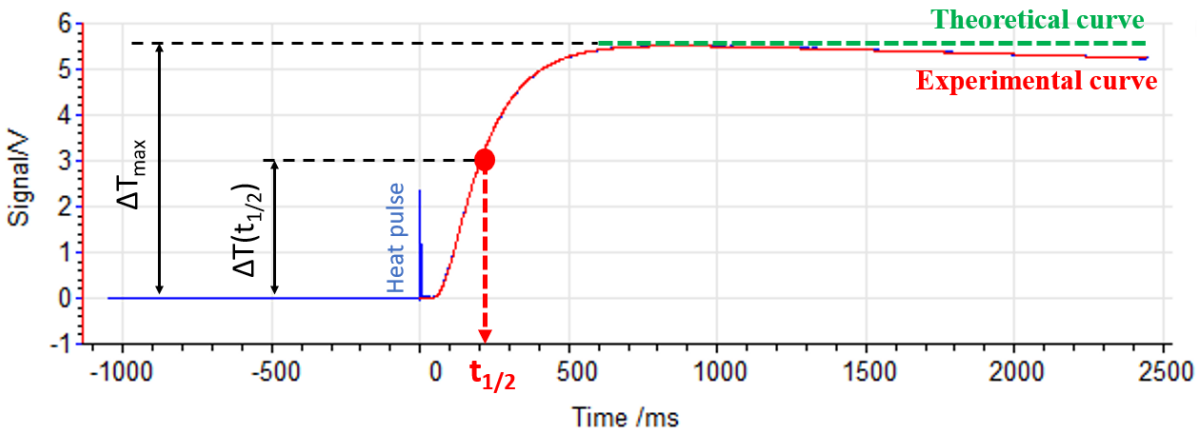

Figure 2.15. Genetic curve to calculate the diffusivity with an A-PLA/ 5 wt% MWCNT).

In this work, thermal diffusivity is calculated using the optimization method suggested by the LFA constructor.

4.2.2. Electrical conductivity

4.2.2.1. Dielectric spectroscopy (cross-plane)

Dielectric spectroscopy is used to measure the cross-plane electrical conductivity of thick samples. Dielectric spectroscopy is also known as impedance spectroscopy. In this experiment, the sample, acting as a capacitor, is mounted between two electrodes connected to the appropriate analyzer which measures the complex impedance Z^* of the material. A sinusoidal voltage is applied to the sample, causing a current to flow at the same frequency in the sample but out of phase with the voltage. In complex terms $Z^* = V^*/I^* = 1/i\omega C^*$ where C^* is the complex capacitance. The measurements in this thesis were carried out in a frequency range of 0.1 Hz to 1 MHz and the amplitude of the applied sinusoidal voltage is 1 V.

So, dielectric spectroscopy allows to characterize the frequency-dependent electrical properties of the CNT-filled systems [17]. This technique is based on the measurement and subsequent evaluation of some frequency-dependent parameters, including particularly the complex dielectric permittivity, $\varepsilon^*(\omega)$:

$$\varepsilon^*(\omega) = \frac{1}{i\omega Z^*(\omega) C_0} = \varepsilon'(\omega) - i\varepsilon''(\omega) \qquad \text{(eq 2.10)}$$

where C_0 is the empty cell capacitance dependent on the surface area A, and the sample thickness t, ε_0 ($C_0=\varepsilon_0 A/t$) is the vacuum permittivity, ω is the angular frequency, $i^2 = -1$ is the imaginary constant, ε' and ε'' are the real and imaginary parts of the complex permittivity, respectively.

The relevant parameter for our thermoelectric study is to find the electrical conductivity. The real part $\sigma'(\omega)$ of the complex electrical conductivity $\sigma^*(\omega)$ is related to $\varepsilon^*(\omega)$ as follows:

$$\sigma'(\omega) = \omega\varepsilon_0\varepsilon_r'' \qquad \text{(eq 2.11)}$$

where $\varepsilon_r"(\omega)$ is the imaginary part of the complex relative permittivity of material ($\varepsilon^* = \varepsilon_0\varepsilon_r^*$) and ε_0 (8.85 x 10^{-12} F m^{-1}) is the vacuum permittivity.

In addition, the frequency dependence of the σ' follows a universal dielectric response proposed by A. K. Jonscher in 1977 [18] and modified by Almond-West latter. This model is widely used to analyze the frequency dependence of the real part of the complex conductivity. Thus, $\sigma'(\omega)$ or the total σ_{AC} conductivity can be represented by a power law as expressed in the following eq. 2.12 [19]:

$$\sigma'(\omega) = \sigma(0) + \sigma_{AC}(\omega) = \sigma_{DC} + A\omega^s = \sigma_{DC}\left(1 + \left(\frac{\omega}{\omega_0}\right)^s\right) \qquad \text{(eq 2.12)}$$

where σ_{DC} is the independent frequency conductivity, also called DC conductivity (at $\omega \to 0$), A is a constant depending on temperature, s is an exponent depending on both frequency and temperature with values in the range 0 – 1, and ω_0 is a critical angular frequency.

Fig. 2.16 demonstrates a typical example of the frequency dependence of $\sigma'(f)$ for semi-conductor materials. This graph can be described in three regions: (i) at low frequencies with decreasing frequency (region I) the observed decrease in conductivity is due to the phenomenon of electrodes polarization, (ii) at intermediate frequencies (region II) a plateau appears which is almost frequency independent and where σ_{DC} can be estimated, (iii) at high frequencies (region III) $\sigma'(\omega)$ increases according to a power law where the critical frequency f_c can be evaluated. Note that regions II and III will be fitted by the previously introduced universal dielectric response (eq. 2.12). In this work, we will not be interested by the electrode polarization.

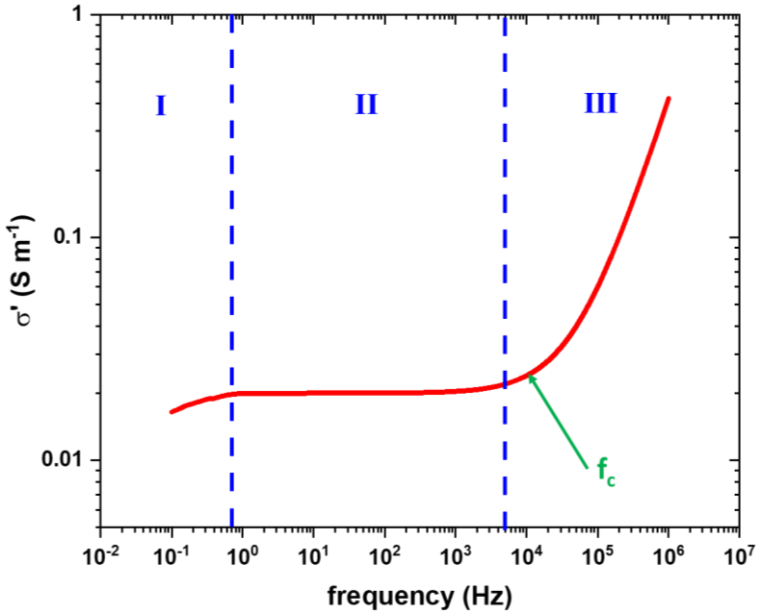

Figure 2.16. Typical evolution of real part of the complex electrical conductivity as a function of frequency for a semi-conductor sample.

The measurement of cross-plane electrical conductivity by dielectric spectroscopy is very sensitive and can be highly dependent on the conditions used for its acquisition. To probe this phenomenon, some dielectric measurements were performed on the same sample at room temperature by using two kinds of dielectric spectroscopy equipment. The first equipment is a ModuLab MTS Materials Test System from Solartron analytical supplied by HTDS (formerly Ameteck), equipped with a sample and reference module (useful for insulating materials) and a 12962A sample holder, which allows work at room temperature only. The second one is a broadband dielectric spectrometer (Novocontrol Technologies Alpha Analyzer) coupled to a high frequencies analyzer (Novocontrol Technologies RF impedance analyzer) and a thermal regulation system (Novocontrol Quatro controller).

For the Novocontrol spectrometer, the sample was placed between two gold-plated brass electrodes which were pressed together with a micrometer screw. There is neither intrinsic control of sample thickness nor clamping force. Thickness is measured with an external micrometer. Measurements were performed with increasing the clamping force. Results are presented in Fig. 2.17 which shows the evolution of σ' versus frequency. Curve 0 is recorded with the lowest clamping force and curve 8 for the highest one. Note that the curve 8 was measured with a so high clamping force that we are at the limit of the equipment damage. The electrical conductivity σ' continuously increases with the clamping force: a variation of about one and a half decades can be obtained. One can assume that the contact between electrodes

and sample is not perfect for the curves 0 to 2. In the case of the Solartron impedance meter, the sample holder includes a micrometer for measuring sample thickness and a system to ensure the same clamping force. In addition, the bottom electrode has a guard ring to reduce the effect of stray fields on the edge of the sample. The curve obtained with the Solartron spectrometer is in the average value of those obtained with the Novocontrol analyzer. The main advantage of this apparatus is the control of the experimental conditions (clamping force and thickness) inducing repeatability of the measurement.

Also, during this PhD study, all the dielectric measurements were performed with the Solartron spectrometer for the calculation of the through-plane electrical conductivity. Three samples for each filler fraction were measured for the reproducibility and the final value is the mean value of all measurements.

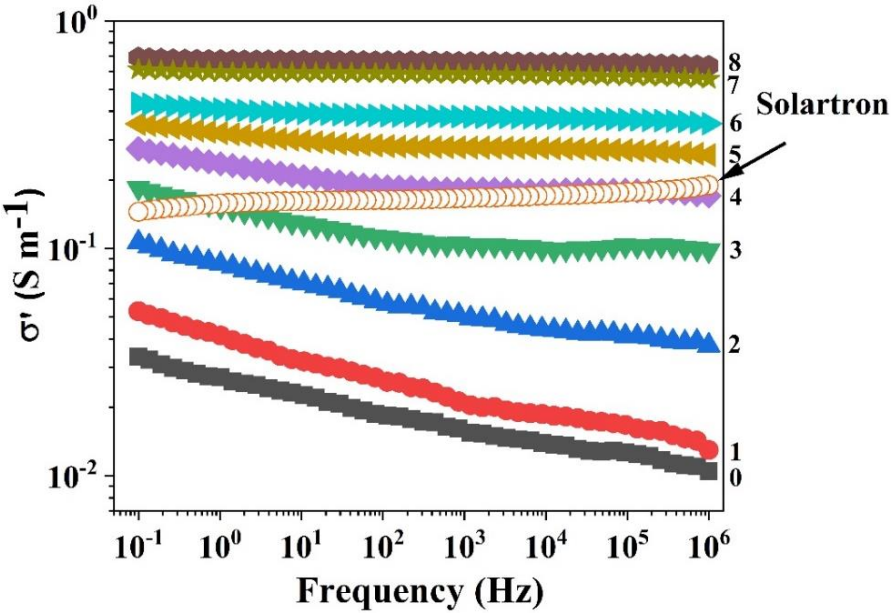

Figure 2.17. Comparison of the cross-plane electrical conductivity as a function of frequency between Novocontrol (full symbols) and Solartron (empty symbols) analyzers. Curves 0 to 8 are recorded with increasing clamping force.

4.2.2.2. 4-point collinear probe (in-plane)

The 4-point probe method was used to measure the surface (in-plane) electrical conductivity. In this technique, the 4 collinear probes, with the same distance (s) between each probe, are brought into contact with the surface of the samples. The two outer probes (1 and 4) are connected to a DC current source. The two inner probes (2 and 3) are used to measure the resulting voltage drop across the surface of the sample (Fig. 2.18).

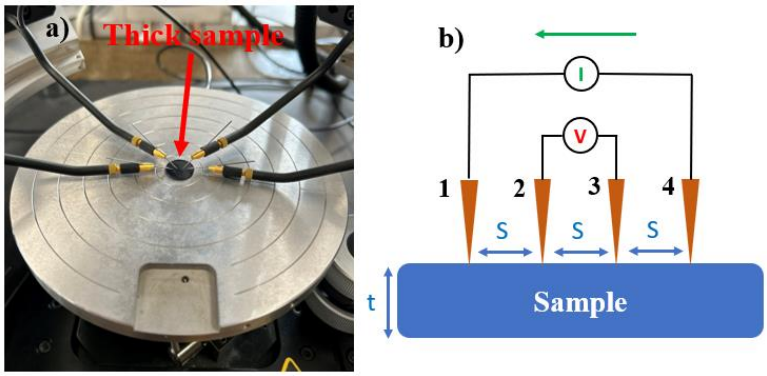

Figure 2.18. a) the experimental set-up, and b) schematic drawing of the 4-point collinear probe method.

The resistivity (ρ) is calculated as follows:

$$\rho = \frac{\pi}{ln2}\frac{V}{I}\,t\,F = 4.532\,\frac{V}{I}\,t\,F \qquad \text{(eq 2.13)}$$

where ρ is the resistivity (Ω cm), V is the voltage measured between probes 2 and 3 (V), I is the magnitude of the source current (A), t is the sample thickness (cm), and F is a geometrical correction factor.

Electrical conductivity (σ) is then defined as the reciprocal of resistivity, that is:

$$\sigma = \frac{1}{\rho} \qquad \text{(eq 2.14)}$$

The geometrical correction factor F depends on the thickness and surface area of the sample and the probe spacing. F is divided into 3 corrections factors as $F = F_1.F_2.F_3$. F_1 (eq. 2.15) is the factor related to the finite thickness (t) of the sample, F_2 (eq. 2.16) is related to the alignment of the probes near the edge of the sample, and F_3 (eq. 2.17) takes into account the finite lateral width of the sample [20].

$$F_1 = \frac{ln2}{ln\left\{\frac{\left[sinh\left(\frac{t}{s}\right)\right]}{\left[sinh\left(\frac{t}{2s}\right)\right]}\right\}} \qquad \text{(eq 2.15)}$$

$$F_2 = \left(1 + \frac{s}{2d+s} - \frac{s}{2d+2s} - \frac{s}{2d+4s} + \frac{s}{2d+5s}\right)^{-1} \qquad \text{(eq 2.16)}$$

$$F_3 = \frac{\ln 2}{\ln 2 + \ln\left\{\frac{\left[\left(\frac{d}{s}\right)^2 + 3\right]}{\left[\left(\frac{d}{s}\right)^2 - 3\right]}\right\}} \quad \text{(eq 2.17)}$$

In the present study, the resistance $\left(\frac{U}{I}\right)$ was measured by a 4-point collinear Cascade Microtech EP6 probe station (Süss Microtec) equipped with a Keithley 2635 source meter. The probe spacing was 2 mm and the geometry of the sample was a circle. For each sample, measurements were made with the probes placed in different positions (but centered with respect to the circular sample) and on both sides of the sample. In our case the correction factor F_1 varies from 0.9523 to 0.9896, while F_2 and F_3 are equal to 1 and 0.8297, respectively. Three samples were measured for each filler fraction, and the final value of resistivity is obtained by taking the mean value of all measurements.

4.2.3. Seebeck coefficient

Seebeck coefficient (also known as thermoelectric power) is an essential parameter to evaluate the nature and density of charge carriers and the potential thermoelectric performances as well. The principle is to measure a voltage difference (ΔV) induced by a small temperature gradient (ΔT) applied across the sample. The Seebeck coefficient is then calculated using the following equation:

$$S = -\frac{\Delta V}{\Delta T} \quad \text{(eq 2.18)}$$

In other words, ΔV is the voltage difference between the hot and cold sides of the sample and $\Delta T = T_{hot} - T_{cold}$.

In this work, the cross-plane Seebeck coefficient was measured with an in-house built device (Fig. 2.19). In this device, the samples are mounted between two 13 mm diameter aluminum discs, to which copper wires for voltage measurement and K-type thermocouples for temperature gradient ΔT measurement are connected. The two aluminum discs are crimped into brass blocks and clamped to each other with four plastic screws to ensure good contact. Each brass block is crossed by a heating cartridge controlled by an accurate homemade system (software + power supply). During the measurement, one block is kept at a constant temperature (25 °C), while the other one is heated in 0.5 °C increments from 25 °C up to 35 °C. The generated thermoelectric voltage ΔV is measured by a Keithley 2182 nanovoltmeter (Keithley Instruments Inc.). The Seebeck coefficient is derived from the slope of the ΔV vs ΔT curves by

linear fitting. The device was calibrated with well-known materials (Cu, Ni, Ag and Si) so that a $S_{circuit}$ = − 3.3 µV K^{-1} correction appears to be necessary in order to consider the contribution of copper wires and aluminum discs to the measured thermoelectric voltage.

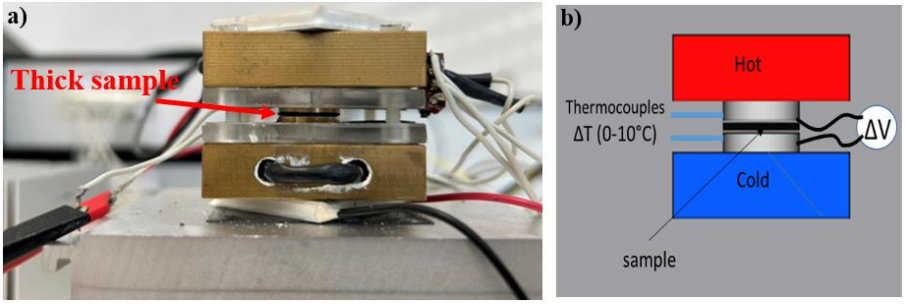

Figure 2.19. a) the experimental set-up, and b) schematic layout for the Seebeck coefficient measurement.

4.2.4. Figure of merit (cross-plane)

After obtaining all the values of thermal conductivity, electrical conductivity (cross-plane), and Seebeck coefficient, the figure of merit (cross-plane) for thick nanocomposites samples was calculated at room temperature (T = 300 K) using eq. 1.14 in Chapter I.

4.3. Thermoelectric properties for thin films (in-plane)

The thermoelectric figure of merit ZT of thin nanocomposites films, was measured using the TFA-Linseis Thin Film Analyzer (Linseis, Germany) (Fig. 2.20) within a temperature range of 25 to 125 °C. The VDP chips are put into a vacuum chamber pumped by a Pfeiffer HiCube pumping station reaching a vacuum below 5 x 10^{-4} mbar. Pumping is necessary to avoid radiation transfer with the air during the thermal conductivity measurement. The three measurements including electrical conductivity, Seebeck coefficient and thermal conductivity, are taken successively at each temperature level. It should be noted that most of the following is taken directly from the manual supplied by the manufacturer, Linseis.

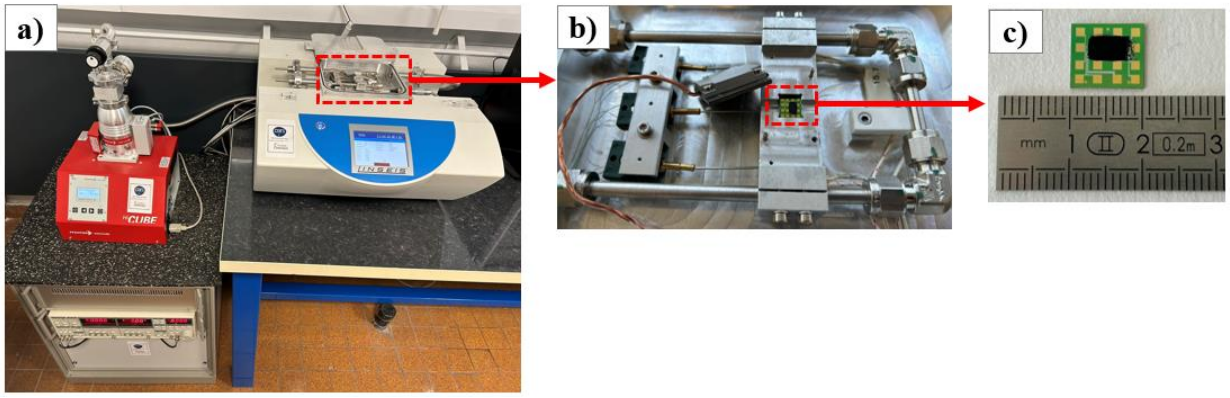

Figure 2.20. a) TFA - Thin Film Analyzer (Linseis, Germany), b) testing chamber, and c) VDP chip.

VDP chips are based on Si substrate passivated with a Al_2O_3 layer. The used electrodes and contact material are Platinum. The red area (Fig. 2.21) for solution deposition is 100 nm thin SiN membranes, which are used for the thermal conductivity and Seebeck coefficient measurements.

Pads 2, 4, 6, and 7 are used for Van-der Pauw (VDP) measurements (electrical conductivity) and are directly connected to the sample. The Seebeck coefficient is measured by the Pads 2, 8, 10, 11, 12. Finally, the Pads 13-18 are used for thermal conductivity. Detailed mechanism set-up and preparation of the VDP chip have been described in the work of Linseis [21].

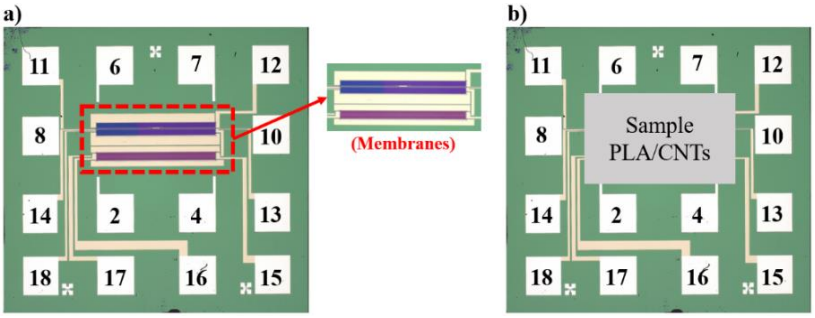

Figure 2.21. Schematic of Van-der Pauw chip before (a) and after (b) deposition.

4.3.1. Thermal conductivity (3-omega method)

The TFA is the only commercially available instrument that implements the so called 3-omega method (3ω method). Aside from thermo reflectance techniques (Time-domain or frequency-domain TDTR/FDTR), which are dedicated to thin films with thicknesses below 1 µm only, the 3-omega method is currently the most accurate technique to measure the thermal

conductivity of polymer films. It was first introduced by D.G. Cahill in 1987 [22] and since then many papers have been published, particularly on polymers [23].

We will give here the fundamentals of this technique, but for particulars of the specific implementation into the Linseis TFA, please refer to the paper of Vincent Linseis [24].

In this measurement, an AC current $I(t) = I_o * cos(\omega t)$ is applied to a metallic heating stripe, causing a rise in temperature of the membrane by the Joule effect. In fact, the power dissipated in a resistor is made up of a constant part P_{rms} and an alternating part $P_{AC}(t)$ (frequency 2ω). P_{rms} is responsible of the increase of temperature T_{DC} and P_{AC} induces oscillation in temperature (ΔT_{AC}) with $\Delta T = T_{DC} + \Delta T_{AC}(t)$ appears in the form of $\Delta T_{AC}(t) = \Delta T_0 cos(2\omega t + \varphi)$ where φ is the thermal phase (phase shift between P_{AC} power and temperature oscillations). Consequentially an oscillation in the resistance of the stripe occurs $R = R_0(1 + \beta \Delta T)$ at the angular frequency of 2ω, where R_0 is the initial resistance and β is the temperature coefficient resistance. By measuring the voltage drop across the heater, according to Ohm's law $V = RI$, one gets an amplitude modulated signal which has a small component at the third harmonic 3ω, which can be extracted with a lock-in amplifier. $V = RI$ results in:

$$V(t) = R_0 I_0 \left[(1 + \beta \Delta T_{DC}) cos(\omega t) + \frac{1}{2}\beta |\Delta T_{AC}| cos(\omega t + \varphi) + \frac{1}{2}\beta |\Delta T_{AC}| cos(3\omega t + \varphi) \right] \quad \text{(eq 2.19)}$$

The 3ω oscillation is then given by:

$$V_{3\omega} = \frac{1}{2} R_0 I_0 \beta |\Delta T_{AC}| \, cos(3\omega t + \varphi) \quad \text{(eq 2.20)}$$

By solving the 2D partial differential heat equation across the sample with regard to the given boundary conditions, the theoretical expression of $\Delta T_{AC} cos(3\omega t + \varphi)$ can be obtained and linearized, and appears as a function of P_{rms} and ω. The latter can then be extracted by fitting $|V_{3\omega}|$ as a function of ω with the appropriate equation [24]. It should be added that the only limitation for thermal conductivity measurement with the TFA, aside from the potential difficulties of deposition on the chips, is that the thermal conductance of the sample ($\kappa_{Sample} * T_{Sample}$) must be higher than 3 x 10^{-7} W K^{-1}, which is the thermal conductance of the membrane supporting the sample.

4.3.2. Electrical conductivity (Van-der-Pauw method)

In-plane electrical conductivity of thin films was measured by the Van der Pauw technique. In the measurement chip, this determination has been performed using contacts 2, 4,

6, 7 (see Fig. 2.21). The resistivity of the sample is measured by applying a current between two contacts and by measuring the voltage drop between the other contacts. After cyclic changing of the contacts, the measurement is repeated and the resistivity ρ can be calculated by solving the Van-der-Pauw formula (eq 2.21). To perform a good measurement, the sample surface must be closed and of homogenous thickness.

$$exp\left(-\frac{\pi d}{\rho}.R_{24,67}\right)+exp\left(-\frac{\pi d}{\rho}.R_{26,47}\right)=1 \qquad \text{(eq 2.21)}$$

Since the electrical conductivity (σ) is the reciprocal of resistivity, the conductivity can be easily obtained from the result eq. 2.14.

4.3.3. Seebeck coefficient

For measurement, a current will be applied to the heating stripe on the larger membrane, leading to temperature distribution along the membrane (Fig. 2.22). The temperature gradient causes a thermovoltage between the hot contact in the middle of the membrane and the cold contact located on the bulk silicon chip body. The temperature of the hot contact can be measured using the passivated resistance thermometer, which connects to Pads 8, 10, 11 and 12 (see Fig. 2.21). The cold temperature can be measured with a thermocouple, located in the sample holder.

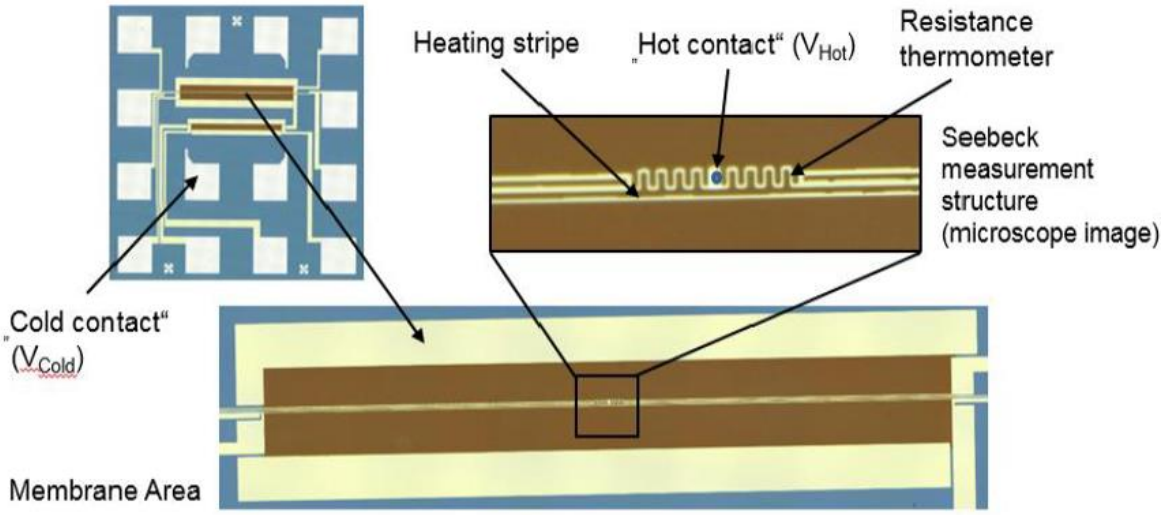

Figure 2.22. VDP chip setup with heater and resistance thermometer on the larger membrane [25].

The Seebeck coefficient is calculated using the classical formula:

$$S=\frac{-V_{Th}}{\Delta T}=\frac{-(V_{Hot}\ -\ V_{Cold})}{T_{Hot}-T_{Cold}} \qquad \text{(eq 2.22)}$$

4.3.4. Figure of merit

The in-plane ZT value for all samples was obtained directly from the TFA measurement. The experimental bar calculation for each value, including σ, κ, and S, are associated with errors of the equipment provided by the manufacturer which are ± 10 % for thermal conductivity (κ), ± 6 % for electrical conductivity (σ), and ± 7 % for Seebeck coefficient (S). The error bar for ZT values was calculated from the combination of these errors. The main advantage of this TFA device is that it can simultaneously measure the three quantities involved in the figure of merit: the experimental conditions are therefore identical.

References

1. Ruellan, A., Ducruet, V., Gratia, A., Saelices Jimenez, L., Guinault, A., Sollogoub, C., … Domenek, S. (2016). Palm oil deodorizer distillate as toughening agent in polylactide packaging films: Palm oil deodorizer distillate in PLA packaging films. *Polymer International*, *65*(6), 683–690. https://doi.org/10.1002/pi.5114

2. Vivien, B. (2021). Développement d'un multifilament biocompatible à résorbabilité contrôlée pour des structures textiles destinées à la croissance de cellules adipocytes dans le cadre du projet MAT(T)ISSE. *Centrale Lille*.

3. Barrau, S., Vanmansart, C., Moreau, M., Addad, A., Stoclet, G., Lefebvre, J.-M., & Seguela, R. (2011). Crystallization Behavior of Carbon Nanotube−Polylactide Nanocomposites. *Macromolecules*, *44*(16), 6496–6502. https://doi.org/10.1021/ma200842n

4. Zhang, J., Tashiro, K., Tsuji, H., & Domb, A. J. (2008). Disorder-to-Order Phase Transition and Multiple Melting Behavior of Poly(L-lactide) Investigated by Simultaneous Measurements of WAXD and DSC. *Macromolecules*, *41*(4), 1352–1357. https://doi.org/10.1021/ma0706071

5. Wang, L., Qiu, J., Sakai, E., & Wei, X. (2016). The relationship between microstructure and mechanical properties of carbon nanotubes/polylactic acid nanocomposites prepared by twin-screw extrusion. *Composites Part A: Applied Science and Manufacturing*, *89*, 18–25. https://doi.org/10.1016/j.compositesa.2015.12.016

6. Bouhamed, A., Kia, A. M., Naifar, S., Dzhagan, V., Müller, C., Zahn, D. R. T., … Kanoun, O. (2017). Tuning the adhesion between polyimide substrate and MWCNTs/epoxy nanocomposite by surface treatment. *Applied Surface Science*, *422*, 420–429. https://doi.org/10.1016/j.apsusc.2017.05.177

7. Bauer, J., Drescher, G., & Illig, M. (1996). Surface tension, adhesion and wetting of materials for photolithographic process. *Journal of Vacuum Science & Technology B: Microelectronics and Nanometer Structures Processing, Measurement, and Phenomena*, *14*(4), 2485–2492. https://doi.org/10.1116/1.588757

8. Risoluti, R., Gullifa, G., Carcassi, E., Masotti, A., & Materazzi, S. (2020). TGA/Chemometrics addressing innovative preparation strategies for functionalized carbon nanotubes. *Journal of Pharmaceutical Analysis*, *10*(4), 351–355. https://doi.org/10.1016/j.jpha.2020.02.009

9. Bai, L., Zhao, X., Bao, R.-Y., Liu, Z.-Y., Yang, M.-B., & Yang, W. (2018). Effect of temperature, crystallinity and molecular chain orientation on the thermal conductivity of polymers: a case study of PLLA. *Journal of Materials Science*, *53*(14), 10543–10553. https://doi.org/10.1007/s10853-018-2306-4

10. Kim, S. H., Mulholland, G. W., & Zachariah, M. R. (2009). Density measurement of size selected multiwalled carbon nanotubes by mobility-mass characterization. *Carbon*, *47*(5), 1297–1302. https://doi.org/10.1016/j.carbon.2009.01.011

11. Laurent, Ch., Flahaut, E., & Peigney, A. (2010). The weight and density of carbon nanotubes versus the number of walls and diameter. *Carbon*, *48*(10), 2994–2996. https://doi.org/10.1016/j.carbon.2010.04.010

12. Thomas, L. C. Modulated DSC® Paper #9 Measurement of Accurate Heat Capacity Values.

13. Mano, J. F. (2007). Structural evolution of the amorphous phase during crystallization of poly (l-lactic acid): A synchrotron wide-angle X-ray scattering study. *Journal of non-crystalline solids*, *353*(26), 2567–2572.

14. Stoclet, G., Seguela, R., Lefebvre, J. M., & Rochas, C. (2010). New insights on the strain-induced mesophase of poly(d,l-lactide): In situ WAXS and DSC study of the thermo-mechanical stability. *Macromolecules*, *43*(17), 7228–7237. https://doi.org/10.1021/ma101430c

15. Saito, Y., Yoshikawa, T., Bandow, S., Tomita, M., & Hayashi, T. (1993). Interlayer spacings in carbon nanotubes. *Physical Review B*, *48*(3), 1907–1909. https://doi.org/10.1103/PhysRevB.48.1907

16. Oh, M. O., & Kim, S. H. (2014). Conformational development of polylactide films induced by uniaxial drawing. *Polymer International*, *63*(7), 1247–1253. https://doi.org/10.1002/pi.4630

17. Monti, M., Armentano, I., Faiella, G., Antonucci, V., Kenny, J. M., Torre, L., & Giordano, M. (2014). Toward the microstructure–properties relationship in MWCNT/epoxy composites: Percolation behavior and dielectric spectroscopy. *Composites Science and Technology*, *96*, 38–46. https://doi.org/10.1016/j.compscitech.2014.03.008

18. Jonscher A. K. (1977). Review article - The 'universal' dielectric response. *Nature*, *267*, 673–679. https://doi.org/10.1038/267673a0

19. Kremer, F., & Schönhals, A. (Eds.). (2003). *Broadband Dielectric Spectroscopy*. Berlin, Heidelberg: Springer Berlin Heidelberg. https://doi.org/10.1007/978-3-642-56120-7

20. Miccoli, I., Edler, F., Pfnür, H., & Tegenkamp, C. (2015). The 100th anniversary of the four-point probe technique: the role of probe geometries in isotropic and anisotropic systems. *Journal of Physics: Condensed Matter*, *27*(22), 223201. https://doi.org/10.1088/0953-8984/27/22/223201

21. Linseis, V., Völklein, F., Reith, H., Nielsch, K., & Woias, P. (2018). Advanced platform for the in-plane *ZT* measurement of thin films. *Review of Scientific Instruments*, *89*(1), 015110. https://doi.org/10.1063/1.5005807

22. Cahill, D. G. (1990). Thermal conductivity measurement from 30 to 750 K: the 3ω method. *Review of Scientific Instruments*, *61*(2), 802–808. https://doi.org/10.1063/1.1141498

23. Al-Khudary, N., Cresson, P. Y., Orlic, Y., Coquet, P., Pernod, P., & Lasri, T. (2014). Measurement of the Thermal Conductivity of Polydimethylsiloxane Polymer Using the Three Omega Method. *Key Engineering Materials*, *613*, 259–266. https://doi.org/10.4028/www.scientific.net/KEM.613.259

24. Linseis, V., Völklein, F., Reith, H., Woias, P., & Nielsch, K. (2016). Platform for in-plane *ZT* measurement and Hall coefficient determination of thin films in a temperature range from 120 K up to 450 K. *Journal of Materials Research*, *31*(20), 3196–3204. https://doi.org/10.1557/jmr.2016.353

25. Linseis. Instruction Manual - TFA. *Product instruction*, *Version 1.1*.

Chapter III. Thermoelectric properties of bulk PLA/MWCNT nanocomposites

1. Introduction

The aim of chapter 3 is focused on discussing the relationships between the elaboration processes, structure and cross-plane thermoelectric properties of thick discs of PLA/CNT nanocomposites at room temperature. For that, A-PLA and Sc-PLA were chosen as the polymer matrix and multi-walled Carbon Nanotube (referred as CNT in this chapter) was selected as filler.

In the first part of this chapter, thick discs of PLA/CNT nanocomposites with various CNT content will be prepared by using two elaboration processes including melt-blending (up to 10 wt%) and solution mixing (up to 40 wt%), and then the influence of these elaboration processes on the cross-plane thermoelectric properties at room temperature will be examined. Then, the impact of the polymer structure (amorphous/semi-crystalline) on the thermoelectric properties will be explored. Finally, the anisotropy of the electrical conductivity (σ) and figure of merit (ZT) of thick discs of PLA/CNT nanocomposites will be investigated and discussed. All these results are presented in the form of a publication.

With the expect to improve the dispersion of CNT in the PLA matrix, thick discs of A-PLA/CNT nanocomposite (2 wt%) will be prepared through a combination of solution mixing and melt-blending elaboration processes. The results are presented in the second part of this chapter. In particular, the cross-plane thermoelectric properties of these samples will be compared with those of samples elaborated from the melt-blending or the solution mixing processes.

In the third part, the influence of CNT orientation on the electrical conductivity of thick discs of PLA-based nanocomposites containing 2 and 5 wt% CNT will be investigated at room temperature.

Finally, thick discs of Sc-PLA/CNT nanocomposites will be prepared and their thermoelectric properties will be investigated. The results will be compared with those obtained for A-PLA/CNT samples.

2. Publication

In-plane vs cross-plane electrical conductivity of Poly(lactic acid)/multi-walled carbon nanotubes: impact on thermoelectric properties

Van-Hau VO LE, Corinne BINET, Jean-François TAHON, Jean-François BRUN*, Valérie GAUCHER

Univ. Lille, CNRS, INRAE, Centrale Lille, UMR 8207 - UMET - Unité Matériaux et Transformations, F-59000 Lille, France

Email:* Jean-Francois.brun@univ-lille.fr

Keywords: electrical conductivity, organic thermoelectrics, polymer nanocomposites, carbon nanotubes

Abstract:

In this work, the influence of the elaboration process, the crystallinity of the polymer matrix and the direction of measurement on the thermoelectric (TE) properties of thick and thin films of poly(lactic acid)/multi-walled carbon nanotubes nanocomposites (PLA/CNT) was investigated at room temperature. Two industrial grades of PLA were used: an amorphous one (A-PLA), and a semi-crystalline one (Sc-PLA). Thick nanocomposite discs, filled with various amount of carbon nanotubes, were prepared by melt-blending (up to 10 wt% CNT) and solution mixing (up to 40 wt% CNT) and the cross-plane TE properties were studied. It appears that the elaboration process and the structure of the PLA (amorphous or semi-crystalline) have no significant impact on the TE properties. In addition, thin films of PLA/CNT nanocomposites, with the same filler content as thick discs, were prepared by drop-casting on dedicated electronic chips and the in-plane TE properties were measured by a thin film analyzer. In-plane values of electrical conductivity (σ) and figure of merit (ZT) appeared 100 to 1000 times higher than those obtained from cross-plane measurements, revealing a strong anisotropy of electrical conductivity. By contrast, the thermal conductivity and the Seebeck coefficient show only slight differences between in-plane and cross-plane values. In both cases, the thermal conductivity exhibits a linear increase with the addition of CNT. The Seebeck coefficient (S) values have positive signs for all nanocomposites demonstrating a p-type semiconducting behavior; besides, these values decreased as increasing the content of fillers and do not seem to be dependent on the thickness of samples either. The highest achieved ZT in this work was 1.2×10^{-4} for thin films with 40 wt% of MWCNT, which is the best ZT value that can be found in the literature for reinforced thermoplastic filled with multi-walled carbon nanotubes.

2.1. Introduction

Thermoelectrics are semiconducting materials that can be used to convert heat directly into electricity. Devices based on these materials can use any heat source but are now expected to harvest and convert waste heat. The thermoelectric performance of a material is generally evaluated by the dimensionless figure of merit $ZT = \frac{\sigma S^2}{\kappa} T$, which depends on the electrical conductivity (σ), the thermal conductivity (κ), the Seebeck coefficient (S), and the temperature (T). Therefore, thermoelectric materials should exhibit a good electrical conductivity, a high Seebeck coefficient, and a low thermal conductivity, in order to reach a ZT as high as possible at a given temperature.

Nowadays, the most efficient thermoelectric materials are inorganic semiconductors and metal alloys such as skutterudites (e.g. $CoSb_3$), telluride-based materials (e.g. PbTe, Sb_2Te_3, Bi_2Te_3), rare earth chalcogenides (e.g. La_3Te_4), copper ion liquid-like materials (e.g. Cu_2Se),…[1]. In particular, for near-ambient temperature applications, only bismuth telluride (Bi_2Te_3) and its derivatives, with a ZT higher than 1, are enough competitive and widely used as thermoelectric materials [2]. However, due to its potential toxicity, and its scarcity, this class of materials is limited to specific applications [3]. Organic thermoelectrics are commonly based either on intrinsically conducting polymers (ICPs), such as poly(3,4-ethylenedioxythiophene): poly(styrenesulfonate) (PEDOT:PSS), polyaniline (PANI), poly(3-hexylthiophene) (P3HT) and their derivatives, or polymers (conducting or insulating) filled with conductive nanoparticles, such as carbon nanotubes (CNT), graphene, or metallic nanoparticles [4–8]. Composites with insulating polymer matrix and conductive fillers have received much attention in recent years, as the low thermal conductivity of the matrix and the potentially high electrical conductivity of the fillers can enable the development of high-performance flexible thermoelectric materials.

Poly(lactic acid) (PLA) is one of the most promising polymer to replace conventional petroleum-based plastics. It is an aliphatic thermoplastic polyester derived from renewable and biodegradable resources. It is synthesized from lactic acid ($C_3H_6O_2$) by direct condensation polymerization or more commonly by ring-opening polymerization of lactide which allows to produce high molecular weight PLA. Its degradation products are non-pollutant and non-toxic. This polyester is used in various applications such as packaging, biomedical and tissue engineering fields [9]. As lactic acid is an enantiomeric molecule with two stereoisomers (L- and D- lactide), different homopolymers (PLLA, PDLA) and random copolymer (PDLLA) grades can be obtained. Depending of the L/D ratio, random copolymers are able or not to

crystallize. Typically, it has been shown that PDLLA holding higher than 10 % of D content are amorphous. At a concentration less than 10 % of D, PDLLA is able to crystallize but its crystallization kinetics are slow. Like most thermoplastics, PLA has a low thermal conductivity ($\kappa \approx 0.1 - 0.5$ W m^{-1} K^{-1} [10]) and is electrically insulating with a very low electrical conductivity ($\sigma \approx 1 \times 10^{-12}$ to 10^{-15} $S.m^{-1}$ [11, 12]).

To improve the intrinsic properties of polymers and extend their field of application, the addition of nanofillers represents an interesting way, particularly for enhancing the thermo-mechanical properties as well as for providing additional functionalities. In this context, nanocomposites based on PLA filled with multi-walled carbon nanotubes (CNT) have been widely studied, for mechanical reinforcement, thermal and electrical performance [13–15], but much less for thermoelectric applications [16].

CNT possess great mechanical strength [17], and electrical conductivity [18] which is a potential candidate to reinforce PLA for thermoelectric performance. The effectiveness of CNT depends on both their inherent properties and their morphological characteristics such as their dispersion and orientation into the polymer matrix. Since CNT usually form aggregates/bundles due to Van der Waals interactions, obtaining a homogenous dispersion in a viscous polymer is quite difficult. Therefore, how to control and improve the dispersion of CNT is one of the biggest challenges in the preparation of nanocomposite. To obtain the dispersion of CNT in PLA matrix, the most two common methods frequently used are melt blending and solution mixing. Melt blending is a highly scalable, and economically appealing process for creating nanocomposites. There have been many reports using this method to prepare and characterize the properties of PLA nanocomposites reinforced with CNT [19–22]. In this method, the CNT are directly incorporated into the molten polymer, and the dispersion state of CNT can be optimized by varying mixing speed, time, and temperature parameters. However, the main disadvantages of this method are the limitation of the fillers content and usually the low dispersion degree of CNT in the polymer matrix due to the viscosity increase during operation. The second process, the solution mixing, allows to increase the filler content and usually improve the dispersion of CNT in the matrix phase [14, 23–25]. This user-friendly efficient method usually involves three main steps: dispersing the CNT in a suitable solvent by mechanical stirring and/or sonication, then dissolving the polymer in the previous dispersion while stirring appropriately, and finally removing all the remaining solvent from the nanocomposites. Each method can bring both advantages and disadvantages in preparing

nanocomposites, and to the best of our knowledge, no researchers have compared the impact of the elaboration process on the thermoelectric properties, especially for composite PLA/CNT.

The orientation of CNT into the sample is also an important parameter to consider, especially for electrical conductivity (σ). The use of electrical and magnetic fields, as well as tape casting, technique involving shear forces, are different methods inducing CNT alignment. In the case of elaboration of polymer/CNT nanocomposite films using the doctor blade technique, some authors have shown a huge increase (x 10^6) of the electrical conductivity in the direction of alignment of CNT compared to that of the composite with random oriented nanotubes. This effect is less marked at high nanotubes concentration [26]. To explain this electrical conductivity anisotropy, the authors suggest the creation of more junctions or contacts between nanotubes resulting in the formation of more conducting channels on the polymer matrix in the direction of the nanotube alignment. Others authors have also observed differences between the surface and bulk electrical conductivities for nanocomposites prepared by solution mixing followed by a hot-pressing step [27, 28]. All these studies show that the anisotropy of σ values is a critical issue that can have a significant impact on the final ZT value.

In addition to the dispersion and orientation of the nanofillers within the matrix, some works have shown that for semi-crystalline matrix, the structure of the polymer could also have an impact on the electrical and thermal conductivities as well as on the Seebeck coefficient. For example, the work of Brun *et al.* [27], focused on poly(vinylidene fluoride)/multi-walled carbon nanotubes (PVDF/CNT) composites, has revealed that the polar γ-phase of PVDF induces a 30 % increase in the Seebeck coefficient compared to the same nanocomposite with PVDF crystallized in a non-polar form. Wang *et al.* [29] observed an increase in electrical conductivity and a reduction in the electrical percolation threshold for polypropylene (PP)/CNT nanocomposites by crystallizing the PP matrix under controlled cooling conditions. Furthermore, Huang *et al.* [18] have reported that electrical conductivity of PLA/CNT composites was enhanced by increasing the crystallinity in PLA matrix for CNT fillers content lower than percolation threshold ($\Phi_c \approx 0.73$ wt%). Most of works dealing with the issue of the impact of crystallinity has focused on composites with CNT content in a range close to the percolation threshold. To our knowledge, few studies only have focused on the aforementioned investigation at CNT content much higher than the percolation threshold.

In the current work, the thermoelectric properties of PLA/CNT nanocomposites, prepared by melt-blending and solution mixing processes, are reported. The cross-plane thermoelectric properties will be fully investigated and discussed for both amorphous and semi-crystalline

thick discs of PLA/CNT samples. A strong anisotropy of the electrical conductivity is evidenced by measuring the in-plane electrical conductivity at the surface of the thick discs and the complete thermoelectric figure of merit of thin films by drop-casting from the same solution.

2.2. Experimental

2.2.1. Materials

Both commercial amorphous PLA grade (4060D) referred to A-PLA and semi-crystalline PLA grade (6202D) referred to Sc-PLA were purchased from NatureWorks LLC. Theirs corresponding weight average molecular weights (M_w) are 240 000 g mol^{-1} and 234 000 g mol^{-1}. Multi-walled carbon nanotubes (CNT) produced from the catalytic chemical vapor deposition (CCVD) process were obtained from Nanocyl (Nanocyl 7000 series, Belgium). The length and average diameter were 1.5 µm and 9.5 nm, respectively. The purity was about 90 wt%, and the CNT were used without purification. Chloroform ($CHCl_3$) was purchased from Sigma-Aldrich.

2.2.2. Elaboration processes

2.2.2.1. Thick discs of PLA/CNT nanocomposites

Melt-blending was used to prepare nanocomposites PLA/CNT as the first elaboration process. Dry-mixed PLA pellets and CNT were extruded by using a twin-screw extruder (Thermo Scientific Process 11 Parallel Twin-Screw Extruder). The adjusted temperature profile along the melting zone was from 190 to 210 °C (from the feed zone to the die one), and the weight fraction of CNT was 2, 5, and 10 wt%. The obtained final materials were cut into small pellets for the next steps.

Solution mixing procedure was employed as a second protocol to prepare PLA/CNT nanocomposites containing 2, 5, 10, 20, 30, and 40 wt% of CNT. In this procedure, CNT was first dispersed in $CHCl_3$ by tip-ultrasonic at room temperature. Since CNT form stabilized bundles, different conditions were processed to investigate the dispersion of CNT in $CHCl_3$ by tip-ultrasonic and the optimum condition being used in this step is at 20 % of maximum amplitude, during 15 seconds (maximum power: 200W). PLA pellets were then dissolved in solution of CNT, the mass ratio of (PLA/CNT)/$CHCl_3$ was 1:20 (weight to weight). Finally, the solution was magnetically stirred at 40 °C, for 12 h. To allow solvent evaporation, the obtained solutions were poured into a silicon mold and left at room temperature under atmospheric pressure for 12 h. The residual solvent was removed by placing the nanocomposites in a vacuum oven at 120 °C for 8 h. The duration of this thermal treatment has been established after

monitoring the evolution of the glass transition temperature as a function of time. It is assumed that all residual solvent is removed from the sample as soon as T_g is constant.

After obtaining the final products from melt-blending and solution mixing processes, thick PLA/CNT discs of 13 mm-diameter were thermo-compressed at 210 °C, under 50 bars using a cooling rate of about - 15 °C min^{-1} (fast cooling conditions). For the sake of comparison, thick discs of pristine PLA were elaborated under similar conditions to ensure an identical elaboration history. The thickness of all thick discs was about 500 µm.

To study the impact of PLA crystallinity on the thermoelectric properties, two thermal treatments were used to induce crystallinity in Sc-PLA/CNT containing 2 and 5 wt% CNT. The former was an annealing of the thermo-compressed samples at 120 °C during 60 min. This annealing conditions were used according to the literature [30, 31]. The latter thermal treatment was a slow-cooling from the melt state to room temperature (cooling rate of about - 1 °C min^{-1}). For sake of comparison, pristine Sc-PLA samples were also processed using the two processes previously described.

2.2.2.2. Thin films of PLA/CNT nanocomposites

Thin films of A-PLA/CNT nanocomposites were prepared by drop casting method on special chips produced by Linseis [32]. The solutions were prepared using the same protocol as described previously for thick discs. Before solution deposition, the surface of the chip was cleaned using a plasma treatment (argon atmosphere during 10 min). The quantity of solution for each chip is between 6 and 10 µl. The final chips were then dried in the oven under vacuum at 120 °C, during 60 min to remove all residual solvents before testing in the Thin Film Analyzer (TFA) chamber. The thin films thickness determined by a stylus profilometer, was in the range 15 to 20 µm.

2.2.3. Morphology and structure of the nanocomposites

The morphology of PLA/CNT nanocomposites was observed by field emission scanning electron microscopy (FE-SEM) using a JEOL 7800F apparatus operating at an acceleration voltage of 3 kV and low current to reduce beam damage. All the samples were cryo-fractured after immersion in liquid nitrogen and the surface was sputter coated with carbon coating to prevent electrical discharge during observation.

The experimental weight content of CNT (wt%) of each nanocomposite was determined by TGA (Thermogravimetric Analyzers TA Discovery – TA instruments). This experiment was processed under nitrogen flow, from 25 to 850 °C with a heating rate of 10 °C min^{-1}. At least

three samples for each composition were measured. The weight fraction of CNT was determined as the weight remaining at 550 °C, *i.e* far above the PLA degradation temperature which is around 380 °C. As necessary, the CNT amount can be converted into volume fraction using the following relation:

$$\Phi_{CNT} = \frac{\rho_{nanocomposite}}{\rho_{CNT}} . w_{CNT} \quad (1)$$

where Φ_{CNTs} is the volume fraction of CNT, $\rho_{nanocomposite}$ and ρ_{CNT} are the density of nanocomposite and CNT, respectively, w_{CNT} is the weight fraction of CNT in nanocomposite. The density ($\rho_{nanocomposite}$) of each sample was determined with a precision scale thanks to a kit for density measurement: the sample was initially weighed in air, and then immersed into ethanol (Fluka, purity ≥ 99.8 %, density = 0.79 g cm^{-3}); the density was calculated by applying the Archimedes' principle, and the detailed values are presented in Table S1 (supplementary document). The density determination of CNT was explained in a supplementary document, and the value was 1.24 ± 0.01 g cm^{-3}.

Thermal characterization was performed on a DSC Q20 (TA instruments) and the thermograms was recorded during the first heating from 10 to 200 °C with a constant heating rate of 10 °C min^{-1}. The glass transition temperature, T_g, was taken at the inflexion point of the heat capacity change; the melting point, T_m, and the cold crystallization temperature, T_{cc}, refer to the maximum of the endotherm peak and the minimum of the exotherm peak respectively. The degree of crystallinity χ_c of pristine Sc-PLA and nanocomposites Sc-PLA/CNT were determined by the following equation:

$$\chi_c = \left[\frac{(\Delta H_m - \Delta H_{cc})}{\Delta H_m^0 . (1 - w_{CNT})}\right] \quad (2)$$

where ΔH_m is the melting enthalpy during the heating process, ΔH_{cc} is the enthalpy of cold crystallization, ΔH_m^0 is the enthalpy of melting of 100 % crystalline PLA, which is 93 J g^{-1} [31], and w_{CNT} is the CNT weight fraction.

The structure of nanocomposites was also investigated by wide-angle X-ray scattering (WAXS). WAXS experiments were performed in transmission mode at room temperature on a Xeuss 2.0 (Xenocs) operating under vacuum with a GeniX3D microsource (λ = 1.54 Å) at 0.6 mA and 50 kV and a 2D Pilatus 3R 200 K detector. The sample-to-detector distance was 121 mm.

2.2.4. Thermoelectric properties measurements for thick discs

All thermoelectric measurements for thick discs were performed through the sample thickness at room temperature. The same samples (13 mm-diameter discs) were used for electrical, thermal conductivities, and Seebeck coefficient measurements. At least three samples of each composition were measured to ensure reproducibility.

Broadband dielectric spectroscopy (BDS) was used to measure the cross-plane electrical conductivity. BDS measurements were carried out using a ModuLab-MTS impedance analyzer (Solartron Analytical, Ametek) in the frequency range from 0.1 to 10^6 Hz. The amplitude of the applied sinusoidal voltage was 1 V. The complex dielectric permittivity $\varepsilon^*(f) = \varepsilon'(f) - i\varepsilon''(f)$ is linked to the complex conductivity by $\sigma^*(f) = i2\pi f\varepsilon^*(f) = \sigma' + i\sigma''$. The static electrical conductivity σ_{DC} is extrapolated from the real part of the complex conductivity calculated with $\sigma' = 2\pi f\varepsilon''$ and σ_{DC} corresponds to the plateau value from the low frequency side of $\sigma'(f)$ [33].

To compare both cross-plane and in-plane electrical conductivities, a 4-point collinear probe (Süss MicroTec + Keithley 2635 source meter) was used to measure the in-plane electrical conductivity at the sample surface. This method involves applying a direct current to the material while measuring the produced voltage across the surface sample. The slope of the current-voltage characteristic and corrective factors were used to obtain the resistivity and the reverse gives the in-plane conductivity of the samples [34].

The cross-plane thermal conductivity (κ) of the samples was calculated using the formula (3):

$$\kappa = \alpha\rho C_p \tag{3}$$

where α is the thermal diffusivity ($mm^2\ s^{-1}$), ρ is the density ($g\ cm^{-3}$) and C_p the specific heat capacity ($J\ g^{-1}\ °C^{-1}$). A Netzsch light flash device LFA 467 HyperFlash (Netzsch-Gerätebau GmbH) was used to measure thermal diffusivity (α). In this technique, a light pulse generated by a xenon flash lamp heats the lower side of a plane-parallel sample while an infrared (IR) detector measures the increases of the temperature resulting at on the upper side. The thermal diffusivity is then calculated using an optimization method: in this work, all measured curves were perfectly fitted by a Cowan model with a pulse correction. In contrast to the nanocomposites, for which no dusting was necessary due to the CNT' excellent light absorption, the pristine PLA sample required a small dusting of graphite paint on both sides.

Density has been measured by Archimedes' principle as previously described.

Specific heat capacity (C_p) was performed from DSC measurements using a Modulated DSC Q2000 (TA Instruments). After calibration with sapphire, the C_p of samples (weight around 15 mg) was determined at 26.85 °C.

The cross-plane Seebeck coefficient (or thermoelectric power in V K^{-1}) was measured with an in-house built device, already described in [27].

Finally, the cross-plane figure of merit (ZT) was calculated at T = 300 K as follows: $ZT = \frac{S^2\sigma}{\kappa}T$, using all cross-plane values.

2.2.5. Thermoelectric properties measurements for thin films

Thermoelectric properties of thin films, including Seebeck coefficient (S), electrical conductivity (σ), thermal conductivity (κ), and figure of merit (ZT) were measured using Thin Film Analyzer (TFA, Linseis, Germany).

In the TFA, the in-plane electrical conductivity and the in-plane thermal conductivity are determined by the Van-der-Pauw and the 3-omega methods, respectively. For the Seebeck coefficient, the measurement of the thermovoltage at different temperature gradients is used to calculate $S = -\frac{V_{th}}{\Delta T}$. Details of the operation mechanism for TFA have been described in the work of Linseis *et al.* [32].

The error of the equipment provided by the manufacturer which is ± 10 % for thermal conductivity, ± 6 % for electrical conductivity, and ± 7 % for Seebeck coefficient. The error bar for ZT values was calculated from the combination of these errors.

2.3. Results and discussion

2.3.1. The influence of elaboration processes on thermoelectric properties of thick discs of A-PLA/CNT nanocomposites

The dispersion of CNT in the A-PLA matrix for all elaboration processes was investigated by SEM observations. Fig. 1 a-d and 1 e-h show the micrographs of the cross-sectional area of nanocomposites, with 2 wt% and 10 wt% of CNT for samples from melt blending, and with 2 wt% and 40 wt% for samples from solution mixing, respectively. For the lowest CNT concentration, both isolated and bundles of CNT are observed at high magnification, whatever the elaboration process. This may be surprising considering that a better CNT dispersion is usually expected for the solution process [35]. This indicates that the elaboration conditions used in this study are not sufficient to break or prevent the Van der Waals interactions between CNT, leading to the presence of CNT aggregates in the matrix, even in the case of the solution

process. At higher concentration, the dispersion of CNT within the PLA matrix is homogenous at a few micrometer scales and no difference is evidenced between the elaboration process.

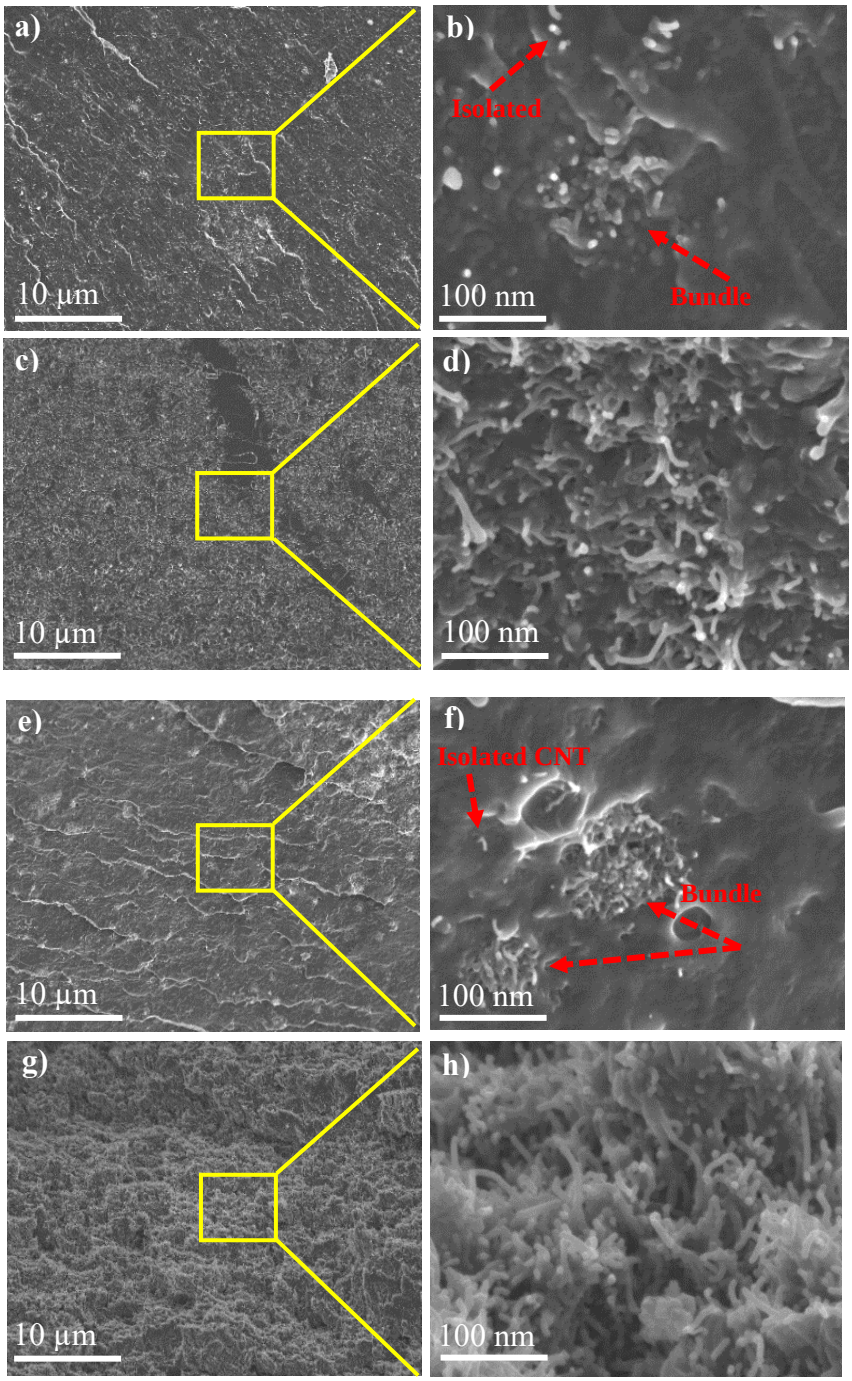

Figure 1. SEM images of cross-section samples from melt-blending process with a-b) 2 wt%, c-d) 10 wt% of CNT and from solution mixing process with e-f) 2 wt% CNT, g-h) 40 wt% CNT.

The weight fractions (wt%) of CNT determined by TGA are reported in Table 1. The measured CNT weight ratios are in agreement with the expected values. In the following, the

thermoelectrical properties will be presented as a function of the actual content of CNT. Regarding the thermal transition, whatever the CNT content, all nanocomposites display the same glass transition temperature around 55 ± 2 °C, similar to pristine PLA. For more details, thermograms are presented in supporting information (Fig. S2). Literature has already reported several studies in which the T_g of PLA is not influenced by the presence of CNT [31, 36, 37] or other nanofillers such as Halloysite nanotubes [38] even at high concentrations. This suggests that there is poor interfacial interaction between CNT and PLA.

Table 1. Experimental content (wt%) of CNT in each nanocomposite at 550 °C with A-PLA matrix obtained from TGA analysis. The number in italic is the corresponding volume fraction (vol%).

Samples	**2 wt%**	**5 wt%**	**10 wt%**	**20 wt%**	**30 wt%**	**40 wt%**
Melt-blending	2.1 ± 0.4 *(1.5 ± 0.3)*	4.8 ± 0.5 *(3.5 ± 0.4)*	9.6 ± 0.1 *(7.1 ± 0.1)*			
Solution mixing	2.0 ± 0.3 *(1.4 ± 0.2)*	4.8 ± 0.3 *(3.5 ± 0.2)*	9.8 ± 0.4 *(7.2 ± 0.3)*	22.8 ± 1.7 *(17.3 ± 1.3)*	29.7 ± 2.6 *(23.3 ± 2.1)*	43.3 ± 2.5 *(35.2 ± 2.1)*

The cross-plane thermoelectric properties (σ, κ, S, and ZT) of thick A-PLA/CNT discs as a function of CNT content are presented in Fig. 2 at room temperature for both elaboration processes.

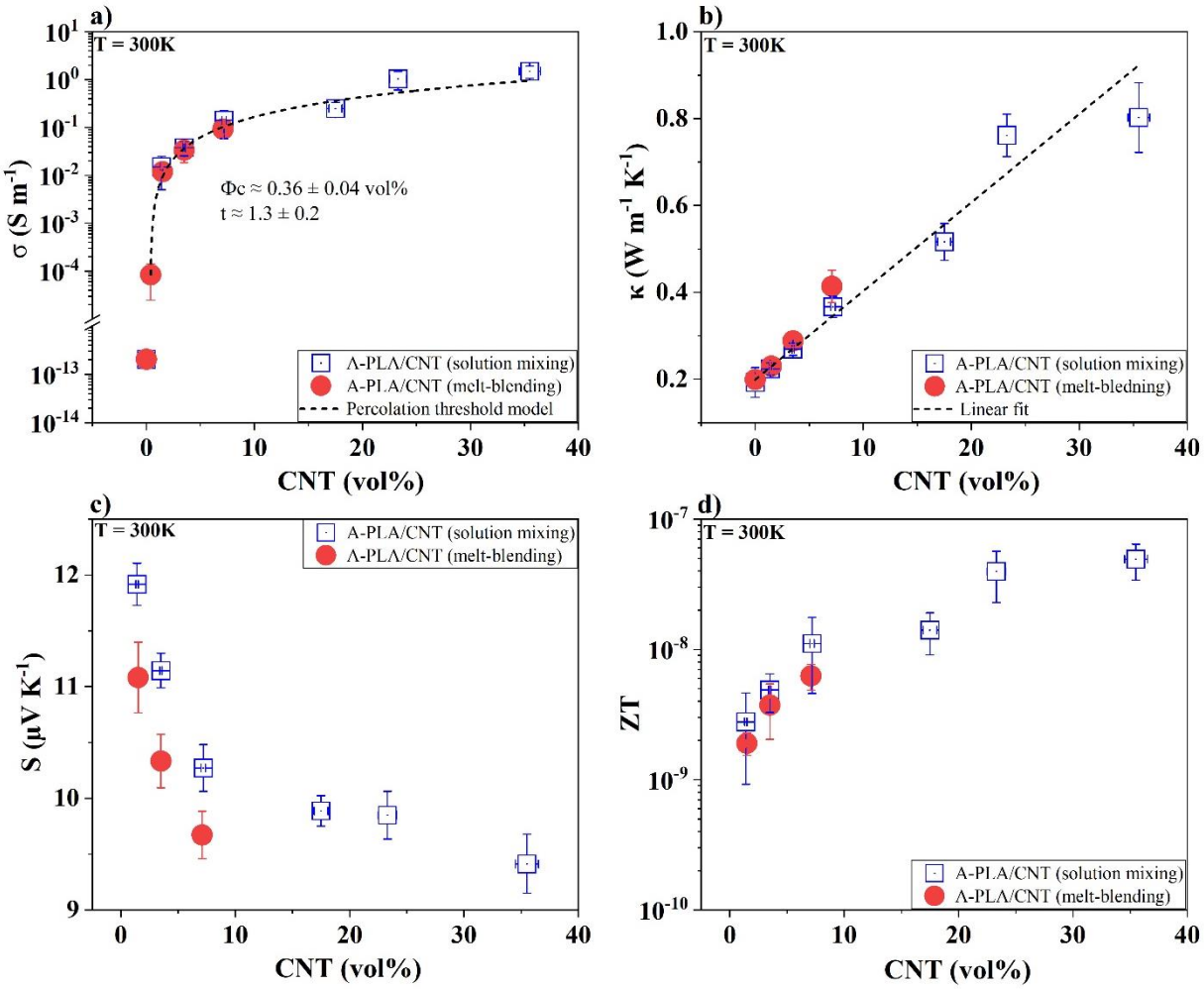

Figure 2. Cross-plane thermoelectric properties as a function of CNT volume fraction. a) electrical conductivity (σ), b) thermal conductivity (κ), c) Seebeck coefficient (S), and d) figure of merit (ZT).

As expected, while pristine PLA is electrically insulating (2.0 x 10^{-13} S.m^{-1}), an increase of σ of about 13 orders of magnitude is observed with the addition of CNT. The electrical conductivity is 1.5 x 10^{-2} S m^{-1} for sample with 2 wt% of CNT and reach a value of 1.5 S m^{-1} for sample with 40 wt% (Fig. 2a). These values are much higher than those obtained by Ivanov *et al.* [39] for composites prepared by a melt-blending process (σ = 7.86 x 10^{-4} S m^{-1} at 3 wt% of MWCNT). However, they are lower than those obtained by Antar *et al.* [16] (σ = 1.15 x 10^{2} S m^{-1} at 18 vol% ≈ 22 wt% of CNT) for samples elaborated by melt-blending and thermocompression. By comparing with the values in Table 3, the obtained cross-plane electrical conductivity values are of the same order of magnitude to the other polymer/CNT nanocomposite. According to the electrical conductivity level, the nanocomposites can be considered as semi-conductor. It can be seen that for a given CNT content, the electrical

conductivity values are similar whatever the elaboration process, in accordance with the morphological observations.

The percolation theory model was used to explain the nanocomposite electrical response as a function of CNT fraction. This model predicts that a critical concentration is required for the formation of an effective conductive network into the composite, changing it from an insulator to a conductor. The equation that describes this theory is:

$$\sigma_{nanocomposite} = \sigma_{CNT}(\Phi_{CNT} - \Phi_c)^t \; for \; \Phi_{CNT} > \Phi_c \quad (4)$$

where Φ_{CNT} is the volume fraction of CNT (vol%) and Φ_c is the percolation volume fraction (vol%), σ_c and σ_{CNT} (S m^{-1}) are the electrical conductivities of nanocomposite and CNT respectively, t is the critical power law exponent which depends on the dimensionality of the network, t ~ 1.3 and t ~ 2 corresponding to two- and three-dimensional percolation systems, respectively [40, 41]. Due to the pretty similar values in electrical conductivity from the two elaboration processes and only few data at low CNT concentration, only one percolation threshold curve has been fitted for all samples and the obtained threshold concentration is 0.36 vol% (0.44 wt%). The nanocomposites from this work have a threshold concentration lower than that obtained in the work of Huang *et al*. [18] which was 0.73 wt% CNT in the case of PLA/CNT. This shows that the two elaboration processes allow to obtain a rather good CNT dispersion inside the PLA matrix. Note that Faraguna *et al.* [35] clearly showed the difference between melt and solution blending in the case of polystyrene (PS)/CNT nanocomposites. Indeed, they found a lower percolation threshold (0.15 wt%) for samples prepared by solution mixing than for samples by melt-blending process (0.50 wt%). In the present study, we are unable to distinguish the two processes regarding their ability of CNT dispersion because we have no specific studies around the percolation threshold and the lowest CNT concentration is far above the percolation threshold.

The cross-plane thermal conductivity is shown in Fig. 2b as a function of CNT volume fraction. A linear increase of κ is observed, from 0.19 W m^{-1} K^{-1} for pristine PLA to 0.80 W m^{-1} K^{-1} for samples with 40 wt% CNT. These values are close to those already reported for PLA/MWCNT nanocomposites which mostly range between 0.2 – 1.0 W m^{-1} K^{-1} [16, 39]. At low concentrations (from 2 to 10 wt% CNT), the thermal conductivity values of samples from the two elaboration processes are pretty similar. Besides, PLA/CNT nanocomposites have thermal conductivity values almost one order of magnitude lower than the thermal conductivity of pristine 3D bulk multi-walled CNT, which is approximately 3.0 W m^{-1} K^{-1} [42]. In semi-conductor, thermal transport mechanisms come from both lattice thermal conductivity (phonon)

and charge carrier thermal conductivity. The well-known Wiedemann-Franz law, $\kappa_e = L\sigma T$, give the link, at the temperature T, in metals, between the thermal and the electrical conductivity due to electrons ($L = 2.44\ 10^{-8}\ V^2K^{-2}$ is the Lorentz constant) [43]. In our case, for the sample with 40 wt% CNT at 300 K, it leads to $\kappa_e = 1.1\ x\ 10^{-5}\ W\ m^{-1}\ K^{-1}$, which demonstrates that the contribution of electrons (more exactly holes in the present case of a p-type semi-conductor) is far negligible in front of the contribution of phonons. Some authors have claimed that the thermal conduction of 3D bulk CNT materials is mostly dominated by the lattice thermal conductivity [42]. The low thermal conductivity of PLA/CNT nanocomposites, even at very high concentration, may be due to phonon scattering occurring at the CNT-CNT and CNT-polymer interfaces which shortens the mean free path of phonons and hence the thermal conductivity.

The value of the cross-plane Seebeck coefficient (Fig. 2c) shows a decrease when the content of CNT is increased, from 11.9 µV K^{-1} (2 wt%) down to 9.4 µV K^{-1} (40 wt%) for solution mixing samples and 11 µV K^{-1} (2 wt%) down to 9.6 µV K^{-1} (10 wt%) for melt-blending samples. This drop is in accordance with the empirical trend generally observed in thermoelectric materials considering that the Seebeck coefficient is mostly dependent on the concentration of charge carriers and the Fermi level [44, 45]. In addition, all Seebeck values are positive, meaning that the majorities of charge carriers are holes, which is consistent with the known p-type semiconducting behavior of multi-walled CNT bundle. These values are consistent and close to those already reported for polymer/MWCNT nanocomposites which mostly range between 9 and 14 µV K^{-1} [16, 46].

Finally, the dimensionless figure of merit (ZT) has been calculated at 300 K and values are reported as a function of CNT volume fraction in Fig. 2d. As expected, the values continuously increase with CNT content, and with a maximum of 4.9 x 10^{-8} obtained, at 300 K, for samples containing 40 wt% of CNT, elaborated by solution mixing. Due to no clear difference in σ, κ, and S values between both elaboration processes, the final ZT in this study appears independent on the elaboration protocols. The main benefit of the solution mixing process has been to enable the preparation of nanocomposites with high levels of CNT. Table 2 gathers the thermoelectric values obtained with insulating/multiwall CNT composites. By comparing with data from literature, the ZT value obtained for our best composite seems quite low. However, it is important to note that depending of the studies, the calculation of the ZT parameter can be based on a mixture of thermoelectric quantities measured in-plane and in-volume, notably regarding the electrical conductivity. As will be shown later, this has a huge

impact on the value of the thermoelectric properties. In any case, the ZT value obtained for our best nanocomposite is acceptable but is still largely insufficient for applications in waste heat harvesting.

Table 2. Thermoelectric performances of insulating polymer/CNT composites.

Samples	$\sigma_{in\text{-}plane}$ (S m^{-1})	$\sigma_{cross\text{-}plane}$ (S m^{-1})	$S_{cross\text{-}plane}$ (µV K^{-1})	$\kappa_{cross\text{-}plane}$ (W m^{-1} K^{-1})	ZT (T = 300 K)
PLA + 18 vol% CNT [16]	1.15×10^{2}		9.0	0.41	6.8×10^{-5}
PLA + 40 wt% CNT (this work)		1.5	9.4	0.8	2.5×10^{-8}
Polycarbonate (PC) + 2.5 wt% CNT [46]	7.3		8.5	0.33	6.8×10^{-7}
Polypropylene (PP) + 2 wt% CNT [46]	1.6		9.5	0.28	1.7×10^{-7} *(313 K)*
Acrylonitrile butadiene styrene (ABS) + 4 wt% CNT [46]	25.7		3.6	0.28	1.7×10^{-7} *(313 K)*
Polyamide 66 (PA66) + 2 wt% CNT [46]	5.0		6.3	0.28	2.2×10^{-7} *(313 K)*
Cellulose film + 5 wt% CNT [47]	15		10	0.08	6.8×10^{-6}
Polyvinylidene fluoride (PVDF) + 50 wt% CNT [27]		1.2×10^{2}	20	0.87	1.6×10^{-5}
PVDF + 8 wt% CNT [48]		2.0×10^{-2}	12	0.55	1.6×10^{-9}
PVDF foam + 8 wt% CNT [48]		4.0×10^{-3}	8.0	0.10	7.7×10^{-10}

2.3.2. The impact of crystallinity on thermoelectric properties of thick discs of Sc-PLA/CNT nanocomposites

Pristine Sc-PLA and Sc-PLA /MWCNT nanocomposites filled with 2 wt% and 5 wt% CNT prepared by melt-blending were used to study the impact of polymer matrix crystallinity on thermoelectric properties. The real CNT content of these two nanocomposites determined by TGA were 2 ± 0.5 wt% and 4.6 ± 0.3 wt%. Initial thick discs of pristine Sc-PLA and Sc-PLA/CNT nanocomposites obtained by thermo-compression molding using fast cooling rate condition (around – 15°C min^{-1}) were analyzed by DSC and WAXS. The thermograms (Fig. 3a) of pristine Sc-PLA and nanocomposites show a clear glass transition (T_g) step around 59 ±

1°C whatever the samples, and two distinct exo- and endothermic peaks related to cold crystallization ($113 < T_c < 126$ °C) and melting ($T_m \sim 160$ °C), respectively. Note that the cold crystallization peak is more pronounced for nanocomposites which indicates that CNT promotes the crystallization of PLA matrix. The degrees of initial crystallinity (Table 3) are closed to zero showing that the Sc-PLA is globally in amorphous state for all samples.

To confirm this result, WAXS diffraction profiles have been performed in the 2θ range from 5° to 46°. The X-ray pattern of Sc-PLA (Fig. 3b) is deconvoluted using three Pearson functions located to $2\theta \approx 15.5°$, $2\theta \approx 21.5°$, and $2\theta \approx 32.5°$. As established by Stoclet *et al.* [49], these broad diffraction halos were assigned to the amorphous state of PLA. In the case of nanocomposites (Fig. 3 c, d), the three same Pearson functions are used for the PLA part and a fourth reflection peak at $2\theta \approx 26°$ is added for the nanotube contribution. This reflection is attributed to the (002) lattice planes of CNT. Its position of this peak is related to the inter-sheet distance which is in the present case in the order of 0.34 nm, in agreement with literature [50]. Besides, the intensity of this peak increase according to the content of CNT fillers. To summarize, this WAXS analysis confirm the amorphous state of Sc-PLA in all samples.

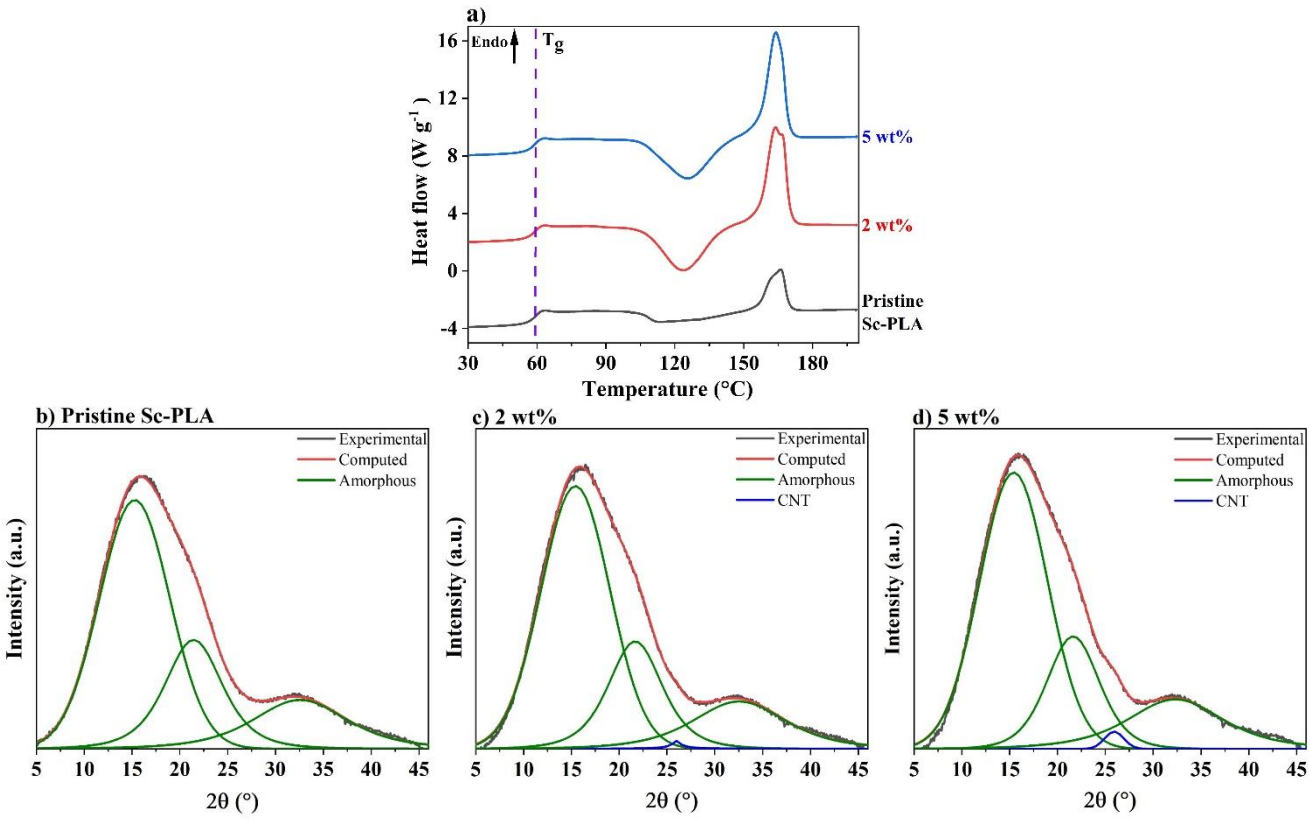

Figure 3. a) Heating thermograms of pristine Sc-PLA and Sc-PLA/CNT nanocomposites (2 wt% and 5 wt%) obtained after a fast cooling process. Treatment of WAXS intensity profile of b) pristine Sc-PLA, c) Sc-PLA/2 wt% CNT and d) Sc-PLA/5 wt% CNT obtained after fast cooling from melt state.

Fig. 4a exhibits the thermograms of both pristine Sc-PLA and Sc-PLA/CNT nanocomposites after thermal treatments (annealing at 120 °C and slow cooling from the melt). In all cases, a predominant melting peak is observed without no cold crystallization phenomenon. This indicates that both thermal treatments have induced crystallinity inside the Sc-PLA matrix in agreement with was expected from literature [30]. WAXS diffractograms (Fig. 5) confirm the presence of the orthorhombic α-crystalline structure of PLA for all samples as shown by the presence of the diffraction peaks located at $2\theta \approx 16.6°$, 14.7°, 19.0°, and 22.2°. Whatever the thermal treatment, the presence of CNT does not modify the crystalline structure of PLA matrix. Note that the reflection peak corresponding to the (002) lattice planes of CNT is not visible due to its low intensity compared with that of the crystalline peaks of PLA. The crystal content relative to the PLA part is reported in Table 3. It seems that annealed samples exhibit a slightly higher crystallinity than samples slow cooled from the melt whatever the composition. However, a slight increase in crystallinity is observed with the addition of CNT for samples slow cooled from the melt while no clear trend is noted for annealed samples. To

further investigate the role of CNT regarding the crystallization behavior of PLA, Fig. 4b shows the thermograms recorded during the slow cooling step of pristine Sc-PLA (black line) and nanocomposite 5 wt% CNT (red line). The more pronounced exothermic peak around 120 °C for the Sc-PLA/CNT sample confirms that CNT promote the crystallization of PLA by inducing a strong heterogeneous nucleation effect.

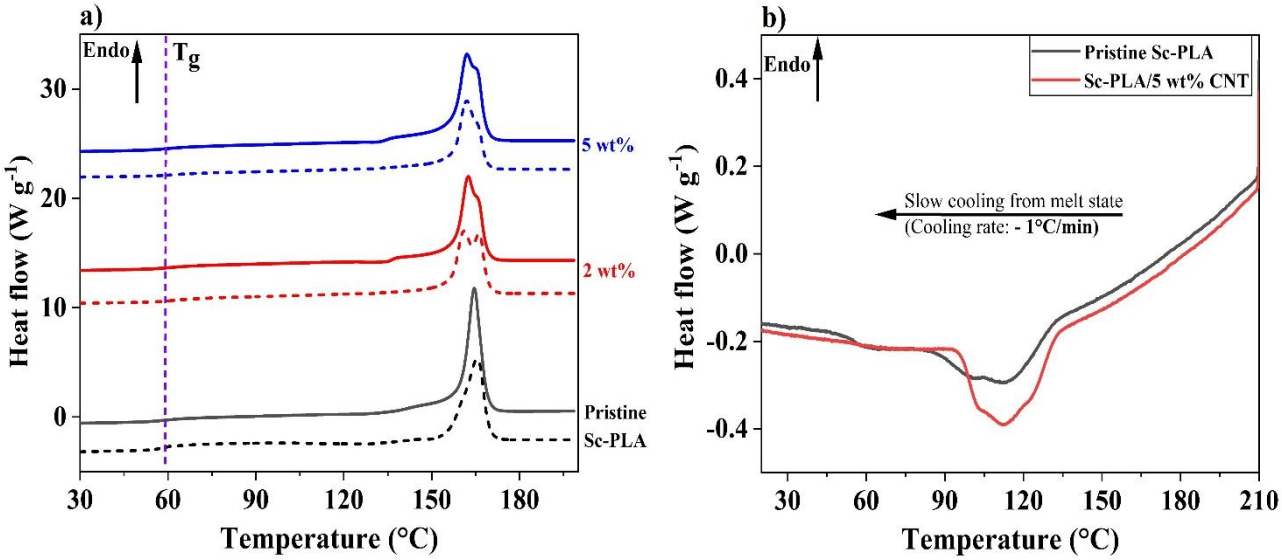

Figure 4. a) DSC thermograms of pristine Sc-PLA and Sc-PLA/CNT nanocomposites (2 wt% and 5 wt%) after thermal treatments. Straight lines for annealing and dash lines for slow cooling from the melt. b) Cooling thermograms of pristine PLA and Sc-PLA/5 wt% CNT with a rate of - 1°C min^{-1} (slow cooling from melt state).

Table 3. Degree of crystallinity (χ_c) of Sc-PLA/CNT nanocomposites.

Samples		$\chi_c(\%)^a$ **(± 2%)**	$\chi_c(\%)^b$ **(± 2%)**
Pristine Sc-PLA	Fast cooling	2	–
	Annealing	59	49
	Slow cooling	44	48
2 wt%	Fast cooling	2	–
	Annealing	54	49
	Slow cooling	48	48
5 wt%	Fast cooling	1	–
	Annealing	56	53
	Slow cooling	52	58

[a] Calculated by DSC

[b] Calculated by WAXS diffractograms

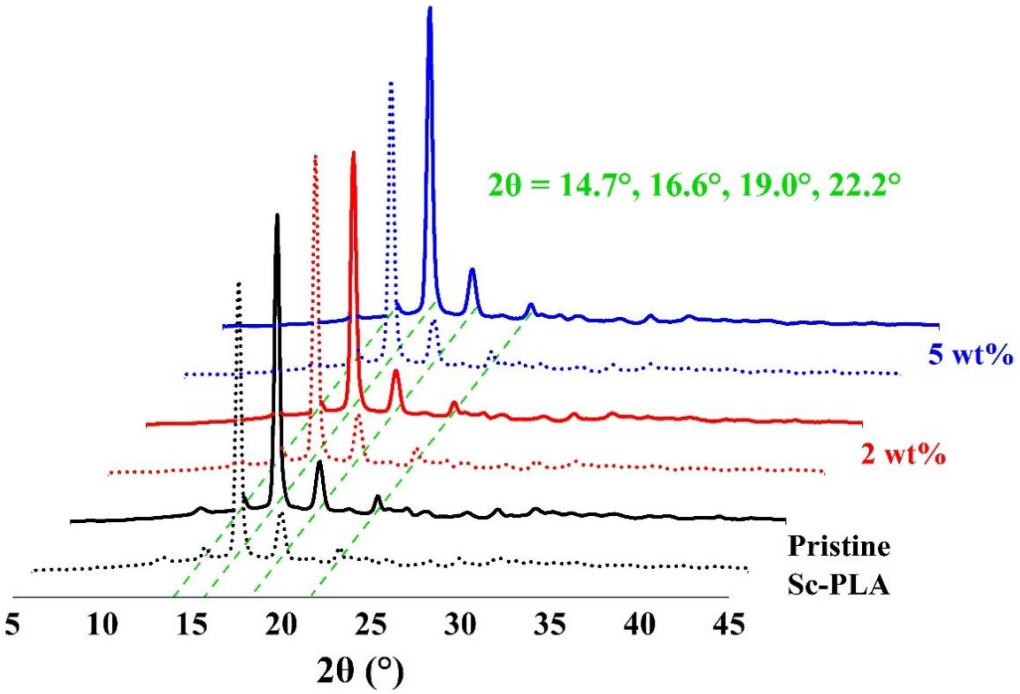

Figure 5. WAXS intensity profiles of Sc-PLA/CNT nanocomposites. Straight lines and dash lines are used to distinguish the both pretreatments: annealing and slow cooling from melt state, respectively.

The thermoelectric response of all samples has been measured at 300 K and reported in Table 4. Regarding the electrical conductivity, at the same CNT content, similar values of σ is measured within the error bars whatever the Sc-PLA matrix is in amorphous or semi-crystalline state. Huang *et al.* [18] have reported a significant increase of σ with the crystallinity for PLLA filled with low content of CNT (0.75 and 1 wt%). In this range, the lower the CNT concentration, the greater the impact of crystallinity on electrical conductivity. However, this effect is no longer observed at 2 wt% of CNT; *i.e.* far above the percolation threshold, in agreement with ours results. Considering that electrical conductivity is only related to the CNT conductive network, the link between the structure (amorphous/semi-crystalline) of the non-conductive matrix and the electrical properties may seem rather confusing. In fact, the crystallization of the PLA from the melt state may significantly change the CNT network, due to selective exclusion of CNT from crystalline phase. This subsequently induces an increase of CNT ratio in the amorphous phase which in the case of concentration close to the percolation threshold, can reach the required CNT concentration to form a conductive network. By contrast, at filler concentration well above the percolation threshold as in our study, the matrix crystallization will not significantly modify the CNT network which is already conductive

leading to similar electrical conductivity. Regarding the annealing treatment, samples remain in the solid state so the CNT network is not modified when PLA crystallization occurs.

Regarding the Seebeck coefficient values, a slightly improvement of S is observed with the presence of crystals. Indeed, values increase from 11 to 12 µV K^{-1} and from 10 to 11 µV K^{-1} for samples containing 2 wt% and 5 wt% CNT, respectively. The same trend was reported in the previous work of Brun *et al.* [27], studying thermoelectric properties of PVDF/MWCNT composites. To the best of our knowledge, the origin of this evolution is not understood up to now.

Crystallinity increases the thermal conductivity of PLA nanocomposites as shown in Table 4. The effect is especially observed for nanocomposites containing 5 wt% of CNT. for which κ increases from 0.29 W $m^{-1}K^{-1}$ for the fast-cooled sample to 0.37 W $m^{-1}K^{-1}$ (+27%) for the slow cooled sample. This could be due to the increased thermal conductivity of the PLA matrix when it is in a semi-crystalline state, as the more ordered structures favor the heat transport [51].

Within the error bars, as electrical conductivity remains unchanged, Seebeck coefficient and thermal conductivity slightly increases, ZT value is almost the same when comparing samples with the same filler fraction whatever the degree of crystallinity. To summarize, no impact of crystallinity on thermoelectric properties is evidenced in this study focused on PLA/CNT with fillers content higher than the percolation threshold.

Table 4. Thermoelectric properties of Sc-PLA/CNT samples from different pre-treatments to induce or not crystallinity.

		σ (x 10^{-2}) (S m^{-1})	**S (µV K^{-1})**	**κ (W $m^{-1}K^{-1}$)**	**ZT (x 10^{-9}) (T = 300 K)**
Fast cooling (amorphous)	**2wt%**	1.3 ± 0.1	11 ± 0.3	0.24 ± 0.01	2.1 ± 0.7
	5wt%	5.0 ± 0.3	10 ± 0.2	0.29 ± 0.01	5.6 ± 1.6
Annealing	**2wt%**	0.9 ± 0.5	12 ± 0.3	0.26 ± 0.02	1.3 ± 0.7
	5wt%	4.0 ± 0.3	11 ± 0.2	0.32 ± 0.01	4.4 ± 2.6
Slow cooling	**2wt%**	1.3 ± 1.0	12 ± 0.2	0.27 ± 0.02	2.1 ± 1.6
	5wt%	3.4 ± 2.0	11 ± 0.2	0.37 ± 0.03	3.7 ± 1.9

2.3.3. Comparison of thermoelectric properties of thin and thick films of A-PLA/CNT nanocomposites at 300 K

The in-plane electrical conductivity of thin films and both cross-plane and in-plane electrical conductivities of thick discs of A-PLA/CNT are compared in Fig. 6a.

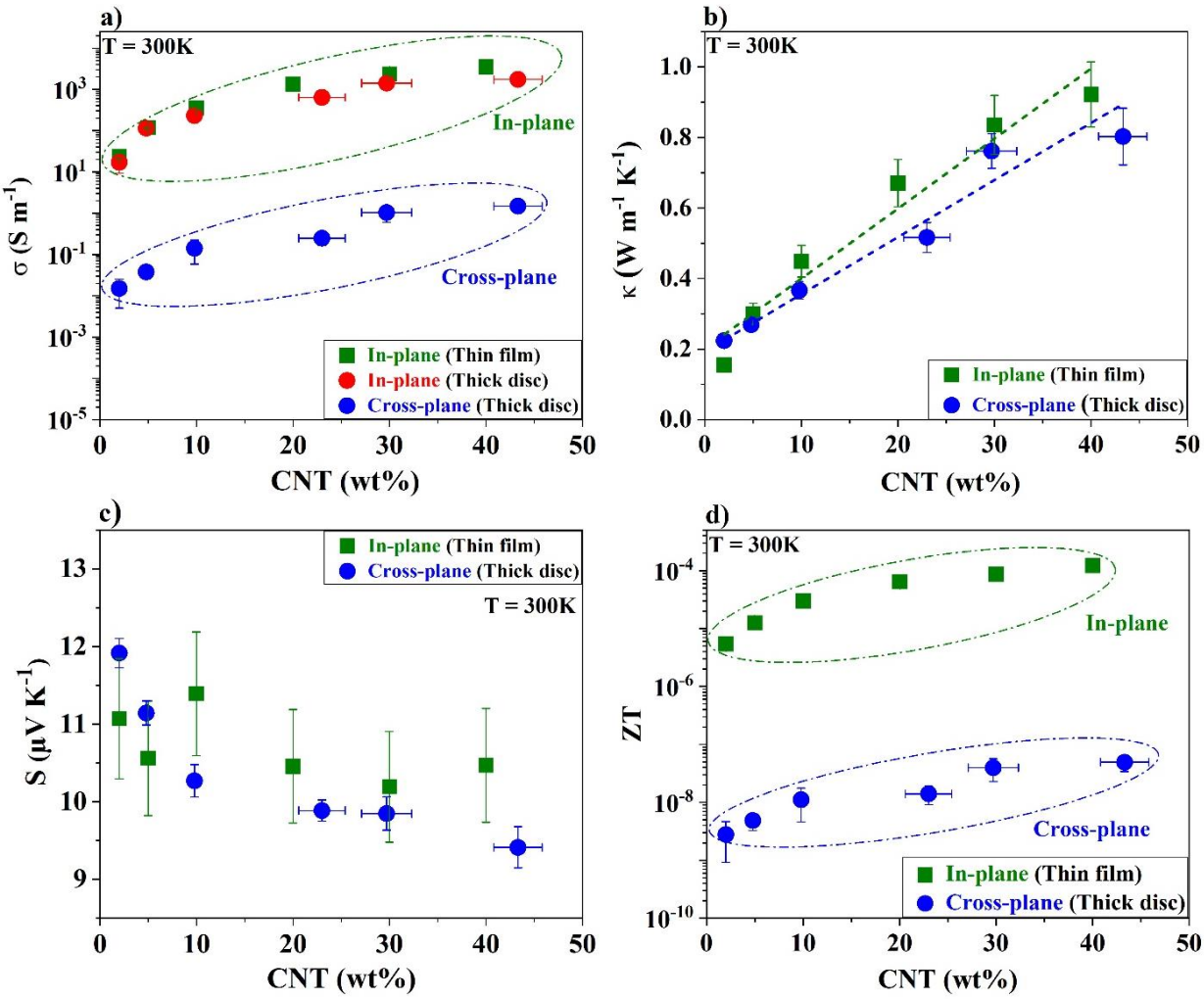

Figure 6. Cross-plane and in-plane thermoelectric properties at 300 K as a function of CNT concentration: a) electrical conductivity (σ), b) thermal conductivity (*κ*), c) Seebeck coefficient (S), and d) figure of merit (ZT).

As a reminder, the in-plane electrical conductivity for thick discs was assessed by 4-point collinear probe technique. Two major results are observed: first of all, the in-plane electrical conductivity values of thin films are about 100-1000 times higher than the cross-plane measurements of thick discs for the same CNT composition; in addition, it is very interesting to note that the values of the in-plane electrical conductivity of thick discs and thin films are of the same order of magnitude for the same filler content, showing an independence of $\sigma_{in\text{-}plane}$ on

sample thickness. This result clearly establishes that the electrical conductivity is highly anisotropic in thick discs: the electrical conductivity at the surface is 100-1000 times higher than the one in volume measured cross-plane. This result is in line with the work of Audoit *et al.* [52] focused on 2D-silver microplates/PVDF nanocomposites. These authors have shown that $\sigma_{in\text{-}plane}$ was 1000 times higher than $\sigma_{cross\text{-}plane}$ and that the percolation threshold was lower through the sample thickness than on the surface. In the case of PVDF/MWCNT nanocomposites, Brun *et al.* [27] have also revealed that $\sigma_{in\text{-}plane}$ was 10 times higher than $\sigma_{cross\text{-}plane}$. In all these cases, samples were prepared using a hot-pressing step. One hypothesis to explain this anisotropic behavior in electrical conductivity could be that during the thermocompression step, nanotubes close to the surface are preferentially oriented in the surface plane, favoring conductive paths. Indeed, CNT near the surface would orient their long axis perpendicular to the compression stress whereas CNT in the bulk would be aligned more randomly. Considering that carbon nanotubes have higher electrical conductivity along their long axis [53], their specific orientation close to the surface will then induce a higher in-plane electrical conductivity. Note that this effect is equally observed on both sides of thick discs. Regarding the similar results in $\sigma_{in\text{-}plane}$ of thin films and thick discs, as thin films do not have a thermocompression step in their elaboration process, the explanation lies elsewhere. Min et al. [54] explained that "Slight tilting of the nanotubes in the composite film could easily create additional contacts between nanotubes resulting into higher electrical conductivities in the film than in the bulk". In other words, nanotubes in solvent can be thought of as toothpicks thrown into water and they tend to organize themselves horizontally, which is undoubtedly due to their high aspect ratio, and what creates numerous new and "better" horizontal contacts between them. The correct assessment of the electrical conductivity is of prime importance considering the thermoelectric performance. To the best of our knowledge, only few works have highlighted the difference in electrical conductivity between in-plane and cross-plane for thermoelectric applications [27]. To evaluate the ZT parameter, a lot of authors use surface electrical conductivity while the other properties are assessed in volume, as summarized in Table 2.

The comparison of thermal conductivity between thick discs and thin films is shown in Fig. 6b. It can be seen that contrary to electrical conductivity which presents a clear anisotropy according to direction measurements, the obtained in-plane and cross-plane thermal conductivity values show nearly the same values for a same filler fraction of CNT. Theoretically, this means that the mean free path of phonons remains the same in both thin films and thick discs and that phonons are affected more by the number of contacts between the tubes rather than by their orientation to each other.

For the Seebeck coefficient (Fig. 6c), the values of S for thin films are of the same order of magnitude as for thick samples with values around 11 to 10 μV K^{-1}. Therefore, the Seebeck coefficient values obtained in the investigation are almost equal in both directions (cross-plane and in-plane). The order of magnitude of S values is normal but the decrease was expected to be more significant. The explanation could be related to the way the measurement is performed by the TFA in which the area used on the chip to evaluate the Seebeck is very small (~1 μm) and the corresponding thickness and volume concentration cannot be perfectly controlled. Therefore, the values obtained in this study will be considered equal in both directions.

As a result, the final thin-films (in-plane) ZTs are shown in Fig. 6d. The values lie between 5.4 x 10^{-6} for 2 wt% of MWCNT and 1.2 x 10^{-4} for 40 wt% and are about 10^3 times higher than that of thick discs. This shows that the thermoelectric properties of thermoplastic based composites are mainly controlled by the electrical conductivity and that the ZT of thin films is much higher than that of thick discs for the same composition. This behavior also confirmed that thermoelectric properties can be highly anisotropic, hence one can emphasize that in order to accurately evaluate the thermoelectric efficiency of materials, all parameters including σ, κ, and S must be measured along the same direction as the applied temperature gradient. To the best of our knowledge, until now only one research by Antar *et al.* [16] has reported a figure of merit (ZT) for similar PLA based nanocomposites with the highest value at 7 x 10^{-5} (18 vol% ≈ 22 wt% of CNT). Regarding thermoplastic/MWCNT composites, the ZT value of 1.2 x 10^{-4} obtained in this study for samples with 40 wt% of MWCNT is the best value that can be found in the literature.

2.4. Conclusions

In the present study, thick PLA/CNT nanocomposite discs (from 2 to 40 wt% of CNT) have been prepared by melt-blending and solution mixing processes. For each sample, the CNT content was controlled by TGA, which confirmed that the final values were close to those expected. The electrical percolation model was used to fit the electrical conductivity as a function of CNT volume fraction yielded a percolation threshold value at 0.36 vol% CNT, which is lower than other literature. All thermoelectric parameters including electrical conductivity (σ), thermal conductivity (κ), Seebeck coefficient (S), and figure of merit (ZT) were determined and compared for the two elaboration processes. It can be concluded that the preparation methods have no significant effect on the thermoelectric properties when the filler content is well above the percolation threshold. In addition, the impact of PLA crystallinity on the thermoelectric response of the nanocomposites have been investigated. Although electrical

conductivity remains at the same values compared to amorphous PLA/CNT and Seebeck coefficient and thermal conductivity are slightly enhanced by the crystallinity of PLA, the final ZT of nanocomposites is almost unchanged after inducing crystallinity in PLA. Finally, thin nanocomposite films were prepared with the same filler as thick discs and thermoelectric properties were measured using thin films analyzer (TFA). The comparison of thermoelectric properties between thick discs and thin films revealed a strong anisotropy of the electrical conductivity and the resulting figure of merit, with in-plane values 1000 times higher than cross-plane values.

Acknowledgments

The authors are indebted University of Lille and Région Haut-de-France for funding the research. Financial support from Région Nord Pas-de-Calais and European FEDER for SAXS/WAXS laboratory equipment is also gratefully acknowledged. We would like to thank to the support of GEMTEX laboratory, ENSAIT.

References:

1. Rull-Bravo, M., Moure, A., Fernández, J. F., & Martín-González, M. (2015). Skutterudites as thermoelectric materials: revisited. *RSC Advances*, *5*(52), 41653–41667. https://doi.org/10.1039/C5RA03942H

2. He, M., Ge, J., Lin, Z., Feng, X., Wang, X., Lu, H., … Qiu, F. (2012). Thermopower enhancement in conducting polymer nanocomposites via carrier energy scattering at the organic–inorganic semiconductor interface. *Energy & Environmental Science*, *5*(8), 8351. https://doi.org/10.1039/c2ee21803h

3. Zhang, Q., Sun, Y., Xu, W., & Zhu, D. (2014). Organic Thermoelectric Materials: Emerging Green Energy Materials Converting Heat to Electricity Directly and Efficiently. *Advanced Materials*, *26*(40), 6829–6851. https://doi.org/10.1002/adma.201305371

4. Gao, C., & Chen, G. (2016). Conducting polymer/carbon particle thermoelectric composites: Emerging green energy materials. *Composites Science and Technology*, *124*, 52–70. https://doi.org/10.1016/j.compscitech.2016.01.014

5. Zheng, Y., Zeng, H., Zhu, Q., & Xu, J. (2018). Recent advances in conducting poly(3,4-ethylenedioxythiophene):polystyrene sulfonate hybrids for thermoelectric applications. *Journal of Materials Chemistry C*, *6*(33), 8858–8873. https://doi.org/10.1039/C8TC01900B

6. Fan, W., Liang, L., Zhang, B., Guo, C.-Y., & Chen, G. (2019). PEDOT thermoelectric composites with excellent power factors prepared by 3-phase interfacial electropolymerization and carbon nanotube chemical doping. *Journal of Materials Chemistry A*, *7*(22), 13687–13694. https://doi.org/10.1039/C9TA03153G

7. Qu, D., Li, X., Wang, H., & Chen, G. (2019). Assembly Strategy and Performance Evaluation of Flexible Thermoelectric Devices. *Advanced Science*, *6*(15), 1900584. https://doi.org/10.1002/advs.201900584

8. Qu, D., Huang, X., Li, X., Wang, H., & Chen, G. (2020). Annular flexible thermoelectric devices with integrated-module architecture. *npj Flexible Electronics*, *4*(1), 1. https://doi.org/10.1038/s41528-020-0064-2

9. Gonçalves, C., Gonçalves, I., Magalhães, F., & Pinto, A. (2017). Poly(lactic acid) Composites Containing Carbon-Based Nanomaterials: A Review. *Polymers*, *9*(12), 269. https://doi.org/10.3390/polym9070269

10. Han, Z., & Fina, A. (2011). Thermal conductivity of carbon nanotubes and their polymer nanocomposites: A review. *Progress in Polymer Science*, *36*(7), 914–944. https://doi.org/10.1016/j.progpolymsci.2010.11.004

11. Rizvi, R., Kim, J.-K., & Naguib, H. (2010). The effect of processing and composition on the properties of polylactide–multiwall carbon nanotube composites prepared by solvent casting. *Smart Materials and Structures*, *19*(9), 094003. https://doi.org/10.1088/0964-1726/19/9/094003

12. Yang, L., Li, S., Zhou, X., Liu, J., Li, Y., Yang, M., … Zhang, W. (2019). Effects of carbon nanotube on the thermal, mechanical, and electrical properties of PLA/CNT printed parts in the FDM process. *Synthetic Metals*, *253*, 122–130. https://doi.org/10.1016/j.synthmet.2019.05.008

13. Kim, H.-S., Chae, Y. S., Park, B. H., Yoon, J.-S., Kang, M., & Jin, H.-J. (2008). Thermal and electrical conductivity of poly(l-lactide)/multiwalled carbon nanotube nanocomposites. *Current Applied Physics*, *8*(6), 803–806. https://doi.org/10.1016/j.cap.2007.04.032

14. Kumanek, B., & Janas, D. (2019). Thermal conductivity of carbon nanotube networks: a review. *Journal of Materials Science*, *54*(10), 7397–7427. https://doi.org/10.1007/s10853-019-03368-0

15. Lebedev, S. M., Gefle, O. S., Amitov, E. T., Berchuk, D. Yu., & Zhuravlev, D. V. (2017). Poly(lactic acid)-based polymer composites with high electric and thermal conductivity and their characterization. *Polymer Testing*, *58*, 241–248. https://doi.org/10.1016/j.polymertesting.2016.12.033

16. Antar, Z., Feller, J. F., Noël, H., Glouannec, P., & Elleuch, K. (2012). Thermoelectric behaviour of melt processed carbon nanotube/graphite/poly(lactic acid) conductive biopolymer nanocomposites (CPC). *Materials Letters*, *67*(1), 210–214. https://doi.org/10.1016/j.matlet.2011.09.060

17. Moon, S., Jin, F., Lee, C., Tsutsumi, S., & Hyon, S. (2005). Novel Carbon Nanotube/Poly(L-lactic acid) Nanocomposites; Their Modulus, Thermal Stability, and Electrical Conductivity. *Macromolecular Symposia*, *224*(1), 287–296. https://doi.org/10.1002/masy.200550625

18. Huang, C., Bai, H., Xiu, H., Zhang, Q., & Fu, Q. (2014). Matrix crystallization induced simultaneous enhancement of electrical conductivity and mechanical performance in poly(l-lactide)/multiwalled carbon nanotubes (PLLA/MWCNTs) nanocomposites. *Composites Science and Technology*, *102*, 20–27. https://doi.org/10.1016/j.compscitech.2014.07.016

19. Villmow, T., Pötschke, P., Pegel, S., Häussler, L., & Kretzschmar, B. (2008). Influence of twin-screw extrusion conditions on the dispersion of multi-walled carbon nanotubes in a poly(lactic acid) matrix. *Polymer*, *49*(16), 3500–3509. https://doi.org/10.1016/j.polymer.2008.06.010

20. Pötschke, P., Andres, T., Villmow, T., Pegel, S., Brünig, H., Kobashi, K., … Häussler, L. (2010). Liquid sensing properties of fibres prepared by melt spinning from poly(lactic acid) containing multi-walled carbon nanotubes. *Composites Science and Technology*, *70*(2), 343–349. https://doi.org/10.1016/j.compscitech.2009.11.005

21. Kuan, C.-F., Kuan, H.-C., Ma, C.-C. M., & Chen, C.-H. (2008). Mechanical and electrical properties of multi-wall carbon nanotube/poly(lactic acid) composites. *Journal of Physics and Chemistry of Solids*, *69*(5–6), 1395–1398. https://doi.org/10.1016/j.jpcs.2007.10.060

22. Lin, W.-Y., Shih, Y.-F., Lin, C.-H., Lee, C.-C., & Yu, Y.-H. (2013). The preparation of multi-walled carbon nanotube/poly(lactic acid) composites with excellent conductivity. *Journal of the Taiwan Institute of Chemical Engineers*, *44*(3), 489–496. https://doi.org/10.1016/j.jtice.2012.12.012

23. Chiu, W., Chang, Y., Kuo, H., Lin, M., & Wen, H. (2008). A study of carbon nanotubes/biodegradable plastic polylactic acid composites. *Journal of Applied Polymer Science*, *108*(5), 3024–3030. https://doi.org/10.1002/app.27796

24. Shao, S., Zhou, S., Li, L., Li, J., Luo, C., Wang, J., … Weng, J. (2011). Osteoblast function on electrically conductive electrospun PLA/MWCNTs nanofibers. *Biomaterials*, *32*(11), 2821–2833. https://doi.org/10.1016/j.biomaterials.2011.01.051

25. Chiu, W.-M., Kuo, H.-Y., Tsai, P.-A., & Wu, J.-H. (2013). Preparation and Properties of Poly (Lactic Acid) Nanocomposites Filled with Functionalized Single-Walled Carbon Nanotubes. *Journal of Polymers and the Environment*, *21*(2), 350–358. https://doi.org/10.1007/s10924-012-0514-6

26. Lanticse, L. J., Tanabe, Y., Matsui, K., Kaburagi, Y., Suda, K., Hoteida, M., … Yasuda, E. (2006). Shear-induced preferential alignment of carbon nanotubes resulted in anisotropic electrical conductivity of polymer composites. *Carbon*, *44*(14), 3078–3086. https://doi.org/10.1016/j.carbon.2006.05.008

27. Brun, J.-F., Binet, C., Tahon, J.-F., Addad, A., Tranchard, P., & Barrau, S. (2020). Thermoelectric properties of bulk multi-walled carbon nanotube - poly(vinylidene fluoride) nanocomposites: Study of the structure/property relationships. *Synthetic Metals*, *269*, 116525. https://doi.org/10.1016/j.synthmet.2020.116525

28. Kunz, K., Krause, B., Kretzschmar, B., Juhasz, L., Kobsch, O., Jenschke, W., … Pötschke, P. (2019). Direction Dependent Electrical Conductivity of Polymer/Carbon Filler Composites. *Polymers*, *11*(4), 591. https://doi.org/10.3390/polym11040591

29. Wang, J., Kazemi, Y., Wang, S., Hamidinejad, M., Mahmud, M. B., Pötschke, P., & Park, C. B. (2020). Enhancing the electrical conductivity of PP/CNT nanocomposites through crystal-induced volume exclusion effect with a slow cooling rate. *Composites Part B: Engineering*, *183*, 107663. https://doi.org/10.1016/j.compositesb.2019.107663

30. Zhang, J., Tashiro, K., Tsuji, H., & Domb, A. J. (2008). Disorder-to-Order Phase Transition and Multiple Melting Behavior of Poly(L -lactide) Investigated by Simultaneous Measurements of WAXD and DSC. *Macromolecules*, *41*(4), 1352–1357. https://doi.org/10.1021/ma0706071

31. Wang, L., Qiu, J., Sakai, E., & Wei, X. (2016). The relationship between microstructure and mechanical properties of carbon nanotubes/polylactic acid nanocomposites prepared by twin-screw extrusion. *Composites Part A: Applied Science and Manufacturing*, *89*, 18–25. https://doi.org/10.1016/j.compositesa.2015.12.016

32. Linseis, V., Völklein, F., Reith, H., Nielsch, K., & Woias, P. (2018). Advanced platform for the in-plane *ZT* measurement of thin films. *Review of Scientific Instruments*, *89*(1), 015110. https://doi.org/10.1063/1.5005807

33. Kremer, F., & Schönhals, A. (Eds.). (2003). *Broadband Dielectric Spectroscopy*. Berlin, Heidelberg: Springer Berlin Heidelberg. https://doi.org/10.1007/978-3-642-56120-7

34. Miccoli, I., Edler, F., Pfnür, H., & Tegenkamp, C. (2015). The 100th anniversary of the four-point probe technique: the role of probe geometries in isotropic and anisotropic systems. *Journal of Physics: Condensed Matter*, *27*(22), 223201. https://doi.org/10.1088/0953-8984/27/22/223201

35. Faraguna, F., Pötschke, P., & Pionteck, J. (2017). Preparation of polystyrene nanocomposites with functionalized carbon nanotubes by melt and solution mixing: Investigation of dispersion, melt rheology, electrical and thermal properties. *Polymer*, *132*, 325–341. https://doi.org/10.1016/j.polymer.2017.11.014

36. Ceregatti, T., Pecharki, P., Pachekoski, W. M., Becker, D., & Dalmolin, C. (2017). Electrical and thermal properties of PLA/CNT composite films. *Matéria (Rio de Janeiro)*, *22*(3). https://doi.org/10.1590/s1517-707620170003.0197

37. Park, S. H., Lee, S. G., & Kim, S. H. (2013). Isothermal crystallization behavior and mechanical properties of polylactide/carbon nanotube nanocomposites. *Composites Part A: Applied Science and Manufacturing*, *46*, 11–18. https://doi.org/10.1016/j.compositesa.2012.10.011

38. Mulla, M. Z., Rahman, M. R. T., Marcos, B., Tiwari, B., & Pathania, S. (2021). Poly Lactic Acid (PLA) Nanocomposites: Effect of Inorganic Nanoparticles Reinforcement on Its Performance and Food Packaging Applications. *Molecules*, *26*(7), 1967. https://doi.org/10.3390/molecules26071967

39. Ivanov, E., Kotsilkova, R., Xia, H., Chen, Y., Donato, R., Donato, K., … Angelov, V. (2019). PLA/Graphene/MWCNT Composites with Improved Electrical and Thermal Properties Suitable for FDM 3D Printing Applications. *Applied Sciences*, *9*(6), 1209. https://doi.org/10.3390/app9061209

40. Spinelli, G., Kotsilkova, R., Ivanov, E., Georgiev, V., Ivanova, R., Naddeo, C., & Romano, V. (2020). Dielectric Spectroscopy and Thermal Properties of Poly(lactic) Acid Reinforced with Carbon-Based Particles: Experimental Study and Design Theory. *Polymers*, *12*(10), 2414. https://doi.org/10.3390/polym12102414

41. Nan, C.-W., Shen, Y., & Ma, J. (2010). Physical Properties of Composites Near Percolation. *Annual Review of Materials Research*, *40*(1), 131–151. https://doi.org/10.1146/annurev-matsci-070909-104529

42. Zhang, H.-L., Li, J.-F., Zhang, B.-P., Yao, K.-F., Liu, W.-S., & Wang, H. (2007). Electrical and thermal properties of carbon nanotube bulk materials: Experimental studies for the 328 – 958 K temperature range. *Physical Review B*, *75*(20), 205407. https://doi.org/10.1103/PhysRevB.75.205407

43. Stojanovic, N., Maithripala, D. H. S., Berg, J. M., & Holtz, M. (2010). Thermal conductivity in metallic nanostructures at high temperature: Electrons, phonons, and the Wiedemann-Franz law. *Physical Review B*, *82*(7), 075418. https://doi.org/10.1103/PhysRevB.82.075418

44. Gayner, C., & Kar, K. K. (2016). Recent advances in thermoelectric materials. *Progress in Materials Science*, *83*, 330–382. https://doi.org/10.1016/j.pmatsci.2016.07.002

45. Russ, B., Glaudell, A., Urban, J. J., Chabinyc, M. L., & Segalman, R. A. (2016). Organic thermoelectric materials for energy harvesting and temperature control. *Nature Reviews Materials*, *1*(10), 16050. https://doi.org/10.1038/natrevmats.2016.50

46. Krause, B., Barbier, C., Levente, J., Klaus, M., & Pötschke, P. (2019). Screening of Different Carbon Nanotubes in Melt-Mixed Polymer Composites with Different Polymer Matrices for Their Thermoelectrical Properties. *Journal of Composites Science*, *3*(4), 106. https://doi.org/10.3390/jcs3040106

47. Gnanaseelan, M., Chen, Y., Luo, J., Krause, B., Pionteck, J., Pötschke, P., & Qi, H. (2018). Cellulose-carbon nanotube composite aerogels as novel thermoelectric materials. *Composites Science and Technology*, *163*, 133–140. https://doi.org/10.1016/j.compscitech.2018.04.026

48. Sun, Y.-C., Terakita, D., Tseng, A. C., & Naguib, H. E. (2015). Study on the thermoelectric properties of PVDF/MWCNT and PVDF/GNP composite foam. *Smart Materials and Structures*, *24*(8), 085034. https://doi.org/10.1088/0964-1726/24/8/085034

49. Stoclet, G., Seguela, R., Lefebvre, J.-M., & Rochas, C. (2010). New Insights on the Strain-Induced Mesophase of Poly(D , L -lactide): *In Situ* WAXS and DSC Study of the Thermo-Mechanical Stability. *Macromolecules*, *43*(17), 7228–7237. https://doi.org/10.1021/ma101430c

50. Saito, Y., Yoshikawa, T., Bandow, S., Tomita, M., & Hayashi, T. (1993). Interlayer spacings in carbon nanotubes. *Physical Review B*, *48*(3), 1907–1909. https://doi.org/10.1103/PhysRevB.48.1907

51. Barkhad, M. S., Abu-Jdayil, B., Mourad, A. H. I., & Iqbal, M. Z. (2020). Thermal Insulation and Mechanical Properties of Polylactic Acid (PLA) at Different Processing Conditions. *Polymers*, *12*(9), 2091. https://doi.org/10.3390/polym12092091

52. Audoit, J., Laffont, L., Lonjon, A., Dantras, E., & Lacabanne, C. (2015). Percolative silver nanoplates/PVDF nanocomposites: Bulk and surface electrical conduction. *Polymer*, *78*, 104–110. https://doi.org/10.1016/j.polymer.2015.09.062

53. Qin, C., Shi, X., Bai, S. Q., Chen, L. D., & Wang, L. J. (2006). High temperature electrical and thermal properties of the bulk carbon nanotube prepared by SPS. *Materials Science and Engineering: A*, *420*(1–2), 208–211. https://doi.org/10.1016/j.msea.2006.01.055

54. Min, C., Shen, X., Shi, Z., Chen, L., & Xu, Z. (2010). The Electrical Properties and Conducting Mechanisms of Carbon Nanotube/Polymer Nanocomposites: A Review. *Polymer-Plastics Technology and Engineering*, *49*(12), 1172–1181. https://doi.org/10.1080/03602559.2010.496405

3. Thermoelectric properties of A-PLA/CNT nanocomposite (2 wt%) obtained from solution mixing combining melt-blending process

In order to optimize the dispersion of CNT, an A-PLA/CNT nanocomposite containing 2 wt% of fillers was prepared by combining solution mixing followed by melt blending. Fig. 3.1 presents the dispersion of CNT in PLA matrix using SEM. The SEM images show no significant difference in the distribution of CNT within the PLA matrix compared to the sample containing 2 wt% CNT produced via either the melt-blending or solution mixing process (see Fig. 1), where both isolated and bundles of CNT can also be observed at high magnification.

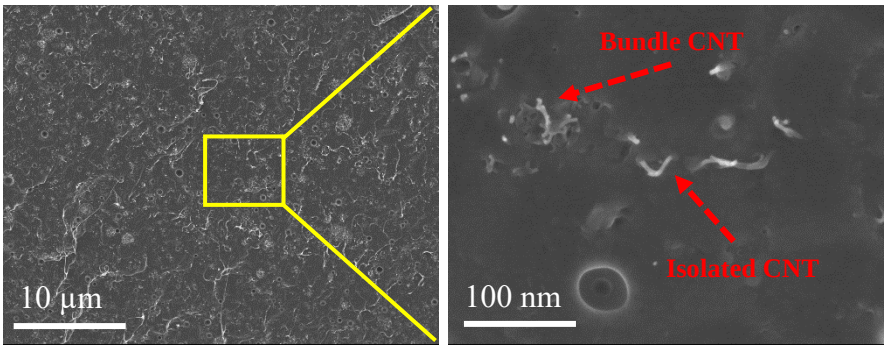

Figure 3.1. SEM images of cryofractured cross-sections of sample 2 wt% obtain from solution mixing and melt-blending.

The actual weight fraction of CNT (wt%) in this sample was also determined by TGA and the obtained value close to the expected content which is 1.2 ± 0.2 vol% CNT (equivalent to 1.6 ± 0.2 wt%). Concerning thermal transition, the glass transition temperature was around 55 °C, which is similar to the sample prepared from solution mixing or melt-blending protocols with the same CNT content.

In terms of thermoelectric properties, Fig 3.2 (a-d) illustrates a comparison of the cross-plane thermoelectric properties of the nanocomposite (2 wt% CNT) produced through three elaboration processes. It can be seen that, within the error bars, the achieved values of the sample from the combination of solution mixing and melt-blending present no discernible difference when compared to the samples produced by other process. The values of electrical conductivity (σ), thermal conductivity (κ), Seebeck coefficient (S), and figure of merit (ZT) are 8.3 x 10^{-3} S m^{-1}, 0.22 W m^{-1} K^{-1}, 11.7 µV K^{-1}, and 1.6 x 10^{-9}, respectively.

To summarize, it can be concluded that the combination of solution mixing and melt-blending process does not exhibit a pronounced effect on the thermoelectric properties in the

case of nanocomposite containing 2 wt% of CNT (*i.e.* concentration higher that the percolation threshold).

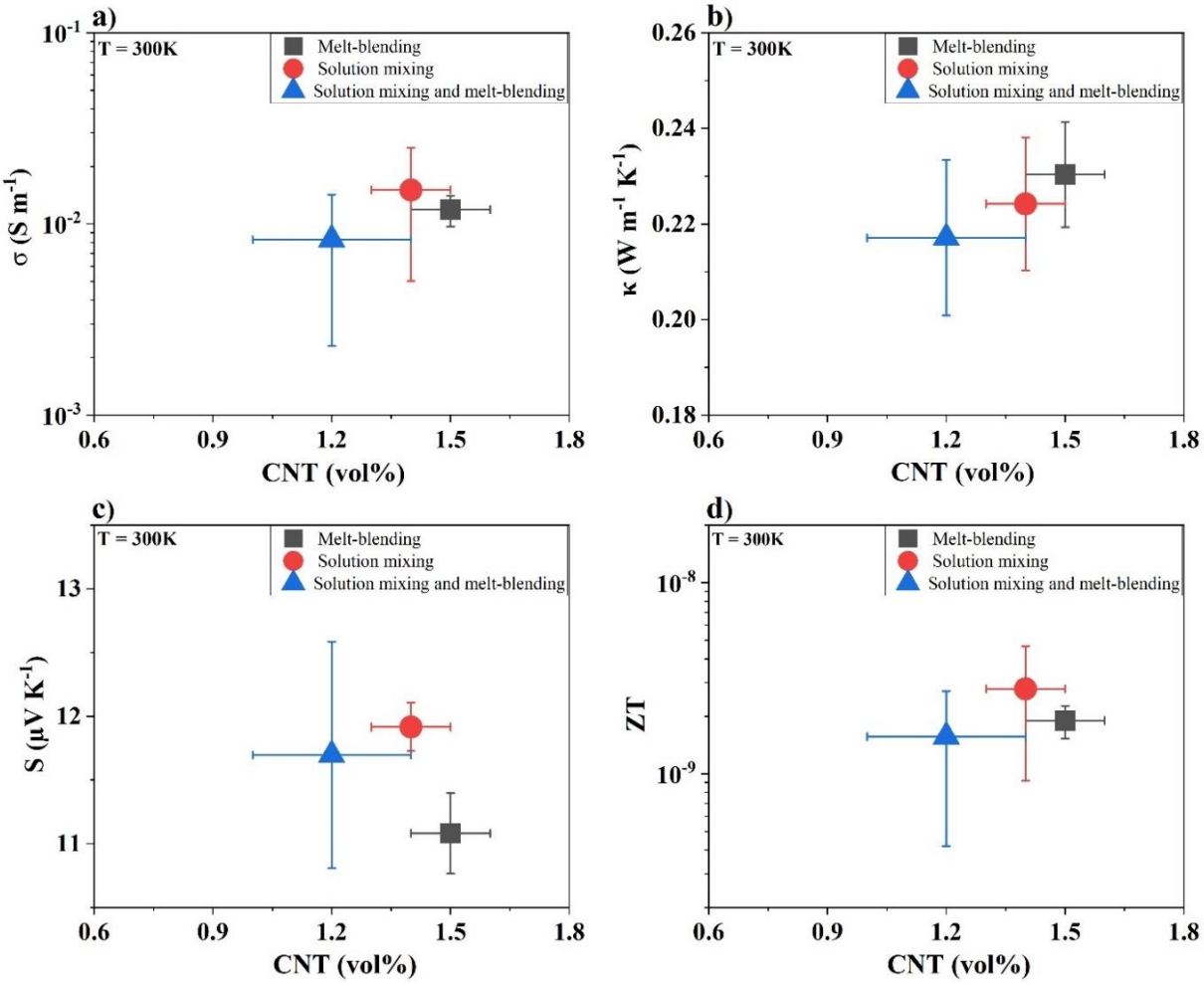

Figure 3.2. Cross-plane thermoelectric properties comparison of nanocomposite (2 wt% CNT) from three elaboration processes. a) electrical conductivity (σ), b) thermal conductivity (κ), c) Seebeck coefficient (S), and d) figure of merit (ZT).

4. The influence of CNT orientation on thermoelectric properties

In order to better understand the influence of CNT orientation on thermoelectric properties, A-PLA/CNT nanocomposites have been uniaxially drawn at 70 °C (just above T_g) at different draw ratios. Fig. 3.3 displays SEM images of the surface of uniaxially drawn samples at various strains, ranging from 100 % to 150 % for sample containing 2 wt% CNT (Fig. 3.3 a1 – a3), and from 100 % to 250 % for sample containing 5 wt% (Fig. 3.3 b1 – b4). Note that, to clearly observe the distribution and orientation of CNT in the polymer matrix, the surface of the nanocomposites was imaged without the use of a carbon coating. While no clear evolution is evidenced for the nanocomposites containing 2 wt% of CNT, the images for the

nanocomposites with 5 wt% reveal that CNT bundles tend to align along the stretching direction, and that this alignment, as expected, becomes more pronounced as the draw ratio increases. Furthermore, as the strain increases, a decohesion between the oriented CNT bundles and the polymer matrix appears. Due to its higher deformation level, this separation is most pronounced in the 5 wt% CNT sample for ε = 250 % (Fig. 3.3 b4). These results suggest that the CNT network within the polymer could be disrupted as the strain increases, with consequent effects on the electrical conductivity and thermoelectric properties of the nanocomposites.

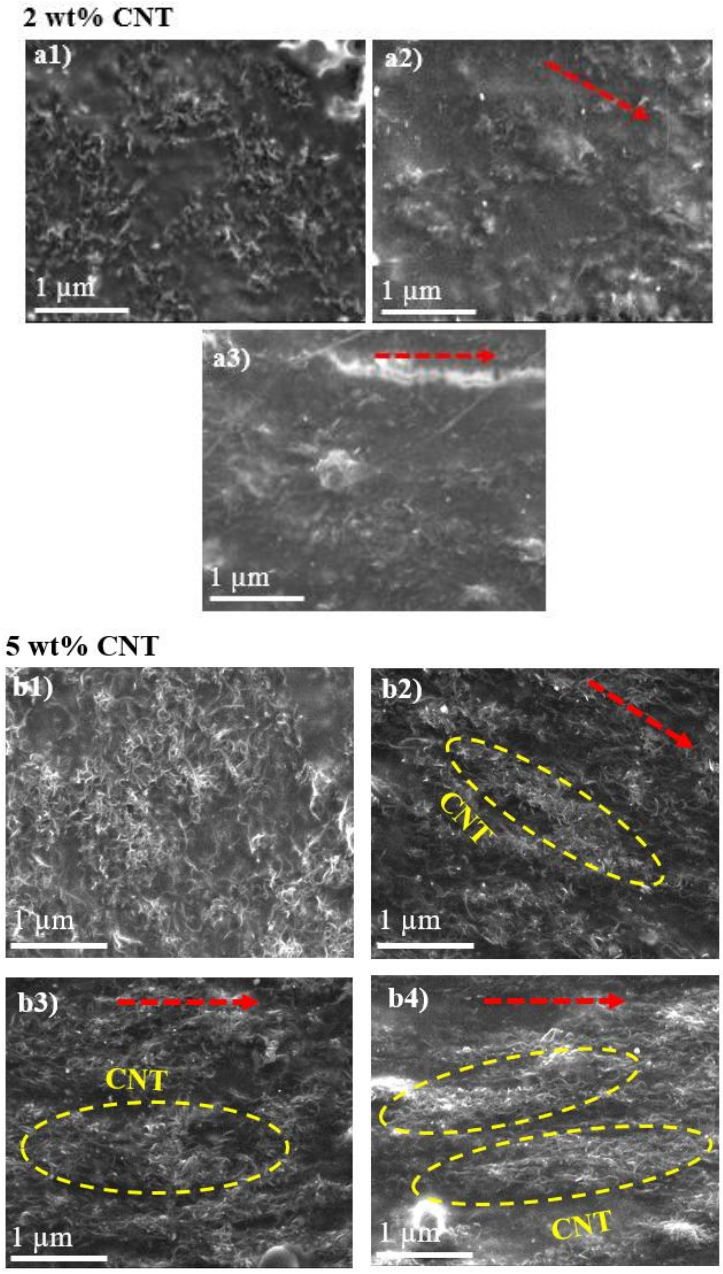

Figure 3.3. SEM images of surface of A-PLA/CNT nanocomposites (2 wt% and 5 wt%). a1-b1), a2-b2) and a3-b3) corresponding to the strain of 0, 100 %, and 150 %, b4) sample 5 wt% at the strain of 250 %. Red arrows show the stretching direction.

Fig. 3.4 illustrates the $\sigma_{cross-plane}$ and $\sigma_{in-plane}$ values of the nanocomposite as a function of strain. Overall, the electrical conductivity values of both samples decrease as the draw ratio increased. Specifically, for the sample containing 2 wt% CNT (Fig. 3.4a), the cross-plane value significantly decreases as the deformation reaches 150 %, dropping from 9.2 x 10^{-3} S m^{-1} to 4.3 x 10^{-5} S m^{-1}. Meanwhile, the nanocomposite with 5 wt% of CNT shows a less pronounced decrease, falling from 2.0 x 10^{-1} S m^{-1} to 4.3 x 10^{-4} S m^{-1}. The decrease of σ with deformation has already been reported in literature for stretchable electrodes based on silicone and various fillers [1,2]. This phenomenon may be explained by the increase of the distance between CNT with strain in the stretching direction which may disrupt the CNT network. This phenomenon is expected to be more pronounced at low CNT concentrations which explains the higher decrease of σ for nanocomposite containing 2 wt%. Moreover, the formation of voids with stretching, as observed in SEM, is another contribution to the decrease of σ.

Regarding the in-plane conductivity values, the sample with 2 wt% of CNT could only be measured for a deformation at ε = 100 %. At 150 %, the measurement becomes impractical probably due to surface fracture, which disrupts the CNT network. By contrast, the 5 wt% CNT sample allows the determination of in-plane values as the deformation increases up to 250 %. To go further about the influence of CNT orientation on the electrical conductivity, the $\sigma_{in-plane}$ measurement was conducted in both directions including parallel (//) (to the stretching direction) and perpendicular direction (⊥). The values obtained at low deformation were similar for both directions, but at the deformation of 250 % for 5 wt% CNT sample (Fig. 3.4 b), a significant difference in values between the two measurement directions was observed, with the perpendicular direction being less than 10 times that of the parallel direction. These results indicate that $\sigma_{\mathrm{in-plane}}$ is significantly influenced by the orientation of CNT. In particular, for the sample drawn at ε = 250 %, it can be assumed that the nanotubes are more aligned along the drawn direction. As expected, the higher value of $\sigma_{\mathrm{in-plane}}$ parallel to the stretching direction indicates that the conductivity along the nanotubes is higher than that perpendicular to the nanotube [3,4].

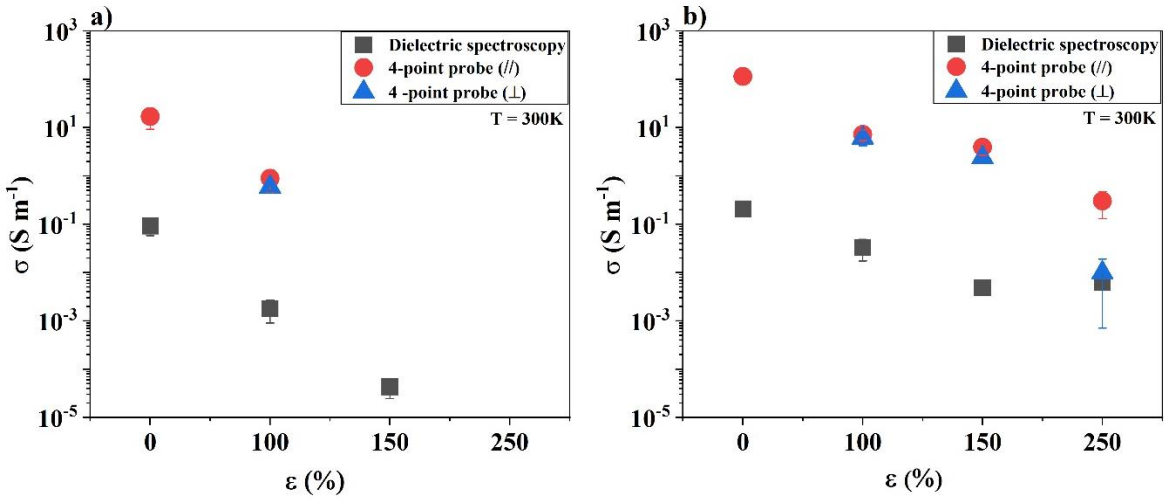

Figure 3.4. The effect of deformation on the cross-plane and in-plane (parallel and perpendicular to the measurement direction) electrical conductivity of PLA/MWCNT nanocomposites containing 2 wt% (a) and 5 wt% of CNT (b).

5. Thermoelectric properties of Sc-PLA/CNT nanocomposites

This part is dedicated to the results obtained on thick samples of nanocomposites based on crystallizable PLA. As a reminder, the elaboration conditions are similar as those previously used for A-PLA/CNT nanocomposites. Similar approach is used to investigate the relation between structure and thermoelectric properties on these nanocomposites. The distribution of CNT within the Sc-PLA matrix is presented in Fig. 3.5 a-d and 3.5 e-h for nanocomposites containing 2 wt% and 10 wt% CNT for samples produced through the melt-blending process, and 2 wt% and 40 wt% CNT for samples from the solution mixing process, respectively. In comparison to the A-PLA/CNT nanocomposites with the same CNT content (see Fig. 1), the dispersion of CNT in the Sc-PLA matrix does not show significant differences compared to that of A-PLA matrix, and there is no difference between the two elaboration processes.

The weight fraction (wt%) of CNT in nanocomposites was determined by TGA and their conversion to volume fraction (vol%) is given in Table 2.5 of Chapter 2.

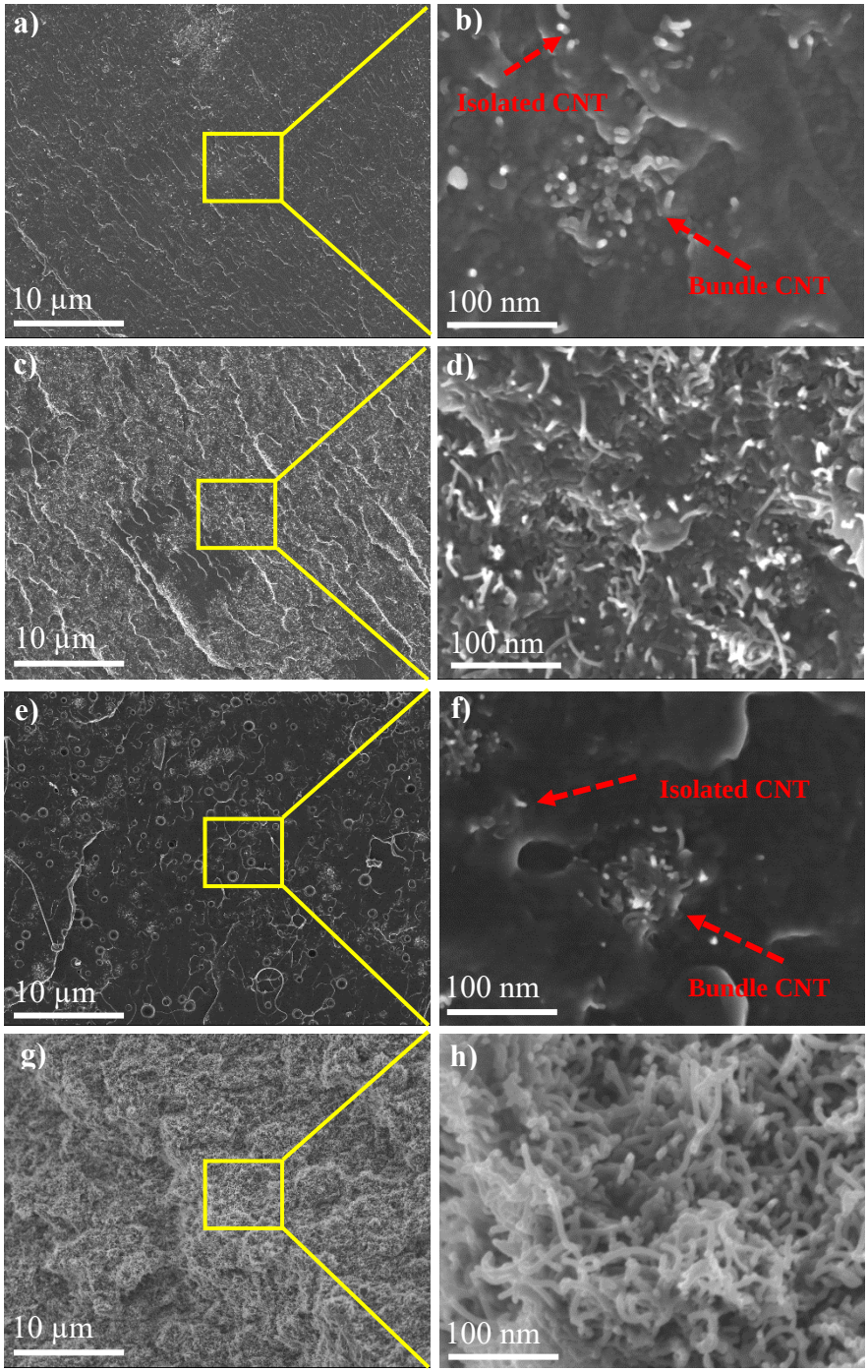

Figure 3.5. SEM images of cross-section Sc-PLA/MWCNT samples from melt-blending process with a-b) 2 wt%, c-d) 10 wt% of CNT and from solution mixing process with e-f) 2 wt% CNT, g-h) - 40 wt% CNT.

Fig. 3.6 shows the cross-plane thermoelectric properties (σ, κ, S, ZT) of thick Sc-PLA/CNT discs as a function of CNT content (vol%) at room temperature for both elaboration processes.

Fig. 3.6 a illustrates the anisotropy of electrical conductivity of Sc-PLA/CNT thick discs, where the $\sigma_{in\text{-}plane}$ is 100-1000 times higher than $\sigma_{cross\text{-}plane}$. The underlying rationale of this behavior has already been deliberated in the publication (section 2.3.3), and will not be discussed again. Note that the order of magnitude for σ values is comparable to that observed for the thick discs of A-PLA/CNT nanocomposite. In addition, we also observe the similarity in σ of samples from the two elaboration processes which is similar to that in the case of A-PLA/CNT.

Following the same evolution as A-PLA/CNT samples, Sc-PLA/CNT nanocomposites also show a linear increase in thermal conductivity as function of CNT content, in which the minimum value is 0.19 W m^{-1} K^{-1} for pristine Sc-PLA and, and the maximum is 0.8 W m^{-1} K^{-1} for the sample containing 40 wt% CNT (Fig. 3.6 b), *i.e.* in the same order of magnitude that for A-PLA/CNT samples.

The cross-plane Seebeck coefficient decreases as a function of CNT, as presented in Fig. 3.6c. The values fall within the range of 9 – 12 µV K^{-1} for nanocomposites from two elaboration processes, which is consistent with the range of values observed for A-PLA/CNT sample.

Finally, the ZT value has been calculated at 300 K, and the results are graphically presented in Fig. 3.6d as a function of CNT concentration. The data exhibits a consistent upward trend with increasing CNT content, with the highest achieved value reaching 4.2 x 10^{-8} for the sample containing 40 wt% CNT prepared through the solution mixing process. Due to no clear difference in the values of σ, κ, and S between both elaboration processes up to 10 wt%, the final ZT in this section appears to be independent of the elaboration processes.

The similarity in the cross-plane thermoelectric properties between the thick discs of Sc-PLA/CNT and A-PLA/CNT nanocomposites could be attributed to the fabrication process. Specifically, the thermo-compression process, followed by fast cooling condition step, results in an amorphous structure in the thick Sc-PLA/CNT discs, as confirmed by the results from DSC and WAXS in section 2.3.2. Therefore, in this research, the Sc-PLA/CNT nanocomposites obtained through the fast cooling condition correspond to an amorphous sample with thermoelectric properties similar to those of A-PLA/CNT. Additionally, these results serve as evidence that the thermoelectric properties are independent of the elaboration process when the CNT content used exceeds the percolation threshold.

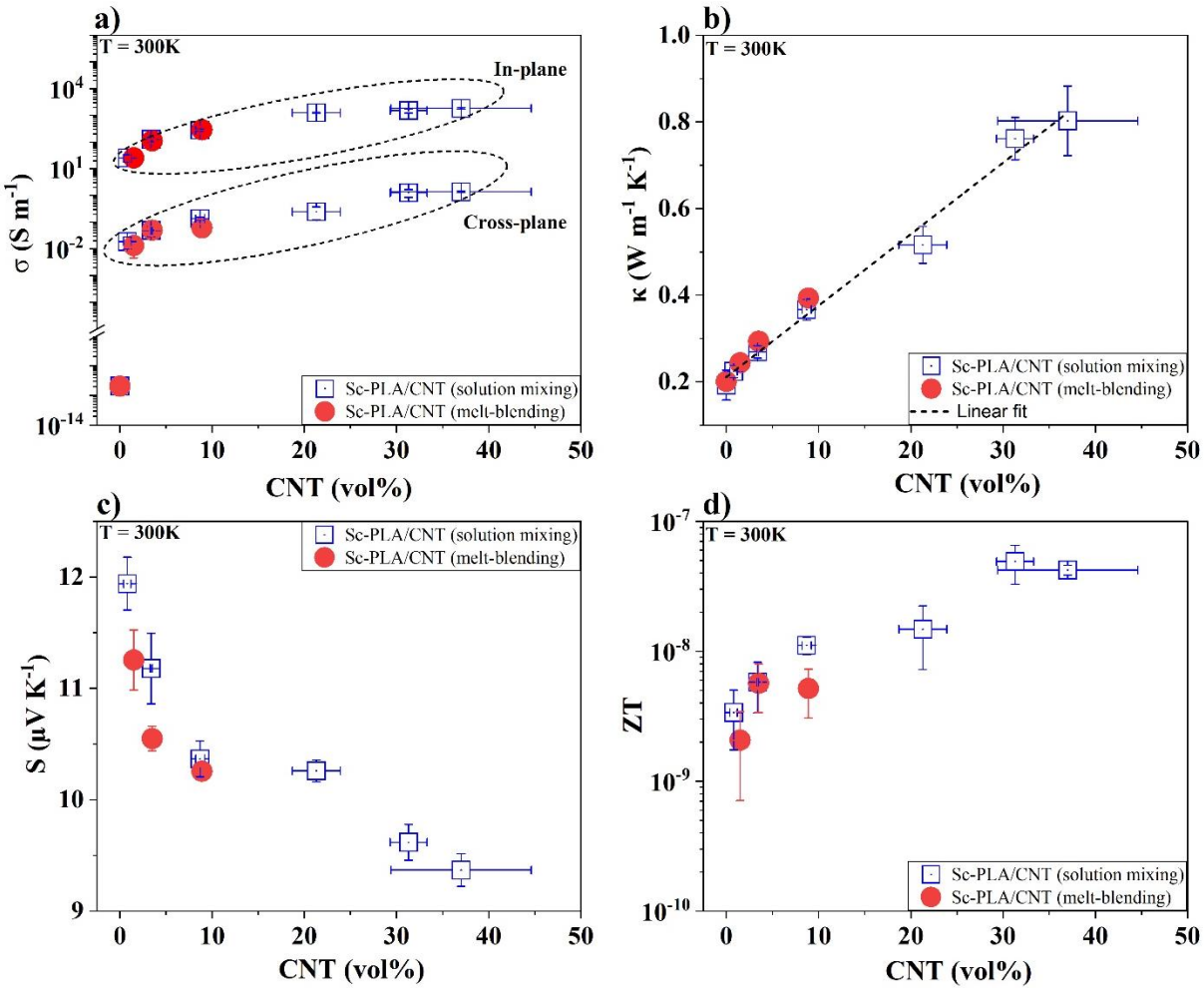

Figure 3.6. Cross-plane thermoelectric properties of nanocomposites-based Sc-PLA as a function of CNT volume fraction. a) electrical conductivity (σ), b) thermal conductivity (κ), c) Seebeck coefficient (S), and d) figure of merit (ZT).

6. Conclusion

Thick discs of PLA/CNT nanocomposites containing CNT concentration that far exceeds the percolation threshold (from 2 to 40 wt% CNT) were prepared by different elaboration processes and cross-plane thermoelectric properties were investigated at room temperature. The first result demonstrated that thermoelectric properties of all nanocomposites were independent on the elaboration processes. Crystallinity was induced into the Sc-PLA matrix to evaluate the impact of the crystalline structure on the thermoelectric properties. The results show that there was no impact of crystallinity degree on thermoelectric properties of PLA/CNT nanocomposites when the filler content exceeds the percolation threshold.

The impact of CNT orientation within the polymer matrix on the thermoelectric properties was investigated by deforming the thick samples at different levels. The results suggest that

both in-plane and cross-plane electrical conductivity decreases with material deformation, with a notable difference in the in-plane measurement along the direction of CNT.

Finally, an important outcome result of this chapter is that we have demonstrated the anisotropic characteristics of electrical conductivity and ZT values in thick disc nanocomposites, where in-plane values are 100 – 1000 times higher than the cross-plane values at the same CNT contents.

References

1. Michel, S., Chu, B. T. T., Grimm, S., Nüesch, F. A., Borgschulte, A., & Opris, D. M. (2012). Self-healing electrodes for dielectric elastomer actuators. *Journal of Materials Chemistry*, *22*(38), 20736. https://doi.org/10.1039/c2jm32228e

2. Iglesias, S. (2019). Composites conducteurs polymères hautement déformables pour la récupération d'énergie houlomotrice. *INSA-Lyon*.

3. Goh, P. S., Ismail, A. F., & Ng, B. C. (2014). Directional alignment of carbon nanotubes in polymer matrices: Contemporary approaches and future advances. *Composites Part A: Applied Science and Manufacturing*, *56*, 103–126. https://doi.org/10.1016/j.compositesa.2013.10.001

4. Bliznyuk, V. N., Singamaneni, S., Sanford, R. L., Chiappetta, D., Crooker, B., & Shibaev, P. V. (2006). Matrix mediated alignment of single wall carbon nanotubes in polymer composite films. *Polymer*, *47*(11), 3915–3921. https://doi.org/10.1016/j.polymer.2006.03.072

Chapter IV. Thermoelectric properties of thin film PLA/CNT nanocomposites

1. Introduction

The aim of chapter 4 is to discuss the TE properties of thin A-PLA/CNT films. For that, A-PLA was chosen as the polymer matrix and three kinds of fillers including MWCNT, SWCNT, and SWCNT-COOH were selected. The nanocomposites were prepared by solution mixing with filler content up to 40 wt%. All the thermoelectric properties were assessed on the sample surface (in-plane measurements) by TFA.

In chapter 3, the in-plane TE properties of thin A-PLA/MWCNT films were compared with the cross-plane TE properties of thick A-PLA/MWNCT discs at room temperature (300 K). The obtained results allowed to clarify the anisotropic behavior of electrical conductivity and thermoelectric properties for these PLA/CNT nanocomposites.

In the first part of this chapter, the influence of different types of CNT fillers (MWCNT, SWCNT, and SWCNT-COOH) on the thermoelectric properties of PLA-based nanocomposites will be investigated. The electrical conductivity, thermal conductivity, and Seebeck coefficient were systematically measured and compared at 300 K. The expected result will be valuable for comparing and optimizing the thermoelectric performance of PLA/CNT nanocomposites.

In the second part of this chapter, the temperature-dependence of thermoelectric properties for these three kinds of nanocomposites was shown over a temperature range from 300 to 400 K. This evolution will provide information about the relationship between temperature and thermoelectric properties of thin PLA/CNT films.

2. Effect of carbon nanotube type (MWCNT, SWCNT, and SWCNT-COOH) on thermoelectric properties at 300K

In this section, in order to improve the TE properties of our nanocomposites, the results obtained with MWCNT, previously studied, are compared to those of SWCNT and functionalized SWCNT-COOH at room temperature.

2.1. Electrical conductivity

The in-plane electrical conductivities of thin films of A-PLA-based nanocomposites filled with different types of CNT are shown in Fig 4.1 and Table 4.1. As expected, it can be seen that the $\sigma_{in-plane}$ values of all the nanocomposites increased with CNT concentration. Regarding the effect of CNT nature, the best values of $\sigma_{in-plane}$ are obtained for A-PLA/SWCNT nanocomposites are 10 times higher than those obtained for A-PLA/MWCNT. The A-PLA/SWCNT-COOH nanocomposites display intermediate $\sigma_{in-plane}$ values. Here, the highest values obtained with 40 wt% of MWCNT, SWCNT, are SWNCT-COOH are 3.5 x 10^3 S m^{-1}, 1.3 x 10^5 S m^{-1}, and 3.5 x 10^4 S m^{-1}, respectively**.** Compared with the σ values of insulating polymer-based nanocomposites summarized in Table 9 and 10 of Chapter 1, it is observed that these obtained values are in the same order of magnitude at the same filler contents of CNT.

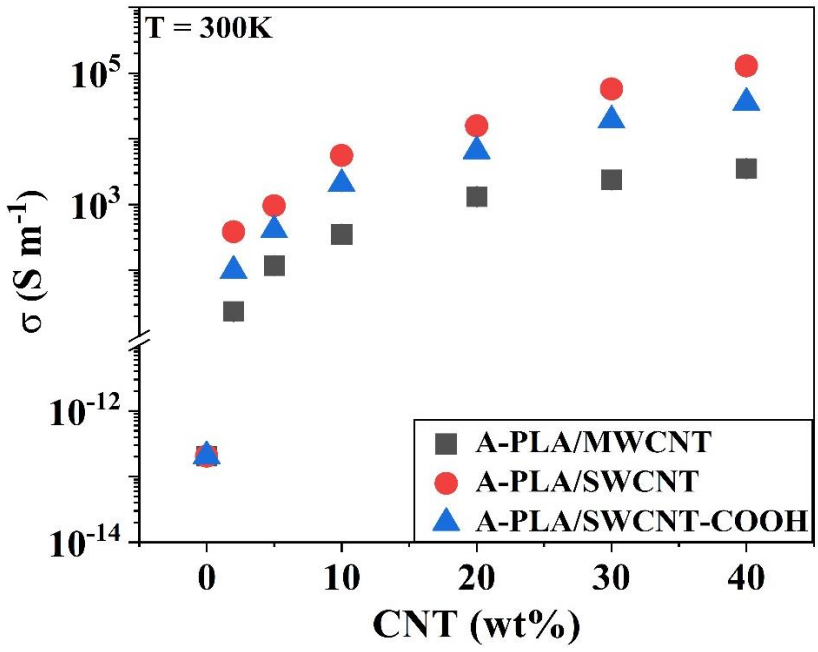

Figure 4.1. In-plane electrical conductivity measured by TFA of thin A-PLA/CNT (MWCNT, SWCNT, and SWCNT-COOH) films at 300 K as a function of CNT weight fraction.

Table 4.1. Electrical conductivity measured by TFA of thin A-PLA/CNT (MWCNT, SWCNT and SWCNT-COOH) films at 300 K. The uncertainty of these values is 6 %.

CNT (wt%)	$\sigma_{A\text{-}PLA/MWCNT}$ (S m^{-1})	$\sigma_{A\text{-}PLA/SWCNT}$ (S m^{-1})	$\sigma_{A\text{-}PLA/SWCNT\text{-}COOH}$ (S m^{-1})
Pristine A-PLA	2.0×10^{-13}	2.0×10^{-13}	2.0×10^{-13}
2	2.4×10^{1}	3.8×10^{2}	9.8×10^{1}
5	1.2×10^{2}	9.6×10^{2}	4.0×10^{2}
10	3.5×10^{2}	5.6×10^{3}	2.0×10^{3}
20	1.3×10^{3}	1.6×10^{4}	6.5×10^{3}
30	2.4×10^{3}	5.7×10^{4}	1.9×10^{4}
40	3.5×10^{3}	1.3×10^{5}	3.5×10^{4}

It is well known that the difference in the structure between MWCNT and SWCNT leads to a difference in electrical conductivity [1]. SWCNT consist of a single layer of carbon atoms and can be visualized as a rolled-up sheet of graphene. Therefore, the transport of electrons can only occur over distances along the wall axis of the tubes. Meanwhile, electron transport through MWCNT is more complex, involving movement both along the wall axis and between different layers. This complexity results in lower conductivity compared to SWCNT [2].

Regarding the difference in electrical conductivity between nanocomposites filled with SWCNT and SWCNT-COOH, the lower value of SWCNT-COOH compared to SWCNT could be attributed to two main reasons as proposed in literature. Firstly, the introduction of a functional group - COOH into a conjugated π-electron system induces the carbon hybridization from sp^2 to sp^3, the structural changes interrupt the conjugation and induce a distortion of the SWCNT layer. According to [3], this phenomenon induces the half-occupied state around the Fermi level and significantly may affect the carrier transport of nanotubes. In addition, these sp^3 carbons on the SWCNT wall can also be regarded as defects or scattering centers, which reduce the conductivity of nanotubes [4].

To conclude, using SWCNT showed a significant enhancement in the electrical conductivity of nanocomposites compared to using MWCNT. Although A-PLA/SWCNT-COOH nanocomposites show a lower conductivity than A-PLA/SWCNT ones, the value is still 10 times higher than that of MWCNT based films. Therefore, in general, SWCNT demonstrate a potential to improve the electrical performances of PLA/CNT nanocomposites.

2.2. Thermal conductivity

The thermal conductivity of all A-PLA/CNT nanocomposites is shown in Fig 4.2 and Table 4.2. As expected, the κ values increase with CNT fraction and are between 0.15 W m^{-1} K^{-1} for 2 wt% of CNT and 1.0 W m^{-1} K^{-1} for 40 wt% of CNT. As can be seen, the values are just slightly higher in the case of SWCNT than for MWCNT, which is far less significant compared to the evolution of the electrical conductivity: for concentrations higher than 5 wt%, a difference of 10 % only is observed. In addition, although the functional groups can act as defects on the surface of SWCNT, and could then decrease the thermal conductivity, COOH-functionalized SWCNT do not show any significant effect on the thermal conductivity of the PLA-based nanocomposites at a same filler content. These values are close to those already reported for PLA/CNT nanocomposites which mostly range between 0.2 – 1.0 W m^{-1} K^{-1} [5,6].

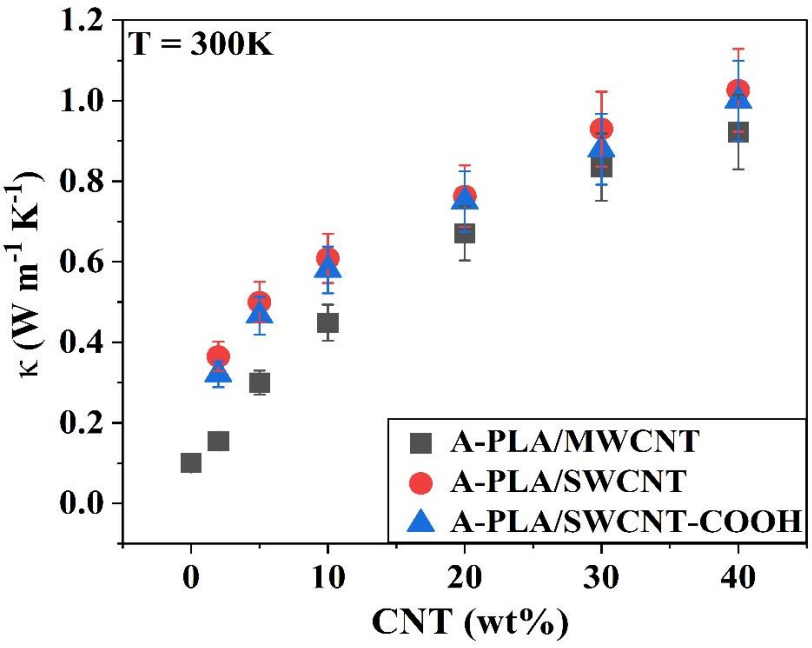

Figure 4.2. Thermal conductivity measured by TFA of thin A-PLA/CNT (MWCNT, SWCNT, and SWCNT-COOH) films at 300 K as a function of CNT weight percent.

Table 4.2. Thermal conductivity measured by TFA of thin A-PLA/CNT (MWCNT, SWCNT and SWCNT-COOH) films at 300 K. The uncertainty of these values is 10 %.

CNT (wt%)	$\kappa_{A\text{-}PLA/MWCNT}$ (W m^{-1} K^{-1})	$\kappa_{A\text{-}PLA/SWCNT}$ (W m^{-1} K^{-1})	$\kappa_{A\text{-}PLA/SWCNT\text{-}COOH}$ (W m^{-1} K^{-1})
Pristine A-PLA	0.10	0.10	0.10
2	0.15	0.36	0.32
5	0.30	0.50	0.47
10	0.45	0.61	0.58
20	0.67	0.76	0.75
30	0.84	0.93	0.88
40	0.92	1.0	0.99

As mentioned in Chapter 1, the thermal conductivity of MWCNT and SWCNT can significantly vary from 6000 W m^{-1} K^{-1}, for a perfect individual tube, to below 0.1 W m^{-1} K^{-1} for some bundled forms, almost perfect insulators [7]. The lower thermal conductivity for MWCNT is due to higher phonon scattering through all the inner walls. The SWCNT also show a high number of phonon vibrational modes, but a relatively low defect density compared to MWCNT, leading to a potentially higher thermal conductivity [8]. It is also important to notice that even with nanotube concentrations as high as 40 wt%, the thermal conductivity does not exceed 1.0 W m^{-1} K^{-1}, indicating a clear decorrelation between electrical and thermal conductivity, and confirming that the contribution of phonons is greater than that of charge carriers [7]. In addition, this low thermal conductivity, whereas the electrical conductivity is hugely enhanced, is a key property for the optimization of thermoelectric performances.

2.3. Seebeck coefficient

Fig. 4.3 and Table 4.3 show the Seebeck coefficients obtained with TFA for the 3 A-PLA/CNT nanocomposite types. All values are positive, meaning that the majority of the charge carriers are holes, which is consistent with the behavior of p-type semiconductors of MWCNT and SWCNT [9].

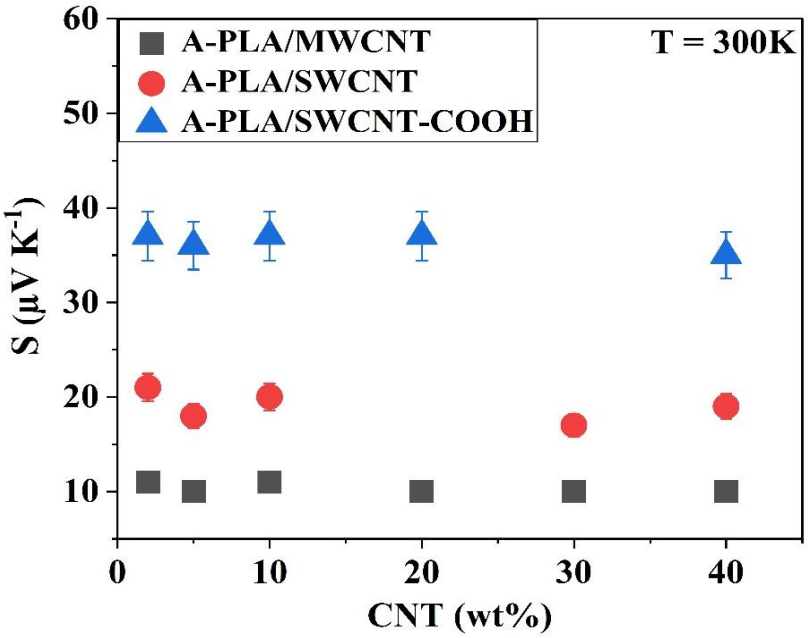

Figure 4.3. Seebeck coefficient measured with TFA of thin A-PLA/CNT (MWCNT, SWCNT, and SWCNT-COOH) films at 300 K as a function of CNT weight fraction.

Table 4.3. Seebeck coefficient values of thin A-PLA/CNT (MWCNT, SWCNT, and SWCNT-COOH) films at 300 K. The uncertainty of these values is 7 %.

CNT (wt%)	$S_{A\text{-}PLA/MWCNT}$ ($\mu V\ K^{-1}$)	$S_{A\text{-}PLA/SWCNT}$ ($\mu V\ K^{-1}$)	$S_{A\text{-}PLA/SWCNT\text{-}COOH}$ ($\mu V\ K^{-1}$)
2	11	21	37
5	10	18	36
10	11	20	37
20	10	-	37
30	10	17	-
40	10	19	35

In the case of SWCNT-COOH, it should be mentioned that the carboxyl group (- COOH) affects the structure of SWCNT backbone as the electron-withdrawing leading to the introduction of holes in the SWCNT structure as charge carriers, so that the Seebeck coefficient for A-PLA/SWCNT-COOH nanocomposites is also in positive sign [10]. As observed in the previous section, one can see that the values as a function of filler content are unexpectedly almost constant, or just slightly decreasing. Nevertheless, the 3 sets of measures are significantly different: A-PLA/SWCNT-COOH nanocomposites exhibit the highest Seebeck coefficients around 35~37 μV K^{-1}, then 20~21 μV K^{-1} for SWCNT and finally 10~11 μV K^{-1} for MWCNT (the lowest). These results are close to those reported by Lan *et al.* [4], which are

34.8 µV K^{-1} and 21.7 µV K^{-1} for SWCNT-COOH and SWCNT films, respectively. Such a significant increase between SWCNT and SWCNT-COOH is due to the local conversion of sp^2 to sp^3 hybridized bonding by the introduction of functional groups on the SWCNT walls. According to Lan *et al.*, this effect brings a significant impact on the charge carrier scattering, resulting in a decreased charge carrier concentration and an increased Seebeck coefficient. In addition, the Seebeck coefficient is directly related to an asymmetric shape of density of states (DOS) around the Fermi level [11]. It can be assumed that the introduction of – COOH groups on SWCNT backbone can promote an asymmetry increase in the DOS at the Fermi level, leading to an enhancement of the Seebeck coefficient.

When comparing our Seebeck values with those of all nanocomposites summarized in Table 1.9 and 1.10 of Chapter 1, the Seebeck values obtained in this study are within the same order of magnitude. They typically fall in the range of 9 and 14 µV K^{-1} for MWCNT, and in the range of 24 and 58 µV K^{-1} for SWCNT-based nanocomposites. The only exception is the value of 325 µV K^{-1}, reported by Du *et al.* [12], for a porous PVDF/MWCNT nanocomposite containing 15 wt% of fillers.

2.4. Figure of merit

The figure of merit (ZT) has been calculated at 300 K. The CNT concentration dependence of ZT has been reported in Fig. 4.4 and Table 4.4. As can be seen, ZT evolution for all nanocomposites followed the same trend as the electrical conductivity, showing a continuous increase up to 20 wt% of fillers and then more or less a plateau. It is interesting to note that A-PLA/SWCNT and A-PLA/SWCNT-COOH nanocomposites eventually exhibit the same values, the higher electrical conductivity of one offsetting the higher Seebeck of the other. More interesting is that due to their much higher Seebeck coefficient and electrical conductivity values, these nanocomposites have a much higher ZT, of 2 orders of magnitude, than A-PLA/MWCNT ones for the same filler content, which increase from 1.2 x 10^{-4} for 2 wt% of fillers content up to 0.02 for 40 wt% compared to 5.4 x 10^{-6} and 1.4 x 10^{-4}, respectively.

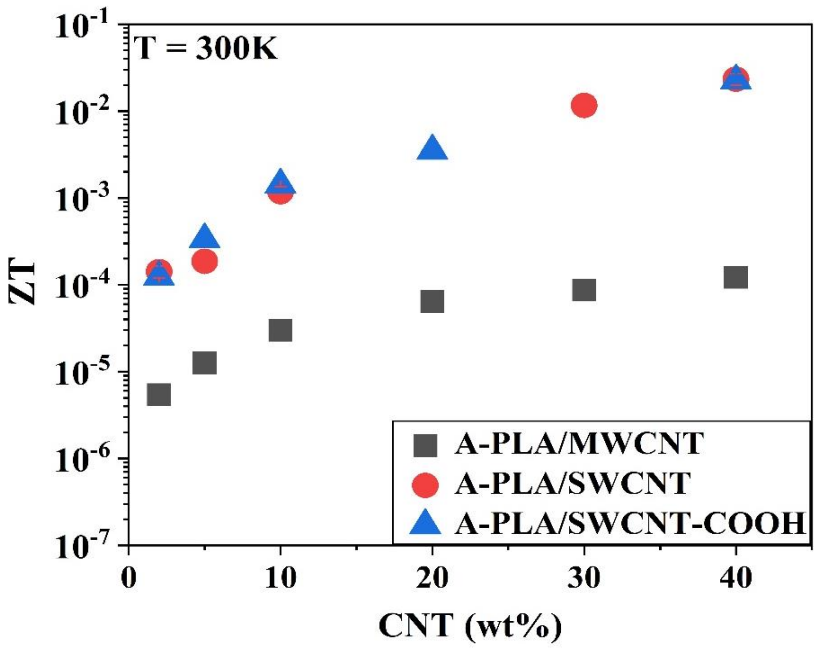

Figure 4.4. Figure of merit of thin A-PLA/CNT (MWCNT, SWCNT, and SWCNT-COOH) films at 300 K as a function of CNT weight fraction deduced from TFA measurements.

Table 4.4. Figure of merit values of thin A-PLA/CNT (MWCNT, SWCNT, and SWCNT-COOH) films at 300 K.

CNT (wt%)	$ZT_{A\text{-}PLA/MWCNT}$	$ZT_{A\text{-}PLA/SWCNT}$	$ZT_{A\text{-}PLA/SWCNT\text{-}COOH}$
2	5.4×10^{-6}	1.4×10^{-4}	1.2×10^{-4}
5	1.3×10^{-5}	1.8×10^{-4}	3.3×10^{-4}
10	3.0×10^{-5}	1.2×10^{-3}	1.4×10^{-3}
20	6.4×10^{-5}	-	3.5×10^{-3}
30	8.7×10^{-5}	1.2×10^{-2}	-
40	1.2×10^{-4}	2.3×10^{-2}	2.2×10^{-2}

As far as we know, ZT = 0.023 at room temperature is one of the best ZT value that can be found in the literature for a thermoplastic based nanocomposite filled with SWCNT. Until now, one of the highest value that has been found was 0.006 for PVAc/20 wt% SWCNT [13], which is fully comparable to the value found in this work for similar SWCNT content.

3. The evaluation of thermoelectric properties as a function of temperature (300 – 400 K)

In this section, the evolution with temperature of the thermoelectric properties of the 3 sets of previous thin nanocomposites is studied. The temperature range between 300 and 400 K corresponds to the possible range of use of these materials. Moreover, as the glass transition of

the polymer matrix occurs in this temperature range, it is also interesting to analyze the evolution of TE properties as a function of the glassy or rubbery state of the polymer.

3.1. Electrical conductivity

The evolution of in-plane electrical conductivity on temperature range from 300 to 400 K of all A-PLA/CNT nanocomposites is shown in Fig. 4.5. In the graphs (a-c) of this figure logarithmic-linear scale is used. It can be observed that whatever the CNT type and the CNT content, σ varies poorly with temperature. Generally speaking, as shown previously, the SWCNT-based nanocomposites has better electrical conductivity than the nanocomposites containing SWCNT-COOH fillers, and the lowest electrical conductivity is obtained for nanocomposites containing MWCNT.

To better visualize the effect of T on σ, Fig. 4.5 (a1-c1) presents the normalized electrical conductivity of nanocomposites containing the lowest (2 wt%) and the highest (40 wt%) CNT content, expressed as $\sigma(\mathrm{K})/\sigma(300\ \mathrm{K})$. Over the investigated temperature range, the electrical conductivity does not increase more than 6-8 %. Moreover, different behaviors depending of the type of CNT are highlighted. In the case of A-PLA/MWCNT nanocomposites, the electrical conductivity tends to exhibit a positive correlation with increasing temperature, indicative of a semiconductor behavior [14]. Meanwhile, in the cases of A-PLA/SWCNT and A-PLA/SWCNT-COOH, the conductivity exhibits a decreasing trend over a certain temperature range, rather indicative of a metallic behavior [15]. This result should be related to the composition of the commercial powder batch of SWCNT. Indeed, it is worth reminding that statistically, 1/3 of a commercial powder batch of SWCNT has metallic properties, and the remaining 2/3 exhibits a semiconducting electronic structure [16]. In addition, over the studied temperature range, it can be observed an inflection point between 50 – 70 °C (323 – 343 K) in these conductive curves, *i.e.* around the glass transition temperature (T_g). As the filler content increases, this inflection around the T_g region is less pronounced, or even no present for nanocomposites containing 40 wt% CNT. This behavior was observed in all three kinds of nanocomposites. These phenomena may be attributed to the movement of polymer chain within its glass transition temperature (T_g). In nanocomposite containing 2 wt% CNT, as the temperature approaches the T_g region, σ tends to be independent of the temperature. Considering that the conductivity is related to the connectivity of the conductive network, one may assume that the mobility of polymer chains may disrupt the conductive network established by the CNT. Meanwhile, in the cases of nanocomposite with a higher CNT content (40 wt%), the presence of a larger quantity of CNT and the extensive interconnections between them gives

rise to a significant number of electrical contacts. In these conditions, charge carrier conduction predominates, with minimal influence from the movement of polymer chains when the temperature is around T_g.

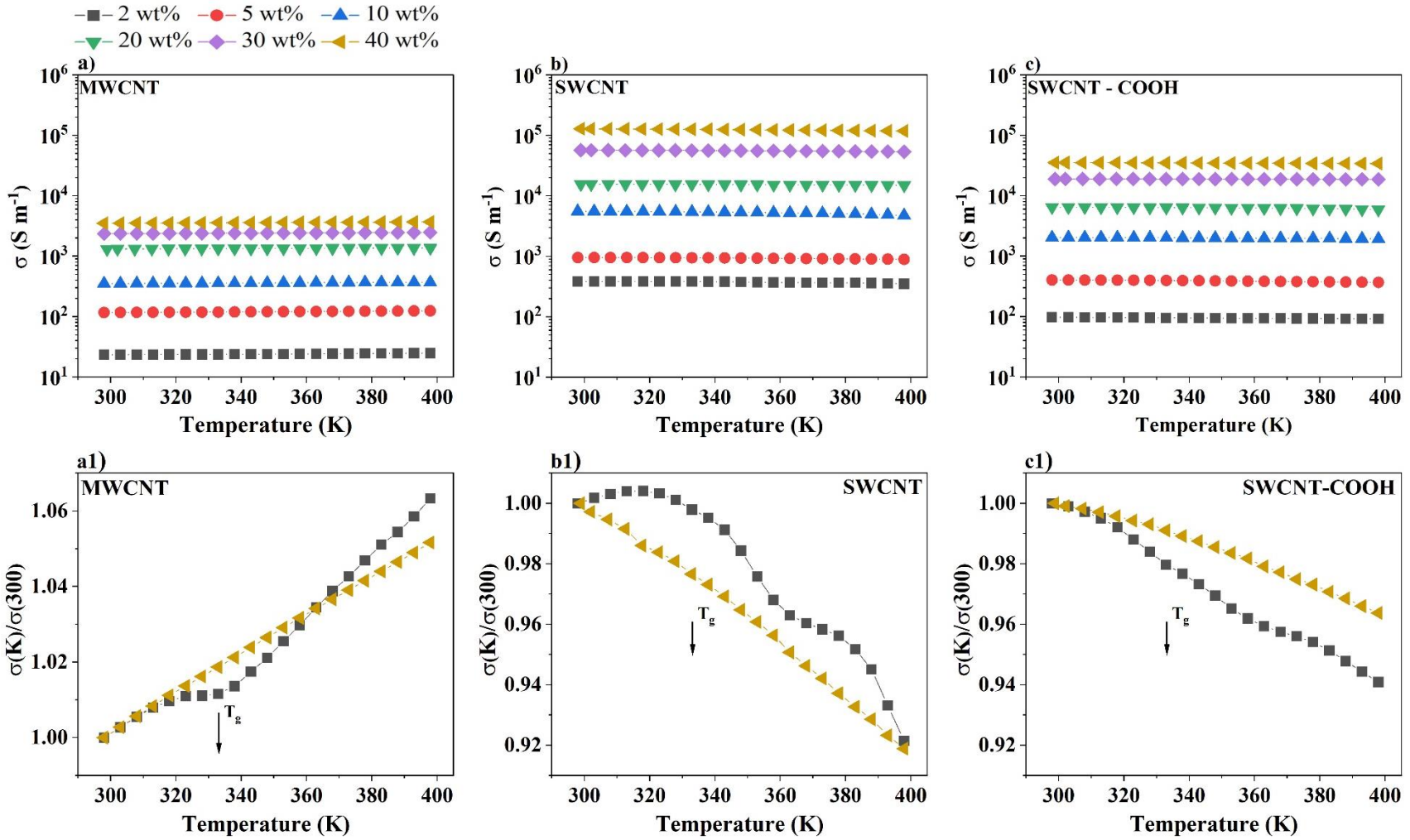

Figure 4.5. Evolution as a function of temperature of the electrical conductivity $\sigma(T)$ and the normalized conductivity $\sigma(K)/\sigma(300)$ of thin A-PLA/CNT films (measured with TFA): a) and a1) A-PLA/MWCNT, b) and b1) A-PLA/SWCNT, c) and c1) A-PLA/SWCNT-COOH. Normalized curves concern only for 2 and 40 wt% of fillers.

In order to discuss what mechanisms control the conduction of PLA/CNT nanocomposites, different theoretical models (presented in Chapter 1) were used.

According to literature, for a random distribution of the conducting particles, a linear relation between ln σ and $w^{-1/3}$ could support a charge transport by tunneling effect [17, 18]. A linear correlation between ln (σ) and $w^{-1/3}$ will be considered as soon as the correlation coefficient is higher than 0.98 [19]. Fig 4.6 a and b presents the ln (σ) versus $w^{-1/3}$ for all A-PLA/CNT nanocomposites at 300 K and 400 K. Based on the correlation coefficient values, only the PLA/MWCNT composites exhibit a linear behavior which suggests that charge carriers are rather transported by tunnel effect in these materials. By contrast, poor correlation is found for all SWCNT-based composites. This may be not surprising considering that as shown previously the behavior of these materials is rather metallic in the investigated temperature range.

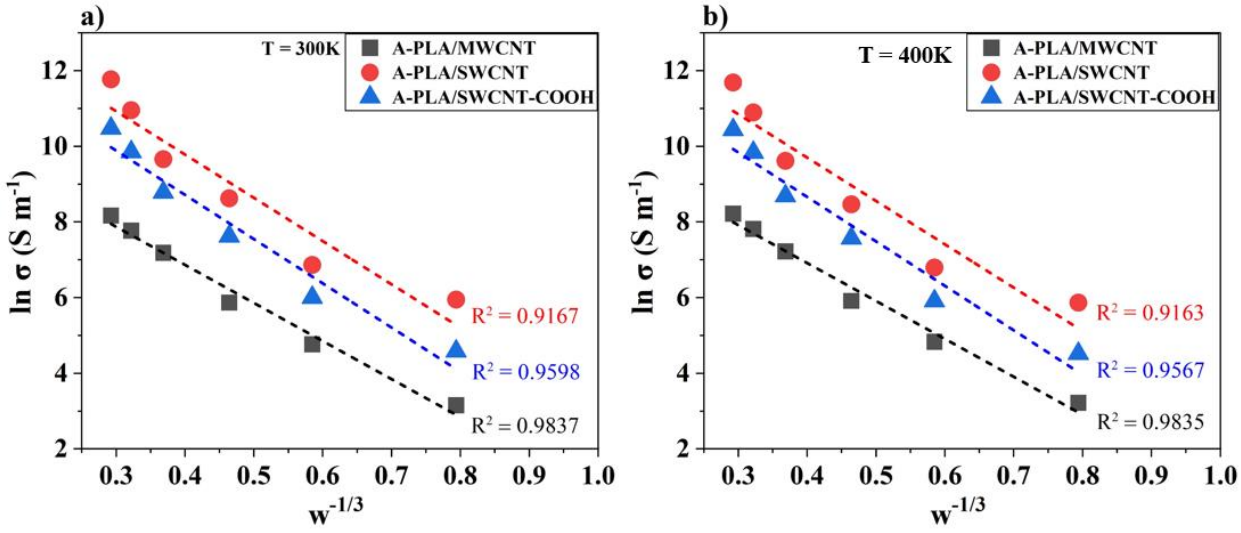

Figure 4.6. logarithmic plot of electrical conductivity versus $w^{-1/3}$ for A-PLA/CNT nanocomposites at 300 K (a) and 400 K (b), where w is the weight fraction.

To try to go further in the case of PLA/MWCNT nanocomposites, the (σ) as a function of T was fitted using the thermal Fluctuation Induced Tunneling (FIT) and the charging energy limited tunneling (CELT) models. Fig. 4.7 illustrates the results for nanocomposites containing 2 wt% and 40 wt% of MWCNT for both models. Considering the poorly evolution of σ with temperature and the error bars, both models are able to fit the experimental data. Also, over the studied temperature range, it is not possible to conclude about the tunneling conduction mechanisms involved in these A-PLA/MWCNT nanocomposites.

Note that in the case of the FIT model, the parameter T_0 which corresponds to the temperature above which the thermal activated conduction over the barrier begins to occur is found to be equal to 0, meaning that the FIT model is reduced to the Arrhenius law. In this case, the calculated activation energy is similar for both samples (Fig 4.7 e and f).

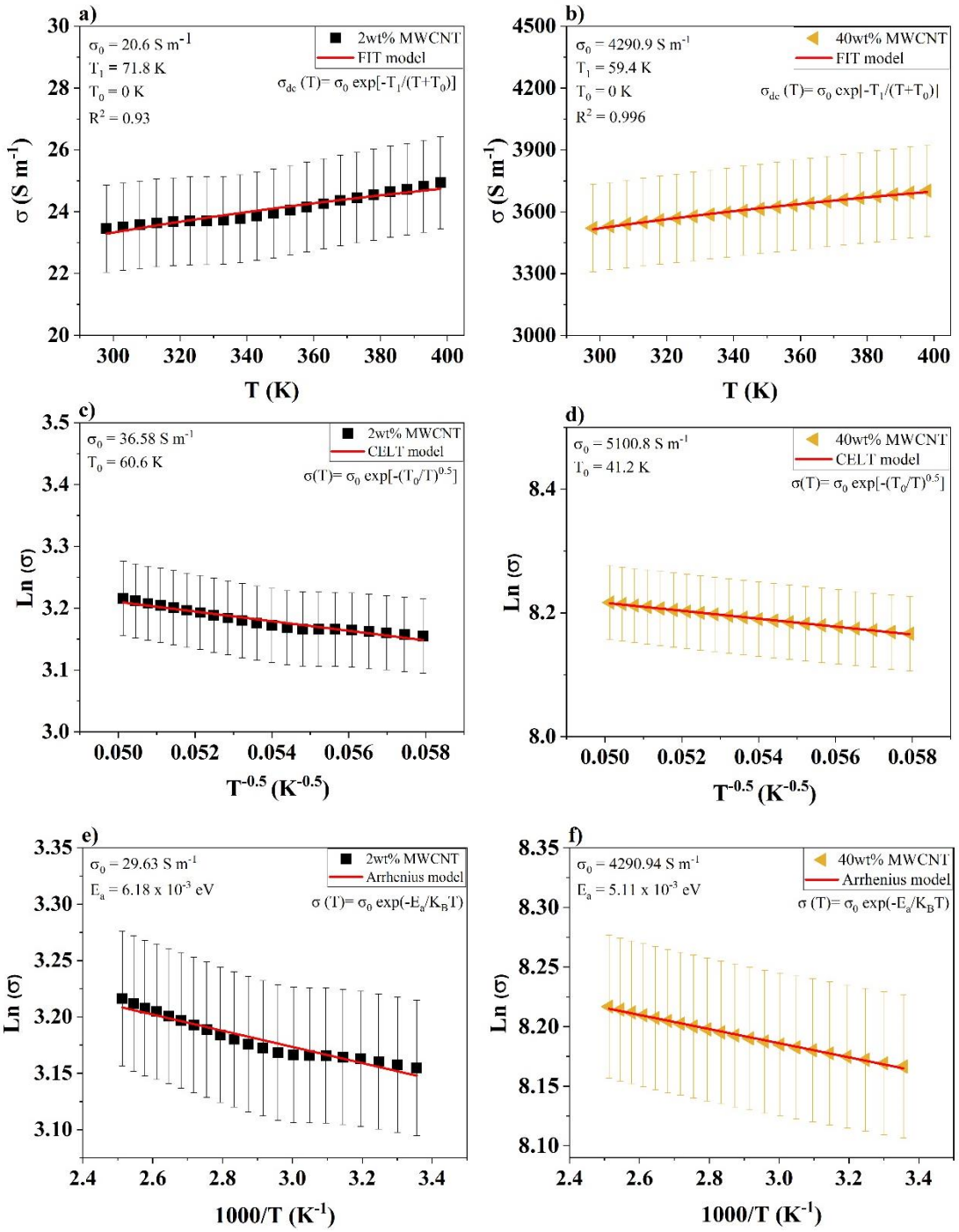

Figure 4.7. Fitting models for electrical conductivity values of A-PLA/MWCNT nanocomposites (2 and 40 wt% MWCNT). a) and b) corresponding to FIT model, c) and d) corresponding to CELT model, e) and f) corresponding to Arrhenius model.

3.2. Thermal conductivity

Fig 4.8 (a-c) shows the measured thermal conductivity κ over a temperature range between 300 and 400 K for all kinds of nanocomposites. Generally, no clear effect of T in κ values is observed when comparing the three nanocomposites at the same scale while the thermal conductivity increases with the CNT fillers content, as shown previously.

Regarding the temperature dependence of thermal conductivity, to better visualized the evolution of the results, the normalized conductivities $\kappa(K)/\kappa(300)$ are represented in Fig 4.8 (a1-b1) corresponding to A-PLA/MWCNT, A-PLA/SWCNT, and A-PLA/SWCNT-COOH nanocomposites, respectively. For the sake of clarity, only the curves for the lowest and highest concentrations of fillers are shown. The normalized curves have a change around the T_g region of the polymer matrix between 50 – 70 °C and this phenomenon is more pronounced for low concentrations of CNT and almost no visible for the highest CNT concentration. Moreover, we can notice the jump of the thermal conductivity around T_g is more marked for the PLA/MWCNT than for PLA/SWCNT nanocomposites. Theoretically, the thermal conductivity is related to the specific heat, the density, and the mean speed and the mean free path of the phonons. The evolution of the thermal conductivity looks like the increase specific heat with temperature suggesting that the main factor which governs κ(T) is the change of C_p(T).

According to the study of dos Santos *et al.* [20], the changes in thermal conductivity around T_g region can be explained in terms of molecular mobility. Below T_g, κ increases with temperature due to the specific heat increase effect and the fact that the mean free path of the phonons is assumed almost constant. When the temperature increases to T_g, the polymer undergoes a transition from a glassy state to the soft rubbery state. In the rubbery state (just above T_g), there is an increase in the large-scale mobility of macromolecules, and chain segments undergo thermal motion and torsional rotations. This introduction of movement in the polymer chains results in the formation of scattering center for phonons, leading to alterations in thermal conductivity. In the case of the nanocomposites containing high concentration of CNT, we can suspect that the large-scale mobility of chains is limited.

Note that, at temperatures well above the glass transition, the evolution of thermal conductivity as a function of temperature was not the same for the three kinds of nanocomposites. Indeed, in this study, nanocomposites containing MWCNT continue to show an increasing trend with temperature while SWCNT and SWCNT-COOH are almost temperature independent.

In conclusion, based on the normalized curve, it is possible to highlight an increase in thermal conductivity of each nanocomposite over the studied temperature range. From the lower to the highest temperature, the thermal conductivity increases of 20, 5 and 10 % for PLA/MWCNT, PLA/SWCNT and PLA/SWCNT-COOH, respectively.

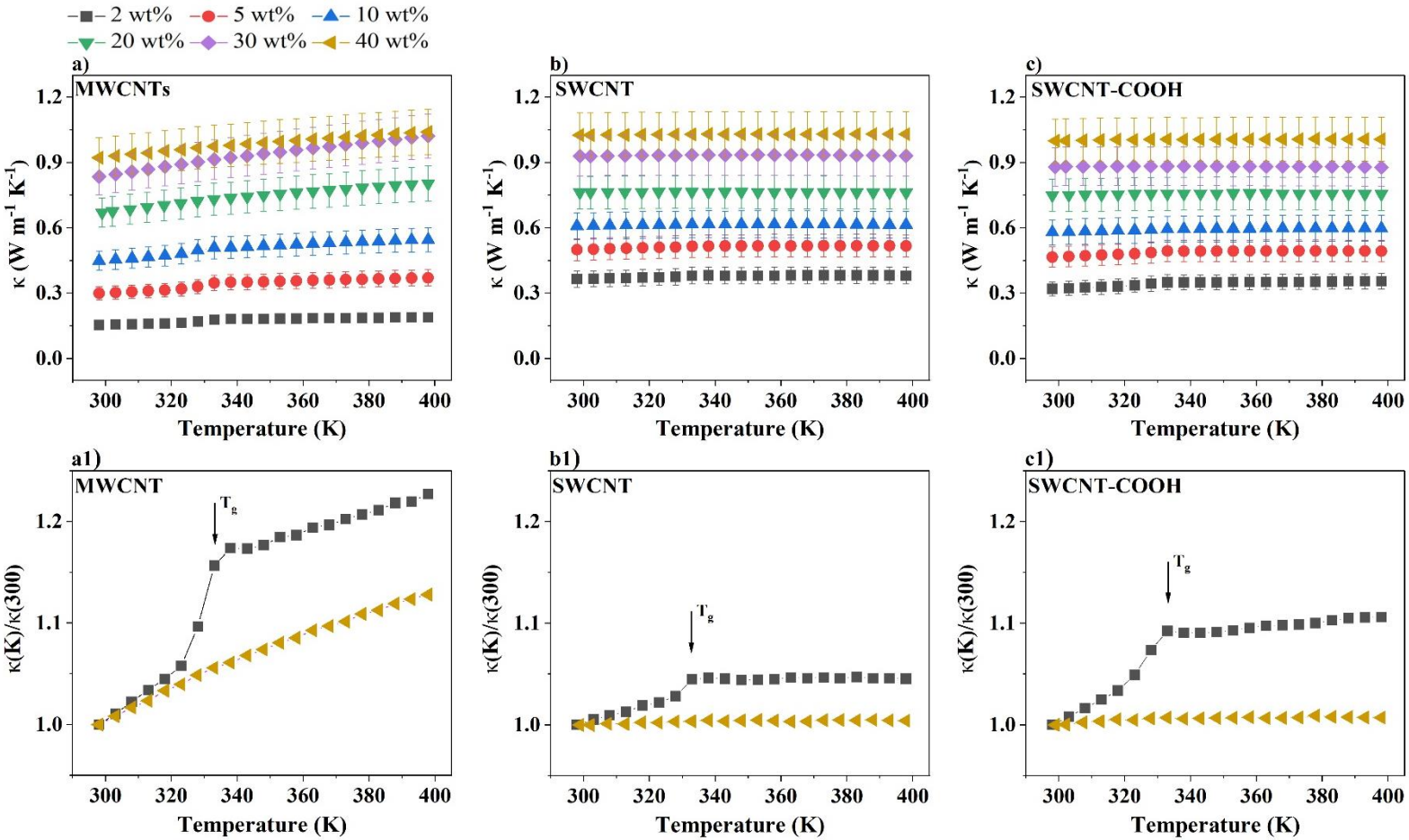

Figure 4.8. Thermal conductivity and normalized thermal conductivity evolutions of thin film nanocomposites as a function of temperature for various loading concentrations and measured with TFA: a) and a1) A-PLA/MWCNT, b) and b1) A-PLA/SWCNT, c) and c1) A-PLA/SWCNT-COOH. Normalized curves concern only for 2 and 40 wt% of fillers.

3.3. Seebeck coefficient

Fig. 4.9 (a-c) show the temperature dependence of the Seebeck coefficient for the previous studied nanocomposites. The Seebeck coefficient of the three types of nanocomposites increases almost linearly with the temperature, from 300 to 400 K. This could be expected considering the theoretical expression of the Seebeck coefficient (see eq. 1.7 in chapter I). By drawing S with the same scale, it can be observed that SWCNT-COOH nanocomposites show the highest Seebeck coefficient values, followed by SWCNT and then MWCNT ones. The reason for this difference has already been discussed in the section 2.3. In the considered temperature range, the Seebeck coefficient values are found to be between 10 and 11 µV K^{-1} for the A-PLA/MWCNT composite, between 19 and 25 µV K^{-1} for the A-PLA/SWCNT and between 35 and 43 µV K^{-1} for the A-PLA/SWCNT-COOH ones. In addition, there is no significant difference in the Seebeck coefficient value of each nanocomposite according to the increase in filler contents.

Unlike the two others parameters involved in thermoelectricity (σ and κ), the normalized Seebeck coefficient curves (S(K)/S(300)) of all nanocomposites are showed in Fig. 4.9 (a1-c1) for the lowest and the highest CNT concentration. Contrary to σ and κ, it can be observed that the glass transition of the polymer has no impact on Seebeck coefficient.

Over the investigated temperature range, the Seebeck coefficient increase of 40 to 60% for the three kind of nanocomposites. This increase is a good point to improve the ZT values and optimize the TE performance of nanocomposites A-PLA/CNT at high temperatures.

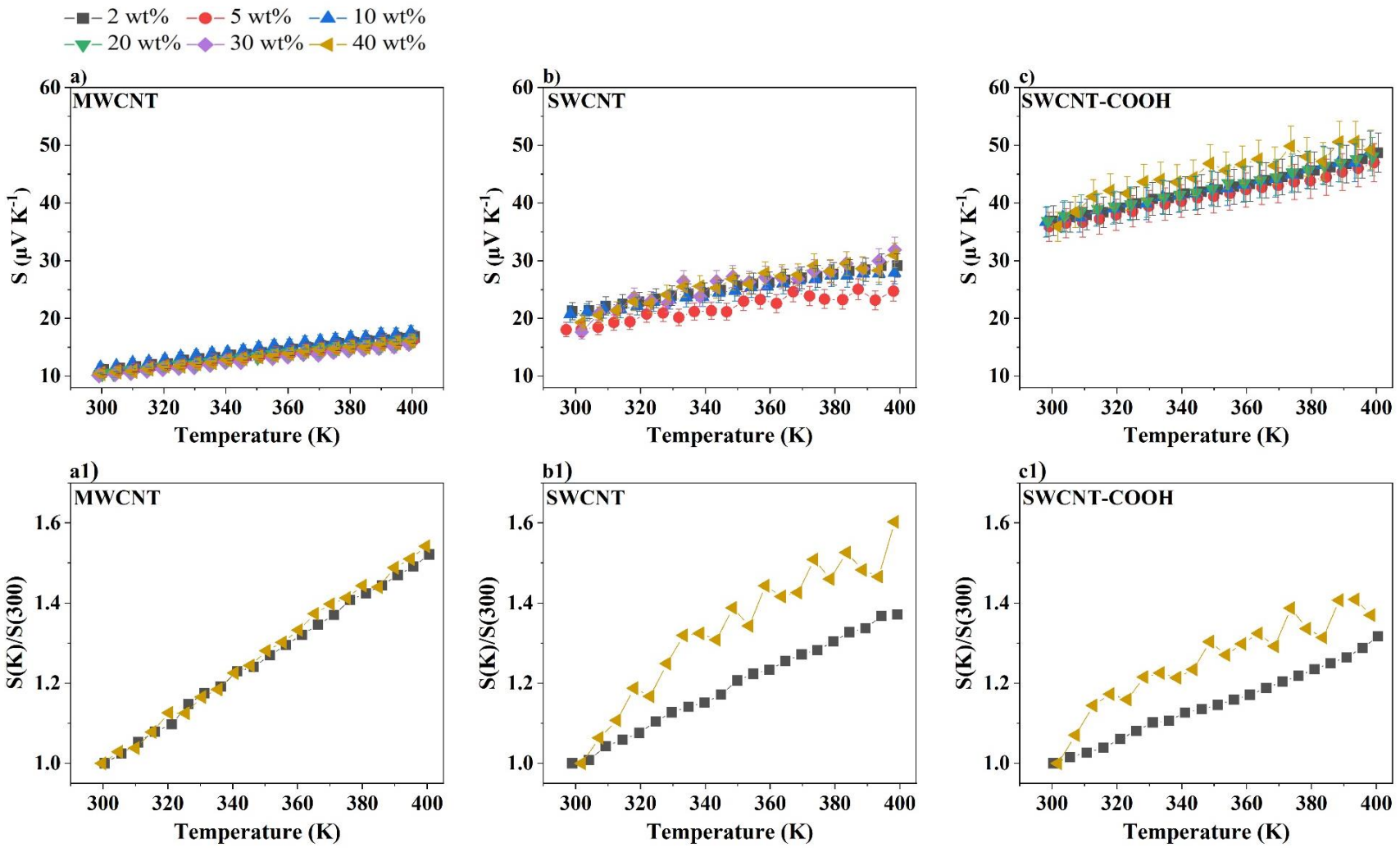

Figure 4.9. Seebeck coefficient and normalized Seebeck coefficient evolutions of thin film nanocomposites as a function of temperature for various loading concentrations and measured with TFA: a) and a1) A-PLA/MWCNT, b) and b1) A-PLA/SWCNT, c) and c1) A-PLA/SWCNT-COOH. Normalized curves concern only for 2 and 40 wt% of fillers.

3.4. Figure of merit

Finally, the temperature dependence of the figure of merit (ZT) is shown in Fig. 4.10 for the three previous types of nanocomposites. First of all, it can be seen that ZT increases nearly linearly with temperature. As already reported in the room temperature study of the previous section, an increase in ZT values is observed when the loading concentration increases. The ZT values of A-PLA/SWCNT and A-PLA/SWCNT-COOH nanocomposites appear 1000 times higher than those of the A-PLA/MWCNT sample. The highest ZT values are recorded at 400 K and 40 wt% fillers, *i.e.* 3.5×10^{-5} for A-PLA/MWCNT sample, 4.2×10^{-2} for A-PLA/SWCNT nanocomposite, and 3.3×10^{-2} for A-PLA/SWCNT-COOH one. The values at 400 K are almost double the values at 300 K and remain among the best values found in the literature for insulating polymer/SWCNT composites.

If we assume that the evolution of electrical and thermal conductivities over the studied temperature range (only 100 °C variation) is roughly constant, it is the increase of Seebeck coefficient values with temperature that leads to the improvement of ZT with temperature. Although the glass transition has an impact on the evolution with temperature of σ and κ, there is no evidence in the evolution of ZT, even when the concerned area is zoomed in. Finally, although the Seebeck coefficient evolution with temperature is more marked in A-PLA/SWCNT-COOH nanocomposites than in A-PLA/SWCNT ones, the achieved ZT values of both samples are in the same order of magnitude. Therefore, the introduction of -COOH functionalization in SWCNT in this study did not show any positive effect on the final ZT value.

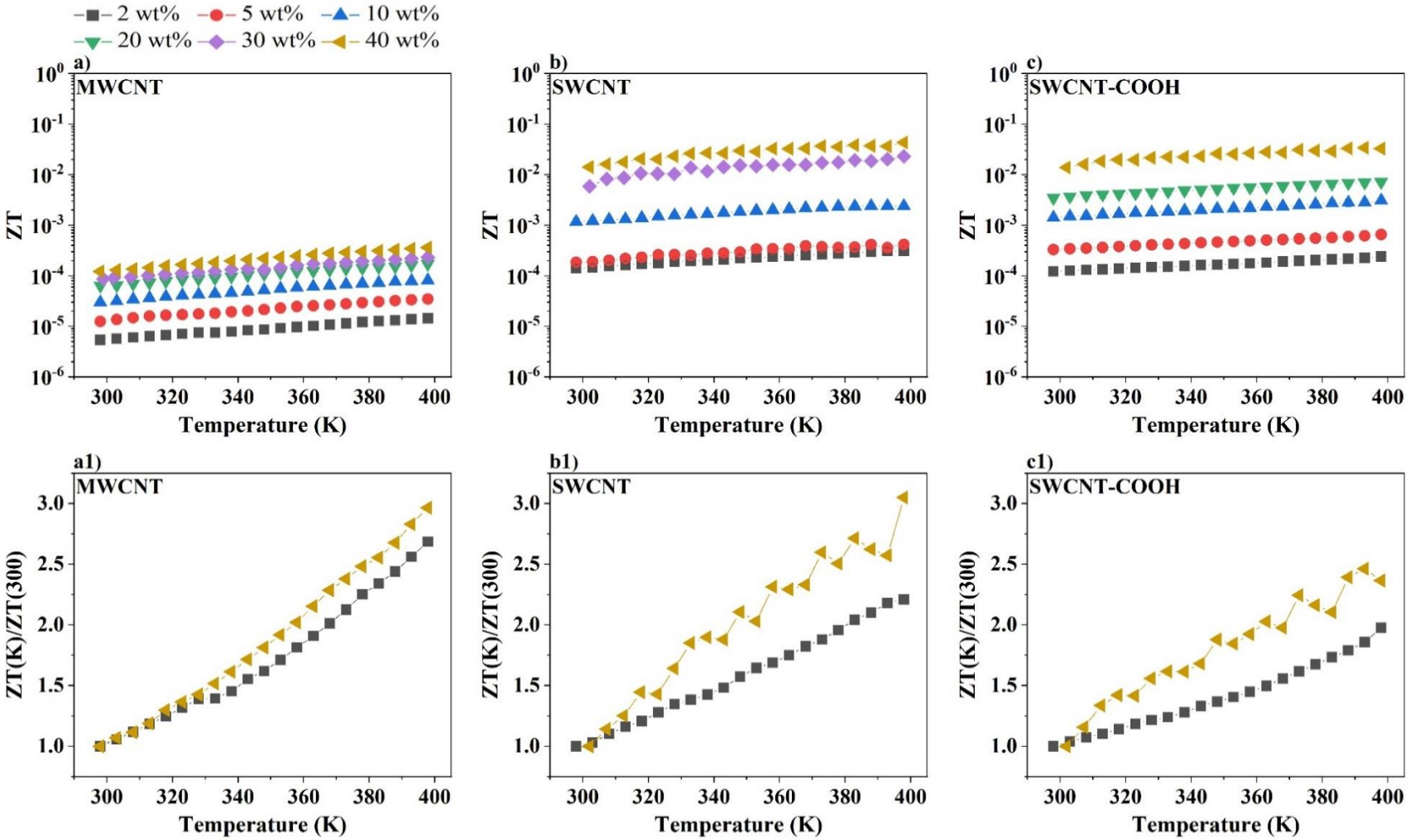

Figure 4.10. Figure of merit of thin films nanocomposites as a function of temperature for different filler concentration and obtained from TFA measurement: a) and a1) A-PLA/MWCNT, b) and b1) A-PLA/SWCNT, c) and c1) A-PLA/SWCNT-COOH. Normalized curves concern only for 2 and 40 wt% of filler

4. Conclusion

In summary, in this chapter, we have successfully characterized and compared the TE properties of thin film PLA-based nanocomposites with different kinds of fillers including MWCNT, SWCNT, and SWCNT-COOH whose loading concentration ranged from 2 to 40 wt%.

It can be found that SWCNT fillers significantly improve the thermoelectric performance of PLA/CNT nanocomposites, the maximum value achieved at room temperature and 40 wt% of loading is 2.3×10^{-2} compared with 1.2×10^{-4} of using MWCNT fillers. Meanwhile, although SWCNT-COOH fillers enhance the Seebeck coefficient value of nanocomposites, this functionalization of SWCNT lowers their electrical conductivity values leading to final ZT values in the same order of magnitude of A-PLA/SWCNT samples.

Finally, the evolution of thermoelectric properties of PLA/CNT (MWCNT, SWCNT, SWCNT-COOH) nanocomposites as a function of temperature was demonstrated from 300 K to 400 K. The results present the relationship between temperature and thermoelectric properties of PLA/CNT.

References

1. Bandaru, P. R. (2007). Electrical Properties and Applications of Carbon Nanotube Structures. *Journal of Nanoscience and Nanotechnology*, *7*(4), 1239–1267. https://doi.org/10.1166/jnn.2007.307

2. Miao, M. (2011). Electrical conductivity of pure carbon nanotube yarns. *Carbon*, *49*(12), 3755–3761. https://doi.org/10.1016/j.carbon.2011.05.008

3. Zhao, J., Park, H., Han, J., & Lu, J. P. (2004). Electronic Properties of Carbon Nanotubes with Covalent Sidewall Functionalization. *The Journal of Physical Chemistry B*, *108*(14), 4227–4230. https://doi.org/10.1021/jp036814u

4. Lan, X., Liu, C., Wang, T., Hou, J., Xu, J., Tan, R., … Jiang, F. (2019). Effect of Functional Groups on the Thermoelectric Performance of Carbon Nanotubes. *Journal of Electronic Materials*, *48*(11), 6978–6984. https://doi.org/10.1007/s11664-019-07519-6

5. Antar, Z., Feller, J. F., Noël, H., Glouannec, P., & Elleuch, K. (2012). Thermoelectric behaviour of melt processed carbon nanotube/graphite/poly(lactic acid) conductive biopolymer nanocomposites (CPC). *Materials Letters*, *67*(1), 210–214. https://doi.org/10.1016/j.matlet.2011.09.060

6. Ivanov, E., Kotsilkova, R., Xia, H., Chen, Y., Donato, R., Donato, K., … Angelov, V. (2019). PLA/Graphene/MWCNT Composites with Improved Electrical and Thermal Properties Suitable for FDM 3D Printing Applications. *Applied Sciences*, *9*(6), 1209. https://doi.org/10.3390/app9061209

7. Kumanek, B., & Janas, D. (2019). Thermal conductivity of carbon nanotube networks: a review. *Journal of Materials Science*, *54*(10), 7397–7427. https://doi.org/10.1007/s10853-019-03368-0

8. Namasivayam, M., & Shapter, J. (2017). Factors affecting carbon nanotube fillers towards enhancement of thermal conductivity in polymer nanocomposites: A review. *Journal of Composite Materials*, *51*(26), 3657–3668. https://doi.org/10.1177/0021998317692398

9. Zhang, H.-L., Li, J.-F., Zhang, B.-P., Yao, K.-F., Liu, W.-S., & Wang, H. (2007). Electrical and thermal properties of carbon nanotube bulk materials: Experimental studies for the 328 – 958 K temperature range. *Physical Review B*, *75*(20), 205407. https://doi.org/10.1103/PhysRevB.75.205407

10. Liebscher, M., Gärtner, T., Tzounis, L., Mičušík, M., Pötschke, P., Stamm, M., … Voit, B. (2014). Influence of the MWCNT surface functionalization on the thermoelectric properties of melt-mixed polycarbonate composites. *Composites Science and Technology*, *101*, 133–138. https://doi.org/10.1016/j.compscitech.2014.07.009

11. Russ, B., Glaudell, A., Urban, J. J., Chabinyc, M. L., & Segalman, R. A. (2016). Organic thermoelectric materials for energy harvesting and temperature control. *Nature Reviews Materials*, *1*(10), 16050. https://doi.org/10.1038/natrevmats.2016.50

12. Du, F.-P., Qiao, X., Wu, Y.-G., Fu, P., Liu, S.-P., Zhang, Y.-F., & Wang, Q.-Y. (2018). Fabrication of Porous Polyvinylidene Fluoride/Multi-Walled Carbon Nanotube Nanocomposites and Their Enhanced Thermoelectric Performance. *Polymers*, *10*(7), 797. https://doi.org/10.3390/polym10070797

13. Yu, C., Kim, Y. S., Kim, D., & Grunlan, J. C. (2008). Thermoelectric Behavior of Segregated-Network Polymer Nanocomposites. *Nano Letters*, *8*(12), 4428–4432. https://doi.org/10.1021/nl802345s

14. Yakuphanoglu, F., Yahia, I. S., Barim, G., & Filiz Senkal, B. (2010). Double-walled carbon nanotube/polymer nanocomposites: Electrical properties under dc and ac fields. *Synthetic Metals*, *160*(15–16), 1718–1726. https://doi.org/10.1016/j.synthmet.2010.06.007

15. Fuhrer, M. S., Cohen, M. L., Zettl, A., & Crespi, V. (1998). Localization in single-walled carbon nanotubes. *Solid State Communications*, *109*(2), 105–109. https://doi.org/10.1016/S0038-1098(98)00520-1

16. Xie, P., Sun, Y., Chen, C., Guo, S.-Y., Zhao, Y., Jiao, X., … Cheng, H.-M. (2023). Enrichment of Large-Diameter Semiconducting Single-Walled Carbon Nanotubes by Conjugated Polymer-Assisted Separation. *Nanomaterials*, *13*(13), 2001. https://doi.org/10.3390/nano13132001

17. Connor, M. T., Roy, S., Ezquerra, T. A., & Baltá Calleja, F. J. (1998). Broadband ac conductivity of conductor-polymer composites. *Physical Review B*, *57*(4), 2286–2294. https://doi.org/10.1103/PhysRevB.57.2286

18. Kilbride, B. E., Coleman, J. N., Fraysse, J., Fournet, P., Cadek, M., Drury, A., … Blau, W. J. (2002). Experimental observation of scaling laws for alternating current and direct current conductivity in polymer-carbon nanotube composite thin films. *Journal of Applied Physics*, *92*(7), 4024–4030. https://doi.org/10.1063/1.1506397

19. Iglesias, S. (2019). Composites conducteurs polymères hautement déformables pour la récupération d'énergie houlomotrice. *INSA-Lyon*.

20. dos Santos, W. N., de Sousa, J. A., & Gregorio, R. (2013). Thermal conductivity behaviour of polymers around glass transition and crystalline melting temperatures. *Polymer Testing*, *32*(5), 987–994. https://doi.org/10.1016/j.polymertesting.2013.05.007

Conclusion and perspectives

Conclusion

In this work, a comprehensive study to understand the correlation between elaboration, structure and thermoelectric properties of PLA/CNT nanocomposites was conducted. To do this, both industrial grades of PLA, an amorphous one and a crystallizable one, were chosen as a polymer matrix. Different types of CNT including MWCNT, SWCNT and functionalized SWCNT were selected as fillers.

The PLA-based nanocomposites filled with different percentages of CNT were prepared by two different elaboration processes: melt-blending (up to 10 wt% CNT) and solution mixing (up to 40 wt% CNT). In addition, two kinds of samples were elaborated: a) thick discs of PLA/MWCNT were prepared by thermocompression method, in which TE properties were characterized in the cross-plane direction, b) thin films (PLA/MWCNT, PLA/SWCNT and PLA/SWCNT-COOH) were obtained by drop-casting method for which in-plane TE properties were studied. The combination of the two previous elaboration processes (solution mixing and melt-blending) was also employed to prepare samples with the purpose to improve the dispersion of MWCNT in PLA matrix.

In the case of thick samples, it has been first shown that the dispersion of MWCNT in the PLA matrix was little affected by the elaboration process: for the lowest CNT concentrations, isolated CNT and CNT bundles have been observed, while a homogeneous dispersion of fillers was appeared at higher concentrations. As regards the polymer matrix, PLA was in amorphous state for all the nanocomposites, even for the crystallizable grade under the elaboration conditions used. Regarding the cross-plane thermoelectric properties, as expected, the ZT values increased according to filler content, the highest value reaching 4.9×10^{-8} for 40 wt% MWCNT at room temperature. This result was mainly attributed to a significant enhancement by several orders magnitude of the electrical conductivity σ with the addition of CNT, while the increase of thermal conductivity κ was very slight, and the decrease of the Seebeck coefficient S remained limited. The positive Seebeck values S indicated a p-type semi-conducting material. No clear difference in σ, κ, and S values between the melt-blending and solution mixing processes were observed in the resulting final ZT, which seems then independent of the elaboration protocols. Regardless of the process used, both grades of PLA were in amorphous under the elaboration processes used leading to similar cross-plane TE values for all nanocomposites with the same filler fraction. Besides, the electrical percolation threshold has been estimated to 0.36 vol% MWCNT, in the same order of magnitude found by other researchers. But more importantly, the values of the in-plane electrical conductivities were

100-1000 higher than the cross-plane ones, revealing a strong anisotropic behavior. It has been discussed that this behavior may be due to a preferential horizontal orientation of the CNT in the solvent and across the sample during its evaporation, especially at the surface of both sides.

The impact of crystallinity on the thermoelectric properties has been studied on Sc-PLA based nanocomposites containing 2 and 5 wt% of MWCNT. Two protocols involving an annealing or a slow cooling from the melt step have been used to induce crystallinity into the PLA matrix. The crystal structure and crystal content were determined by WAXS and DSC analysis. The TE properties were compared with those of amorphous nanocomposites containing the same filler fraction. Although σ value remains unchanged compared to that of A-PLA/MWCNT, the crystal phase of PLA lead to a slight increase of S and κ values, resulting in unchanged ZT values. This study showed no effect of the crystallinity on the TE properties probably because the filler content well above the percolation threshold.

The effect of CNT orientation has been studied thanks to uniaxially stretched nanocomposites containing 2 and 5 wt% MWCNT. The electrical conductivities were measured at room temperature along the sample thickness ($\sigma_{\mathrm{cross-plane}}$), and at the surface ($\sigma_{\mathrm{in-plane}}$) of the film. In the latter case, measurements perpendicular ($\sigma_{\mathrm{in-plane}\perp}$) and parallel ($\sigma_{\mathrm{in-plane}//}$) to the stretching direction were carried out. A decrease of all electrical conductivities with the draw ratio has been observed due to the disrupt in the CNT network. For the sample containing 5 wt % MWCNT uniaxially stretched at the highest draw ratio, the in-plane electrical conductivity is anisotropic ($\sigma_{\mathrm{in-plane}//} > \sigma_{\mathrm{in-plane}\perp}$) due to the orientation of the CNT along the stretching direction.

The last part of this work was dedicated to the effect of CNT type on the in-plane TE properties of thin A-PLA based nanocomposite films. The effect of MWCNT was thus compared with that of SWCNT and functionalized SWCNT-COOH, which are also commercially available. The nanocomposites reinforced with SWCNT showed the best TE properties with a maximum ZT value of 2.3×10^{-2} at 300 K for the sample containing 40 wt% of nanotubes. Even though the -COOH functionalization of SWCNT significantly increased the Seebeck coefficient values, it also slightly decreased the electrical conductivity, resulting in no improvement regarding of the ZT values. Finally, the influence of the temperature on the in-plane thermoelectric properties over the range from 300 and 400 K was studied for all three types of thin nanocomposite films. An increase in ZT with increasing temperature was systematically observed for each type of CNT, and the values almost double between 300 and 400 K, with a maximum value of 4.2×10^{-2} at 400 K for 40 wt% of SWCNT.

Perspectives

A number of questions remain unanswered from this experimental PhD work, requiring further studies. In the future works, it will be interesting to prepare PLA/CNT nanocomposites by *in-situ* polymerization which is known to favor a core/shell nanostructure. *In-situ* polycondensation of the commercially available lactic acid monomer in the presence of CNT or reactive extrusion process could be envisaged [1]. The purpose will be to evaluate the impact of *in-situ* polymerization on the CNT dispersion and the morphology of nanocomposite then to compare the thermoelectric properties of such nanocomposites with those of this research. In addition, beside different types of CNT (MWCNT, SWCNT, and SWCNT-COOH) were used in this study, it will be interesting to elaborate nanocomposite filled with double-walled carbon nanotubes (DWCNT). DWCNT have demonstrated the ability to significantly enhance the Seebeck coefficient and electrical conductivity, thereby expected to improve the thermoelectric properties of PLA/CNT nanocomposites [2,3].

From a long-term perspective of manufacturing a prototype of thermoelectric generator, it would be interesting to develop organic n-type semiconductor materials. The Bi_2Te_3 possesses a negative Seebeck coefficient and recently a novel synthetic methodology to prepare Bi_2Te_3 nanoparticles with a nanotubular morphology has been developed at ENSICAEN [4,5]. Therefore, it could be interesting to investigate PLA/Bi_2Te_3 nanocomposites in order to perhaps obtain n-type semiconductors and to consider manufacturing TE generator prototypes for flexible and portable application, operating at low temperature and with very low power. IoT objects such as connected watches and all types of self-powered micro-sensors could be among the most envisaged direct applications.

References

1. Bourbigot, S., Fontaine, G., Gallos, A., & Bellayer, S. (2011). Reactive extrusion of PLA and of PLA/carbon nanotubes nanocomposite: processing, characterization and flame retardancy. *Polymers for Advanced Technologies*, *22*(1), 30–37. https://doi.org/10.1002/pat.1715

2. Blackburn, J. L., Ferguson, A. J., Cho, C., & Grunlan, J. C. (2018). Carbon-Nanotube-Based Thermoelectric Materials and Devices. *Advanced Materials*, *30*(11), 1704386. https://doi.org/10.1002/adma.201704386

3. Mousavi, Z., Heuzey, M.-C., Kamal, M. R., Flahaut, E., & Carreau, P. J. (2021). Rheological, electrical, and dynamic thermomechanical properties: Comparison between multiwall and double-wall carbon nanotubes in polylactide and polyamide 11. *Physics of Fluids*, *33*(11), 113103. https://doi.org/10.1063/5.0068537

4. Baimyrza, A. (2022). Bismuth telluride nanoparticles for thermoelectrical application, synthesis and incorporation into polymer hybrid composites. *Normandie Université.*

5. Rijal, B., Baimyrza, A., Parein, T., Lonné, Q., Blond, D., Retoux, R., … Lemouchi, C. (2021). 1-dodecanthiol-assisted aqueous synthesis and characterization of Bi 2 Te 3 nanotubes. *Nano-Structures & Nano-Objects*, *25*, 100629. https://doi.org/10.1016/j.nanoso.2020.100629

Appendices

Appendix-1. Elaboration processes

A.1.1. Checking remaining solvent in PLA/CNT nanocomposites

DSC was used to ensure all residual solvent in sample from solution mixing process was evaporated**.** For example, Fig. A.1 shows the evolution of the DSC thermal response of A-PLA filled with 10 wt% of MWCNT for various durations of time spent in the vacuum oven (T = 120 °C), from 2 to 8 h. It can be seen that 8 h is the minimum time because no trace of solvent is present in the sample (no peak between 90 and 150 °C) and the obtained T_g value is closed to the T_g one of pristine A-PLA (60 °C).

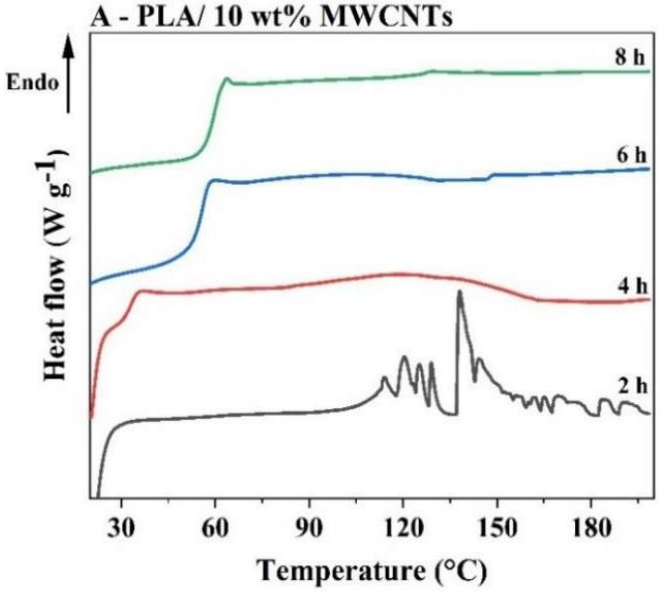

Figure A.1. DSC thermograms for checking remaining solvent in nanocomposite containing 10 wt% MWCNT.

A.1.2. Investigation of CNT dispersion condition in solvent

In the solution mixing process of preparing PLA/MWCNT nanocomposites, the crucial step is the dispersion of the nanotubes in the solvent. Since MWCNT form stabilized bundles due to Van der Waals interactions, the dispersion of MWCNT in $CHCl_3$ and PLA matrix is a challenge. Therefore, different ultrasonic conditions were used to investigate the dispersion of MWCNT in $CHCl_3$, and the final thick discs were conductively investigated by dielectric spectroscopy (Solartron) to select optimal conditions. Two ultrasonic systems were used. The former is an ultrasonic cleaning unit Elmasonic S 30H operating at 37 kHz with a power of 80 W, namely ultrasonic bath. The latter is an ultrasonic homogenizer Bandelin Sonoplus UW 3200 used with a TT13 probe, abbreviated ultrasonic tip. The ultrasound frequency of this

equipment is 20 kHz and the maximum of HF-power is 200 W. The applied power used is given in percentage of the amplitude of maximum power. All experiments were performed at room temperature.

Table A.1 demonstrates different conditions for preparing the solution of MWCNT, $CHCl_3$, and A-PLA pellets. The first step is the dispersion of MWCNT in $CHCl_3$ by using the ultrasonic bath during 3 h or the ultrasonic tip with different powers and durations. Then, the solutions were mixed with A-PLA and stirred for 12 h. Finally, the solutions were dispersed again by the ultrasonic bath or not before evaporating the solvent and thermo-compressing samples.

Table A.1. The dispersion conditions of MWCNT in $CHCl_3$ (10 wt% MWCNT).

Sample	Dispersion parameters
1	Ultrasonic bath (3 h) – mixing with PLA – Ultrasonic bath (3 h)
2	Ultrasonic tip (10 %, 15 min) – mixing with PLA (12 h)
3	Ultrasonic tip (10 %, 15 min) – mixing with PLA (12 h) – Ultrasonic bath (3 h)
4	Ultrasonic tip (20 %, 30 min) – mixing with PLA (12 h)
5	Ultrasonic tip (20 %, 30 min) – mixing with PLA (12 h) – Ultrasonic bath (3 h)
6	Ultrasonic tip (30 %, 30 min) – mixing with PLA (12 h) – Ultrasonic bath (3 h)
7	Ultrasonic tip (40 %, 30 min) – mixing with PLA (12 h) – Ultrasonic bath (3 h)
8	Ultrasonic tip (50 %, 30 min) – mixing with PLA (12 h) – Ultrasonic bath (3 h)
9	Ultrasonic tip (20 %, 15 seconds) – mixing with PLA (12 h)

Figure A.2 shows the cross-plane electrical conductivity as a function of the dispersion conditions. As can be seen, the values (σ_{DC}) of all samples are in the same order of magnitude when changing the dispersion conditions. But, sample number 9 which used 20 % amplitude of maximum power of ultrasonic tip during 15 seconds to make the dispersion of MWCNT shows the highest value in σ. These conditions with a quite small power and the shortest time in elaboration process allow to spare energy and spent time. Therefore, throughout this study, these conditions will be chosen as optimum conditions to make the dispersion of all kinds of CNT in $CHCl_3$.

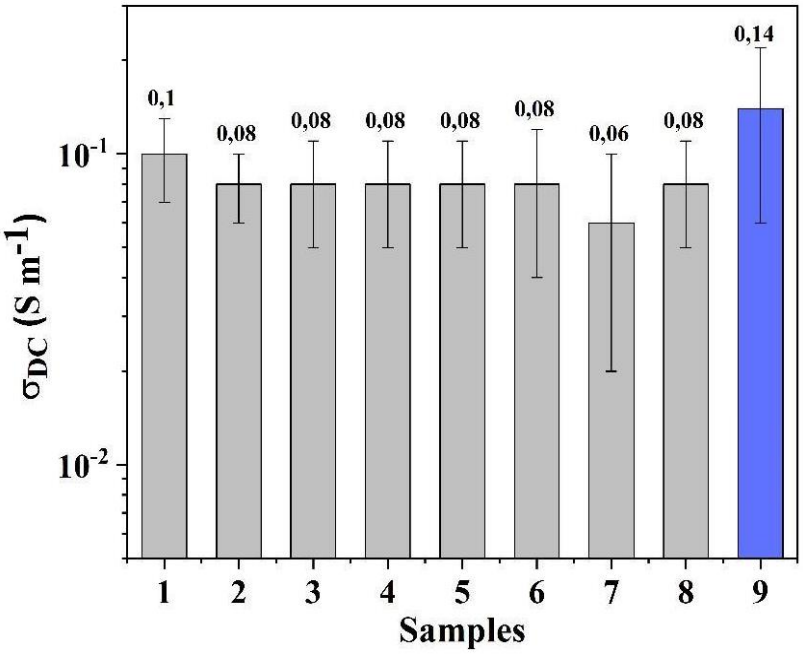

Figure A.2. Cross-plane electrical conductivity of A-PLA/ 10 wt% MWCNT samples at different dispersion conditions summarized in table A.1.

Appendix-2. Thermal analysis

Fig. A.3 shows DSC thermograms of A- and Sc-PLA/MWCNT nanocomposites from two elaboration processes. The DSC data of A- and Sc-PLA/MWCNT nanocomposite from two processes are presented in Table A.2 and A.3 corresponding to melt-blending and solution mixing, respectively.

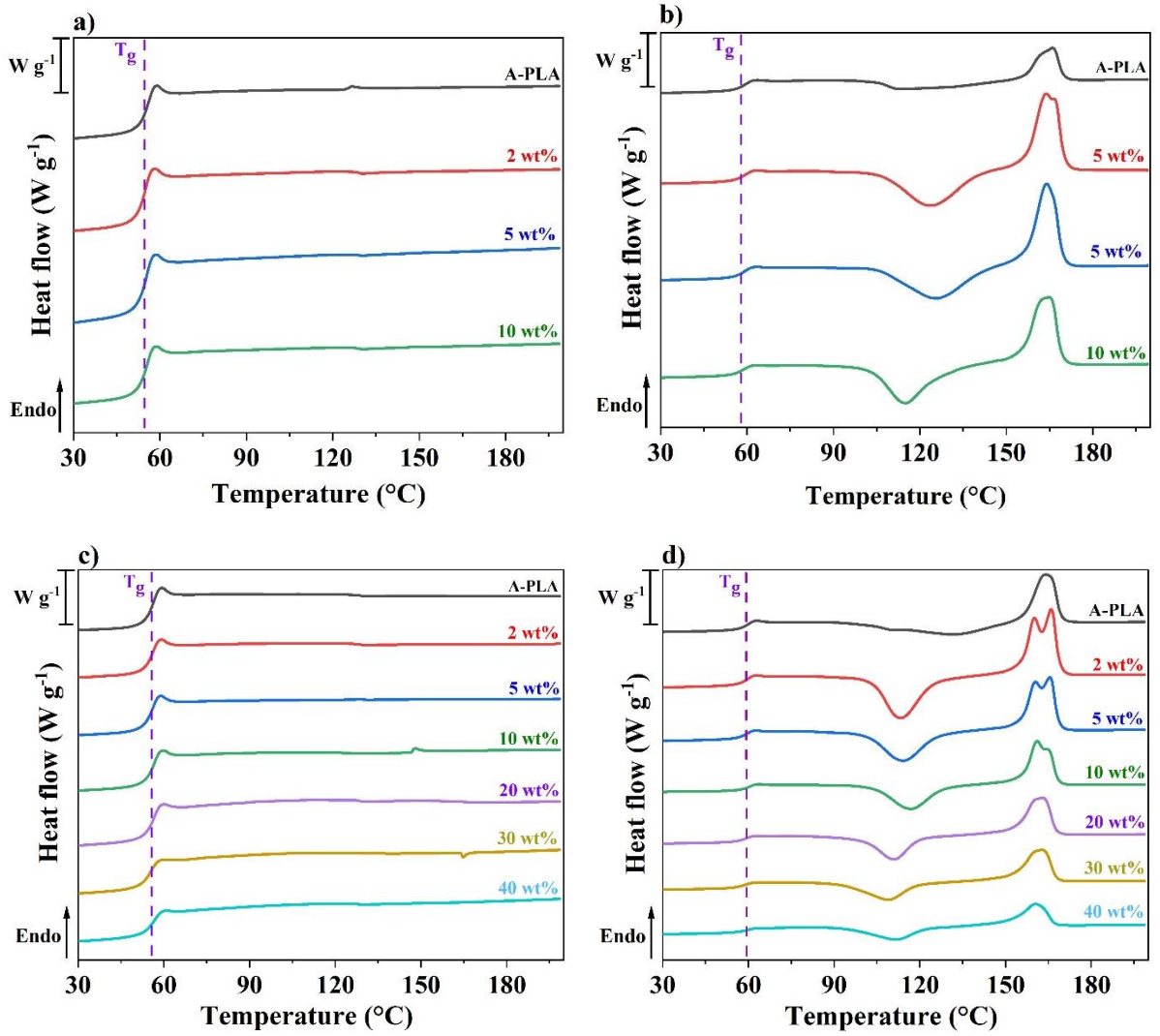

Figure A.3. DSC thermograms of nanocomposites from two elaboration processes. a) and b) corresponding to A- and Sc-PLA/MWCNT from melt-blending process, c) and d) corresponding to A- and Sc-PLA/MWCNT from solution mixing

Table A.2. DSC data of the pristine PLA and PLA/CNT nanocomposite from melt-blending.

Sample	MWCNT (wt%)	T_g (°C)	T_c (°C)	T_m (°C)	ΔH_{cc} (PLA fraction) (J g^{-1})	ΔH_{mm} (PLA fraction) (J g^{-1})	χ_c (%) (±2%)
A-PLA/MWCNT	0	55	-	-	-	-	-
	2	55	-	-	-	-	-
	5	55	-	-	-	-	-
	10	55	-	-	-	-	-
Sc-PLA/MWCNT	0	59	113	166	13	15	~ 2
	2	59	124	164	39	40	~ 1
	5	59	126	164	36	38	~ 2
	10	59	115	165	34	37	~ 3

Table A.3. DSC data of the pristine PLA and PLA/CNT nanocomposite from solution mixing.

Sample	MWCNT (wt%)	T_g (°C)	T_c (°C)	T_m (°C)	ΔH_{cc} (PLA fraction) ($J\ g^{-1}$)	ΔH_{mm} (PLA fraction) ($J\ g^{-1}$)	χ_c (%) (±2%)
A-PLA/MWCNT	0	56	-	-	-	-	-
	2	56	-	-	-	-	-
	5	56	-	-	-	-	-
	10	56	-	-	-	-	-
	20	56	-	-	-	-	-
	30	56	-	-	-	-	-
	40	56	-	-	-	-	-
Sc-PLA/MWCNT	0	60	131	164	26	27	~ 1
	2	60	113	166	36	39	~ 3
	5	60	114	165	37	39	~ 2
	10	60	117	161	35	37	~ 2
	20	60	110	162	28	33	~ 5
	30	60	109	162	27	32	~ 5
	40	60	111	160	21	26	~ 5

Appendix-3. Thermoelectric properties

A.3.1. Dielectric spectroscopy

The cross-plane electrical conductivity measurement for nanocomposites was systematically performed by using two kinds of dielectric spectroscopy equipment. The first is a ModuLab MTS Materials Test System from Solartron analytical supplied by HTDS (formerly Ameteck), equipped with a sample and reference module (useful for insulating materials) and a 12962A sample holder, which allows work to be carried out at room temperature only (Fig. A.4 a). The second is a broadband dielectric spectrometer (Novocontrol Technologies Alpha Analyzer) coupled to a high frequencies analyzer (Novocontrol Technologies RF impedance analyzer) and a thermal regulation system (Novocontrol Quatro controller) (Fig. A.4 b).

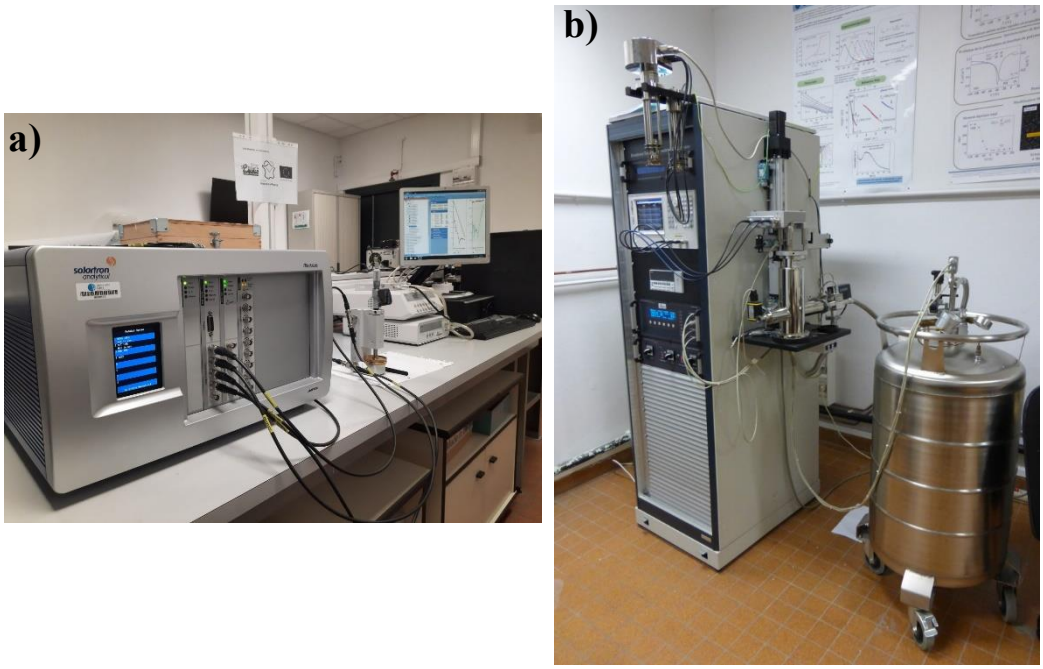

Figure A.4. Broadband dielectric spectroscopy a) Solartron and b) Novocontrol.

A.3.2. Hydrostatic density balance

The density (ρ) of each sample was determined with a precision scale thanks to a kit for density measurement (Fig. A.5)

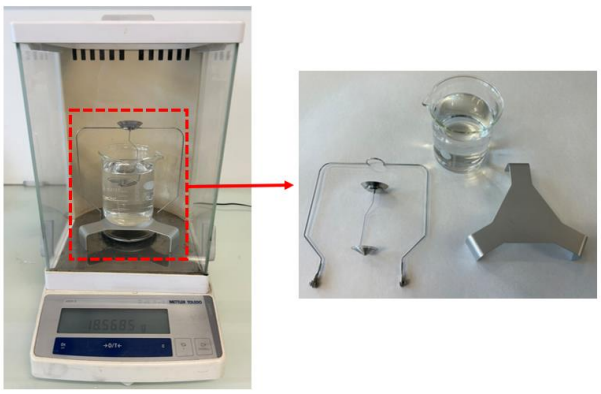

Figure A.5**.** A kit for density measurement.

Abstract

This project is part of a scientific and economic context in which energy recovery has become a major issue for our society. In this context, the development of organic thermoelectric materials for converting waste heat into electricity at low temperatures (T < 100 °C) is essential. This work has focused on investigating the relationships between elaboration process, structure and thermoelectric properties of polylactic acid/carbon nanotubes (PLA/CNT) nanocomposites. Both industrial grades of PLA including an amorphous (A-) and a semi-crystalline (Sc-) were used as a polymer matrix, and different types of CNT including multi-walled (MWCNT), single-walled (SWCNT), and functionalized single-walled (SWCNT-COOH) were used as filler.

Thick discs of PLA/CNT nanocomposites containing different amounts of MWCNT were prepared by two elaboration processes: melt-blending (up to 10 wt% MWCNT) and solution mixing (up to 40 wt% MWCNT). The cross-plane thermoelectric figure of merit $ZT = \frac{S^2\sigma}{\kappa}T$ of these thick discs were measured at room temperature by measuring the electrical conductivity (σ) with dielectric spectroscopy, the Seebeck coefficient S (also known as "thermoelectric power") with an in-house built device and the thermal conductivity (κ) by laser Flash Analysis (LFA). The results show that the elaboration process and the structure of PLA do not significantly affect the thermoelectric properties of the nanocomposites, but the in-plane values measured for the electrical conductivity (σ), by a 4-point collinear probe, are 100 to 1000 times higher than the cross-plane values, revealing a strong anisotropy of the thermoelectric properties in these samples. In addition, thin PLA/CNT nanocomposite films were elaborated by drop-casting, using the same solution mixing procedure and with the same filler content as the thick discs. The complete in-plane figure of merit (ZT) has been measured by a Thin Film Analyzer (TFA), from room temperature and up to 400 K, and the room temperature electrical conductivity appears completely similar to the in-plane values measured on the thick discs.

A study the impact of nanotube orientation was carried out. Uniaxial stretching has been performed on thick specimens with different strains to induce the alignment of CNT within the A-PLA matrix. The in-plane and cross-plane electrical conductivities of these samples were measured at room temperature, revealing a decrease in σ value with an increasing percentage of deformation. Particularly, at high deformation level, a clear difference in surface electrical conductivity has emerged between the measurements taken perpendicular and parallel to the

orientation of the CNT. In this case, the parallel conductivity values were found to be 10 times higher than the perpendicular values.

Finally, thin A-PLA based nanocomposite films with different types of CNT fillers (MWCNT, SWCNT, and SWCNT-COOH) were prepared and their in-plane thermoelectric figure of merit (ZT) was measured with the TFA from 300 K to 400 K. The obtained result show that SWCNT filler improve the thermoelectric properties of PLA/CNT nanocomposites by 2 orders of magnitude, with a maximum ZT value of 2.3×10^{-2} for 40 wt% of SWCNT at 300 K compared to 1.2×10^{-4} for 40 wt% of MWCNT at the same temperature. Moreover, these values are the best values in the literature for thermoplastic-based composites filled with CNT.

Keywords: Organic thermoelectrics, polymer composites, carbon nanotubes

Résumé

Ce projet s'inscrit dans un contexte scientifique et économique où la récupération d'énergie est devenue un enjeu majeur de notre société. Dans ce cadre, le développement de matériaux thermoélectriques organiques pour la conversion de chaleur fatale en électricité, à basse température (T<100 °C) est primordial. Cette thèse de doctorat s'est concentrée sur l'étude des relations entre l'élaboration, la structure et les propriétés thermoélectriques de nanocomposites Acide polylactique/nanotubes de carbone (PLA/NTC). Deux grades de PLA industriels ont été utilisés en tant que matrice polymère : un PLA amorphe (A-) et un PLA semi-cristallin (Sc-). Les charges conductrices sont, quant à elles, différents types de NTC : des nanotubes de carbone multi-feuillets (MWCNT), mono-feuillet (SWCNT), et mono-feuillet fonctionnalisés (SWCNT-COOH).

Des nanocomposites épais PLA/NTC, ont été élaborés sous forme de disques, pour différentes quantités de MWCNT, par 2 procédés : par mélange en voie fondue (jusqu'à 10 % en masse de NTC) et par mélange en solution (jusqu'à 40 % en masse de NTC). La figure de mérite thermoélectrique transversale (dans l'épaisseur) $ZT = \frac{S^2\sigma}{\kappa}T$ de ces disques a été mesurée, à température ambiante, en mesurant la conductivité électrique (σ) par spectroscopie diélectrique, le coefficient Seebeck S (aussi appelé "pouvoir thermoelectrique") avec un appareil développé en interne et la conductivité thermique (κ) par Laser Flash Analysis (LFA). Les résultats démontrent que le processus d'élaboration et la structure du PLA n'ont pas d'impact significatif sur les propriétés thermoélectriques des nanocomposites, mais les valeurs dans le plan (à la surface) mesurées pour la conductivité électrique (σ), par la méthode des 4 pointes alignées, sont 100 à 1000 fois plus élevées que les valeurs transversales, révélant une forte anisotropie des propriétés thermoélectriques dans ces échantillons. De plus, des films minces PLA/CNT ont été élaborés par « drop-casting », en utilisant la même procédure de mélange en solution et avec la même teneur en charge que les pastilles. La figure de mérite (ZT) dans le plan a été mesurée par un analyseur de film mince (TFA), de la température ambiante et jusqu'à 400 K, et la conductivité électrique à température ambiante apparaît complètement similaire aux valeurs mesurées dans le plan sur les pastilles.

Une étude de l'impact de l'orientation des nanotubes a été réalisée. Pour ce faire, un étirement uniaxial a été appliqué sur des échantillons épais à différents taux de déformation afin d'induire l'alignement des nanotubes au sein de la matrice A-PLA. Les conductivités électriques, dans le plan et transverses, ont été mesurées à température ambiante, révélant une

diminution des valeurs de σ avec une augmentation du pourcentage de déformation. En particulier, à forte déformation, une nette différence de conductivité électrique de surface est apparue lorsque les mesures ont été effectuées perpendiculairement et parallèlement à l'orientation des NTC. Dans ce cas, les valeurs de conductivité parallèle se sont révélées être 10 fois supérieures aux valeurs perpendiculaires.

Enfin, des films minces de nanocomposites à base de PLA amorphe (A-PLA), avec différents types de NTC (MWCNT, SWCNT, and SWCNT-COOH) ont été préparés, et leur figure de mérite thermoélectrique dans le plan a été mesurée avec le TFA, de 300 K à 400 K. Les résultats obtenus montrent que les nanotubes de carbone mono-feuillet (SWCNT) améliorent de 2 ordres de grandeur les propriétés thermoélectriques des nanocomposites, comparées aux MWCNT, avec une valeur maximale du facteur de mérite (ZT) de 2.3×10^{-2} à une concentration de 40 % en masse de SWCNT, à 300 K, pour une valeur maximale de 1.2×10^{-4} pour 40% en masse de MWCNT, à la même température. Ces valeurs de (ZT) sont par ailleurs les meilleures valeurs de la littérature concernant des thermoplastiques chargés en nanotubes de carbone.

Mots clés: Thermoélectricité organique, composites polymères, nanotubes de carbone